Follow the turbulent flow!

Berg, Jacob

Publication date:
2006

Document Version
Publisher's PDF, also known as Version of record

Follow the turbulent flow!

By

Jacob Berg

Ph.D. Thesis

Niels Bohr Institute
University of Copenhagen

September 2006

Abstract

A series of Particle Tracking Velocimetry experiments in turbulent flow have been performed. In Particle Tracking Velocimetry small, passive tracer particles are seeded in the fluid and illuminated. From camera recordings the trajectory of each tracer particle can be reconstructed in three dimensions. This thesis reports on Lagrangian measurements in hydromechanical turbulence.

Following only a single particle the diffusive behavior of the Lagrangian second order structure function is observed. Finite size effects of Lagrangian measurements of velocity are discussed. From studying the pdf of temporal velocity increments on a particle trajectory we find strong signatures of intermittent behavior. These reveal themselves as highly non-Gaussian tails in the distributions for small time lags. The scaling exponents of higher order structure functions is calculated and agreement with the multifractal prediction is found.

Much focus is on the separation between two particles - both as an initial value problem and as a boundary value problem.

Occupation and transit times defined as the time two particles are within a certain distance of each other conditioned on a uniformly distributed initial separation or a fixed separation, respectively, are investigated. We present a simple relation between the occupation and transit times and observe K41 similarity scaling within the inertial range. Simple models are presented and the relevance for zoo-plankton feeding rates is discussed.

The dispersion properties of particle pairs are measured with time running both forwards and backwards. An asymmetry is found: backwards dispersion is approximately twice as fast as the corresponding forward. This behavior is explained as a direct consequence of the positiveness of the intermediate eigenvalue of coarse-grained strain. Taking this approach further we find that the stretching rate in the inertial range is self-similar with a characteristic time scale which is a function of the second order Eulerian structure function. The time scale is closely related to the coarse-grained strain for the particular scale in question. A simple stochastic model is constructed based on the principle of self-similarity of stretching rates. For small times backwards and forwards dispersion occur with equal rates. This is the ballistic Batchelor regime and is in a high Reynolds number experiment found to be very robust.

Multi-particle statistics have been measured. The principle axes of triangles and tetrahedra are preferentially oriented with the eigenframe of coarse-grained strain. Scaling laws predicted by the K41 similarity theory are observed in the inertial range for coarse-grained quantities.

Acknowledgments

A number of people have been involved in the work leading to this thesis. Both as important co-workers and as moral supporters.

First of all I would like to thank my supervisor Jakob Mann. He invited me, a geophysicist, to Risø to do experimental turbulence. His inspiration and guidance are invaluable. Through conferences, lab sessions, Friday runs, paper reading and writing his enthusiasm have always been present.

Søren Ott has also been truly exceptional by all means. Doing things his own way - but always the correct way! - he has been a great help and inspiration. Late-comer, Beat Lüthi arrived to Risø and moved into my office and became a very important player in forming this Ph.D. Introducing me to *material line science* and travelling to Israel are different but both very memorable moments.

Peter Ditlevsen is my university supervisor and the one who encouraged me to consider a Ph.D. career in the first place. During the last three years we have had meetings where I have been presenting my latest work to him. This has been quite fruitful for my own understanding of what I often thought I already *had* understood: his ability to ask fundamental but still pedagogical questions is incredible.

A special thanks goes to the Cornell crew: Eberhard Bodenschatz for inviting me over to his *state of the art* lab, Nick Ouellette, Haitao Xu and Mickael Burgoin for helping me out in the lab and making Ithaca a very pleasant stay.

At Oslo university I would like to thank Hans Pécsèli. The symposium in Lysebu was both inspiring and joyful: skiing with *Dupont* and *Dupond* in the morning, delightful scientific discussions in the afternoon accompanied by great food and wine: it does not get much better than that!

I would also like to thank the Risø Wind Energy department especially people in the meteorology program for hosting me and making me feel welcome and at home. Office mates and colleagues Frederik Zahle, Andreas Hansen, Ferhat Bingöl, Xiaoli Guo Larsén and Alfredo Peña Díaz have been (and still are!) great friends.

For understanding and patience, friends and family are highly acknowledged, not least Malene.

Contents

Chapter 1

Foreword

I will present results on hydromechanical turbulence obtained from Particle Tracking Velocimetry experiments. Particle Tracking Velocimetry is a machine vision system which can measure Lagrangian quantities, i.e. the motion of individual tracer particles in a turbulent flow. Results from one-particle statistics, two-particle statistics and the generalization of multi-particles in coarse-grained fields are presented.

The dissertation thesis is the outcome of my Ph.D. studies during the last three years.

The dissertation is presented to the Niels Bohr Institute at the University of Copenhagen in partial fulfillment of the requirement for the degree of Doctor of Philosophy. My *internal* supervisor has been Dr. Peter D. Ditlevsen of the Theoretical Geophysics group at the Niels Bohr Institute.

During the three years I have been employed by the Wind Energy Department at the Risø National Laboratory. My *external* supervisor has been Research Professor Jakob Mann at the Risø National Laboratory. Besides him, the group of turbulent particle tracking also consists of Senior Researcher Søren Ott and Post.doc. Beat Lüthi.

From September 2004 to February 2005 I stayed at the Laboratory of Atomic and Solid State Physics at Cornell University, NY, USA under instructions of Professor Eberhard Bodenschatz.

The thesis is a monograph of papers appearing in or submitted to international peer-reviewed journals (the last three papers are exceptions as they have not yet been submitted).

The papers are:

I *Experimental studies of occupation and transit times in turbulent flows.* **J. Berg Jørgensen**, J. Mann, S. Ott, H. L. Pécseli and J. Trulsen *Physics of Fluids* 17, p. 035111 (2005).

II *The role of pair dispersion in turbulent flow.*
M. Bourgoin, N. T. Ouellette, H. Xu, **J. Berg** and E. Bodenschatz
Science 311, p. 835 (2006).

III *Backwards and forwards relative dispersion in turbulent flow: An experimental investigation.*
J. Berg, B. Lüthi, S. Ott and J. Mann
Physical Review E 74, p. 016304 (2006).

IV *Self similar two particle separation model.*
B. Lüthi, **J. Berg**, S. Ott and J. Mann
Submitted to *Physics of Fluids.*

V *Lagrangian multi-particle statistics.*
B. Lüthi, **J. Berg**, S. Ott and J. Mann
Manuscript.

VI *Coarse-grained strain dynamics and backwards/forwards dispersion*
J. Berg, B. Lüthi, S. Ott and J. Mann
Manuscript.

VII *Lagrangian one-particle velocity statistics from the Risø PTV experiment*
J. Berg
Manuscript.

The roman numbers will throughout the thesis refer to the papers. The papers are included in their original form and layout at the end of the thesis. Before reaching the papers I have included a general introduction to some theoretical concepts in turbulence as well as the experimental technique of Particle Tracking Velocimetry (PTV). This general text will hopefully make the understanding of the papers more clear as well as putting them in a somehow broader context. A summary of the main results is included in the end.

Chapter 2

Introducing turbulence

Turbulence is the state of fluid flow far from rest. It is vivid and random although the governing equation, the Navier-Stokes equation, is deterministic. Merging fluid mechanics with concepts from statistical physics it continuous to puzzle every man from laboratory scientists to kids setting up a kite.

People often talk about turbulence as the last unsolved problem in the realm of classical physics. It is certainly true that many problems concerning turbulence are still not solved today even though the Navier-Stokes equation was formulated more than hundred years ago. What is *the problem of turbulence*, is, however, not even very clear. A complete mathematical description capable of describing experimental results as well as predicting future events would of course be the ultimate goal. We are, however, nowhere close to such a theory, and probably much more important: it may not exist at all.

Water falls, fast pipe flows, aerodynamics of planes and wind turbines, mixing and combustion processes, pollution release, prey-predator dynamics in marine ecosystems, fluxes of heat and momentum between interfaces, solar surface activity and short-term weather forecasting are only a few of the phenomena for which turbulence plays a crucial role. So... *What is turbulence?*

Everybody who has been on an aeroplane would associate turbulence with sudden violent burst of air with forces large enough to move the aeroplane out of its course. This observation, although a crude description, is rather good. It indicates that turbulent air is far from being a system in equilibrium. The intermittent nature is also of great significance: the relative frequent occurrence of extreme energy bursts characterize non-simple dynamics.

The Clay Mathematics Institute named seven Millennium price Problems in the year 2000. Among these were the problem of turbulence defined as the existence of smooth solutions to the Navier Stokes equation. If a smooth

solution exists and is found we, I agree, have come a long way. It will, however, not change much when it comes to applications and usage. Predicting the trajectory path of a single fluid particles *is not* turbulence. Turbulence *is* the statistical fluctuations in a large ensemble of fluid trajectory. The intrinsic property of chaotic unpredictability (the exponential divergence of initially close particles) would still make a perfect weather forecast impossible even though a general solution to the Navier Stoke equation was known. Defining *the problem of turbulence* is therefore of essential importance.

In popular reviews chaos theory and turbulence is often juxtaposed. Nothing could be more wrong. Turbulence certainly has chaotic properties. Chaos is, however, *not* turbulence. Lorenz (1963) found that a simple dynamical non-linear system with only three degrees of freedom, in certain configurations, would exhibit sensitive dependence on the initial conditions and hence show chaotic behavior. In a turbulent flow, as we shall see, the number of degrees of freedom increase as we increase the level of turbulence. This is in contrast to the simple system as for example the one by Lorenz where the number of degrees of freedom remain constant. We could say that where the Lorenz system *only* show temporal chaos turbulence also show spatial chaos. This observation motivated Bohr et al. (1998) to define turbulence as *chaotic dynamics in a temporally and spatially extended system.* I tend to agree.

Today terms as universality, scale invariance and intermittency of statistical fields are important and useful tools in narrowing down the main question: *What is turbulence?*

2.1 The Navier-Stokes equation

We believe that turbulence is contained in the rich dynamics governed by the Navier-Stokes equation and the continuity equation of an incompressible fluid.

$$\partial_t u_i + u_j \partial_j u_i = -\partial_i p + \nu \partial_{jj} u_i + f_i \tag{2.1}$$

$$\partial_i u_i = 0, \tag{2.2}$$

where u_i and $\partial_i p$ are components of the velocity $\mathbf{u}(\mathbf{x}, t)$ and pressure gradient $\nabla p(\mathbf{x}, t)$ fields, respectively. The density of the fluid ρ has been absorbed in the pressure and ν is the kinematic viscosity of the fluid while $\mathbf{f}(\mathbf{x}, t)$ denotes the forcing of the fluid in question.

The Navier-Stokes equation expresses momentum conservation while the continuity equation expresses mass conservation. The left hand side of eqn. 2.1

is the total derivative of velocity, i.e. the acceleration of a fluid particle (defined by the continuums approximation (Lautrup, 2005)) in the coordinate system following the particle:

$$\frac{Du_i}{Dt} = \partial_t u_i + u_j \partial_j u_i. \tag{2.3}$$

The coordinate system following a fluid particle is denoted the Lagrangian frame of reference opposed to the perhaps more familiar Eulerian frame, where the coordinate system is fixed in the laboratory system. More formally we consider a three dimensional field of some arbitrary scalar ϕ. In the Lagrangian frame $\phi^L(\mathbf{y}, t)$ is the scalar field expressed by the fluid trajectory with position $\mathbf{y}$ at time $t = 0$. The same field is in the Eulerian frame denoted $\phi^E(\mathbf{x}, t)$. Only when $\mathbf{y} = \mathbf{x}(\mathbf{y}, t)$ do the two representations refer to the same point in space. $\mathbf{x}(\mathbf{y}, t)$ is the location of the fluid trajectory at time t conditioned on that it was at $\mathbf{y}$ at time $t = 0$.

A scale analysis of eqn. 2.1 with characteristic time and length scales $\widetilde{T}$ and $\widetilde{L}$ with $\widetilde{U} = \widetilde{L}/\widetilde{T}$ gives the Reynolds number

$$Re \equiv \frac{\widetilde{U}\widetilde{L}}{\nu}. \tag{2.4}$$

Low values of Re means that the non-linear effects are very small compared to the dissipation. This is the laminar state where the velocity field is smooth and regular. In this lower limit solutions to problems in simple geometries exist and these can be found in most textbooks on fluid mechanics. In the opposite range of Re one finds the turbulent regime where fluid motion is non-regular and highly chaotic. A possible definition of turbulence would therefore be that *turbulence is the state of fluid motion corresponding to (almost) infinite Reynolds number.* I write *almost* in parenthesis because laboratory experiments and computer simulations of turbulence often are quite far from the asymptotic limit. Bridging this asymptotic limit, for which, as we shall see, theoretical predictions exist, with current finite Reynolds number experiments is a great challenge and will be central in the work presented in this thesis.

Turbulence experiments and Direct Numerical Simulations (DNS) of the Navier-Stokes equation traditionally measure the degree of turbulence by the Taylor micro-scale Reynolds number Re_λ:

$$Re_\lambda = \frac{\sigma_u \lambda}{\nu}. \tag{2.5}$$

The Taylor micro-scale is defined through the velocity derivative of the stan-

dard deviation of velocity u_i of a single component $i = 1$

$$\frac{1}{\lambda^2} = \frac{\langle(\partial_1 u_1)^2\rangle}{\sigma_u^2} \tag{2.6}$$

and the standard deviation of all three velocity components $\sigma_u^2 = \frac{1}{3}\langle u_1^2 + u_2^2 + u_3^2\rangle$. Compared to the Reynolds number defined in eqn. 2.4, eqn. 2.5 does not require any information on the large scale velocity $\widetilde{U}$ and length $\widetilde{L}$ of the flow. Re_λ is therefore more suitable for flow away from boundaries, i.e. isotropic and homogeneous flow.

In the laminar regime where the non-linear term can be neglected the Navier-Stokes equation is subject to a large number of symmetries (provided that the forcing allows it); space and time translations, Galilean transformations, parity, rotation and scaling. As the Reynolds number is increased and the non-linear effects become important, the symmetries are broken one by one and the flow becomes seemingly more and more random. At a sufficiently high Reynolds number corresponding to a fully developed turbulent regime the symmetries are restored in a statistical sense far away from any boundaries (Frisch, 1995): the velocity of a fluid particle can be treated as a stochastic variable and tools of stochastic calculus can be applied (Pope, 2000).

2.2 Phenomenology and K41

With no complete theory derived rigourously from the Navier-Stokes equation the British meteorologist L. F. Richardson's phenomenological picture is still the best we got. Richardson's picture of turbulence as a pool of eddies of various sizes which break up in yet smaller eddies which again break up... and so on until dissipation ultimately takes over, is still widely accepted as a zero order explanation of turbulence. Although very simple, it introduces some important concepts such as energy cascade and the assumption of local interactions.

Perhaps indirectly motivated by Richardson the Russian mathematician A. N. Kolmogorov revolutionized turbulence theory in 1941 with his similarity theory. Besides some simple (but strong) hypotheses about the fully developed turbulent regime he derived one of the only exact results on statistical turbulence related directly to the Navier-Stokes equation. A summary of his theory is well described by Frisch (1995) who even name his textbook *Turbulence - The legacy of A. N. Kolmogorov*. I will briefly go thought the concepts of the K41 similarity theory (as it is commonly named) as it, despite its flaws, is the foundation of modern turbulence theory.

Kolmogorov put forward three hypothesis for the fully developed turbulence regime:

The hypothesis of local isotropy Away from forcing and boundaries the small scales in a turbulent flow are homogeneous and isotropic.

The first similarity hypothesis The small scales are controlled by the viscosity ν and the mean kinetic energy dissipation ε.

The second similarity hypothesis There exist a range of scales where the effect of dissipation and forcing can not directly be felt so that the motion is controlled solely by the mean kinetic energy dissipation ε. This range is named the inertial range.

The kinetic energy dissipation is an important parameter and its relevance is justified by the statistical invariance of energy $E \equiv \langle \frac{1}{2} u^2 \rangle$ in the inviscid Navier-Stokes equation (The Euler equation). ε may, however, best be described through concept of energy cascade...

2.2.1 The Energy cascade

In Richardson's picture the turbulence consists of eddies of different size r with characteristic velocity $u(r)$ and time scale $\tau(r) \equiv r/u(r)$.

The kinetic energy enters the system, i.e. the turbulent fluid, at the largest scales equal to the size of the largest eddies in the flow, often denoted the integral scale L_{int}, and is then transferred by inviscid processes to the smallest scales in the system. At these smallest scales dissipation converts the energy into heat. A system which is not continuously forced will therefore after some time come to rest.

From the first similarity hypothesis one can construct the Kolmogorov scales characterizing the typical length, time and velocity of dissipation:

$$\eta = \left(\frac{\nu^3}{\varepsilon}\right)^{1/4} \tag{2.7}$$

$$\tau_\eta = \left(\frac{\nu}{\varepsilon}\right)^{1/2} \tag{2.8}$$

$$u_\eta = (\varepsilon\nu)^{1/4}. \tag{2.9}$$

For eddies with size r and for which $\eta << r < L_{int}$ is valid the motion according to the second similarity hypothesis is only dependent on the mean kinetic energy dissipation ε.

Because of energy conservation ε must be equal to the energy input into the system due to forcing on the largest scales and therefore

$$\varepsilon \sim \frac{\sigma_u^3}{L_{int}}. \tag{2.10}$$

We can, however, also express ε at the scales of dissipation:

$$\varepsilon = 2\nu\langle s^2\rangle, \tag{2.11}$$

where $s^2 = s_{ij}s_{ij}$. The rate of strain tensor s_{ij} is the symmetric part of the velocity derivative tensor $a_{ij} = \partial_i u_j$, hence $s_{ij} = \frac{1}{2}(\partial_j u_i + \partial_i u_j)$. From homogeneity and isotropy (the hypothesis of local isotropy) one can calculate $\langle s^2\rangle = \langle \frac{15}{2}(\partial_1 u_1)^2\rangle$ so that

$$Re_\lambda = \sqrt{15}\frac{\sigma_u^2}{\sqrt{\nu\varepsilon}}. \tag{2.12}$$

ε, σ_u and ν therefore solely determine the *strength* of a homogeneous and isotropic turbulent flow.

Manipulating eqn. 2.10 and eqn. 2.12 we find that the Reynolds number can also be expressed as $Re_\lambda = \sqrt{15}(L_{int}/\eta)^{2/3}$. If we define the number of degrees of freedom N_{dof} of a turbulent system as the number of spatial points needed to resolve all eddies in the three dimensions we will need $N_{dof} \sim (L_{int}/\eta)^3$ and hence

$$N_{dof} \sim Re_\lambda^{9/2}. \tag{2.13}$$

This has direct consequences for computer simulations of turbulence. For example can DNS only be performed for Reynolds numbers many times smaller than Reynolds numbers in natural flows such as for example the atmosphere.

Local quantities are defined as differences over some distance r in the flow. The effect of large scales can hence be damped by considering values of r smaller than the integral scale L_{int}. The velocity change over a distance r is $\delta u(r)$. From the second similarity hypothesis this quantity can only be a function of the scale r and ε and dimensionality dictates

$$\delta u(r) \sim \varepsilon^{1/3} r^{1/3}. \tag{2.14}$$

In the Richardson picture the inertial range consists of eddies breaking up into smaller eddies. Only eddies of comparable size interact predominantly with each other. This is called localness of interactions. For example will eddies with much greater size sweep smaller eddies without distorting their structure. Every time an eddy breaks up it *forgets* something from the past

so that at the smallest scales there is no longer any memory of the large scale structure. This is the physical interpretation of the hypothesis of local isotropy.

Several experiment have addressed this issue which is considered quite fundamental since it is one of the main assumptions of Kolmogorov similarity theory. A wind tunnel experiment of a linear shear flow has shown that anisotropy on the largest scales due to the mean shear is also present on the smallest scale in the flow - although to a lesser degree (Shen and Warhaft, 2000, 2002). A relaxation towards isotropy is thus taken place although a perfect isotropic state is not observed. Ouellette et al. (2006b) also find a significant anisotropic component on the smallest scales. A similar observation is presented in paper V, VI and VII.

How can this be interpret in terms of the Navier-Stokes equation? If we take the curl of the Navier-Stokes equation we end up with an equation for the vorticity $\boldsymbol{\omega}(\mathbf{x},t) = \nabla \times \mathbf{u}(\mathbf{x},t)$:

$$\partial_t \omega_i + u_j \partial_j \omega_i = \omega_i s_{ij} + \nu \partial_{jj} \omega_i + \epsilon_{ijk} \partial_j f_k \tag{2.15}$$

The left hand side is the total derivative $\frac{D\omega_i}{Dt}$. On the right hand side, the first term involves both vorticity and the rate of strain and is responsible for stretching (or compression) and tilting of vorticity, the next term accounts for dissipation while the last term is the curl of the forcing field. Solving the equation implies solving the non-local equation $u = (\nabla\times)^{-1}\omega$ appearing in the total derivative, where $(\nabla\times)^{-1}$ is the inverse of the curl operator. To solve it knowledge about the whole domain of vorticity is necessary. If we use K41 similarity scaling $\delta u(r) \sim \varepsilon^{1/3} r^{1/3}$; the largest velocity $\delta u(r)$ are related to the largest scales, and the largest vorticityis are similarly related to the smallest scales ($\delta u(r)/r \sim \varepsilon^{1/3} r^{-2/3}$). The equation $u = (\nabla\times)^{-1}\omega$ can therefore be interpreted as a coupling between large and small scales and hence a violation of localness of interactions.

2.2.2 A statistical representation

We define the velocity difference between two points at the same time instance t in a fluid separated by a vector $\mathbf{r}$ as

$$\delta u_i(\mathbf{x},\mathbf{r},t) = u_i(\mathbf{x}+\mathbf{r},t) - u_i(\mathbf{x},t). \tag{2.16}$$

We define structure functions $S^n_{ij}(\mathbf{x},\mathbf{r},t)$ as the statistical ensemble average of the nth moment of $\delta u_i(\mathbf{x},\mathbf{r},t)$. The second order structure tensor is thus given by

$$S^2_{ij}(\mathbf{x},\mathbf{r},t) = \langle [u_i(\mathbf{x},t) - u_i(\mathbf{x}+\mathbf{r},t)][u_j(\mathbf{x},t) - u_j(\mathbf{x}+\mathbf{r},t)] \rangle \tag{2.17}$$

Applying the hypothesis of local isotropy and assuming time-stationarity we have that

$$S_{ij}^2(r) = \langle [u_i(\mathbf{x}) - u_i(\mathbf{x}+\mathbf{r})][u_j(\mathbf{x}) - u_j(\mathbf{x}+\mathbf{r})] \rangle \tag{2.18}$$

must be a second-order isotropic tensor, that is:

$$S_{ij}^2(r) = A(r) r_i r_j + B(r)\delta_{ij} \tag{2.19}$$

We now define the longitudinal structure function $f(r) = \langle S_{ij}^2 n_i n_j \rangle$ and the transverse structure function $g(r) = \langle S_{ij}^2 t_i t_j \rangle$ with unit vectors n_i and t_i defines as $n_i = r_i/r$ and $n_i t_i = 0$. Inserting $f(r)$ and $g(r)$ in eqn. 2.19 gives

$$f(r) = A(r)r^2 + B(r) \tag{2.20}$$
$$g(r) = B(r). \tag{2.21}$$

and we arrive at

$$S_{ij}^2(r) = g(r)\delta_{ij} + [f(r) - g(r)]\frac{r_i r_j}{r^2}. \tag{2.22}$$

One can derive an interesting relationship between these structure functions and the change in acceleration in the longitudinal direction (see appendix A).

In the inertial subrange K41 similarity theory predicts

$$f(r) = C_K \varepsilon^{2/3} r^{2/3}. \tag{2.23}$$

Here C_K is the non-dimensional Kolmogorov constant. Numerous experiments have found that $C_K = 2.13$ (Pope, 2000).

The third order longitudinal structure function

$$\langle \delta u_{||}^3(r) \rangle = -\frac{4}{5}\langle \varepsilon \rangle r. \tag{2.24}$$

is special since it is directly accessible from the Navier-Stokes equation. Kolmogorov derived the equation based on an earlier study by von Kármán and Howarth. The equation is *perhaps* the still only acknowledged exact result in turbulence, and it is known as the *four-fifth* law (Frisch, 1995).

We define the velocity co-variance tensor as

$$R_{ij}(\mathbf{x}, \mathbf{r}, t) = \langle u_i(\mathbf{x}, t) u_j(\mathbf{x}+\mathbf{r}, t) \rangle. \tag{2.25}$$

Since it involves contributions from eddies at all scales the covariance tensor is not local in scale and does therefore not follow K41 similarity scaling. Under

homogeneous and isotropic condition the covariance tensors can just like the structure functions be split up into a longitudinal $R_{||}(r)$ and a transverse function $R_{\perp}(r)$. In the longitudinal direction we have:

$$f(r) = 2(\sigma_u^2 - R_{||}(r)). \tag{2.26}$$

One can use the Navier-Stokes equation to write up an equation for the time derivatives of the co-variance tensors. This equation will, however, lead to the famous *closure problem:* a solution to the equation of the second order correlation tensor is dependent on the knowledge of the third order tensor. Solving then for the third order correlation tensor knowledge about the fourth order correlation function is needed, and so on...

Intermittency corrections

ε is the mean kinetic energy dissipation. Formerly we should therefore properly have been writing $\langle\varepsilon\rangle$ instead of just ε. We now assume that $\langle\varepsilon\rangle$ is not capturing the full dynamics characterizing the energy flux from large to small scales as assumed in the first similarity hypothesis, but that higher order moments of ε are also important in the description of the energy flux. If we look at a structure function of order n K41 similarity scaling could either mean that $\langle S^n(r)\rangle \sim \langle\varepsilon\rangle^{n/3} r^{n/3}$ or that $\langle S^n(r)\rangle \sim \langle\varepsilon^{n/3}\rangle r^{n/3}$. For $n \neq 3$, $\langle\varepsilon\rangle^{n/3} \neq \langle\varepsilon^{n/3}\rangle$. This is known as the Landau objection and it introduces the notion of intermittency in turbulence, which can be though of as corrections to K41 similarity theory.

Kolmogorov himself refined his theory in 1962 suggesting that $\delta u(r)$ depends on the local value of ε defined as the average over a sphere with radius r instead of the globally averaged value of ε. Assuming a log-normal distribution of ε he managed to calculate the corrections to his 1941 similarity theory.

The log-normal distribution of ε has been shown not to be entirely correct (Anselmet et al., 1984). At present the distribution of ε is not well known. The most successful theory of intermittency is the phenomenological multifractal framework which in contrast to the Richardson picture assumes that eddies are not *space-filling*. By *space-filling* we mean that when an eddy breaks up into smaller eddies, the smaller eddies do not occupy the same amount of physical space in the flow as the larger eddy. It is assumed that the dimension of space occupied by the smaller eddies is fractal and can take any value between zero and three. This again means that we have a distribution of different fractal dimensions each with an associated scaling exponent h so that $\delta u(r) \sim r^h$ as opposed to the K41 picture where $h = 1/3$ everywhere in the flow. A physical interpretation is that you have regions in space

with different turbulence activity and thus with different scaling of δu. A lengthy discussion of the multifractal model and intermittency in general can be found in Frisch (1995). In paper VII intermittency and the multifractal model are explored in the Lagrangian frame.

2.2.3 Lagrangian scaling

We define the velocity difference along a particle trajectory $\mathbf{y}(\mathbf{x}_0, t)$ originating at $\mathbf{x}_0$ at time $t = t_0$ as

$$\delta u_i(\tau, t) = u_i(t + \tau) - u_i(t). \tag{2.27}$$

Like in the Eulerian frame where structure functions was constructed as statistical averages of spacial velocity increments $\delta u(r)$, we can construct Lagrangian structure functions as statistics moments of temporal velocity increments along a fluid trajectory. Under stationary conditions $\delta u_i(\tau, t)$ does not depend on t and hence the K41 similarity theory predicts for the second order Lagrangian structure function in the inertial range:

$$\langle \delta u_{ij}^2(\tau) \rangle = C_0 \varepsilon \tau \delta_{ij} \tag{2.28}$$

The constant C_0 is supposed to be universal in the limit of infinite Reynolds number. The second order structure function in eqn. 2.28 is linear in ε and hence not supposed to be affected by intermittency.

Compared to Eulerian statistics, Lagrangian K41 similarity scaling is much harder to measure: whereas the inertial range in the Eulerian frame scales as $L_{int}/\eta \sim Re_\lambda^{3/2}$, the inertial range in the Lagrangian frame scales as $T_L/\tau_\eta \sim Re_\lambda$, where $T_L = L_{int}/\sigma_u$. This means that a higher Reynolds number is required for a Lagrangian inertial range of same significance as the corresponding Eulerian in terms of scale separation L_{int}/η and T_L/τ_η.

In paper VII we study Lagrangian one-particle statistics and find evidence of intermittency in agreement with the multifractal prediction.

Chapter 3

Particle tracking velocimetry

Particle Tracking Velocimetry (PTV) is an experimental technique where Lagrangian trajectories of fluid particles can be studied.

By illuminating passively advected, neutrally buoyant tracer particles with light and recording the reflected light with several cameras the Lagrangian trajectories of the tracer particles can be reconstructed in time and space. The method is thus essentially Lagrangian. It can, however, also be used to measure Eulerian statistics, such as two-point correlations and structure functions by sampling particle velocities at fixed distances.

A complete understanding of turbulence is only achieved if both the Eulerian and Lagrangian descriptions are studied. So far most experimental work has focused on the Eulerian way. Recent years have, however, focused and shed light on the Lagrangian description through both experiments (Ott and Mann, 2000, 2005; Porta et al., 2001; Mordant et al., 2001, 2004a,b; Lüthi et al., 2005; Xu et al., 2006) and DNS (Biferale et al., 2005a,b, 2006; Boffetta and Sokolov, 2002; Ishihara and Kaneda, 2002; Yeung, 2002; Yeung and Borgas, 2004; Pumir et al., 2000). The work presented in this thesis can be viewed as a continuation of this work.

The possibility of measuring both Lagrangian and Eulerian quantities makes the PTV technique superior to more standard methods such as hot wires, laser doppler velocimetry (LDV) and particle image velocimetry (PIV). Another advantage over the mentioned systems is the true three-dimensional representation (recently PIV was extended to three dimensions by holography (Tao et al., 2002)). On the negative side both temporal and spatial resolution is not comparable with PIV (spatial) and hot-wires and LDA (temporal).

The speed of the recording system in PTV is a limiting factor. This means that studies of very fast flows are currently not accessible with PTV. Hot wires would be utilized for such a purpose. Hot wires, however, have the

drawback that not only are you affecting the flow by placing your wires in the flow but you also have to rely on the Taylor hypothesis, ie. assuming that the root-mean-square of velocity is much smaller than the mean flow and hence that temporal fluctuations of velocity can be interpreted as spatial fluctuations.

The papers presented in the thesis are all except one (paper IV) based on the PTV technique. The first paper I is based on data obtained from the first Risø experiment (Mann et al., 1999; Ott and Mann, 2000, 2005). Paper II presents results from the Cornell PTV setup while data analyzed in III, V, VI and VII have been obtained from the second Risø experiment performed during the last three years.

3.1 PTV at Risø

The second Risø experiment (2003-) is an update of the first Risø experiment (1998-2000). Many issues of technical relevance can therefore be found in Mann et al. (1999). The most fundamental stuff relevant for understanding the pros and cons of PTV will, however, be presented in this section.

3.1.1 Apparatus

A tank with dimensions $32 \times 32 \times 50\text{cm}^3$ is filled with ion-switched water at $\sim 25^\circ$ Celsius. A top plate is preventing air from entering the water. Two glass plates are placed on the sides.

The flow is generated by eight rotating propellers which change their rotational direction in fixed intervals in order to suppress a mean flow. The propellers are placed in the corners of the tank. A photo of the experiment is shown in Figure 3.1 (a) and a sketch of the experiment can be found in paper III.

Tracer particles are seeded in the flow and illuminated by a 200W flash lamp (Figure 3.1. (b)). A data acquisition system consisting of four PCs with frame grabber cards connected to four commercial CCD cameras (Basler A202K with Nikon lenses: Micro-Nikkor 60mm f/2.80) with a maximum frame rate of 50Hz at 1000×1000 pixels is recording the light reflected from the particles. The cameras are placed on top of each other two-by-two at a 90 degree angle. In this way a nice three-dimensional picture can be obtained with no ambiguities in three-dimensional correspondence between the cameras. At the maximum frame rate the exposure time of the cameras is 21ms while the light pulse duration is of order 1ms. With a capacitor of

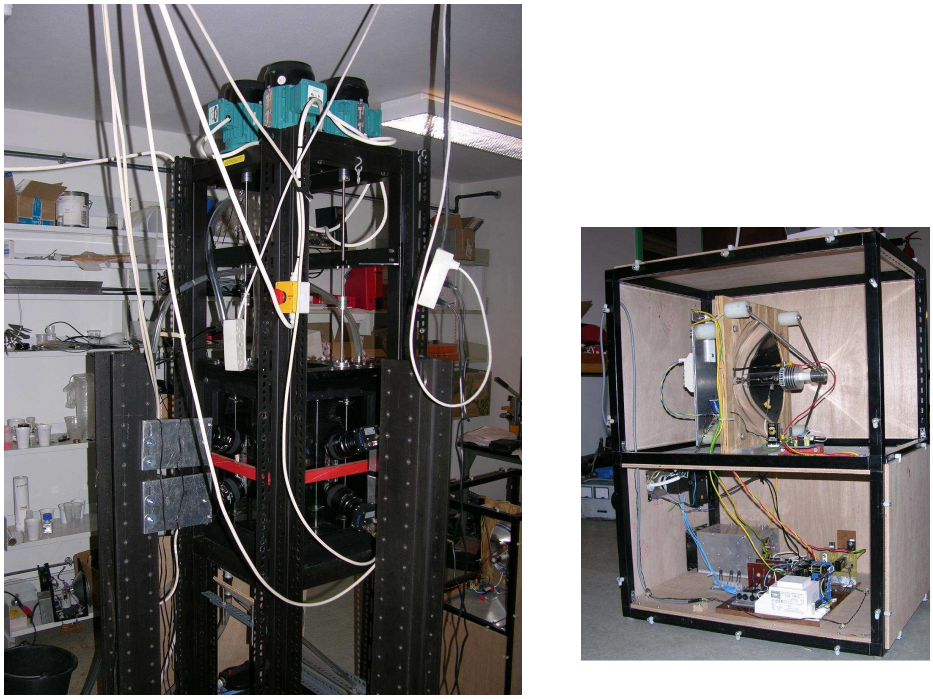

Figure 3.1: a) Experimental setup: four motors on the top of the post are generating the forcing through four aluminium rods with propellers. The cameraes are pointing toward the same volume roughly placed at the center of the tank. b) Light source: flash lamp (designed by Søren Ott).

3μF and a potential of 1200V each pulse carries around 2J. This turns out to give a well behaved signal-to-noise ratio of the recorded images.

3.1.2 Setups

Two different setups are used:

Micro Tracking This setup is suited for studying the viscous scales. A volume of 2cm$*$2cm$*$2cm is covered. The propellers have a diameter of 5cm. We use cenosphere particles with size $\sim 100\mu$m and density $\rho \sim 0.7 - 0.8$ of water. The cameras are placed very close to the windows of the tank ($\sim$ 3cm). This results in a large angle between the camera center plane and the window and we can thus expect a significant refraction of light due to the air-glass-water interface. To get around this problem we put a small device with water between the lenses and the window so that the light leaves the water at zero angle before hitting the cameras.

Macro Tracking The cameras cover a volume of 15cm $*$ 15cm $*$ 15cm. In practise we, however, only use a sub-volume of this. The propellers have a diameter of 10cm. This gives a large integral scale which makes inertial range investigations possible. We use polystyrene particles with size $\sim 400\mu$m and density 1.06g/cm^3. The particles contain a small amount of gas in the interior. By boiling the particles we make them lighter by expanding the gas in the plastic and thus neutrally buoyant. The cameras are places half a meter from the window.

In both setups the Stokes number, τ_I/τ_η (τ_I denotes the inertial relaxation time for the particle to the flow while τ_η is the Kolmogorov time) is much less than one and the particles can therefore be treated as passive tracers in the flow. Before recording, the water in the tank is flushed through a filter ($d \sim 10\mu$m) for several days in order to get rid of impurities in the water.

An important and crucial step is calibration of the camera positions. The four cameras need to point toward the same spot in the tank. By placing a known object in the tank, a laboratory coordinate system can be constructed. In our case two different plates were constructed from Perspex with lines carefully spaced. From pictures of the calibration object by all four cameras each coordinate on the camera chip can be mapped onto the new 3d laboratory frame by solving a series of linear algebra equations (Maas et al., 1993; Trucco and Verri, 1998).

Literarily speaking the end result never gets better than the calibration.

3.1.3 Image routines

The road from two-dimensional (2d) images of the four camera chips to three-dimensional (3d) trajectories in time are long and tedious. Several steps are taken. In short, these are:

1. Finding particle centers for each camera.

2. Stereo matching of the four cameras.

3. Construction of 3d trajectories by linking consecutive images in time.

In Figure 3.2 four raw images from the cameras are shown. In Figure 3.3 a close up of Figure 3.2 is shown. The particles are the tall mountains in the landscape on top of a relatively low noisy background. The signal-to-noise ratio is very good. Since the particles covers in average around 25 pixels we can (after subtracting the background) fit a 2d Gaussian kernel to each particle and hence obtain the particle position with sub pixel accuracy. Only

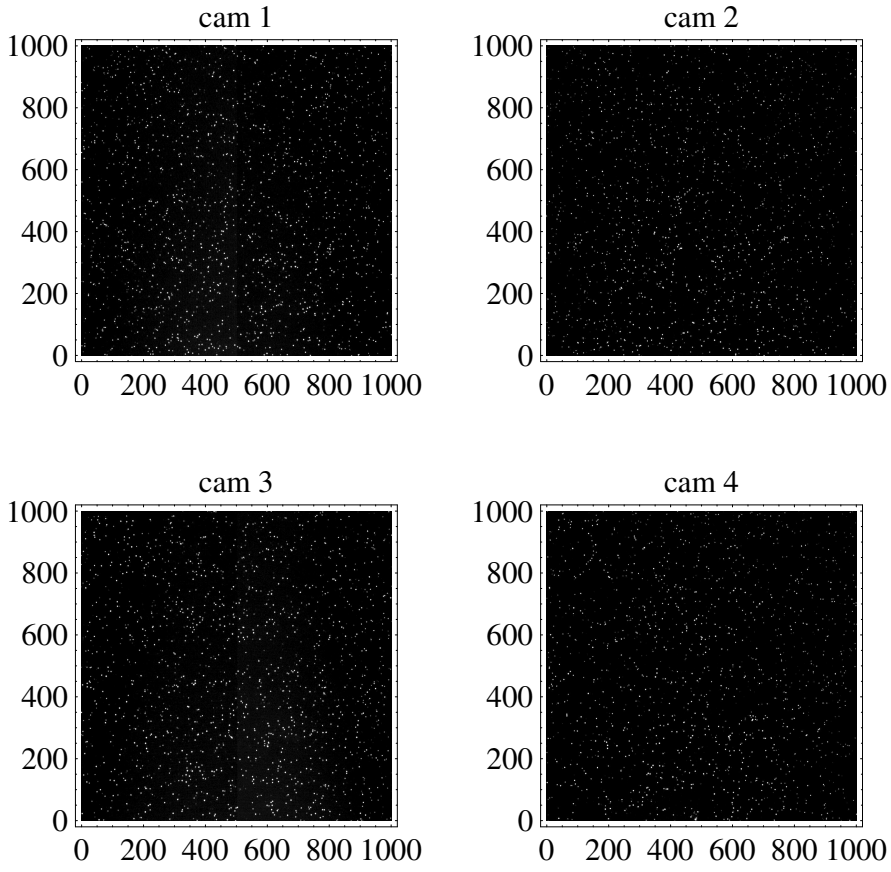

Figure 3.2: 2d images from the camera chips. The cameras have 8bit monochrome pixel depth. The plot range in the figures is set to $4 - 20$.

shapes with local maximum over some threshold value above the background are considered as real particles. Images from the four cameras are then matched by use of the calibration, and 3d coordinates in the laboratory frame are generated. In practice each particle on the 2d image represents a line in the 3d laboratory frame. Four cameras give four lines for each particle. The crossing of these lines defines the 3d point in the laboratory frame. Due to imperfect calibration and random error in the position determination on the camera chip the lines do not cross. We therefore define the 3d particle position as the minimum of the sum of the squared distances. In the macro setting a two media (water-air) optical model is used to reduce the negative influence of Snell's law at the interface (deflection of the lines).

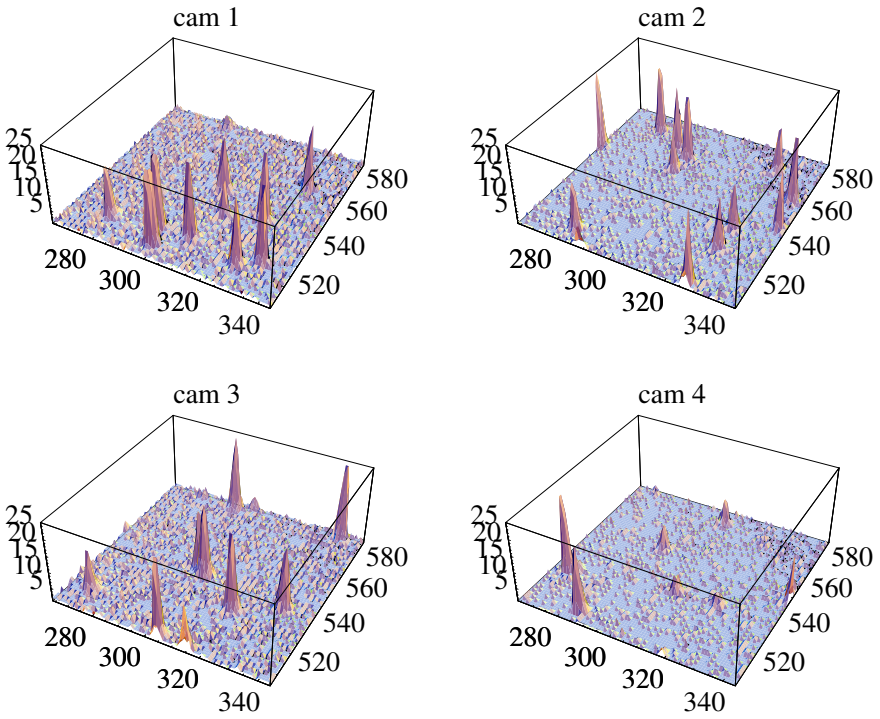

Figure 3.3: 3d representation of a small part of the 2d images from Figure 3.2.

The mean error in crossing is less than 10μm. Only particles which can be seen by three or four cameras are stored.

The last step is linking of particles from images from consecutive time steps into 3d trajectories in time. We use the kinematic principle of minimum change in acceleration to link particles. Details of tracking algorithms can be found in Malik et al. (1993); Willneff (2003); Ouellette et al. (2006a).

An upper bound of particle seeding density seems to be $\sim$ 1200. 70% of these are linked from stereo matching of all four cameras, 20% are linked from stereo matching of only three cameras while the remaining 10% are lost. Decreasing the seeding density, the linking improves as fewer particles are shadowing each other. A snapshot of 3d trajectories are shown in Figure 3.4.

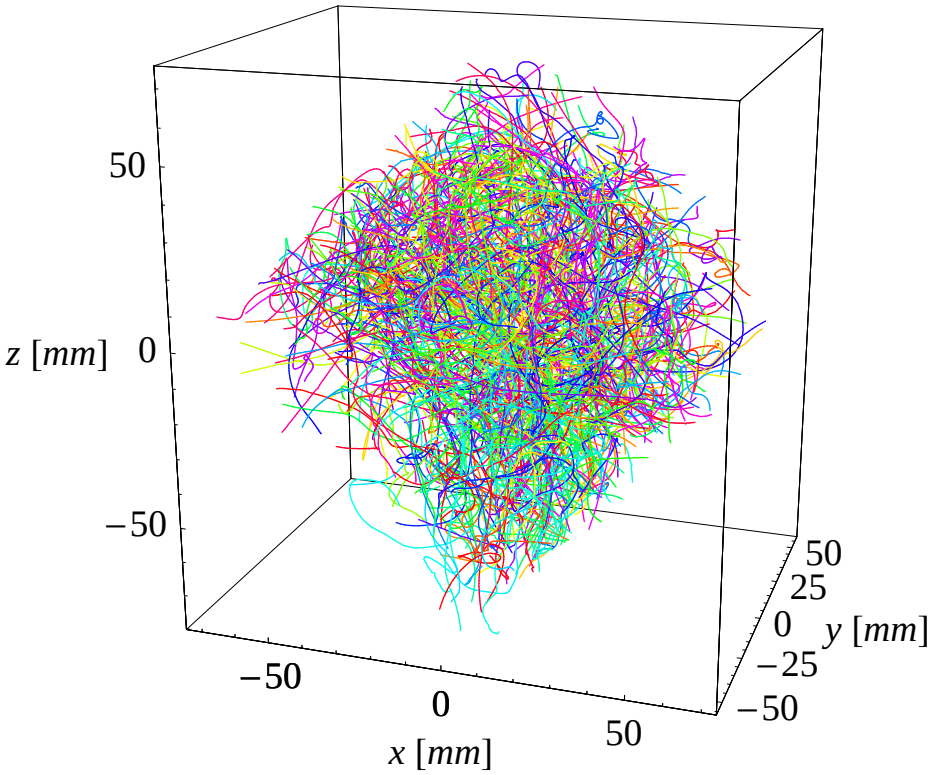

Figure 3.4: 3d trajectories from macro tracking.

3.1.4 Velocity and Acceleration statistics

The components of velocity and acceleration are determined through centered finite difference along trajectories:

$$\tilde{u}_i(\tilde{\mathbf{x}}, t) = \frac{\tilde{x}_i(t+dt) - \tilde{x}_i(t-dt)}{2dt}. \tag{3.1}$$

$$\tilde{a}_i(\tilde{\mathbf{x}}, t) = \frac{\tilde{x}_i(t+dt) - 2\tilde{x}_i(t) + \tilde{x}_i(t-dt)}{dt^2}. \tag{3.2}$$

where $\tilde{\mathbf{x}}$ is the measured position. If we assume that the error associated with determination of particle position is white noise we have:

$$\tilde{x}_i(t) = x_i(t) + \eta_i(t) \tag{3.3}$$

where $\langle \eta_i(t) \rangle = 0$ and $\langle \eta_i(t)\eta_j(t+\tau) \rangle = \delta_{ij}\delta(\tau)\sigma_\eta^2$. This implies that statistics of both velocity and acceleration are altered. For example are the second moments of velocity and acceleration given by:

$$\langle \tilde{u}_i^2 \rangle = \langle u_i^2 \rangle + \frac{\sigma_\eta^2}{2dt^2} \tag{3.4}$$

$$\langle \tilde{a}_i^2 \rangle = \langle a_i^2 \rangle + \frac{6\sigma_\eta^2}{dt^4} \tag{3.5}$$

Due to the limited frame rate of the cameras it has not been possible to study a wide range of Reynolds numbers. Only flow with low to intermediate Reynolds numbers have been studied.

The macro tracking flow reported in paper III, V and VI has a Reynolds number $Re_\lambda = 168$. This number was calculated from the von Kármán model (Ott and Mann, 2000) – a simple model spectrum extending the K41 inertial range into the large scale uncorrelated regime. The integral scale L_{int} is therefore defined different from eqn. 2.10. Namely, more formally, as the integral over the co-variance function of velocity. The integral scale is 48mm in agreement with the radius of the forcing propellers. A sample track from the recording is shown in Figure 3.5. We observe that both track positions and velocities are quite smooth. In the acceleration we, however, observe some noisy peaks. A general approach is to smooth the tracks by Gaussian filters (Porta et al., 2001; Xu et al., 2006) or polynomials (Lüthi et al., 2005). In the current flow the ratio of Kolmogorov scale to sampling rate τ_η/dt is only of order three. If we smoothed the signal there would therefore be a significant probability of removing relevant dynamics on the fastest scales of order τ_η. This has therefore not been done.

Mean flow properties of the macro tracking flow are reported in paper III. A relation between the second order structure of turbulence and relative accelerations characterizing local inhomogeneities in a flow is presented in appendix A.

Only very few results from micro tracking are presented (in paper III). Preliminary results on acceleration and kinetic energy dissipation from micro tracking are presented in Mann et al. (2006a). This work is not yet finalized and is not included in the thesis.

Lagrangian one-particle velocity statistics are presented in paper VII. In this paper a discussion on statistical bias due to finite measurement volume has been included.

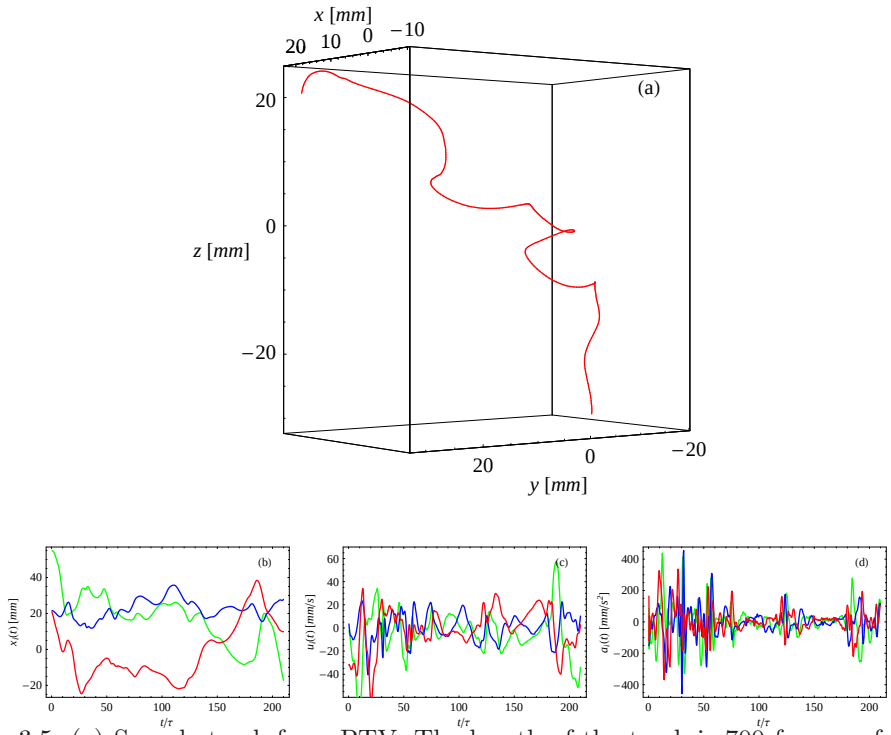

Figure 3.5: (a) Sample track from PTV. The length of the track is 700 frames of $50HZ$. (b) Position $x_i(t)$ along track. $i = 1$ is green, $i = 2$ is blue and $i = 3$ (c) Velocity $u_i(t)$ along track. (d) acceleration $a_i(t)$ along track.

Chapter 4

Dispersion

The phenomenon of pair (and multi-particle) dispersion in turbulence represents the bulk of the papers. A section devoted to additional remarks and theory not included in the papers was therefore found appropriate.

The dispersion $\sigma_x^2 = \langle [x(t+\tau) - x(t)]^2 \rangle$ of a single particle is given by the classic theorem by Taylor (Taylor, 1921):

$$\sigma_x^2 = 2 \int d\tau \, (t - \tau) R_u(\tau), \tag{4.1}$$

involving the Lagrangian co-variance function $R_u(\tau) = \langle u(t)u(t+\tau) \rangle$. The dispersion of a single particle is mainly affected by the large energy containing scales in the turbulent flow and therefore K41 similarity scaling does not apply. In contrast two-particle (or more) statistics are governed by their local dynamics. The velocity fluctuations occurring over the distance separating two particles in the flow alter their relative movement and hence K41 similarity theory plays a crucial role. In this chapter we will focus on dispersion of more than one particle.

In general two fluid particles initially close will on average separate as a function of time. In a constant flow where the velocity field is smooth the separation will be diffusive and the particles will hence undergo Brownian motion. In a turbulent flow, however, particles will separate much faster (super-diffusive). The subject has been widely studied although the final words have not yet been written. One of the reasons that the subject has got so much attention is its applicability in various problems of different character. These include puff release (Jørgensen, 1993; Mikkelsen et al., 1987) and dispersion of agents in the atmosphere and the ocean (Huber et al., 2001; Berloff et al., 2002; Lacorata et al., 2001), mixing of different substances and scalars (Sawford, 2001) and consumption rates of for example

zoo plankton (Mann et al., 2005, 2006b).

To illustrate the applicability we let $\theta(\mathbf{x},t)$ denote a passive scalar, such as temperature or concentration. In a random flow described by the Eulerian incompressible velocity field $\mathbf{u}(\mathbf{x},t)$. The time evolution of $\theta(\mathbf{x},t)$ is governed by the advection-diffusion equation

$$\partial_t\theta + u_i\partial_i\theta = \kappa\partial_{jj}\theta + S, \tag{4.2}$$

where κ is the molecular diffusivity and S is the source term.

The equation can be solved by the method of characteristics. The characteristic curves $\mathbf{y}(t'|x,t)$ are the Lagrangian trajectories of fluid particles passing through $\mathbf{x}$ at time t and *so to speak* carry different values of θ forth. We have:

$$\theta(\mathbf{x},t) = \int_{-\infty}^{t} dt'\; S(\mathbf{y}(t'|\mathbf{x},t),t') \tag{4.3}$$

$$\frac{d\mathbf{y}}{dt} = \mathbf{u}(\mathbf{y}(t'|\mathbf{x},t),t') + \sqrt{2\kappa}\boldsymbol{\eta}(t'), \tag{4.4}$$

where $\sqrt{2\kappa}\boldsymbol{\eta}(t')$ is the white noise contribution due to molecular diffusion (for simplicity we will for all future tasks assume $\kappa = 0$).

The first two statistical moments can be expressed as

$$\langle\theta(\mathbf{x},t)\rangle = \int_{-\infty}^{t} dt'\; \langle S(\mathbf{y}(t'|\mathbf{x},t),t')\rangle \tag{4.5}$$

$$\langle\theta(\mathbf{x}_1,t_1)\theta(\mathbf{x}_2,t_2)\rangle = \int_{-\infty}^{t_1} dt' \int_{-\infty}^{t_2} dt''\; \langle S(\mathbf{y}(t'|\mathbf{x}_1,t_1),t')S(\mathbf{y}(t''|\mathbf{x}_2,t_2),t'')\rangle \tag{4.6}$$

We now choose the correlation function of the source term S to be (Falkovich et al., 2001)

$$\langle S(\mathbf{x}_1,t_1)S(\mathbf{x}_2,t_2)\rangle = \chi(|\mathbf{x}_1-\mathbf{x}_2|)\delta(t_1-t_2). \tag{4.7}$$

This describes a Gaussian pumping which is homogeneous and isotropic in space and white in time. We can now rewrite eqn. 4.6:

$$\langle\theta(\mathbf{x},t)\theta(\mathbf{x}+\mathbf{R},t)\rangle = \int_{-\infty}^{t} dt' \int_{0}^{\infty} d\mathbf{r}\; \chi(r)p(\mathbf{R},t|\mathbf{r},t'). \tag{4.8}$$

Here the pdf $p(\mathbf{R},t|\mathbf{r},t')$ is the probability that a pair of fluid particles is separated a distance R at time t conditioned on a separation r at time t'.

Knowing the pdf of particle pair separation is thus central to calculating the statistical fluctuations of a passive scalar.

In eqn. 4.6 $t_1 > t'$ and $t_2 > t''$. This is what is called the forward dispersion case. In an incompressible fluid where $p(\mathbf{r}, t'|\mathbf{R}, t) = p(\mathbf{R}, t|\mathbf{r}, t')$ we can, however, easily reverse time so that $t_1 < t'$ and $t_2 < t''$. This is called the backwards dispersion case (Sawford et al., 2005).

Calculating a puff from an initial source distribution relates to the forwards case whereas the concentration fluctuations in a gas relates to the backwards case: the different trajectories carry different scalar concentrations from the past. Difference in forward and backward dispersion is the focus of paper III.

An example of the latter backwards dispersion case is here given: we consider an explosive gas with a global mean concentration of, lets say 5 in some arbitrary units. If (in the presence of some ignition source) the gas explodes for concentrations larger than 10, you might think that no danger is currently present. If, however, the concentration, locally, exceeds 10, the whole gas will most likely explode even though the global mean concentration is lower than 10. The concentration fluctuations (the variance) of a scalar is thus very important in some applications and is, as we have seen, directly related to the problem of relative separation of particles through the pdf $p(r, t|r', t')$.

In general we are interested in the time evolution of the separation vector between a pair. Knowledge about the pdf of separation allows us to calculate the different statistical moments and hence solve problems as the one mentioned. From our PTV database of Lagrangian trajectories we can calculate the separation in time of all combinations of pairs given. The Lagrangian nature of the problem is what makes it so hard to solve: lagrangian correlation times are longer than the corresponding Eulerian and the calculation of trustworthy inertial range Lagrangian statistics therefore requires higher Reynolds numbers.

Relative turbulent dispersion can be divided in two classes: initial value problems and boundary value problems and they will here be treated individually. First, however, some basic definitions will be presented.

Kinematic relationships We denote the distance between two fluid particles

$$r_i(t) = x_i^1(t) - x_i^2(t), \tag{4.9}$$

with separation length $r = \sqrt{r_i r_i}$. The relative velocity along the axis of separation is

$$\delta u_r(t) = \frac{d}{dt} r = \frac{\delta u_i r_i}{r}, \tag{4.10}$$

where $\delta u_i = u_i(\mathbf{x}^1) - u_i(\mathbf{x}^2)$. Similar the relative acceleration along the axis of separation is given by:

$$\delta a_r(t) = \frac{d}{dt}\delta u_r = \frac{\delta a_i r_i}{r} + \frac{\delta u_i \delta u_i}{r} - \frac{\delta u_r \delta u_r}{r} = \frac{\delta a_i r_i}{r} + \frac{\delta u_t \delta u_t}{r}. \tag{4.11}$$

The acceleration $\delta a_r(t)$ thus contains contributions from both the longitudinal relative acceleration as well as from the rotation of the separation vector by the transverse velocity component δu_t.

For modelling purposes (Kurbanmuradov, 1995; Borgas and Yeung, 1998) these formulations are very suitable as there exist a one-to-one relationship between $A = \langle \delta a_r | \delta u_r \rangle$; the ensemble average of δa_r conditioned on δu_r, and the Eulerian pdf $p_E(\delta u_r|r)$; the probability of obtaining a relative velocity difference δu_r given a separation r. The E subscript is used to emphasize the Eulerian character.

The relationship is given by the exact kinematic equation known as the Eulerian pdf transport equation:

$$\frac{\delta u_r}{r^2}\frac{\partial r^2 p_E(\delta u_r|r)}{\partial r} = -\frac{\partial A p_E(\delta u_r|r)}{\partial \delta u_r}. \tag{4.12}$$

A derivation of eqn. 4.12 can be found in (Pope, 2000). Solving the equation with a realistic form of $p_E(\delta u_r|r)$ and a functional form of A expressed through the Navier-Stokes equation *might be the essence* of relative pair separation in turbulence and stochastic modelling. A discussion on stochastic modelling of pair separation based on eqn. 4.12 is presented in appendix B.

4.1 Pair dispersion: initial value problems

Pair separation can roughly be divided in four regimes depending on the distance and time travelled since the particles were close together. These are the viscous range, the ballistic regime, the fully developed inertial range and the Brownian uncorrelated limit. The different regimes are illustrated in Figure 4.1.

Viscous range For initial separations r_0 smaller than the Kolmogorov scale η the velocity field can be considered smooth so that $u_i(\mathbf{x}+\mathbf{r},t) \approx u_i(\mathbf{x},t) + r_j \partial_j u_i(\mathbf{x},t)$. This means that

$$\begin{aligned} u_i(\mathbf{x}+\mathbf{r}) - u_i(\mathbf{x}) &= r_j \partial_j u_i(\mathbf{x},t) && (4.13)\\ \delta u_i r_i &= r_i r_j \partial_j u_i(\mathbf{x},t) && (4.14)\\ r\delta u_r &= r_i r_j \partial_j u_i(\mathbf{x},t) && (4.15)\\ \frac{d\ln r}{dt} &= n_i n_j \partial_j u_i(\mathbf{x},t) && (4.16) \end{aligned}$$

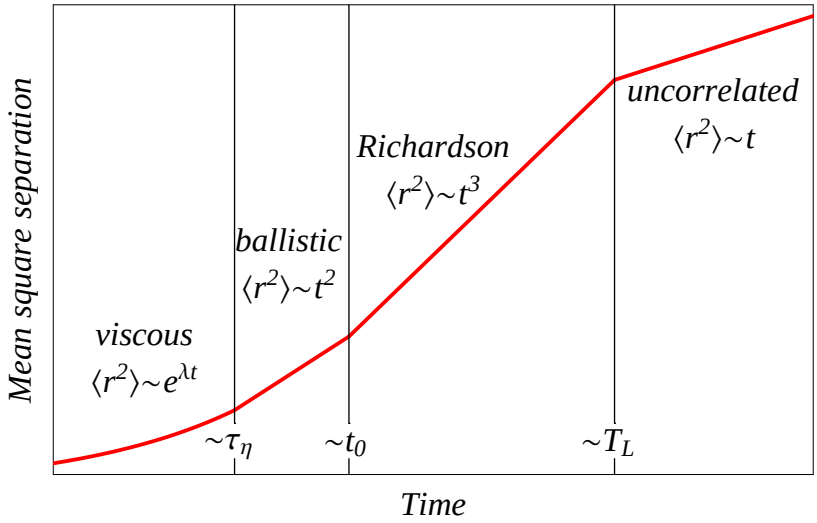

Figure 4.1: The different regimes of pair dispersion. See text for details.

where $n_i = r_i/r$ is the unit vector. Integration, squaring and taking the ensemble average gives

$$\langle r^2 \rangle = r_0^2 \exp(\lambda t). \tag{4.17}$$

where

$$\lambda \equiv \frac{2}{t} \int_0^t dt' \langle n_i n_j \partial_j u_i(\mathbf{x}, t') \rangle \tag{4.18}$$

is known as the finite time Lyapunov exponent characterizing the exponential divergence of initially close trajectories in a chaotic flow (Bohr et al., 1998). An interesting outcome of eqn. 4.17 is that in the limit $r_0/\eta \to 0$ it takes an infinite time for r^2 to grow to η^2.

The ballistic regime Inertial range separation is characterized by initial separations larger that η.

For small times the particles only travel a short distance relative to r_0 and r_0 may therefore contribute significantly to the problem. The particles move in straight lines so that their relative velocity does not change significantly. This regime is known as the ballistic regime or Batchelor regime after its introduction by Batchelor (1950). Paper III focuses on this regime.

A Taylor expansion of $r(t)$ to first order around r_0 gives

$$r(t) \sim r_0 + \delta u_r t. \tag{4.19}$$

Squaring and taking the ensemble average we end up with

$$\langle r^2(t) \rangle \sim r_0^2 + 2\langle r_0 \delta u_r(r_0) \rangle t + \langle \delta u_r(r_0)^2 \rangle t^2. \tag{4.20}$$

If there is no mean flow or the flow is incompressible the correlation $\langle r_0 \delta u_r(r_0)\rangle = r_0\langle \delta u_r(r_0)\rangle$ is zero since

$$\begin{aligned}\langle r_0 \delta u_r(t_0)\rangle &= \frac{1}{4\pi r_0^2}\int_{\partial B_{r_0}} r_0\langle \delta u_r(r_0)\rangle &(4.21)\\ &= \frac{1}{4\pi r_0}\int_{B_{r_0}} \partial_r\langle \delta u_r(r_0)\rangle &(4.22)\\ &= 0,\end{aligned}$$

where $\int_{\partial B_{r_0}}$ is the surface integral and $\int_{B_{r_0}}$ is the volume integral over an ball with radius r_0.

K41 similarity theory (eqn. 2.23) gives $\langle \delta u_r(r_0)^2\rangle = f(r) + 2g(r) = \frac{11}{3}\varepsilon^{2/3} r_0^{2/3}$. This is the same as to say that the separation is governed by eddies with size equal to the separation itself and hence the Eulerian K41 scaling can be used in the Lagrangian frame of reference.

The only relevant time scale we can construct with r_0 is $t_0 = (r_0^2/\varepsilon)^{1/3}$. It is often referred to as the Batchelor time scale and it is the characteristic time for which the initial separations are important in the process of separation.

Normalizing with r_0 and t_0 we arrive at

$$\frac{\langle r^2(t)\rangle}{r_0^2} = 1 + \frac{11}{3} C_K \left(\frac{t}{t_0}\right)^2. \tag{4.23}$$

In paper III it is found that $\langle \delta u_r(r_0)\rangle$ is non-zero. Including this term in the calculation of $\langle r^2(t)\rangle$, a more general expression is obtained: from eqn. 4.19 it follows directly that:

$$\langle [r_i(t) - r_{i0}]^2\rangle = \frac{11}{3} C_K (\varepsilon r_0)^{3/2} t^2. \tag{4.24}$$

Sampling errors of the experimental data is most likely to be held responsible for the non-vanishing correlation found in paper III. As seen from eqn. 4.22 integration must be performed over balls with radius r_0. If we therefore include particle pairs on the boundary of the measuring volume the integral can not be evaluated and is therefore not necessarily zero. Errors in tracking particles could also be an issue for small r_0 (see Appendix A for a longer discussion).

Fully developed inertial range For times larger than t_0 but r_0 still in the inertial range the particles separate according to the celebrated Richardson law:

$$\langle r^2(t)\rangle = g\varepsilon t^3 \tag{4.25}$$

The introduction of ε in the equation was due to Obukhov (1941) who made it consistent with K41 similarity scaling. The constant g is named the Richardson-Obukhov constant.

An important assumption is thus that a regime where the initial separation has been *forgotten* exists.

The derivation is based solely on dimensional arguments:

$$\frac{d}{dt}r^2 = 2r\delta u_r(r) \sim r^{4/3}$$

Differentiation and ensemble averaging leads to eqn. 4.25. By atmospheric balloon experiments Richardson (1926) obtained a scale dependent turbulent eddy diffusivity $K(r,t) \sim r^{4/3}$ of a cloud released at time equal zero. Assuming a fast varying velocity field he guessed that the pdf of separation $p(\mathbf{r},t)$ would be the solution to a diffusion equation with diffusivity $K(r,t)$

$$\partial_t p(\mathbf{r},t) = \nabla(K(r,t)\nabla p(\mathbf{r},t))\,. \tag{4.26}$$

With $K(r,t) \sim r^{4/3}$ the solution is given by

$$p(r,t) = t^{-9/2}\exp\left\{-Ar^{2/3}/t\right\}, \tag{4.27}$$

where A is a constant. Its isotropic counterpart $q(r,t)$ defined as $p(r,t) = 4\pi r^2 q(r,t)$ has been subject to much research and is named the distance-neighbor function (Ott and Mann, 2000; Biferale et al., 2005a).

For times $|t| > t_0$ it is this distance-neighbor function given by eqn. 4.27 which is responsible for the fluctuations of a passive scalar since $p(\mathbf{r},t|\mathbf{r}',t')$ becomes independent of the initial separation, here denoted, $\mathbf{r}'$. We thus have

$$q(r,t) = \int_V d\mathbf{x}\langle\theta(\mathbf{x},t)\theta(\mathbf{x}+\mathbf{r},t)\rangle. \tag{4.28}$$

Eqn. 4.27 is not the only solution to eqn. 4.26. Other forms of $K(r,t)$ will give different solutions but still give the Richardson law. One can show that any diffusivity of the form $K(r,t) \sim r^\alpha t^\beta$ for which $3\alpha + 2\beta = 4$ will give eqn. 4.25. The best known example is the Gaussian distribution for which $K \sim t^2$. This was suggested by Batchelor (1952) but recent experiments have all been in favor of Richardson's original contribution (Ott and Mann, 2000; Biferale et al., 2005a).

Due to the Lagrangian nature the Richardson law is very hard to observe since large separations are needed. In addition the Richardson-Obukhov constant g is only strictly defined in the limit of infinite Reynolds numbers. In paper III we therefore present a generalization of the Richardson law taking finite Reynolds numbers into account. It is based on an earlier approach by Ott and Mann (2000) and utilized by Ishihara and Kaneda (2002) and Biferale et al. (2005a).

Uncorrelated range For times and separations larger than the integral time and length scale, respectively, the particles are uncorrelated. This means that both particles move as Brownian particles. In other words, the diffusivity $K(r,t)$ is constant, $p(r,t)$ becomes gaussian and the solution to eqn. 4.1 for two independent particles is

$$\langle r^2(t)\rangle = 2\sigma_u^2 T_L t, \tag{4.29}$$

where σ_u is the velocity standard deviation for a single particle and T_L is the integral time scale.

4.2 Pair dispersion: boundary value problems

Instead of looking at the separation as a function of time one can study the inverse problem: the time it takes particles to separate fixed distances (Artale et al., 1997). Since turbulence is intermittent some particle pairs separate much faster than others. While some pairs undergo Brownian motion others again experience inertial range separation or even viscous separation. This contamination of scales makes it difficult to observe the Richardson law in finite Reynolds number flow where the different regimes lie within a narrow band (Biferale et al., 2005a). In the fixed scale approach all pairs are sampled at the same scale. This means that the particles pairs are sampled in the same regimes (viscous, ballistic, inertial and Brownian) and therefore can be expected to follow the same scaling laws. Boundary value problems are often denoted fixed scale statistics or just exit time statistics.

An alternate way of defining exit times is presented in paper I.

4.3 Multi-particle statistics

Geometric properties such as size and shape can be studied by looking at the interplay between more than two particles. Three particles are needed to construct a triangle and four particles are necessary to construct a three-dimensional object (a tetrahedron). In the mean the particles pairwise follow the laws of two particle dispersion which *in a sense* restrict the number of possible shapes observed. Going from one-particle statistics to two-particle statistics might therefore be a larger step than going from two to many particles.

The multi-particle approach might be beneficial to the modelling community. In Large Eddy Simulation (LES) models the large scale motion is solved explicitly from integration of the Navier-Stokes equation whereas the

smaller scales are parameterized. Choosing the correct parameterization is thus very crucial for the full modelling as the non-linearity of the system can amplify even the smallest error introduced in the smallest scale. If we denote the truncation scale Δ the parameterization can be though of as a coarse-graining on scale Δ. In an experimental situation we can look at the combined effects of a cluster of particles within some volume equal to Δ^3. The method is know as coarse-graining and results from the Risø experiment are presented in paper V and VI.

Chapter 5

Conclusions

At the Risø National Laboratory there is a long tradition for studying atmospheric boundary layer processes. These include the prediction of wind power potentials, turbulent fluxes, dispersion of gasses and flow over complex terrain. In all these application driven research areas turbulence is central. Considering only the activities at Risø, the need for a PTV experiment is therefore indirectly justified. With the PTV setup at Risø we have managed to collect reliable data which have been an excellent resource from which one can study turbulent properties.

In the first chapter I spend some time trying to present the problem of turbulence. No answer was given at that time and after having read the thesis the question is still not answered, and will not be! Instead the thesis has focused on some Lagrangian properties of fluid flow or more precisely on passive tracers advected by a turbulent flow. The Lagrangian view of turbulence is becoming more and more popular and the number of scientific papers dealing with the Lagrangian view is growing fast. This thesis work can be considered as a part of this trend or simply as an attempt to obtain basic knowledge through physical experiments.

The Lagrangian view has been emphasized as being equally important in the description of turbulence: a complete theory of turbulence must, however, include both Eulerian and Lagrangian descriptions, and maybe more important; be able to go from one to the other. In the last paper an attempt to utilize the multifractal model as *bridging* the two frames of reference was only partly successful. The conclusion was that turbulence theory and physical experiments are often far apart. The Kolmogorov picture and the corrections due to intermittency are only supposed to be valid for infinite Reynolds number - or at least for a robust inertial range. This requirement is far from being fulfilled in the lab. When it comes to the existence of a

Lagrangian inertial range as required by for example the Richardson law, no one have ever proven that it even exists at all! Besides this, homogeneity and isotropy are also assumptions which rarely hold in the lab. In this thesis a lot of attention has been given to especially these properties. Some sort of universality has been obtained: the finding of the Richardson constant $g_f \sim 0.5$ and the ESS scaling exponents might be examples of this.

Dispersion of particle pairs have been at the heart of the thesis. We have performed a PTV experiment which successfully have provided insight in two-particle / multi-particle statistics:

- One- and two-particle dispersion can be viewed as a boundary value problem. We show that simple scaling laws are governing the distribution of transit and occupation times in both the Eulerian and Lagrangian frame of reference. Stochastic models of both one and two particles can be used to model the process.

- The relative separation of two particles are strongly affected by the initial separation of the particles up to the Batchelor time scale.

- Forwards and backwards dispersion are not equally fast. We find that the backwards case is twice as fast compared to the forwards by measuring the ratio g_b/g_f from an expression taking the finite Reynolds number into account.

- The characteristic time scale of the pair separation process is a function of the Eulerian longitudinal structure function and it is closely related to the coarse-grained strain. It thus seems that viscous material line stretching has its counterpart in the inertial range.

- Coarse-grained strain and vorticity are measured. These quantities follow Kolmogorov similarity scaling closely in the inertial range. The principle axes of triangles and tetrahedra are preferentially oriented with the eigenframe of coarse-grained strain.

- The pdf of temporal velocity increments along a fluid particle is strongly non-Gaussian for small times. This is a signature of intermittency which we find is much more pronounced in Lagrangian statistics compared to the corresponding Eulerian statistic for spacial velocity increments.

The results are all robust in the given setup. Other experiments will show if the findings are also universal in the sense that specific details about the mean flow and forcing mechanisms are not important. For example was it

shown that a Direct Numerical Simulation of pair dispersion arrives at the same ratio of g_b and g_f.

The findings in this thesis refer to an experiment done in a laboratory under controlled conditions. I have, however, tried to emphasize the importance and consequences that the results may have for understanding turbulent processes in the real world. I believe that this is the true strength of turbulence research: the interplay between scientific discovery, applications and every day experience.

Appendix A

A relation of local homogeneity

Lets us formally define the longitudinal mean acceleration difference:

$$\langle \delta a_{||}(r) \rangle \equiv \left\langle \frac{1}{4\pi r^2} \int_{\partial B} \delta \mathbf{a}(r) \cdot \frac{\mathbf{r}}{r} \right\rangle, \tag{A.1}$$

where $\int_{\partial B}$ is the surface integral of a ball B with radius r and $\langle \cdot \rangle$ is ensemble averaging.

The longitudinal acceleration difference $\delta a_{||}(r)$ is in the literature often named the normal part of the longitudinal acceleration to distinguish it from the total longitudinal acceleration in eqn. 4.10 which also includes a contribution from the rotation of the separation vector by the two transverse velocity components.

We want to proove the following relation:

$$r\langle \delta a_{||}(r) \rangle = r f'(r) + 2(f(r) - g(r)), \tag{A.2}$$

where $f(r)$ and $g(r)$ are the second order Eulerian longitudinal and transverse structure functions as defined in eqn. 2.23.

We let $\int_B$ be the volume integral and use Gauss theorem extensively. Furthermore $\mathbf{n}$ is the unit vector $\mathbf{n} = \mathbf{r}/r$ and ∇_i denotes differentiation with respect to the separation r_i between two points. The difference in velocity is

defined $\delta\mathbf{u} = \mathbf{u}(\mathbf{x_0} + \mathbf{r}) - \mathbf{u}(\mathbf{x_0})$:

$$\begin{aligned}
\int_{\partial B} \delta\mathbf{a}\cdot\mathbf{r} &= r\int_B \nabla_i \delta a_i \\
&= r\int_B \{\nabla_i \partial_t \delta u_i + \nabla_i \delta u_j \nabla_j \delta u_i\} \\
&= r\int_{\partial B} \nabla_i \nabla_j \delta u_i \delta u_j, \ \ (\nabla_i \delta u_i = 0) \\
&= r\int_{\partial B} n_i \nabla_j \delta u_i \delta u_j \\
&= \int_{\partial B} r_i \delta u_j \nabla_j \delta u_i \\
&= \frac{\partial}{\partial r}\int_B r_i \delta u_j \nabla_j \delta u_i \\
&= \frac{\partial}{\partial r}\int_B (\nabla_j r_i \delta u_i \delta u_j - \delta u^2), \ \ (\nabla_i \delta u_i = 0) \\
&= \frac{\partial}{\partial r}\int_{\partial B} n_j r_i \delta u_i \delta u_j - \int_{\partial B} \delta u^2
\end{aligned}$$

We now take the ensemble average on both sides of the equation and use the definition of the structure functions to evaluate the right hand side

$$\begin{aligned}
f(r) &\equiv \langle \delta u_{\parallel}^2(r)\rangle = \left\langle \frac{1}{4\pi r^2}\int_{\partial B} n_j n_i \delta u_i \delta u_j \right\rangle \\
g(r) &\equiv \frac{1}{2}(\langle \delta u^2(r)\rangle - f(r)).
\end{aligned}$$

After rearranging terms we arrive at the final result.

In a globally homogeneous flow the left hand side equals zero and the second order structure of turbulence is hence solely characterized by only one function:

$$g(r) = f(r) + \frac{1}{2} r f'(r). \tag{A.3}$$

Global homogeneity implies local homogeneity (homogeneity of the velocity difference between two spatial points in the flow) whereas the opposite is not necessarily true. A good example of this is a shear flow which possesses local homogeneity although it is not globally homogeneous.

PTV data In Figure A.1 eqn. A.2 is plotted from data in macro tracking. The right hand side (red dots) and left hand side (blue dots) is coinciding up to $r \sim 60$mm. This is the distance radius for which particles in the

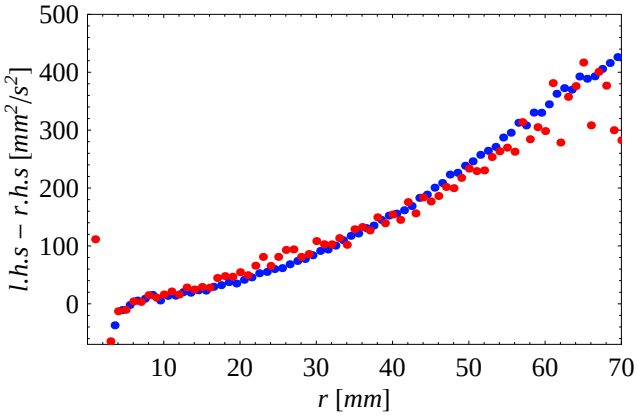

Figure A.1: Left hand side (blue dots) and right hand side (red dots) of eqn. A.2

flow are uniformly distributed (see Figure in paper VI). Outside this inner ball particle detection decreases due to non-focusing of lenses and bad light conditions.

From the axisymmetric properties of the flow we expect the mean acceleration to be of the form $\delta u^2/r$ so that

$$\alpha r = \langle \delta a_{||}(r) \rangle = \delta u^2 \quad \Rightarrow \tag{A.4}$$

$$\phi = \frac{\sqrt{\alpha}}{2\pi} = 0.057\text{s}^{-1} \tag{A.5}$$

where ϕ is the frequency. Because $\alpha > 0$ the flow is straining (in contrast to a full body rotation with $\delta a < 0$). Taking the reciprocal of ϕ gives us a characteristic time scale for the straining motion of the order 18s. This number is much larger than the integral time scale T_L and we do therefore not expect any significant influence of the mean flow on the results involving two-particle statistics.

For consistency Figure A.2 show the first order Eulerian longitudinal structure function $S_{||}(r) = \langle \delta u_r(r) \rangle$. In an incompressible flow the net mean motion across any arbitrary cross section should be zero and hence $\langle \delta u_r(r) \rangle = 0$. Homogeneity on the other hand also makes $\langle \delta u_r(r) \rangle = 0$. For values $r < 60$mm $\langle \delta u_r(r) \rangle$ is approximately zero with positive values for small r comparable to the particle size. These non-zero values are most likely caused by errors in tracking: since $\langle \delta u_r(r) \rangle > 0$ it follows that we have easier in tracking particle pairs separating than particles merging. It is a future aim to improve tracking so that $\langle \delta u_r(r) \rangle = 0$ also for small values of r.

For large values of r the distribution of particles is no longer uniform so the integral over a ball with radius r (eqn. 4.22) can no longer be evaluated

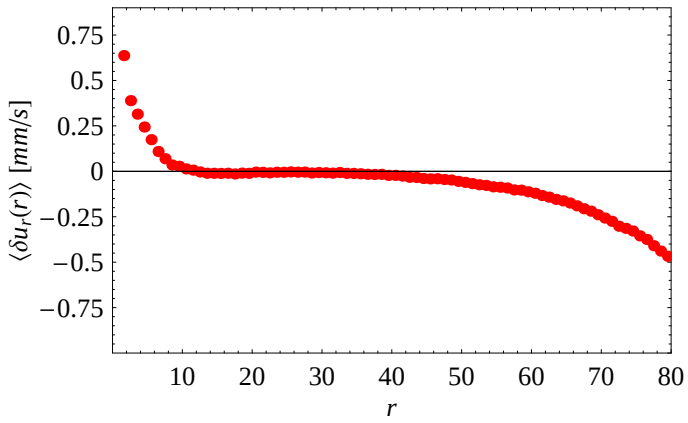

Figure A.2: $\langle u_r(r) \rangle$ as a function of r $[mm]$.

and we can not expect $\langle \delta u_r(r) \rangle = 0$.

Appendix B

Stochastic modelling of relative dispersion

Modelling two particle dispersion by stochastic differential equations is quite a challenge. The literature is vast and full of *engineering* models which although they seem to perform well are not all based on solid, physical ground. An overview is given by Sawford (2001). Paper IV introduces yet another model. It is based on the assumption that the coarse-grained strain field due to which particle pairs separate is self-similar in the inertial range and the statistic is also similar to the viscous range. This rather strong assumption is explored in paper V and paper VI. Our new model does, however, as many others lack some physical features in order to keep it simple and solvable. Generally for all models are stochastic differential equations for the relative radial velocity δu_r. This is feasible since the relative acceleration between pairs is almost uncorrelated in time. The joint evolution of relative velocity and the separation distance can hence be modeled as a Markov process (Borgas and Sawford, 1991).

In this appendix I will present another class of models which is based on the Eulerian pdf transport equation. The model is also a very good example of how Lagrangian and Eulerian statistics must both be used in pair separation problems.

The motivation for the present appendix is two fold:

- Introducing the concept of stochastic modelling to readers of paper IV.
- A first attempt to model the Lagrangian occupation and transit time statistics presented in paper I.

B.1 Experimental observations

The starting point is the Eulerian pdf transport equation already introduced in eqn. 4.12.

$$\frac{\delta u_r}{r^2}\frac{\partial r^2 p_E(\delta u_r|r)}{\partial r} = -\frac{\partial A p_E(\delta u_r|r)}{\partial \delta u_r}, \tag{B.1}$$

where $A = \langle \delta a_r | \delta u_r \rangle$ and $p_E(\delta u_r|r)$ is the Eulerian pdf of relative velocity.

Determining the $p_E(\delta u_r|r)$ or correspondingly A is the main task.

In Figure B.1 the pdf for two different separations are shown from PTV data. Since we will make an attempt to model the Lagrangian exit times in paper I we use PTV data from the first Risø experiment, i.e. the same data as was analyzed in the paper. The present data set is from a flow with $Re_\lambda \sim 100$. For both separations the distribution is definitely not Gaussian

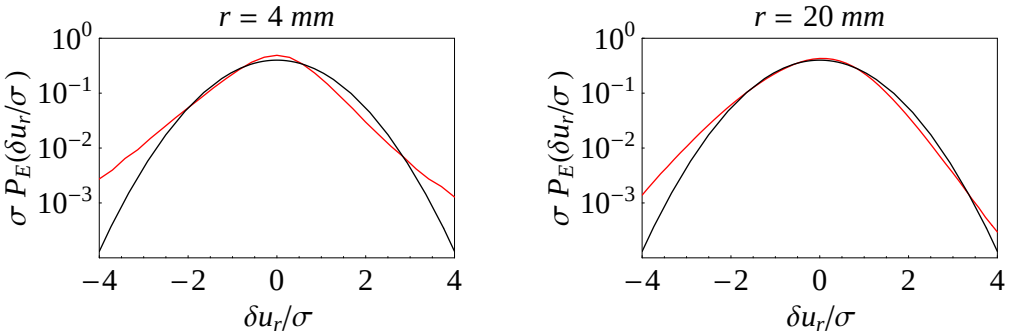

Figure B.1: $p_E(\delta u_r|r)$ for $r = 4$mm (left panel) and $r = 20$mm (right panel) from macro-tracking. A Gaussian distribution is shown for comparison.

as in paper IV. The negative skewness in the inertial range is observed for $r = 20$mm. For $r = 4$mm the effect of the viscous scales might be present and we observe an even stronger non-Gaussianity than in the inertial range. According to Borgas and Yeung (2004) this non-Gaussian behavior for small separations is crucial for the separation process in finite Reynolds number flow. In Figure B.2 the skewness and flatness of $p_E(\delta u_r|r)$ are shown. In the left panel the K41 inertial range skewness value is $S = -0.2573$ not reached for any r and we attribute this to the low Reynolds number. The flatness decreases with r but never reaches the Gaussian asymptotic value indicating that even for separations larger than the inertial range ($L_{int} = 22$mm) a Gaussian distribution is not the best approximation.

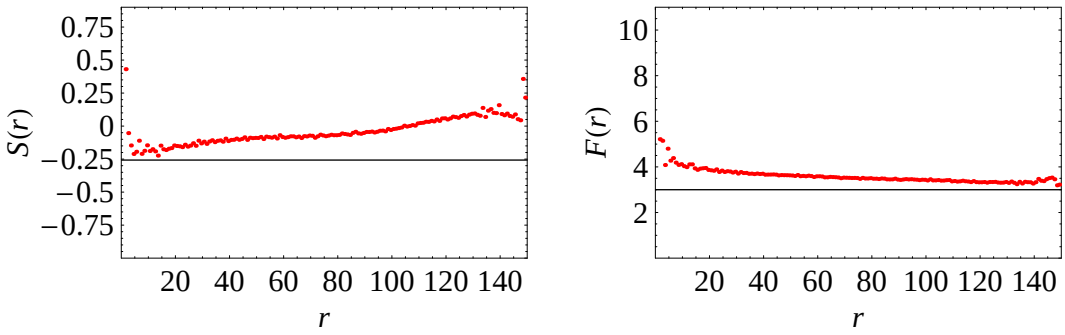

Figure B.2: The third (left) and fourth (right) moment of $p_E(\delta u_r|r)$ from the first Risø PTV experiment: $S = \langle[\delta u_r(r)]^3\rangle/\langle[\delta u_r(r)]^2\rangle^{3/2}$ and $F(r) = \langle[\delta u_r(r)]^4\rangle/\langle[\delta u_r(r)]^2\rangle^2$. The horizontal lines are the K41 skewness (left) and the Gaussian value (right) respectively.

B.2 Model formulation

We will now introduce a very simple stochastic model for pair separation. Even though we have just seen that the data from paper I do *not* exhibit true K41 similarity scaling in the sense that the *four-fifth* law is observed, scaling of the experimentally obtained occupation and transit times with the dimensionless time $r^{2/3}/\varepsilon^{1/3}$ was observed. A first attempt is therefore to restrict ourselves to model the inertial range.

In the inertial range we use K41 similarity scaling so that

$$p_E(\delta u_r|r) = (\varepsilon r)^{-1/3} f_E(\xi), \tag{B.2}$$

where we have introduced the non-dimensional variable $\xi = \delta u_r/(\varepsilon r)^{1/3}$. We now non-dimensionalize eqn. B.1 and arrive at

$$\frac{\xi}{r^2}\frac{\partial}{\partial r}\Big((\varepsilon r)^{1/3} r^2 f_E(\xi)\Big) = -\frac{\varepsilon^{1/3}}{r^{2/3}}\frac{\partial}{\partial \xi}\Big(A(\xi) f_E(\xi)\Big). \tag{B.3}$$

Borgas and Yeung (1998) find that the form of A is very well described by a second order polynomial in δu_r with r dependent coefficients. A similar result is obtained from our PTV data as seen in Figure B.3. For both separations we observe a polynomial shape. In the inertial range the r dependence is vanishing and hence we can write A in a non-dimensionless form

$$A(\xi) = \alpha + \beta\xi + \gamma\xi^2. \tag{B.4}$$

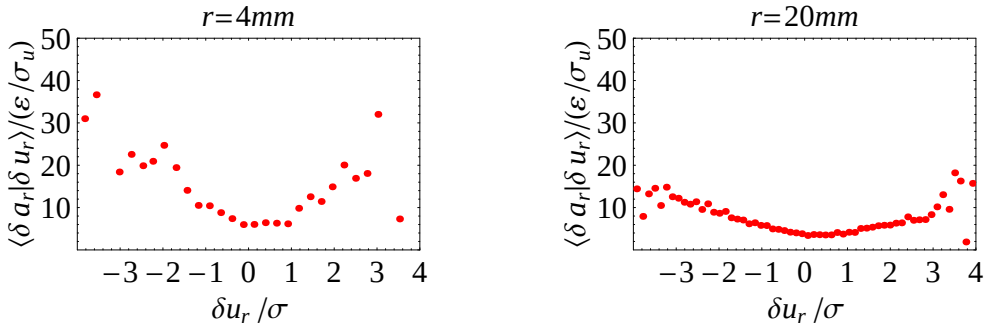

Figure B.3: $\langle \delta a_r | \delta u_r \rangle$ for two different separations.

Following (Borgas and Yeung, 1998; Franzese and Borgas, 2002; Borgas and Yeung, 2004) we insert eqn. B.4 in eqn. B.3 and integrate the resulting equation over $\xi^n d\xi$. Since $f_E(\xi)$ is the probability of ξ the moments of $f_E(\xi)$ are given by

$$\langle \xi^n \rangle = \int d\xi \xi^n f_E(\xi) \tag{B.5}$$

and we end up with the following expression:

$$\frac{1}{n} \frac{\varepsilon^{1/3}}{r^2} \left(\frac{7}{3} \langle \xi^{n+1} \rangle r^{4/3} \right) = \frac{\varepsilon^{1/3}}{r^{2/3}} \left(\alpha \langle \xi^{n-1} \rangle + \beta \langle \xi^n \rangle + \gamma \langle \xi^{n+1} \rangle \right), \tag{B.6}$$

where we have discarded a term involving $\frac{\partial \langle \xi^{n+1} \rangle}{\partial r}$ since we are only modelling the inertial range separation.

For the moments of $f_E(\xi)$ we use K41 similarity scaling and get

$$\langle \xi \rangle = 0 \tag{B.7}$$
$$\langle \xi^2 \rangle = C_K \tag{B.8}$$
$$\langle \xi^3 \rangle = -4/5 \tag{B.9}$$
$$\langle \xi^4 \rangle = C_4 \tag{B.10}$$

Here $C_K = 2.13$ is the Kolmogorov constant and $C_4 = C_K^2 F$ with the Flatness $F = 3.4$. Similarly the skewness is given by $S = -(4/5)/C_K^{3/2}$. We can now

solve eqn. B.6 for $n = 1, 2, 3$:

$$\alpha = C_K\left(\frac{7}{3} - \gamma\right) \tag{B.11}$$

$$\beta = \sqrt{C_K}S\left(\frac{7}{6} - \gamma\right) \tag{B.12}$$

$$\gamma = \frac{7}{9}\frac{F - \frac{3}{2}S^2 - 3}{F - S^2 - 1} \tag{B.13}$$

$$\tag{B.14}$$

The Fokker-Planck equation

Our aim is to model the evolution of ξ and r through stochastic differential equations. We therefore treat the non-dimensional velocity increment ξ as a continuous stochastic process governed by

$$d\xi = \frac{\varepsilon^{1/3}}{r^{2/3}}a(\xi)dt + \frac{\varepsilon^{1/6}}{r^{1/3}}bdW(t) \tag{B.15}$$

$$dr = (\varepsilon r)^{1/3}\xi dt, \tag{B.16}$$

where $dW(t)$ is a Wiener process with $\langle dW(t)\rangle = 0$ and $\langle dW(t)dW(t')\rangle = \delta(t-t')$. b is the diffusion and is in the inertial range equal to $\sqrt{2C_0\varepsilon}$ according to the second order Lagrangian structure function. $a(\xi)$ is the drift and will be discussed later.

We can now write the Fokker Planck equation corresponding to eqn. B.15 for the Lagrangian pdf $P_L(\xi, r, t|r_0)$ where r_0 is the initial separation (Gardiner, 2002):

$$\frac{\partial P_L}{\partial t} + \xi\frac{(\varepsilon r)^{1/3}P_L}{\partial r} + \frac{\varepsilon^{1/3}}{r^{2/3}}\frac{\partial a(\xi)P_L}{\partial \xi} = C_0\frac{\varepsilon^{1/3}}{r^{2/3}}\frac{\partial^2 P_L}{\partial \xi^2}. \tag{B.17}$$

The Eulerian form of this equation is a modelled form of the Eulerian transport equation for the distribution $f_E(\xi)$:

$$\frac{\partial f_E(\xi)}{\partial t} + \frac{\xi}{r^2}\frac{\partial}{\partial r}\left((\varepsilon r)^{1/3}r^2 f_E(\xi)\right) + \frac{\varepsilon^{1/3}}{r^{2/3}}\frac{\partial}{\partial \xi}\left(a(\xi)f_E(\xi)\right) = C_0\frac{\varepsilon^{1/3}}{r^{2/3}}\frac{\partial^2 f_E(\xi)}{\partial \xi^2}. \tag{B.18}$$

The well-mixed criterion (Thomson, 1990) says that an initially uniformly distributed set of particle separations has to remain uniformly distributed for all times, hence $\frac{\partial f_E(\xi)}{\partial t} = 0$. If we compare eqn. B.18 with eqn. B.3 we find that

$$\frac{\partial}{\partial \xi}\left((a(\xi) - A(\xi))f_E(\xi)\right) = C_0\frac{\partial^2 f_E(\xi)}{\partial \xi^2} \tag{B.19}$$

which has the solution:

$$a(\xi) = A(\xi) + C_0 \frac{\partial \ln f_E(\xi)}{\partial \xi}. \tag{B.20}$$

From eqn. B.3 we finally obtain the analytical expression for $\frac{\partial \ln f_E(\xi)}{\partial \xi}$ which is given by

$$\frac{\partial \ln f_E(\xi)}{\partial \xi} = -\frac{\beta + (\frac{7}{3} + 2\gamma)\xi}{\alpha + \beta\xi + \gamma\xi^2} \tag{B.21}$$

B.2.1 Numerical integration and occupation and transit times

Eqn. B.15 and B.16 describe the model. We integrate the equations on a computer with a time step Δt smaller than the smallest time scales in the system (see later). As emphasized by Borgas and Yeung (2004), $f_E(\xi)$ has power-law tails which tends to overestimate the probability of having large positive or negative velocity increments ξ. The pdf is therefore truncated at $\xi = -5.5$ and $\xi = +5.5$. Velocities which fall outside this range are recalculated with a sign change in the diffusion term of eqn. B.15.

The value of C_0 is the only free parameter in the model. Results for C_0 between 4 and 9 are presented. The measured C_0 is $\sim$ 4. We will come back to C_0 in paper VII.

We now want to utilize the model for the occupation and transit times studied in paper I. The times are defined in the following way: we choose a particle in the flow and place an *invisible* sphere of interception in the flow so that the distance between the particle and the surface of the ball is everywhere R. The occupation times are defined as the time T_o it takes another particle which initially is located inside the sphere to leave the sphere. The transit times are defined as the time T_t it takes another particle which initially is located on the surface of the sphere with an inward velocity to leave the sphere. We denote the probabilities in the two cases for $P_o(t_o)$ and $P_t(t_t)$. In paper I we present a kinematical relationship between the two. The relationship is fulfilled for the model (not shown).

One of the results in the paper was the collapse of data from different realizations of ε and R when the transit times was non-dimensionalized by the K41 similarity scaling $R^{1/3}/\varepsilon^{1/3}$.

Occupation times

The initial separation r_0 between the two particles is chosen from a uniform distribution between 0 and R. Since we are working in spherical coordinates

the occupation time for each particle is weighted by r_0^2. The initial velocities ξ_0 are picked randomly from the distribution of $f_E(\xi)$. The distribution is shown in the left panel of Figure B.4.

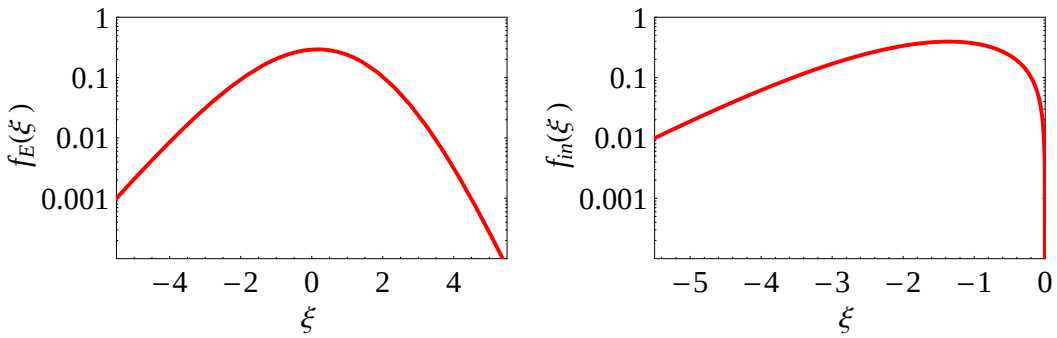

Figure B.4: Left: $f_E(\xi)$. Right: $f_{in}(\xi)$.

The results are plotted in Figure B.5 for different values of C_0. As C_0 is increased the distribution broadens with larger values for the maximum occupation times. For small times all curves collapse. Also on the figure is the result from paper I. Qualitative agreement is observed. The measured distribution of occupation times is broader than the modeled. This is due to the finite Reynolds number effect present in the data.

Transit times

The initial separation is $r_0 = R$. The initial velocities ξ_0 are picked randomly from the distribution:

$$f_{in}(\xi_\perp) = \frac{\xi f_E(\xi)}{\int_{-\infty}^{0} d\xi \xi f_E(\xi)} \tag{B.22}$$

which guaranties a correct flux at the boundary. The distribution is shown in the right panel of Figure B.4.

The results are plotted in Figure B.6 for different values of C_0. Like for the occupation times the distribution becomes broader as C_0 is increased. For small transit times the distribution is significantly altered when C_0 is changed: lowest probabilities occurs for lowest values of C_0. A comparison

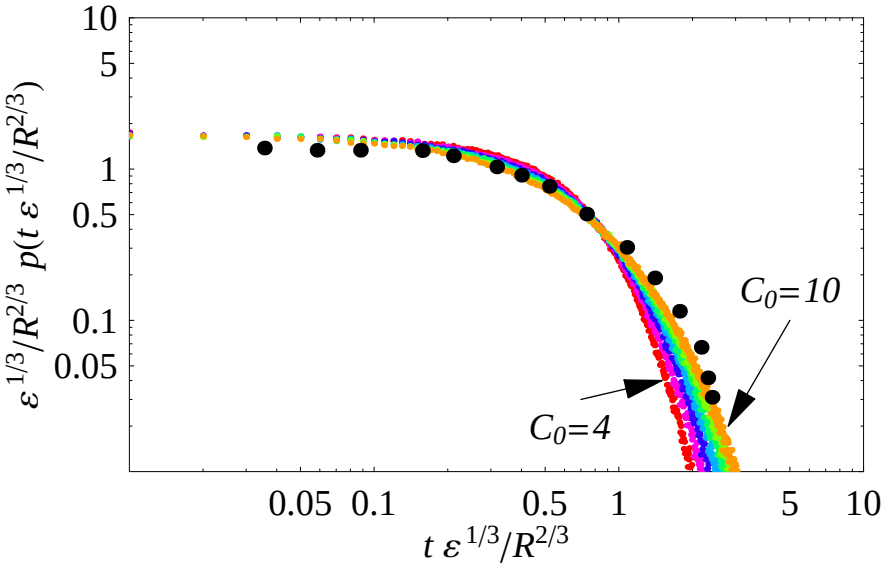

Figure B.5: Model occupation times for $C_0 = 4, ..., 10$. The black dots are the result from paper I. The dots are obtained as the average over points in Fig. 10.

with the results of from paper I does not provide much optimism: the distributions are qualitatively the same. The quantitative characteristics are, however, not the same. The experimental distribution drops down much more for low values of transit times than the modeled. In the model the separation distance r fluctuates much more than in the experiment due to the *pure* inertial range dynamics. This means that small transit times are overestimated compared to the measured data. A representation of viscous effects in the model would probably improve the outcome. Similarly for the long transit times, which are underestimated in the model: a representation of scales outside the inertial range would broaden the distribution.

As speculated in paper I the distribution of transit times might be relevant in marine ecosystem prey-predator interactions. If we assume that the motion due to swimming of the zoo-plankton (both the predator and the prey) is negligible compared to the turbulent fluctuations, we can let one of the particles in our flow (model) represent the predator and the other the prey. The probability that the prey is captured by the predator is then a function of the transit time, i.e. the time the two are close together. These lines are further developed in Mann et al. (2005); Boffetta et al. (2006) and Mann et al. (2006b) who study the opposite problem, namely the flux to an absorbing boundary from data obtained by PTV and DNS. The problem has also recently been treated analytically in the Richardson case by Pigolotti

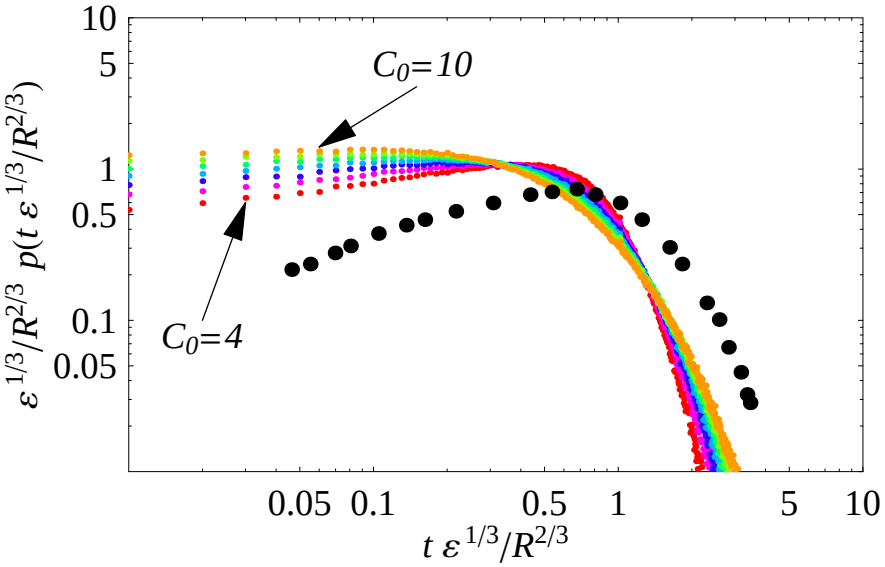

Figure B.6: Modeled transit times for $C_0 = 4, ..., 10$. The black dots are the results from paper I. The dots are obtained as the average over points in Fig. 16.

et al. (2006).

B.2.2 Appendix summary

The current model did not in a satisfactory way model the results in paper I. Some trends were, however, recognized. The main reason of the failure is of course, as already emphasized, the narrow inertial range present in the data analyzed in the paper. A more realistic model which also includes viscous and long range separation will be more suited. Such a model has been developed by Borgas and Yeung (2004). This model is an improvement of the present model and has been shown to capture satisfactorily the shape of the pdf of δu (see Figure B.1 (a)) observed for the initial separation of two particles. More unknowns are introduced and the solutions are far from being simple. For these reasons the model presented in this appendix was considered more pedagogical and hence more suited for an introduction on stochastic modelling.

The model presented in paper IV, does like the model in Borgas and Yeung (2004), treat the different regimes of separation respectively and might therefore give better results than the present model. Its only drawback is its failure to reproduce the *four-fifth* law.

Bibliography

F. Anselmet, Y. Gagne, E. J. Hopfinger, and R. A. Antonia. High-order velocity structure functions in turbulent shear flow. *J. Fluid Mech.*, 140: 63, 1984.

V. Artale, G. Boffetta, A. Celani, M. Cencini, and A. Vulpiani. Dispersion of passive tracers in closed basins: beyond the diffusion coefficient. *Phys. Fluids.*, 9:3162, 1997.

G. K. Batchelor. The application of the similarity theory of turbulence to atmospheric diffusion. *J. R. Meteorol. Soc.*, 76:133, 1950.

G. K. Batchelor. Diffusion in a field of homogeneous turbulence ii:the relative motion of particles. *Proc. Camb. Phil. Soc.*, 48:345, 1952.

P. S. Berloff, J.C. McWilliams, and A. Branco. Material transport in oceanic gyres. part i: Phenomenoogy. *J. Phys. Oceanogr.*, 32:764, 2002.

L. Biferale, G. Boffetta, A. Celani, B. J. Devenish, A. Lanotte, and F. Toschi. Lagrangian statistics of particle pairs in homogeneous isotropic turbulence. *Phys. Fluids*, 17:115101, 2005a.

L. Biferale, G. Boffetta, A. Celani, B. J. Devenish, A. Lanotte, and F. Toschi. Particle trapping in three-dimensional fully developed turbulence. *Phys. Fluids*, 17:021701, 2005b.

L. Biferale, G. Boffetta, A. Celani, A. Lanotte, and F. Toschi. Lagrangian statistics in fully developed turbulence. *J. Turbulence*, 7:6, 2006.

G. Boffetta, H. L. Pécsèli, and J. Trulsen. Numerical studies of turbulent particle fluxes into perfectly absorbing spherical surfaces. *J. Turbulence*, 7:22, 2006.

G. Boffetta and I. M. Sokolov. Relative dispersion in fully developed turbulence: the richardson's law and intermittency corrections. *Phys. Fluids*, 6:094501, 2002.

T. Bohr, M. H. Jensen, G. Paladin, and A. Vulpiani. *Dynamical systems approach to turbulence*. Cambridge, 1998.

M. S. Borgas and B. L. Sawford. The small-scale structure of acceleration correlations and its role in the statistical theory of turbulent dispersion. *J. Fluid Mech.*, 228:295, 1991.

M. S. Borgas and P. K. Yeung. Conditional fluid-particle accelerations in turbulence. *Theo. Comp. Fluid Dyn.*, 11:69, 1998.

M. S. Borgas and P. K. Yeung. *J. Fluid Mech.*, 503:125, 2004.

G. Falkovich, K. Gawedzki, and M. Vergassola. Particles and fields in fluid turbulence. *Rev. Mod. Phys.*, 73:913, 2001.

P. Franzese and M. S. Borgas. A simple relative dispersion model for concentration fluctuations in contaminant clouds. *J. Appl. Met.*, 41:1101, 2002.

U. Frisch. *Turbulence – the legacy of A. N. Kolmogorov*. Cambridge, 1995.

C. W. Gardiner. *Handbook of stochastic methods*. Springer, 2002.

M. Huber, J.C. McWilliams, and M.Ghil. A climatology of turbulent dispersion in the troposhere. *J. Atmos. Sci.*, 58:2377, 2001.

T. Ishihara and Y. Kaneda. Relative dispersion of a pair of fluid particles in the inertial range of turbulence. *Phys. Fluids*, 14:L69, 2002.

H. E. Jørgensen. *Studies of concentration fluctuations in the atmospheric surface layer*. Phd thesis, Risø National Laboratory, 1993.

O. A. Kurbanmuradov. A new lagrangian model of two-particle relative turbulent dispersion. *Monte Carlo Methods and Appl.*, 1:83, 1995.

G. Lacorata, E. Aurell, and A. Vulpiani. Drifter dispersion in the adriatic sea: Lagrangian data and chaotic model. *Ann. Geophysicae*, 19:121, 2001.

B. Lautrup. *Physics of continuous matter: exotic and everyday phenomena in the macroscopic world*. Institute of Physics publication, 2005.

E. N. Lorenz. Deterministic nonperiodic flow. *J. Atmos. Sci.*, 20:130, 1963.

B. Lüthi, A. Tsinober, and W. Kinzelbach. Lagrangian measurements of vorticity dynamics in tubulent flow. *J. Fluid Mech.*, 528:87, 2005.

H. G. Maas, A. Gruen, and D. Papantoniou. Particle tracking velocimetry in three-dimensional flows. part I. photogrammetric determination of particle coordinates. *Exp. in Fluids*, 15:133, 1993.

N. A. Malik, Th. Dracos, and D. A. Papantoniou. Particle tracking velocimetry in three-dimensional flows. part II. particle tracking. *Exp. in Fluids*, 15:133, 1993.

J. Mann, S. Ott, and J. S. Andersen. Experimental study of relative turbulent diffusion. Technical report, Risø National Laboratory, 1999.

J. Mann, S. Ott, J. Berg, and B. Lüthi. The correlation between velocity and acceleration in turbulence. accepted for publication in *Proceedings of iTi 2005, Bad Zwischenahn, Progress in Turbulence, Springer Proceedings in Physics*, 2006a.

J. Mann, S. Ott, H. L. Pécsèli, and J. Trulsen. Turbulent particle flux to a perfectly absorbing surface. *J. Fluid. Mech.*, 534:1, 2005.

J. Mann, S. Ott, H. L. Pécsèli, and J. Trulsen. Laboratory studies of predator-prey encounters in turbulent environments: effects of changes in orientation and field of view. *J. Plankton. Res.*, 28:509, 2006b.

T. Mikkelsen, S. E. Larsen, and H. L. Pécsèli. Diffusion of gaussian puffs. *Q. J. R. Met. Soc.*, 113:81, 1987.

N. Mordant, A. M. Crawford, and E. Bodenschatz. Experimantal lagrangian acceleration probability density function measurement. *Physica D*, 193: 245, 2004a.

N. Mordant, E. Lévêque, and J.-F. Pinton. Experimental and numerical study of the lagrangian dynamics of high Reynolds turbulence. *New. J. Phys.*, 6:116, 2004b.

N. Mordant, P. Metz, O. Michel, and J.-F. Pinton. Mearesurement of lagrangian velocity in fully developed turbulence. *Phys. Rev. Lett.*, 87: 214501, 2001.

A. M. Obukhov. Spectral energy distribution in turbulent flow. *Izv. Akad. Nauk SSSR*, 5:453, 1941.

S. Ott and J. Mann. An experimental investigation of the relative diffusion of particle pairs in three-dimensional flow. *J. Fluid Mech.*, 422:207, 2000.

S. Ott and J. Mann. An experimental test of corrsin's conjecture and some related ideas. *New. J. Phys.*, 7:142, 2005.

N. T. Ouellette, H. Xu, and E. Bodenschatz. A quantitative study of three-dimensional lagrangian particle tracking algorithms. *Exp. in Fluids.*, 40: 301, 2006a.

N. T. Ouellette, H. Xu, M. Bourgoin, and E. Bodenschatz. Small-scale anisotropy in lagrangian turbulence. *New. J. Phys.*, 8:102, 2006b.

S. Pigolotti, M. H. Jensen, and A. Vulpiani. Absorbing processes in richardson diffusion: Analytical results. *Phys. Fluids*, 18:048104, 2006.

S. B. Pope. *Turbulent flows*. Cambridge University press, 2000.

A. La Porta, G. A. Voth, J. Alexander A. M. Crawford, and E. Bodenschatz. Fluid particle accelerations in fully developed turbulence. *Nature*, 409: 1017, 2001.

A. Pumir, B. I. Shraiman, and M. Chertkov. Geometry of lagrangian dispersion in turbulence. *Phys. Rev. Lett.*, 85:5324, 2000.

L. F. Richardson. *Proc. R. Soc. Lond. A*, 110:709, 1926.

B. Sawford. Turbulent relative dispersion. *Annu. Rev. Fluid Mech.*, 422:207, 2001.

B. L. Sawford, P. K. Yeung, and M. S. Borgas. Comparison of backwards and forwards relative dispersion in turbulence. *Phys. Fluids*, 17:095109, 2005.

X. Shen and Z. Warhaft. The anisotropy of the small scale structure in high Reynolds number ($Re_\lambda \sim 1000$) turbulent shear flow. *Phys. Fluids*, 12: 2976, 2000.

X. Shen and Z. Warhaft. Longitudinal and transverse structure functions in sheared and unsheared wind-tunnel turbulence. *Phys. Fluids*, 14:370, 2002.

B. Tao, J. Katz, and C. Meneveau. Statistical geometry of subgrid-scale stresses determined from holographic particle image velocimetry measurements. *J. Fluid Mech.*, 457:35, 2002.

G. I. Taylor. Diffusion by continuos movements. *Proc. London Math. Soc.*, 20:196, 1921.

D. J. Thomson. A stochastic model for the motion of particle pairs in isotropic high-reynolds number turbulence, and its application to the problem of concentration variance. *J. Fluid Mech.*, 210:113, 1990.

E. Trucco and A. Verri. *Introductory techniques for 3-D computer vision*. Prentice Hall, 1998.

J. Willneff. *A spatio-temporal mathing algorithm for 3D-particle tracking velocimetry*. PhD thesis, ETH Zürich, 2003.

H. Xu, M. Bourgoin, N. T. Ouellette, and E. Bodenschatz. High order lagrangian velocity statistics in turbulence. *Phys. Rev. Lett.*, 96:024503, 2006.

P. K. Yeung. Lagrangian investigations of turbulence. *Annu. Rev. Fluid Mech.*, 34:115, 2002.

P. K. Yeung and M. Borgas. Relative dispersion in isotropic turbulence. part 1. direct numerical simulations and reynolds-number dependence. *J. Fluid Mech.*, 503:93, 2004.

Papers

I

Experimental studies of occupation and transit times in turbulent flows

J. Berg Jørgensen, J. Mann, and S. Ott
Risø National Laboratory, VEA, DK-4000 Roskilde, Denmark

H. L. Pécseli
University of Oslo, Institute of Physics, Box 1048 Blindern, N-0316 Oslo, Norway

J. Trulsen
University of Oslo, Institute of Theoretical Astrophysics, Box 1029 Blindern, N-0315 Oslo, Norway

(Received 26 February 2004; accepted 15 December 2004; published online 1 March 2005)

The motion of passively advected particles is studied experimentally in approximately homogeneous and isotropic turbulent flows. The turbulence is generated in water by two moving grids. The simultaneous trajectories of many small passively advected, neutrally buoyant polystyrene particles are followed in time by a particle tracking technique. We estimate the probability distribution of the transit times of such particles in spherical volumes with given radius. A particle which is passively advected by the flow is selected to define the center of a reference sphere, with the transit time being defined as the difference between entrance and exit times of surrounding particles advected through this sphere by the turbulent motions. Simple scaling laws are obtained for the probability density of the transit times in terms of the basic properties of the turbulent flow and the geometry. Also other formulations of the problem have been considered, by assuming, for instance, that particle positions are uniformly distributed within the reference sphere, and then determine the statistical distribution of the time they subsequently spend inside the sphere, i.e., their occupation time. These problems have Eulerian counterparts, and they were analyzed as well. In the present formulation, we find that the results of the analysis are relevant for understanding certain details in the feeding rate of microorganisms in turbulent waters, for instance. © *2005 American Institute of Physics*. [DOI: 10.1063/1.1863259]

I. INTRODUCTION

The problem of turbulent transport of passively advected particles in neutral, turbulent flows can be formulated in different ways, depending on the actual problem. Particular attention has been given to the analysis of Richardson's law for relative diffusion, and more generally to the time evolution of the probability density for separation distances of two initially close particles.[1–3] The problem of absolute diffusion is usually analyzed in a fixed laboratory frame of reference, with the particle position relative to the origin of release being the randomly varying quantity. For the corresponding problem of relative diffusion, the particle positions determine the frame of reference. In the present work we discuss some aspects of turbulent transport, in a formulation which is somewhat different from the more traditional one.

The present analysis was to some extent influenced by the observation that turbulent transport is important for the feeding processes of microorganisms in nature.[4–7] For small predators, fish larvae, for instance,[8] it can be assumed that their self-induced motion is small or negligible, and that they are therefore passively advected by the local flow velocity, at least to a good approximation. Similarly, it can be assumed that their food (microzooplankton, for instance) is also passively advected by the same flow. The feeding process can then be modeled by assuming that any individual prey entering a suitably defined "sphere of interception" is captured with certainty. In turbulent waters, the predator-prey encounter rate is related to the problem of relative diffusion, but now considered as a boundary value problem, with the condition that the prey concentration vanishes at the surface of the sphere of interception. This is the standard model for this particular problem.[4,6,7,9] The general interest in the problem arises essentially from the simple observation that the food concentration in the near region of a predator will rapidly be depleted, and without any self-induced motion a predator will be starving, unless the prey within its sphere of interception is replaced through the turbulent motions in the flow.

The previously outlined simple model assumes that prey is captured with certainty when it enters the sphere of interception. If the turbulent motion is very violent, this assumption can be difficult to argue. The model can evidently be made more realistic and accurate by assuming that the probability of capture depends somehow on the local flow conditions. It seems reasonable to expect that the capture probability is proportional to the time the prey spends in the vicinity of the predator, although not necessarily *linearly* proportional. Information concerning transit time probabilities, for instance, is, however, not readily available. The problem seems to have received only little attention in the literature. The present investigations provide experimentally obtained estimates for relevant probability densities, attempting to provide results which have also a more general applicability.

In the present paper we consider general problems which are related to particle separations by analyzing the time spent by a particle in a reference volume, centered either at a fixed spatial position (the Eulerian case) or at the position of an-

other particle (the Lagrangian case). In the latter case it is assumed that *both* particles passively follow the random turbulent motion of the flow. The reference volume can, in principle, have any shape. We consider here the simplest case, considering spheres with different radii.

Two different problems will be studied. First, the case where a particle happens to be inside the sphere initially, and we analyze the duration of the time interval until it leaves the reference volume. In lack of any established terminology, we denote this time the "occupation time" in the following. Alternatively, we can consider the "transit time" being the difference between the time when a particle enters a reference volume, until it leaves it again. It is, in principle, a simple matter to incorporate the statistical distributions for transit times into reliable models for the flux of captured prey, and this question is given some attention as well. To facilitate comparison of data, we present all figures with the same scales.

Experimentally, and from a data analysis point of view, it is advantageous to distinguish transit time and occupation time statistics. From an analytical point of view, however, the two statistics are related: given a particle orbit which enters the analysis for occupation times, we can always find a transiting particle orbit which contains the given trajectory, and there will be a relation between the two probability distributions. The relation between the transit time and occupation time probability densities [$P_t(t_t)$ and $P_o(t_o)$, respectively] can be determined by the following arguments: Consider an ensemble of long time series measured along a particle trajectory, where we mark time sequences where a particle is *inside* one of the reference volumes distributed at random in the flow. Assuming the system to be ergodic, we can take one of these realizations, take *all* the marked time intervals, and obtain an estimate for the probability density $P_t(t_t)$ of the lengths of these time intervals. This is then the probability density of transit times, as indicated by the subscript *t*. Alternatively, we can select one marked sequence (as defined before) in each realization and then form an ensemble average. These two distributions will, however, be different, since by this latter procedure there will be a preference for selecting long sequences.[10,11] The selection can be seen as a "collision process," where the probability for "hitting" a time interval is proportional to its cross section, i.e., its length.[12] We have

$$\widetilde{P}_t(t_t) = \frac{t_t}{\int_0^\infty t_t P_t(t_t) dt_t} P_t(t_t), \tag{1}$$

where we divide by $\int_0^\infty t_t P_t(t_t) dt_t$ to normalize the distribution. The distribution $\widetilde{P}_t(t_t)$ gives the probability density for transit times, given that we have found the particle inside a reference volume. Given that this condition fulfilled, we then construct the joint probability density $P_J(t_t, t_o)$ of transit times t_t and occupation times t_o. To obtain an occupation time we now select a position within the given interval of length t_t, and subsequently find the occupation time as the difference between this initial time and the end of the transit time interval. We have assumed that the reference spheres are placed randomly in the flow, and that the initial positions of the reference particles are independent of the local flow velocity at the selected initial reference time. For a given transit time t_t the occupation times are then uniformly distributed in the interval $\{0, t_t\}$, irrespective of the length of that interval. Consequently, we find for $P_J(t_t, t_o) = P_o(t_o|t_t)\widetilde{P}_t(t_t)$ the relation

$$P_J(t_t, t_o) = \begin{cases} 0 & \text{for } t_o > t_t, \\ \dfrac{1}{t_t}\widetilde{P}_t(t_t) & \text{for } t_o < t_t. \end{cases} \tag{2}$$

We then have

$$P_o(t_o) = \frac{1}{\int_0^\infty t_t P_t(t_t) dt_t} \int_{t_o}^\infty P_t(t_t) dt_t, \tag{3}$$

where we used (1). With the given assumption of ergodicity, the expression (3) is exact, but of limited use in relation to experimentally obtained distributions. Measuring, for instance, an estimate for $P_t(t_t)$, with some statistical uncertainty, we cannot directly integrate the result and then use (3). The relation is, however, valuable as a test on the consistency of the results, which can be estimated by inspection. By (3) we readily see that $P_o(0)$ must take a finite value, $1/\langle t_t \rangle$ with $\langle t_t \rangle \equiv \int_0^\infty t_t P_t(t_t) dt_t$. It is not evident from (3) that the initial value $P_t(0)$ has to be zero. The result (3) is a consistency relation for $P_o(t_o)$ and $P_t(t_t)$, and applies equally well to the Eulerian as to the Lagrangian case.

The paper is organized as follows: in Sec. II, we discuss details of the experimental setup and the methods of data acquisition. Section III describes Eulerian as well as Lagrangian aspects of the occupation time problem, while Sec. IV describes an analysis of the transit time problem. Some analytical models are discussed as well. They are simple, yet physically realizable, and serve to illustrate some basic properties of the distributions of occupation as well as transit times, in particular, also to illustrate (3). In Sec. V we discuss a somewhat more complicated Eulerian stochastic model. Finally, Sec. VI contains our conclusions. Appendix A contains some model examples for occupation and transit time distributions, which illustrate the relation (3). Some extensions of the transit time problem in a form related to other studies are discussed in Appendix B.

II. EXPERIMENTAL SETUP

The basic features of the present experiment are described elsewhere,[2,13] so a brief summary will suffice here. The tank has $320 \times 320 \times 450$ mm^3 inner dimensions, and the turbulence is generated by the motion of two plastic grids at the top and bottom of the tank. The average distance between the two grids is $\approx$300 mm. The grids are made of an 8 mm sheets of polycarbonate, and the grid spacing is 40 mm, with 32 mm openings. The experimental setup is shown schematically in Fig. 1.

Typical Taylor microscale Reynolds numbers,[14] $R_\lambda = \lambda^2/(\eta^2\sqrt{15})$, are $\sim$100 for the present conditions, using the Taylor microscale $\lambda = \sqrt{15\nu\sigma^2/\epsilon}$, where $\nu \simeq 0.89$ mm^2/s is

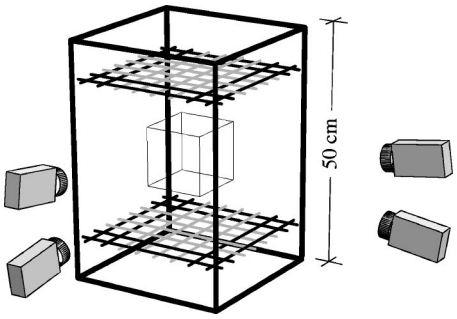

FIG. 1. Experimental setup shown schematically. In particular, we indicate the two movable grids at the top and bottom of the vessel, and the four video cameras for recording particle positions.

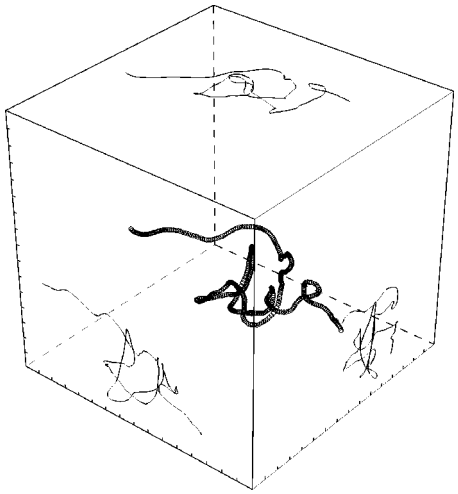

FIG. 2. Sample of particle trajectory obtained experimentally with 1/25 s time resolution. The small spheres give the particle position. The spheres are here shown enlarged for clarity. The distances between tic marks on axes are 10 mm. We also show the projection of the particle orbit on the side walls of the "box" confining the system. The duration of the case shown is ≈21 s, which corresponds to a relatively long trace.

the kinematic viscosity of the water, ϵ is specific energy dissipation, and σ^2 is the variance of one velocity component. The Kolmogorov length scale $\eta=(\nu^3/\epsilon)^{1/4}$ is less than 1/2 mm for the present conditions. The "microscale" η represents the length scales, where the viscous effects become important. A characteristic Eulerian length scale ("outer" scale), $\mathcal{L}_E$, is in the range 20–25 mm. We can interpret $\mathcal{L}_E$ as the lower limit for separations between fixed frame detection points, where the velocities of fluid elements tend to become uncorrelated. As a working hypothesis we can assume that these velocities are also statistically independent.

The motions of small diameter ($d=0.5$–0.6 mm) polystyrene particles in the flow are followed with four video cameras. The simultaneous positions of typically 500–1000 particles are recorded at time intervals of 1/25 s. The positions that are recorded are restricted to a reduced spatial region of $140\times140\times120$ mm^3 in the center of the tank. By a tracking procedure it is then possible to link the positions of particles and follow their individual motion in three spatial dimensions, in particular, also to deduce their time varying velocity. The particles used in the experiment are neutrally buoyant. An illustrative sample trajectory is shown in Fig. 2. The average distance between particles is much larger than their diameter. To the given accuracy, we can assume that the particles follow the flow as passive tracers.[15,16] The Stokes number[17] is approximately 0.08 for the present conditions, meaning that the "slippage" between the flow and the particles is small. Of course, with time, the difference would accumulate between the true particle position and the one that would have resulted by an exact calculation along an ideal Lagrangian orbit in the flow.

We verified that the particles are uniformly distributed in the flow, at least in the central reference region. This is done by counting the number of particles in small subvolumes, and test the distribution against a Poisson distribution that results for particles distributed independently, with a spatially uniform probability. In Fig. 3 we show, as a histogram, the experimental distribution of particles obtained by counting the number of particles N inside spheres with radii $\mathcal{R}=15$ and 30 mm. The analysis is readily carried out on the basis of the experimental data, since we have the simultaneous positions of a large number of particles. The diamonds ◇ give the corresponding theoretical values for a Poisson distribution. As a supplement, we show in Fig. 4 the variation of $(\langle N^2\rangle-\langle N\rangle^2)/\langle N\rangle$. For a Poisson distribution, this quantity has the value 1. We find that the agreement is satisfactory, giving a basis for assuming the positions of different particles to be statistically independent and uniformly distributed in space. The assumption of a spatial Poisson distribution of particles will be used implicitly in the ensuing analysis. The question of the local homogeneity and isotropy of the flow was analyzed as well in previous studies.[2,13]

The present experiment provides a database, which can be used for studying different aspects of turbulent transport.[2,9] The various problems we have considered in the present study are summarized in the following sections.

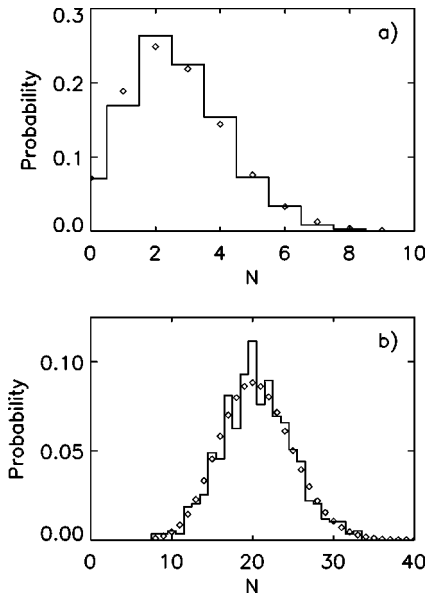

FIG. 3. Two examples for distribution of the number N of particles in randomly placed spheres with radius $\mathcal{R}$. In (a) we have $\mathcal{R}=15$ mm and in (b) 30 mm. The diamonds ◇ denote corresponding analytical values for Poisson distributions.

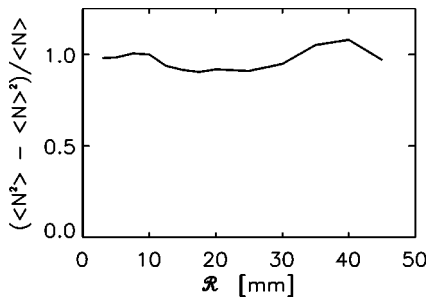

FIG. 4. Experimentally obtained variation of the ratio $(\langle N^2\rangle - \langle N\rangle^2)/\langle N\rangle$ for the distribution of the number N of particles in spheres of varying radius placed in the flow. The results are obtained by distributing 512 spheres for each radius 3, 5, 7.5, 10, 12.5, 15, 17.5, 20, 25, 30, 35, 40, and 45 mm. The analytical value obtained from a Poisson distribution is 1. The test is satisfied within ±10%.

III. DATA ANALYSIS: THE OCCUPATION TIME PROBLEM

One simple question can be formulated as follows: if a particle, at a selected reference time, is within a prescribed sphere of influence of another particle, how long will it spend within this sphere? The question has to be further specified concerning the initial positions. We assume here that they are uniformly distributed within the reference sphere at the reference time. The assumptions of homogeneous and isotropic turbulent flows will be implicit here as well as in the ensuing sections. The problem has evidently a Lagrangian and an Eulerian formulation, where the two are considered separately. The Eulerian problem is the simplest one, so it is considered first, although for the applications we have in mind, the Lagrangian version is the most interesting.

A. Occupation times: The Eulerian case

For the present Eulerian problem, we consider a *fixed* sphere. In this case there is no need to have a particle at the center, since the position is well defined. As a consequence, we can use also events with only one particle inside the sphere at the reference time, and the signal-to-noise ratio on the estimator for the occupation time probability density is significantly improved, in comparison to the Lagrangian problem analyzed later. Illustrative examples are shown in Fig. 5 as a function of real, i.e., non-normalized time.

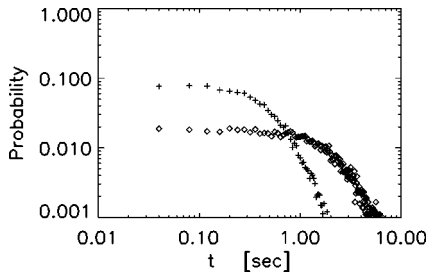

FIG. 5. Experimentally obtained probability densities for the occupation times of particles in a stationary sphere. Two cases are illustrated, one where the radius is $\mathcal{R}=10$ mm (+) and one with $\mathcal{R}=30$ mm ($\diamond$). We have $\epsilon = 225\ \mathrm{mm^2\,s^{-3}}$ and $\sigma = 19\ \mathrm{mm\,s^{-1}}$. The results are to be compared, for instance, with those in Fig. 8.

As an illustrative special case, we can assume $\mathcal{R} \ll \mathcal{L}_E$. This case can be modeled analytically if we assume the flow to be locally uniform at the reference sphere. The model can represent the advection or "sweeping" of the flow by the largest scales, i.e., the largest energy containing eddies with sizes $\sim \mathcal{L}_E$, and ignore the fluctuations associated with smaller scales. This limit corresponds to the short time "ballistic limit" in the analysis of the mean square displacement of a particle due to turbulent motions in the flow.[14] The occupation time distribution for the present model can be calculated analytically as

$$P_o(t|U) = \frac{3}{4}\frac{|U|}{\mathcal{R}}\left[1 - \left(\frac{|U|t}{2\mathcal{R}}\right)^2\right] \tag{4}$$

for $t \leqslant 2\mathcal{R}/|U|$ and $P_o(t|U)=0$ otherwise. We here assumed the local flow velocity U to be uniform and a deterministic constant, and P_o is therefore conditional, as indicated. Within the present simple model, we assume that the velocity is constant in each individual realization of the ensemble, but its magnitude is statistically distributed.

We can obtain a particularly simple relation from (4) by noting that the limit of the shortest occupation times is quite generally obtained from particles close to the surface of the reference volume. For these, we can take the particle velocities to be constant for such very short times, consistent with the assumptions in deriving (4). Upon averaging over all velocities we then have, as a general result for the occupation time probability densities, that $P_o(0)=3\langle|U|\rangle/(4\mathcal{R})$, which by use of (3) implies that the average *transit time* is $\langle t_t\rangle = 4\mathcal{R}/(3\langle|U|\rangle)$. The result is not restricted to Gaussian velocity distribution, although only such will be relevant here. For a Gaussian velocity distribution in three spatial dimensions we have $\langle|U|\rangle^2 = 8\langle U^2\rangle/(3\pi)$.

We allow each realization to include all velocities in such a way that the velocity field is *locally* constant in the vicinity of each reference sphere. Taking the average with respect to the flow velocities with a Gaussian distribution, we find

$$\begin{aligned} P_{oE}(t) &= \int_0^{2\mathcal{R}/t} \frac{3}{4}\frac{U}{\mathcal{R}}\left[1 - \left(\frac{Ut}{2\mathcal{R}}\right)^2\right]\frac{U^2}{\sigma^3}\sqrt{\frac{2}{\pi}} \\ &\quad \times \exp(-U^2/2\sigma^2)dU \\ &= \frac{3\sigma}{\mathcal{R}\sqrt{2\pi}}\left\{1 - \left(\frac{t\sigma}{\mathcal{R}}\right)^2 \right. \\ &\quad \left. + \left[1 + \left(\frac{t\sigma}{\mathcal{R}}\right)^2\right]\exp(-2(\mathcal{R}/t\sigma)^2)\right\}, \end{aligned} \tag{5}$$

which is found to have the asymptotic variation $\sim t^{-4}$. Upon multiplication by $\mathcal{R}/\sigma$ on both sides of (5), we find that $\mathcal{R}P_{oE}/\sigma$ is a dimensionless function of a dimensionless variable $t\sigma/\mathcal{R}$. We will make reference to this scaling in the data analysis.

For the present Eulerian case, we expect that a variation with a normalized time variable can exist for the experimentally obtained occupation times, although it is unlikely to be the same as the one for the Lagrangian case. In the Eulerian case any motion of the flow will give rise to motion of par-

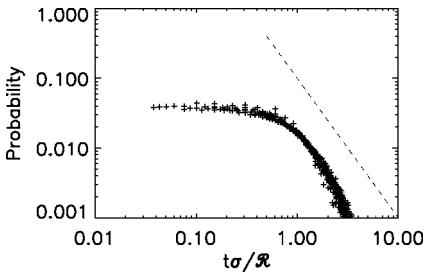

FIG. 6. Experimentally obtained, normalized probability densities for the occupation times of particles in a stationary sphere, showing $(\mathcal{R}/\sigma)P_{oE}(t\sigma/\mathcal{R})$. The figure refers to experimental conditions with $\epsilon = 225\ \mathrm{mm^2\,s^{-3}}$ and $\sigma = 19\ \mathrm{mm\,s^{-1}}$, analyzed for radii $\mathcal{R} = 2.5$, 5, 7.5, 10, 12.5, 15, 17.5, and 20 mm. A dashed line indicates the $\sim t^{-2}$ variation, for reference.

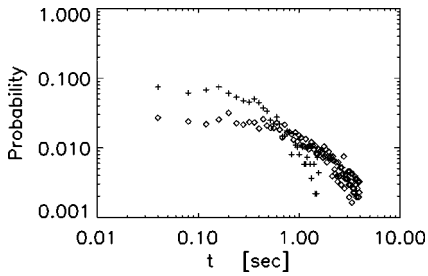

FIG. 8. Experimentally obtained probability densities for the occupation times of particles in a sphere which is moving self-consistently with the flow, i.e., at all times it has the same reference particle in its center. Two cases are illustrated, one where the radius is $\mathcal{R} = 10$ mm (+) and one with $\mathcal{R} = 30$ mm ($\diamond$). We have $\epsilon = 225\ \mathrm{mm^2\,s^{-3}}$ and $\sigma = 19\ \mathrm{mm\,s^{-1}}$. We normalized the results by having the sum of all points being unity. If a continuous curve is fitted to the data points, the values should be multiplied by 25 (originating from the 1/25 s sampling rate) to give the normalization of the probability density $P_{oL}(t)$.

ticles through the reference sphere. For the Lagrangian problem, to be analyzed later on, only relative velocities matter, i.e., the velocity differences between the central particle, and particles near the surface of the reference sphere. To obtain a quantity for scaling the velocities, we anticipate that the occupation times vary mainly due to the sweeping of particles by the largest eddies, which have a scale length approximately given by the Eulerian length scale. We take here $\sigma \equiv \langle U^2 \rangle^{1/2}$ to characterize the entire velocity field, and not the relative velocities. Combining $\mathcal{R}$ and σ, we can only obtain one quantity for normalizing time, i.e., $\mathcal{R}/\sigma$. Consequently, we expect that the probability density for the Eulerian occupation times can be written as a function of a dimensionless variable, as supported also by simple models, as (5).

To obtain an experimental estimate for the occupation time distribution, we carried out a detailed analysis of the Eulerian problem discussed here. First we show, in Fig. 6, the estimate for the normalized probability density of Eulerian occupation times for one particular realization of the turbulent flow, but let the radius $\mathcal{R}$ in the reference sphere be varying. We find that the observed scaling with $\mathcal{R}$ is in good agreement with the proposed model. In Fig. 7 we show the extended version of Fig. 6, in this case with six different realizations for five different σ. We have the values $\sigma = 12$, 16, 17, 19, and 21 $\mathrm{mm\,s^{-1}}$. Two experiments gave $\sigma = 12\ \mathrm{mm\,s^{-1}}$ within the experimental accuracy, but for different ϵ. Both cases are included. We find a good agreement with the proposed scaling. The scatter in data points is here sufficiently small to allow a small systematic variation with σ to be discernible. Large $\mathcal{R}$ seem to fall consistently below the average curve for small times, and lie above it for larger times.

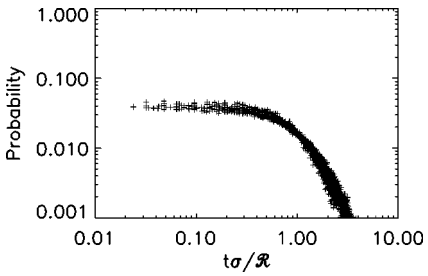

FIG. 7. Experimentally obtained, normalized probability densities for the occupation times of particles in a fixed sphere, showing $(\mathcal{R}/\sigma)P_{oE}(t\sigma/\mathcal{R})$. The figure contains six experimental conditions with $\epsilon = 62$, 65, 135, 160, 225, and 279 $\mathrm{mm^2\,s^{-3}}$, with corresponding values $\sigma = 12$, 12, 16, 17, 19, and 21 $\mathrm{mm\,s^{-1}}$, and each of these analyzed for radii $\mathcal{R} = 5$, 10, 15, and 20 mm as in the Lagrangian counterpart of the analysis in Fig. 10.

B. Occupation times: The Lagrangian case

To analyze the Lagrangian problem, we follow a selected particle in the flow and define a surrounding comoving sphere with prescribed radius $\mathcal{R}$. At a reference time, selected arbitrarily in the data set, we record the positions of all particles which happen to be inside the sphere. At least formally, it is then a straightforward matter to determine the distribution of the times where these particles leave the sphere. The signal-to-noise ratio is of course poor, if we consider the result of one such measurement as an estimate for the occupation time probability density. Since we have a vast amount of data available, it is, however, possible to improve the estimator by repeating the analysis many times, by choosing other reference times, and selecting other particles to define the center of the comoving sphere. As a result we can obtain a figure like Fig. 8 given in real time units. One reason for the scatter in points for small reference radii is that events with more than one particle inside such a sphere are relatively rare for small $\mathcal{R}$.

In the universal subrange of the turbulence, where the effect of viscosity is immaterial (in the present case, length scales typically in the interval 0.30–25 mm) we expect that a universal scaling law should exist. We need a universal "time" for normalization. With the parameters ϵ and $\mathcal{R}$ being the only dimensional parameters available for the universal subrange, the only characteristic time available is $\mathcal{R}^{2/3}/\epsilon^{1/3}$. In the universal subrange, we expect that in terms of the probability density for the Lagrangian occupation times we have $(\mathcal{R}^{2/3}/\epsilon^{1/3})P_{oL}$ to be a dimensionless function of the dimensionless variable $t\epsilon^{1/3}/\mathcal{R}^{2/3}$. We here assume that ϵ is a deterministic constant, and thereby ignore intermittency corrections.[1,3] The conjectured scaling for the occupation time probabilities can readily be tested in the experiment, with results shown in Figs. 9 and 10. If we include data for

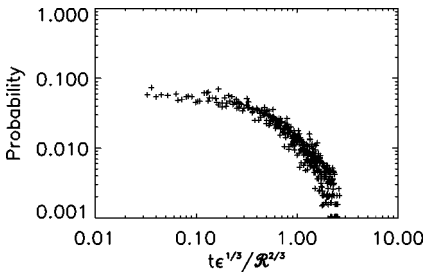

FIG. 9. Experimentally obtained, normalized probability densities for the occupation times of particles in a self-consistently moving sphere, showing $(\mathcal{R}^{2/3}/\epsilon^{1/3})P_{oL}(t\epsilon^{1/3}/\mathcal{R}^{2/3})$. The figure refers to experimental conditions with $\epsilon=225$ mm^2 s^{-3}, analyzed for radii $\mathcal{R}=2.5$, 5, 7.5, 10, 12.5, 15, 17.5, and 20 mm.

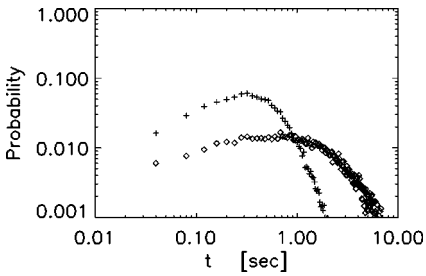

FIG. 11. Experimentally obtained probability densities for the transit times of particles in a stationary sphere. Two cases are illustrated, one where the radius is $\mathcal{R}=10$ mm (+) and one with $\mathcal{R}=30$ mm ($\diamond$). We have $\epsilon=225$ mm^2 s^{-3} and $\sigma=19$ mm s^{-1}.

radii $\mathcal{R}>\mathcal{L}_E$, we find a clear disagreement with the proposed scaling, as expected. We find an excellent scaling with $\mathcal{R}$ for fixed ϵ, see Fig. 9. When we include different experimental conditions, corresponding to different values of ϵ, we find a slight increase in the scatter. This might, however, be an indication of the uncertainties associated with an experimental determination of the dissipation rate ϵ.

IV. DATA ANALYSIS: THE TRANSIT TIME PROBLEM

In Sec. III we considered the occupation time problem, but note that this may not be the formulation which is most relevant for discussions of, for instance, microorganisms and their feeding rate. Rather, one might like to know for this particular problem, the time a particle spends inside a reference sphere, given the condition that it enters the sphere at a reference time t_0. Again the problem has to be specified in somewhat more detail, and we here assume that the "entrance velocity" of the particle has a velocity vector pointing into the sphere at t_0, but its angle with the radius vector pointing towards the particle is randomly distributed.

A. Transit times: The Eulerian case

We first analyze the transit time of a particle through a fixed sphere, immersed in the flow. Obviously, neither in this case, do we need to have a particle placed at the center. The data analysis as such is an extension of the one described in Sec. III A and needs no detailed discussion here.

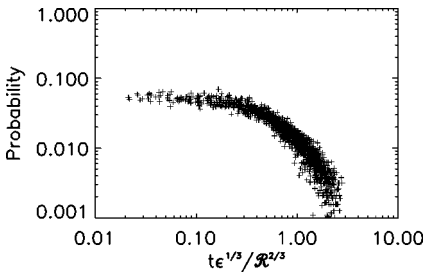

FIG. 10. Experimentally obtained, normalized probability densities for the occupation times of particles in a self-consistently moving sphere, showing $(\mathcal{R}^{2/3}/\epsilon^{1/3})P_{oL}(t\epsilon^{1/3}/\mathcal{R}^{2/3})$. The figure contains six experimental conditions with $\epsilon=62$, 65, 135, 160, 225, and 279 mm^2 s^{-3}, and each of these analyzed for radii $\mathcal{R}=5$, 10, 15, and 20 mm.

In Fig. 11 we show samples of data giving the estimate for the probability density of the transit time as function of time in seconds. We note that the signal-to-noise ratio for the estimator is similar to that in Fig. 5.

As an illustration we can assume $\mathcal{R}\ll\mathcal{L}_E$, so that the advection of flow through the reference sphere can be approximated as a locally uniform flow. The transit time distribution can be calculated analytically as

$$P_t(t|U)=\frac{U^2}{2\mathcal{R}^2}t \tag{6}$$

for $t\leqslant 2\mathcal{R}/|U|$ and $P_t(t|U)=0$ otherwise. We here assumed the local flow velocity U to be uniform and a deterministic constant, and P_t is therefore again conditional, as indicated, just as in (4). Within the present simple model, we again assume that the flow velocity is constant in each individual realization of the ensemble, but its magnitude is statistically distributed. To complete the model we have to give a statistical distribution of velocities over the realizations. We note that (6) together with (4) satisfies the consistency relation (3).

With reference to the procedure for estimating the probability density of transit times, we have to take into account that, in the present case, regions with large U will, in a given fixed time interval, contribute relatively more to the probability density than those with small U. We weight the transit times of individual particles with the corresponding fluxes before averaging to give

$$\begin{aligned}P_{tE}(t)&=\int_0^{2\mathcal{R}/t} t\frac{U^2}{2\mathcal{R}^2}\frac{U^2}{\sigma^3}\sqrt{\frac{2}{\pi}}\\&\quad\times\frac{\exp(-U^2/2\sigma^2)dU}{\displaystyle\int_0^\infty\sqrt{\frac{2}{\pi}}(U^3/\sigma^3)\exp(-U^2/2\sigma^2)dU}\\&=2\frac{\sigma}{\mathcal{R}}\left[\frac{t\sigma}{\mathcal{R}}-\left(2\frac{\mathcal{R}^3}{t^3\sigma^3}+2\frac{\mathcal{R}}{t\sigma}+\frac{t\sigma}{\mathcal{R}}\right)\exp[-2\mathcal{R}^2/(t\sigma)^2]\right],\end{aligned} \tag{7}$$

with the asymptotic variation $\sim t^{-5}$. Upon multiplication by $\mathcal{R}/\sigma$ on both sides of (5), we find that also $\mathcal{R}P_{tE}/\sigma$ is a dimensionless function of a dimensionless variable $t\sigma/\mathcal{R}$.

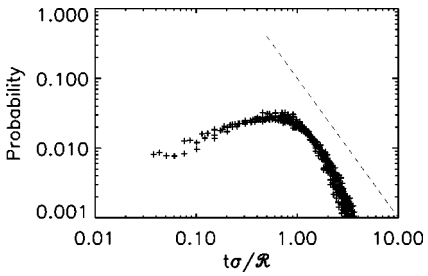

FIG. 12. Experimentally obtained, normalized probability densities for the transit times of particles in a stationary sphere, showing $(\mathcal{R}/\sigma)P_{tE}(t\sigma/\mathcal{R})$. The figure refers to experimental conditions with $\epsilon=225\ \mathrm{mm^2\,s^{-3}}$ and $\sigma=19\ \mathrm{mm\,s^{-1}}$ analyzed for radii $\mathcal{R}=2.5$, 5, 7.5, 10, 12.5, 15, 17.5, and 20 mm. A dashed line gives t^{-2} for reference.

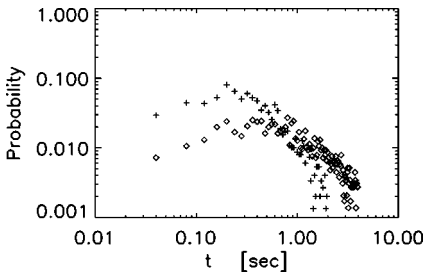

FIG. 14. Experimentally obtained probability densities for the transit times of particles in a sphere which is moving with the flow, i.e., at all times it has the same reference particle in its center. Two cases are illustrated, one where the radius is $\mathcal{R}=10$ mm (+) and one with $\mathcal{R}=30$ mm ($\diamond$). We have $\epsilon=225\ \mathrm{mm^2\,s^{-3}}$ and $\sigma=19\ \mathrm{mm\,s^{-1}}$.

We note that (7) together with (5) satisfies the consistency relation (3).

In Fig. 12 we show an experimentally obtained estimate for the normalized probability density $(\mathcal{R}/\sigma)P_{tE}$, obtained for data from one experiment with $\sigma=19\ \mathrm{mm\,s^{-1}}$, and varying radii $\mathcal{R}$. We find a convincing agreement with the proposed scaling. Finally, in Fig. 13, we show the estimate for the normalized transit time distribution, to be compared, for instance, with the results in Fig. 7. We note that the proposed scaling is well followed by the data, but also in this case we are aware of a systematic scatter, which we attribute to the same effects as in Fig. 7. For short times, the difference between the Eulerian occupation and transit time problems is well explained by the simple models proposed. The difference between our simple analytical model and the observations is due to the shortcoming of the assumed linear trajectories of the transit particles. In reality, due to the meandering motion induced by the small eddies in the turbulence, these trajectories are irregular for a large number of the particles.

B. Transit times: The Lagrangian case

To analyze the Lagrangian transit time problem, we again follow a selected particle in the flow and define a surrounding comoving sphere with prescribed radius $\mathcal{R}$. Determining the entrance and exit times of other particles with respect to the given sphere, we determine the distribution of the times the particles spent inside the sphere, i.e., out of all particles, we take that fraction which has the transit time t for estimating the probability density for transit times. The numerical analysis is lengthy and involves a detailed book keeping of all particles at all times, but the basic principles are self-explanatory, and need not be discussed in detail here. Results from such an analysis are shown in Fig. 14 with abscissa in seconds. Two cases are chosen so that they cover $\mathcal{R}<\mathcal{L}_E$ and $\mathcal{R}>\mathcal{L}_E$. Due to the temporal sampling of particle positions, we will not record particles staying less than $1/25$ s in the sphere, i.e., the "glancing" trajectories. For this reason, the first data point gives an underestimate. Figure 14 illustrates the scatter in data points for different times and $\mathcal{R}$ values, and serves also to introduce the physical time scales (in seconds), while following figures will present results for scaled variables.

In the universal subrange of the turbulence, we expect also for the present problem that a universal scaling law should exist. The arguments will be identical to those given in Sec. III B, and we expect also here that in terms of the probability density for the Lagrangian transit times we have $(\mathcal{R}^{2/3}/\epsilon^{1/3})P_{tL}$ to be a dimensionless function of the dimensionless variable $t\epsilon^{1/3}/\mathcal{R}^{2/3}$. This conjectured scaling for the transit time probabilities can readily be tested in the experiment, with results shown in Figs. 15 and 16. If we try to include data for radii $\mathcal{R}>\mathcal{L}_E$, we find a clear disagreement with the proposed scaling. We find an excellent scaling with $\mathcal{R}$ for fixed ϵ, see Fig. 15. When we include different experimental conditions, with different ϵ, we find also here a slight increase in the scatter of data points. It might be that part of

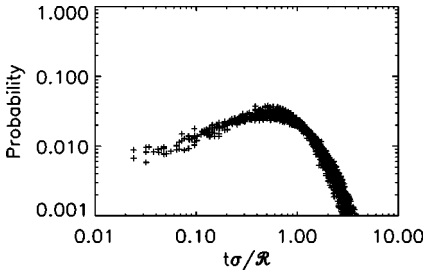

FIG. 13. Experimentally obtained, normalized probability densities for the transition times of particles in a fixed sphere, showing $(\mathcal{R}/\sigma)P_{tE}(t\sigma/\mathcal{R})$. The figure contains six experimental conditions with $\epsilon=62$, 65, 135, 160, 225, and 279 $\mathrm{mm^2\,s^{-3}}$, and each of these analyzed for radii $\mathcal{R}=5$, 10, 15, and 20 mm.

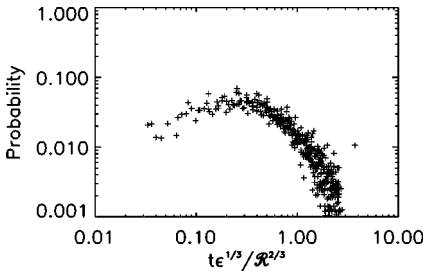

FIG. 15. Experimentally obtained, normalized probability densities for the transit times of particles with respect to a moving sphere. The figure refers to experimental conditions with $\epsilon=225\ \mathrm{mm^2\,s^{-3}}$ analyzed for radii $\mathcal{R}=2.5$, 5, 7.5, 10, 12.5, 15, 17.5, and 20 mm.

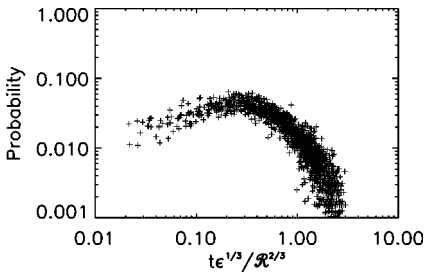

FIG. 16. Experimentally obtained, normalized probability densities for the transit times of particles with respect to a moving sphere. The figure contains six experimental conditions with $\epsilon=62$, 65, 135, 160, 225, and 279 mm^2 s^{-3}, and each of these analyzed for radii $\mathcal{R}=5$, 10, 15, and 20 mm.

this enhanced scatter is due to an experimental uncertainty in determining the ϵ-value for a given experimental condition.

The analytical results discussed here are the simplest relevant ones. A full solution of the transit time problem will address, for instance, the transition probability for a particle initially at one position on the surface of the reference sphere to another arbitrary position on the same sphere, subject to the constraint that the entire trajectory is inside the sphere. We attempt to illustrate models satisfying these requirements by a stochastic model, discussed in Sec. V.

V. STOCHASTIC MODEL

In the simple models of Secs. III and IV we assumed the local velocity field to be constant in time. We will here illustrate the consequences of time varying vector fields by using a stochastic model.

In the Eulerian study of occupation and transit times we use a Lagrangian stochastic model to predict occupation and transit times. The basic idea is to regard the position of a particle in the flow as a stochastic variable. The evolution of the particle can then be modeled by a stochastic differential equation (SDE). A thorough discussion of SDEs in turbulence is given by, for instance, Pope.[18]

In this study we use the model suggested by Sawford.[19] This is a second-order stochastic model and is therefore the simplest one which takes into account the effect of finite Reynolds numbers. This effect seems rather important since the experimental data are far from the inviscid limit.

The governing equations for the position, velocity, and acceleration are

$$dx_i(t) = u_i(t)dt, \tag{8}$$

$$du_i(t) = a_i(t)dt, \tag{9}$$

$$da_i(t) = -\alpha_1 a_i(t)dt - \alpha_2 u_i(t)dt + \sqrt{2\alpha_1\alpha_2\sigma_u^2}dW_i(t). \tag{10}$$

Here α_1 and α_2 are damping constants, σ_u^2 is the velocity variance, while $dW_i(t)$ are three independent Wiener processes, one for each acceleration component.

The one component velocity auto correlation function, $R_u(\tau) \equiv \langle u(t)u(t+\tau)\rangle / \sigma_u^2$ is

$$R_u(\tau) = \frac{\beta_1 \exp(\beta_2|\tau|) - \beta_2 \exp(\beta_1|\tau|)}{\beta_1 - \beta_2}, \tag{11}$$

where β_1 and β_2 are roots of the characteristic polynomium, $z^2+\alpha_1 z+\alpha_2=0$. We can think of β_1 and β_2 as inverse time scales, characterizing the energy containing eddies, and the smallest scales, respectively, and hence their ratio squared acts as an effective Reynolds number.

From the experimental data we can estimate the Lagrangian velocity structure function, $D_u(\tau)=\langle[u(t+\tau)-u(t)]^2\rangle = C\epsilon\tau$, where the last equality is valid for an infinite inertial subrange. $D_u(\tau)$ can also be expressed as

$$D_u(\tau) = 2\sigma_u^2[1 - R_u(\tau)]. \tag{12}$$

In order to get the external model parameters, α_1, α_2, and σ_u^2 we have fitted the autocorrelation function $\sigma_u^2 R_u(\tau)$ to the experimental data. Different fits have been tried out. It was found that fitting to the autocorrelation function $R_u(\tau)$ gave much better results than fitting to the Lagrangian structure function $D_u(\tau)$. Differences in the experimental data and the model was, however, seen when comparing both autocorrelation functions and Lagrangian structure functions. This could be due to lack of stationarity of the Lagrangian velocity, $u_i(t)$. In the experiments particles lose some energy in the measuring volume.[2,13] The flow *is*, however, stationary in the Eulerian sense.

Results

The simulated occupation and transit time distributions are obtained for each set of external parameters, $\alpha_1, \alpha_2, \sigma_u^2$ and the radius R based on 10^6 particle tracks.

In the case of occupation times, the initial position of the particles are randomly distributed in the sphere. The initial velocity and acceleration are Gaussian with zero mean and variances, σ_u^2 and $\sigma_a^2=\beta_1\beta_2\sigma_u^2$, respectively. Whenever $|\mathbf{x}|$ exceeds $\mathcal{R}$ the time is recorded. The assumption of Gaussian accelerations can be questioned,[20] but turns out to give reasonable results here.

In the transit time problem the particles are started on the boundary, $|\mathbf{x}|=\mathcal{R}$. The initial acceleration is again Gaussian while the initial velocity perpendicular to the surface of the sphere is determined by the correct flux at the boundary

$$p_{\text{in}}(u_\perp) = \frac{u_\perp p_G(u_\perp)}{\int u_\perp p_G(u_\perp) du_\perp}, \tag{13}$$

where $p_G(u)$ is the Gaussian distribution. The initial distribution $p_{\text{in}}(u_\perp)$ is a Rayleigh distribution (the length of a Gaussian vector on the sphere). The other two velocity components are Gaussian.

The inverse time scales β_1 and β_2 span an inertial subrange where the scaling laws are expected to apply. We can thus only expect a time scaling, $\mathcal{R}/\sigma_u$ in this regime. This means that as $\mathcal{R}$ increases, we might get outside of the inertial subrange and enter another diffusive regime. Here we would expect a random walk behavior for very large $\mathcal{R}$. For the present parameters this should happen around $R \sim 14$ mm (inertial range, $0.001 \ll \tau \ll 0.78$ s, with $\sigma_{u,\text{fit}}$

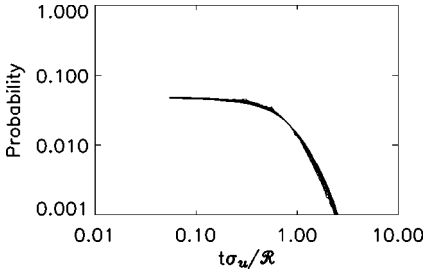

FIG. 17. Eulerian occupation time distributions obtained by a stochastic model to be compared with Fig. 6.

$=18$ mm/s being the fitted parameter corresponding to $\sigma_u = 19$ mm/s, using actual values for β_1 and β_2).

Flaws in the model due to the assumption of Gaussian distributed accelerations are known,[19,21] but they are not believed to be of significance here. In particular, we note that some of the results reported in the literature[20] are obtained for noticeably larger Reynolds numbers than those relevant for the present study. The present numerical analysis has a limited time resolution for smallest transit and occupation times, but this is a limitation it shares with the experiment.

Results from the stochastic simulations are shown in Figs. 17 and 18, calculated for σ values corresponding to the experimental conditions, with radii $\mathcal{R}=2.5$, 5.0, 7.5, 10.0, 12.5, 15.0, 17.5, and 20.0. Closer inspection shows that the distributions obtained from the stochastic model decrease exponentially for large times, i.e., all the moments of the distributions are finite for these cases. In particular, the results in Fig. 17 are found to be in very good agreement with the observations summarized in Fig. 6. We can conclude that the second-order model discussed in the present section can be used for the Eulerian analysis. It is, however, also evident that when dealing with Lagrangian transit and occupation times the model cannot be utilized as it is. A stochastic model that could be used for calculating the Lagrangian transit and occupation times is given in Ref. 22. This is a lengthy future study.

VI. DISCUSSIONS AND CONCLUSIONS

In the present study we analyzed occupation and transit times of particles advected passively through fixed radius spheres in turbulent flows. Both the Lagrangian and the Eulerian aspects of the problem were investigated for varying parameters. Simple analytical models were presented for occupation and transit time probability densities. In all the Eulerian cases investigated, the distributions decayed faster than the simple models, but seem to agree well with the model of Sec. V. In the Lagrangian counterparts of the problems, the scatter on the estimate for probability densities is somewhat increased, and the asymptotic variation is uncertain. These results refer to a limited time range due to experimental constraints and cannot be considered conclusive for the asymptotic variation. The basic features of the distributions are, however, well explained by the simple models, i.e., we find that the occupation time probability densities are maximized by their value at the origin, while transit time distributions start out at a zero value, and have a maximum at approximately unity, in terms of the normalized time variables. This latter result is consistent with estimates obtained from analytical results as those shown in Secs. III and IV. We note also that the variations of the occupation and transit time distributions are as we expect from the consistency relation (3). Recalling the factor 25 we introduced for normalization, we also note that the value $P_{oE}(0) \approx 0.045 \times 25\mathcal{R}/\sigma$ obtained from, e.g., Fig. 7 is within 20% consistent with the estimate found from the discussion in Sec. III A.

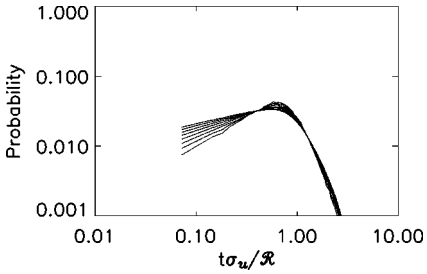

FIG. 18. Eulerian transit time distributions obtained by a stochastic model to be compared with Fig. 12.

As already mentioned, the transit time statistics discussed in the present paper are dealing with only one of many manifestations of relative turbulent transport. There are, however, cases where this formulation is particularly relevant. Our interest in the problem arises, as outlined in the Introduction, in part from discussions of the feeding processes of microorganisms in turbulent environments. Since, at least in a standard formulation of the problem, both predators and prey are passively advected by the flow in which they are embedded,[8] the problem is directly related to relative diffusion of particles. The main difference between the two problems being that we are here dealing with a *boundary value* problem, where the surface of a suitable defined "sphere of interception" in effect acts as a perfectly absorbing surface. By model studies,[4–7] or simple dimensional reasoning,[9,23] it can be argued that the steady state normalized prey flux to such an absorbing surface must scale as $J/\eta_0 \approx C\epsilon^{1/3}\mathcal{R}^{7/3}$. A numerical constant can be estimated as $C=0.32\pm0.05$ by use of Richardson's model diffusion equation for relative diffusion.[2] The density of prey at infinite distances from the predator is introduced as η_0.

It is evident that a nontrivial assumption is implied in these arguments, namely, that prey are captured with certainty within the sphere of interception. Even in the case where the prey concentration is so low that, on average, only one is present at a time in the reference sphere (this is the most relevant case), the turbulent transport of prey past the predator can become so rapid that a capture is unlikely.[24] For a given predator (with a given range $\mathcal{R}$), this process can be modeled by assuming that given a transit time t, the probability of capture is $P(\text{capt.}|t)=t/\tau_0$ for $t \leqslant \tau_0$ and $P(\text{capt.}|t)=1$ for $t>\tau_0$, where τ_0 is a constant time scale characteristic of the species. Obviously, τ_0 will be different for different species, and therefore also for different $\mathcal{R}$. The probability of capture of prey is then obtained by $P(\text{capt.}) = \int P(\text{capt.}|t)P_L(t)dt$ by Bayes theorem, where $P_L(t)$ is the

probability density of transit times which we obtained experimentally before. With reference to the $\epsilon^{1/3}/\mathcal{R}^{2/3}$ time scaling of the saturated prey flux, there are now two obvious limiting cases: $\tau_0 \ll \mathcal{R}^{2/3}/\epsilon^{1/3}$ and $\tau_0 \gg \mathcal{R}^{2/3}/\epsilon^{1/3}$. In the former case we have $P(\text{capt.}) \approx 1$, and the results for J/η_0 apply.[9] In the latter limit we find $P(\text{capt.}) \approx \int_0^\infty (t/\tau_0) P_L(t) dt = \langle t \rangle / \tau_0$, assuming that the average transit time is finite. As we have seen, this assumption is not as trivial as it might seem. Due to the scaling of P_L demonstrated before, we have $P(\text{capt.}) \sim \mathcal{R}^{2/3}/(\epsilon^{1/3}\tau_0)$. In this case we can obtain the scaling of the flux J_c actually captured by the predator under steady state conditions as the product of flux and capture probability

$$J_c/\eta_0 \sim \epsilon^{1/3}\mathcal{R}^{7/3} \times \frac{\mathcal{R}^{2/3}}{\epsilon^{1/3}\tau_0} \sim \frac{\mathcal{R}^3}{\tau_0}, \tag{14}$$

i.e., J_c is independent of ϵ! This means that if we start with a predator in calm waters with a corresponding vanishing prey flux, and then slowly increase ϵ by "external" stirring while $\mathcal{R}$ is constant, we first find $J_c/\eta_0 \sim \epsilon^{1/3}\mathcal{R}^{7/3}$ until $\epsilon \approx \mathcal{R}^2/\tau_0^3$. From then on we have J_c/η_0 independent of ϵ. In this limit, an increase in prey flux is exactly canceled by a corresponding reduction in the capture probability, due to the rapid sweeping of prey past the predator! Some supplementary results were presented previously.[23]

We can elaborate (14) a little further by noting that in order for the turbulent relative dispersion to be of importance for a predator with range of interception $\mathcal{R}$, we require that this length is larger than the Kolmogorov length scale, i.e., $\mathcal{R} \geqslant \nu^{3/4}/\epsilon^{1/4}$. For the limit (14) we require, as mentioned, $\tau_0 > \mathcal{R}^{2/3}/\epsilon^{1/3}$. This implies $\nu^{3/4}/\epsilon^{1/4} \leqslant \mathcal{R} < \tau_0^{3/2}\epsilon^{1/2}$ or $\tau_0 > (\nu/\epsilon)^{1/2}$. This means that τ_0 has to be larger than the Kolmogorov time scale $(\nu/\epsilon)^{1/2}$ for the limit (14) to be relevant. This inequality should be amenable for experimental investigations. It should be noted that the Kolmogorov time scale is rather small for most relevant turbulent flows: for the present experimental conditions it is less than 0.1 s. In nature, we might thus experience that the prey flux to a predating microorganism scales as $\mathcal{R}^3$, independent of the turbulence level, at least in an observable subrange!

We can generalize the previous simple model for the capture probability by allowing for a subrange $(t/\tau_\alpha)^\alpha$ for very small times. With $\alpha \geqslant 2$ this model accounts for a vanishing capture probability for prey with large relative velocities.[25] It is readily demonstrated, by taking $\alpha = 2$, for instance, that (14) is modified to

$$J_c/\eta_0 \sim \epsilon^{1/3}\mathcal{R}^{7/3} \times \left(\frac{\mathcal{R}^{2/3}}{\epsilon^{1/3}\tau_\alpha} \right)^{\alpha=2} \sim \frac{\mathcal{R}^{11/3}}{\epsilon^{1/3}\tau_2^2}, \tag{15}$$

assuming here that $\langle t^2 \rangle$ is finite. Within this modified model, we find $J_c \to 0$ for $\epsilon \to \infty$, but an intermediate "plateau" with constant J_c might be anticipated, in general. The result (15) is trivially generalized to arbitrary values for $\alpha \neq 2$. While the case with $\alpha = 1$ discussed before is the easiest one argued for, the more general case can be used for modeling. The discussion emphasizes also the importance in determining whether higher order averages as $\langle t^\alpha \rangle$ for $\alpha \geqslant 2$ are finite: any asymptotic power law, $P(t) \sim t^{-n}$ with $n \geqslant 2$ will have diverging averages for α sufficiently large. We found that the stochastic model, discussed in Sec. V, seemed to give the moments $\langle t^\alpha \rangle$ to be finite for all α.

Our arguments are easily generalized for different capture probabilities for different transit time subranges, each characterized by some time scale and a time exponent, but it is questionable to what extent actual studies involving living organisms will be able to discriminate the difference between the simple and the more refined models.

In the present study, we have discussed spherical volumes, but the scaling arguments apply equally well also for deformed volumes, as far as we are dealing with a self-similar scaling of the entire volume with just *one* length scale, here denoted by $\mathcal{R}$.

In the present formulation of the problem of relative motion of two particles in turbulent flows, we considered the problem which, in a sense, is *opposite* to the one of particle separation, by investigating the distributions of times that particles spend close together in a turbulent environment. We demonstrated that these distributions contain information which is central for the understanding of, for instance, details of the feeding process of aquatic microorganisms. The entire analysis was carried out for radii in the relevant spheres of interception being in the universal subrange. Actual values of $\mathcal{R}$ are often close to the Kolmogorov length scale, and therefore sensitive to changes in the viscosity of the environment. This observation leads to the conclusion that releases of pollutants can have unexpected consequences for aquatic microorganisms, even when they are chemically inactive, if they can change the viscosity of the water.[15,26]

ACKNOWLEDGMENTS

This work was in part supported by the Danish Technical Research Council, under Contracts No. STVF-9601244 and No. 26-01-0087. Two of the authors (H.L.P. and J.T.) were in part supported by the "Effects of North Atlantic Climate Variability on the Barents Sea Ecosystem" (ECOBE) project.

APPENDIX A: MODELS FOR TRANSIT AND OCCUPATION TIME DISTRIBUTIONS

We can obtain some simple analytical results in limiting cases to illustrate (3). First, it is obvious for a Lagrangian problem, studied in a uniform flow, there will be no particles passing through the reference sphere, irrespective of its radius. The simplest nontrivial case is found when spheres propagate in a linear shear flow. In that case the local relative velocity at the center of the sphere vanishes in the comoving frame, and the flow varies as, for instance,

$$\{U_x, U_y, U_z\} = \{\alpha z, 0, 0\} \tag{A1}$$

in the vicinity of this point, with the constant α being a measure of the flow gradient. The results for this flow can be seen as supplementing the previous analytical model results, given in Secs. III A and IV A, and they might be useful in other contexts.

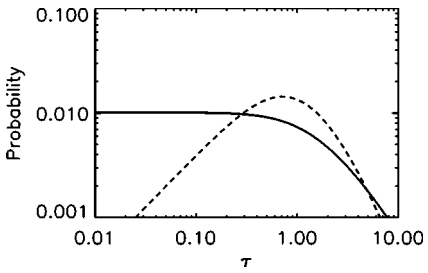

FIG. 19. Analytical results for the Lagrangian transit and occupation time problems in the limit of a local linear shear flow with randomly distributed gradients. The area of the two curves is the same, but they are normalized here to 1/25, see also discussion of Fig. 8, in order to facilitate comparison with experimental results. The normalized time variable is $\tau = t\sigma_\alpha$. A full line shows the occupation time distribution (A3), the dashed line the corresponding transit time distribution (A6).

1. Occupation times

The conditional probability density $P(t|\alpha)$ for occupation times, given α, in the present simple local flow model is found as

$$P_{oL}(t|\alpha) = \frac{\alpha}{\pi[1+(\alpha t/2)^2]}. \tag{A2}$$

It is interesting to note that this result is independent of the radius of the reference sphere. This is in a sense an artifact, being a consequence of the assumed linear velocity shear, which in realistic conditions has to be limited in space.

The velocity shear parameter α, describing the intensity of the velocity shear, is assumed to be statistically distributed. We assume it to have a Gaussian distribution, which would be correct for a Gaussian random process. We introduce σ_α, with dimension *time*, as the standard deviation for the variations in the velocity gradients. We find

$$P_{oL}(t) = 2\int_0^\infty \frac{\alpha}{\pi[1+(\alpha t/2)^2]} \frac{1}{\sigma_\alpha\sqrt{2\pi}} \exp[-\alpha^2/(2\sigma_\alpha^2)]d\alpha$$
$$= \frac{2\sigma_\alpha\sqrt{2}}{\pi^{3/2}(t\sigma_\alpha)^2}\Gamma\left[0, \frac{2}{(t\sigma_\alpha)^2}\right]\exp[2/(t\sigma_\alpha)^2], \tag{A3}$$

expressed in terms of the incomplete Γ function, $\Gamma[a,\xi] = \int_\xi^\infty t^{a-1}e^{-t}dt$. It can be demonstrated that (A3) varies as $t^{-2}\ln t$, for $t\to\infty$. The normalized result $P_{oL}(t)/\sigma_\alpha$ obtained from (A3) is shown in Fig. 19 with a full line. The result shown in Fig. 19 agrees qualitatively with the experimental distributions in Figs. 9 and 10. The results do not, however, have any one-to-one correspondence, since ϵ is not easily related to σ_α, so the normalizations on the time axes are basically different.

2. Transit times

We can obtain some simple analytical results for transit times, for the case where the local velocity at the center of the sphere vanishes in the comoving frame, and the flow varies as in (A1). We consider a particle propagating in the direction of the x axis, with the coordinates x,y,z being distributed on the "back" surface of the sphere with radius $\mathcal{R}$. We have $\mathcal{R}^2 = x^2+y^2+z^2$. The transit time of such a particle is $t = 2x/\alpha z = (2/\alpha z)\sqrt{\mathcal{R}^2-y^2-z^2}$. For a given time t, the locus of such particles is then $y^2+[1+(\alpha t/2)^2]z^2 = \mathcal{R}^2$. The flux of particles at a position $\{x,y,z\}$ is given by the product of a velocity αz and a constant density, irrespective of x and y. The actual particle density is immaterial here, since the distribution will be normalized. The cumulative distribution $F(t)$ of transit times is then obtained as

$$F(t) = C_1 2\int_0^{\mathcal{R}} \int_{\sqrt{\mathcal{R}^2-y^2}/\sqrt{1+(\alpha t/2)^2}}^{\sqrt{\mathcal{R}^2-y^2}} \alpha z dz\, dy$$
$$= C_1\alpha\frac{(\alpha t/2)^2}{1+(\alpha t/2)^2}\int_0^{\mathcal{R}}(\mathcal{R}^2-y^2)dy = C_2\frac{(\alpha t/2)^2}{1+(\alpha t/2)^2}, \tag{A4}$$

with constants determined by the requirement $F(t\to\infty)\to 1$. In particular, we find $C_2 = 1$. The probability density $P(t|\alpha)$ for transit times in the present simple model is then found as

$$P_t(t|\alpha) = \frac{dF(t)}{dt} = \alpha\frac{\alpha t/2}{[1+(\alpha t/2)^2]^2}, \tag{A5}$$

which has its maximum for $\alpha t/2 = 1/\sqrt{3}$. This result is again independent of the radius of the reference sphere. This is an artifact, being a consequence of the assumed linear velocity shear as in (A2) or (A3). The consistency of the results (A2) and (A5), with reference to (3), is easily demonstrated.

The intensity α of the velocity shear is also here, as in the second section of Appendix A, assumed to be statistically distributed, and we assume it to have a Gaussian distribution. We introduce the standard deviation σ_α for the variations in velocity gradients in isotropic homogeneous turbulence, just as in Sec. III B. An ergodic model is here found by the expression

$$P_{tL}(t) = 2\int_0^\infty \frac{\alpha^3 t/2}{[1+(\alpha t/2)^2]^2}\frac{1}{\sigma_\alpha\sqrt{2\pi}}$$
$$\times\frac{\exp[-\alpha^2/(2\sigma_\alpha^2)]d\alpha}{2\int_0^\infty(\alpha/\sigma_\alpha\sqrt{2\pi})\exp[-\alpha^2/(2\sigma_\alpha^2)]d\alpha}$$
$$= \frac{4\sigma_\alpha}{(t\sigma_\alpha)^5}\left([2+(t\sigma_\alpha)^2]\Gamma\left[0,\frac{2}{(t\sigma_\alpha)^2}\right]\right.$$
$$\left.\times\exp[2/(t\sigma_\alpha)^2]-(t\sigma_\alpha)^2\right), \tag{A6}$$

with asymptotic variation $\sim t^{-3}\ln t$. As a general feature of the Lagrangian transit time distributions based on (A5), we find that $P_{tL}(0) = 0$. The normalized result $P_{tL}(t)/\sigma_\alpha$ obtained from (A6) is shown in Fig. 19 with a dashed line as function of normalized time τ. It can be demonstrated that (A3) and (A6) satisfy (3).

APPENDIX B: EXTENSIONS OF THE TRANSIT TIME PROBLEM

The analysis discussed in Sec. IV for the Lagrangian case has an interesting generalization in relation to experimental estimates of Richardson's constant. We can thus in-

troduce *two* concentric shells, with radii $\mathcal{R}_1$ and $\mathcal{R}_2$, where their common center is defined by a particle moving with the flow. Assuming another particle to be inside the innermost shell, we let a reference time t_0 be defined where the particles leaves the inner shell to enter the intermediate region between the two surfaces, $\mathcal{R}_1 < r < \mathcal{R}_2$. As a later time we define t_1 as the time where the given particle for the first time leaves also the outer shell, $r > \mathcal{R}_2$. The transit time $\tau \equiv t_1 - t_0$ is a randomly varying quantity, described by a probability density $P_2(\tau)$, where we added a subscript 2 to distinguish the present "two shell" problem from the single shell version discussed before. We have now two length scales $\mathcal{R}_1$ and $\mathcal{R}_2$, and a time scale $\mathcal{R}_2^{2/3}/\epsilon^{1/3}$. The function P_2 has the dimension time^{-1}. For dimensional reasons,[27] we have the general form

$$\mathcal{G}\left(\frac{\mathcal{R}_2^{2/3}}{\epsilon^{1/3}}P_2, t\frac{\epsilon^{1/3}}{\mathcal{R}_2^{2/3}}, \frac{\mathcal{R}_1}{\mathcal{R}_2}\right) = 0, \tag{B1}$$

where $\mathcal{G}$ is, for the time being, an unknown dimensionless function of dimensionless quantities. Other dimensionless quantities can be formed, but they are not linearly independent of those entering (B1). We cannot make any general statements of significance for the form (B1). However, in the limit $\mathcal{R}_1 \ll \mathcal{R}_2$, we expect $\mathcal{G}$ to be essentially independent of the ratio $\mathcal{R}_1/\mathcal{R}_2$. In that case, the relation (B1) can be inverted to give

$$P_2 = \frac{\mathcal{R}_2^{2/3}}{\epsilon^{1/3}}\mathcal{P}_2\left(t\frac{\epsilon^{1/3}}{\mathcal{R}_2^{2/3}}\right). \tag{B2}$$

The scaling of this probability density is the same as for P, as discussed in Secs. III B and IV B, but the physical meaning of P_2 is of course different. We are still not able to make general statements concerning $\mathcal{P}_2$, but we can argue for a scaling of the average transition time as $\langle t \rangle \sim \mathcal{R}_2^{2/3}/\epsilon^{1/3}$. This result is related to the standard form of the Richardson law[28] for relative diffusion, $\langle r^2 \rangle \sim t^3 \epsilon$, as is readily seen by taking the third power of $\langle t \rangle$.

A practical advantage of the form (B2) has been noted.[1,3] Thus, in case an experimental study of relative diffusion is attempted for realistic experimental or numerical conditions, a problem arises because of the finite size of the inertial, or universal, subrange. To obtain the numerical constant C_R appearing in Richardson law for relative mean square particle separations, experimentally[2,13] or numerically,[1,3] a large number of realizations are needed in order to obtain the average value $\langle r^2(t) \rangle$. Even for short times, a significant number of particle pairs entering this average will, however, have a separation which is large and outside the universal subrange. This crossover effect can be avoided by considering a fixed spatial scale, given by $\mathcal{R}_2$ discussed before, and rather taking the average time $\langle t \rangle$ associated with this scale, using only $\mathcal{R}_2$ values inside the universal subrange. It is evident that the numerical constant obtained this way is specific for the fixed scale problem and different from the corresponding constant associated with the fixed time problem. It was demonstrated[1,3] that these two constants can be related by use of Richardson diffusion equation.[28]

[1] G. Boffetta, A. Celani, A. Crisanti, and A. Vulpiani, "Pair dispersion in synthetic fully developed turbulence," Phys. Rev. E **60**, 6734 (1999).
[2] S. Ott and J. Mann, "An experimental investigation of the relative diffusion of particle pairs in three dimensional turbulent flow," J. Fluid Mech. **422**, 207 (2000).
[3] G. Boffetta and I. M. Sokolov, "Relative dispersion in fully developed turbulence: The Richardson law and intermittency corrections," Phys. Rev. Lett. **88**, 094501 (2002).
[4] B. J. Rothschild and T. R. Osborn, "Small-scale turbulence and plankton contact rates," J. Plankton Res. **10**, 465 (1988).
[5] S. Sundby and P. Fossum, "Feeding conditions of arcto-norwegian cod larvae compared with the Rothschild–Osborn theory on small-scale turbulence and plankton contact rates," J. Plankton Res. **12**, 1153 (1990).
[6] T. Kiørboe and E. Saiz, "Planktivorous feeding in calm and turbulent environments, with emphasis on copepods," Mar. Ecol.: Prog. Ser. **122**, 135 (1995).
[7] T. Osborn, "The role of turbulent diffusion for copepods with feeding currents," J. Plankton Res. **18**, 185 (1996).
[8] J. H. Muelbert, M. R. Lewis, and D. E. Kelley, "The importance of small-scale turbulence in the feeding of herring larvae," J. Plankton Res. **16**, 927 (1994).
[9] J. Mann, S. Ott, H. L. Pécseli, and J. Trulsen, "Predator-prey encounters in turbulent waters," Phys. Rev. E **65**, 026304 (2002).
[10] W. Feller, *An Introduction to Probability Theory and its Applications* (Wiley, New York, 1971), Vol. 2.
[11] F. Zernike, "Wahrscheinlichkeitsrechnung und matematische statistik," in *Handbuch der Physik*, edited by R. Geiger and K. C. Scheel (Springer, Berlin, 1928), Vol. 3, pp. 419–492.
[12] H. L. Pécseli, *Fluctuations in Physical Systems* (Cambridge University Press, Cambridge, UK, 2000).
[13] J. Mann, S. Ott, and J. S. Andersen, "Experimental study of relative, turbulent diffusion," Technical Report No. Risø-R-1036(EN), Risø National Laboratory, DK-4000 Roskilde, Denmark, 1999 (can be downloaded from http://www.risoe.dk/rispubl/VEA/ris-r-1036.htm).
[14] J. O. Hinze, *Turbulence*, 2nd ed. (McGraw-Hill, New York, 1975).
[15] P. S. Hill, A. R. M. Nowell, and P. A. Jumars, "Encounter rate by turbulent shear of particles similar in diameter to the Kolmogorov scale," J. Mar. Res. **50**, 643 (1992).
[16] M. R. Maxey and J. J. Riley, "Equation of motion for a small rigid sphere in a nonuniform flow," Phys. Fluids **26**, 883 (1983).
[17] A. Babiano, J. H. E. Cartwright, O. Piro, and A. Provenzale, "Dynamics of a small neutrally buoyant sphere in a fluid and targeting in Hamiltonian systems," Phys. Rev. Lett. **84**, 5764 (2000).
[18] S. B. Pope, "Lagrangian PDF methods for turbulent flows," Annu. Rev. Fluid Mech. **26**, 23 (1994).
[19] B. L. Sawford, "Reynolds number effects in Lagrangian stochastic models of turbulent dispersion," Phys. Fluids A **3**, 1577 (1991).
[20] A. La Porta, G. A. Voth, A. M. Crawford, J. Alexander, and E. Bodenschatz, "Fluid particle accelerations in fully developed turbulence," Nature (London) **409**, 1017 (2001).
[21] A. M. Reynolds, "Third-order Lagrangian stochastic modeling," Phys. Fluids **15**, 2773 (2003).
[22] M. S. Borgas and P. K. Yeung, "Relative dispersion in isotropic turbulence. Part 2. A new stochastic model with Reynolds-number dependence," J. Fluid Mech. **503**, 125 (2004).
[23] J. Mann, S. Ott, H. L. Pécseli, and J. Trulsen, "Experimental studies of occupation times in turbulent flows," Phys. Rev. E **67**, 056307 (2003).
[24] T. C. Granata and T. D. Dickey, "The fluid mechanics of copepod feeding in turbulent flow: A theoretical approach," Prog. Oceanogr. **26**, 243 (1991).
[25] B. R. Mackenzie and T. Kiørboe, "Larval fish feeding and turbulence: A case for the downside," Limnol. Oceanogr. **45**, 1 (2000).
[26] G. Boffetta, A. Celani, and S. Musacchio, "Two-dimensional turbulence in dilute polymer solutions," Phys. Rev. Lett. **91**, 034501 (2003).
[27] E. Buckingham, "On physically similar systems; illustrations of the use of dimensional equations," Phys. Rev. **4**, 345 (1914).
[28] L. F. Richardson, "Atmospheric diffusion shown as a distance-neighbour graph," Proc. R. Soc. London, Ser. A **110**, 709 (1926).

II

Examination of the τ_1/τ_3 ratio provides an even clearer picture; this ratio is calculated to be 3.3 from the MD simulations, in good agreement with the extended jump model prediction of 4.0, whereas the purely diffusive model yields a value of 6 (*27*).

Therefore the extended jump model, whose parameters are determined in the accompanying simulations, is shown to be fully consistent with the experimental reorientation times and is clearly supported by MD simulations. These results thus call for a reinterpretation of the many experimental data for which water rotation is assumed to be purely diffusive in character.

Further confirmation of the molecular mechanism presented here could emerge from the resolution of the remaining controversial issues for water reorientation, such as the experimental isotope effect in the reorientation times (*15*), and a possible laser OH excitation frequency dependence of the reorientation times (*12*, *13*, *15*) and angular displacement (*28*).

References and Notes

1. D. Eisenberg, W. Kauzmann, *The Structure and Properties of Water* (Oxford Clarendon, London, 1969).
2. B. Bagchi, *Chem. Rev.* **105**, 3197 (2005).
3. I. Ohmine, H. Tanaka, *Chem. Rev.* **93**, 2545 (1993).
4. C. J. Fecko, J. D. Eaves, J. J. Loparo, A. Tokmakoff, P. L. Geissler, *Science* **301**, 1698 (2003).
5. R. Rey, K. B. Møller, J. T. Hynes, *J. Phys. Chem. A* **106**, 11993 (2002).
6. K. Ando, J. T. Hynes, *J. Mol. Liq.* **64**, 25 (1995).
7. K. Ando, J. T. Hynes, *Adv. Chem. Phys.* **110**, 381 (1999).
8. D. Marx, M. E. Tuckerman, J. Hutter, M. Parrinello, *Nature* **397**, 601 (1999).
9. N. Agmon, *Chem. Phys. Lett.* **244**, 456 (1995).
10. S. H. Chen, J. Teixeira, *Adv. Chem. Phys.* **64**, 1 (1986).
11. S. Woutersen, U. Emmerichs, H. J. Bakker, *Science* **278**, 658 (1997).
12. C. P. Lawrence, J. L. Skinner, *J. Chem. Phys.* **118**, 264 (2003).
13. H. S. Tan, I. R. Piletic, M. D. Fayer, *J. Chem. Phys.* **122**, 174501 (2005).
14. C. J. Fecko, J. J. Loparo, S. T. Roberts, A. Tokmakoff, *J. Chem. Phys.* **122**, 054506 (2005).
15. Y. L. A. Rezus, H. J. Bakker, *J. Chem. Phys.* **123**, 114502 (2005).
16. K. Winkler, J. Lindner, H. Bürsing, P. Vöhringer, *J. Chem. Phys.* **113**, 4674 (2000).
17. C. Rønne, P. O. Åstrand, S. R. Keiding, *Phys. Rev. Lett.* **82**, 2888 (1999).
18. D. van der Spoel, P. J. van Maaren, H. J. C. Berendsen, *J. Chem. Phys.* **108**, 10220 (1998).
19. A. Luzar, D. Chandler, *Nature* **379**, 55 (1996).
20. J. D. Eaves *et al.*, *Proc. Natl. Acad. Sci. U.S.A.* **102**, 13019 (2005).
21. In Csajka and Chandler's paper on some aspects of H-bond breaking in water (as opposed to reorientation), jumps occur in producing a predefined broken H-bond final state, which is an unstable state, without a new partner in most cases and with the former accepting water still in the first hydration shell (*31*). This process is to be distinguished from that of the present work, where jumps terminate in a new stable state, with a new partner, and with the former partner now in the second hydration shell (Fig. 1).
22. F. Sciortino, A. Geiger, H. E. Stanley, *Nature* **354**, 218 (1991).
23. F. N. Keutsch, R. J. Saykally, *Proc. Natl. Acad. Sci. U.S.A.* **98**, 10533 (2001).
24. E. N. Ivanov, *Sov. Phys. JETP* **18**, 1041 (1964).
25. I. M. Svishchev, P. G. Kusalik, *J. Phys. Chem.* **98**, 728 (1994).
26. A. Szabo, *J. Chem. Phys.* **81**, 150 (1984).
27. The τ_3 time is currently available only through MD simulations, but promising time-resolved hyper-Rayleigh scattering techniques should allow its determination for water in the near future (*32*).
28. G. Gallot *et al.*, *J. Chem. Phys.* **117**, 11301 (2002).
29. A. Wallqvist, B. J. Berne, *J. Phys. Chem.* **97**, 13841 (1993).
30. P. Madden, D. Kivelson, *Adv. Chem. Phys.* **56**, 467 (1984).
31. F. S. Csajka, D. Chandler, *J. Chem. Phys.* **109**, 1125 (1998).
32. T. Buckup, personal communication.

33. This work has been supported by the CNRS and NSF grant CHE-0417570.

2 November 2005; accepted 12 January 2006
Published online 26 January 2006;
10.1126/science.1122154
Include this information when citing this paper.

The Role of Pair Dispersion in Turbulent Flow

Mickaël Bourgoin,[1] Nicholas T. Ouellette,[2] Haitao Xu,[2,3] Jacob Berg,[4] Eberhard Bodenschatz[2,3]*

Mixing and transport in turbulent flows—which have strong local concentration fluctuations—are essential in many natural and industrial systems including reactions in chemical mixers, combustion in engines and burners, droplet formation in warm clouds, and biological odor detection and chemotaxis. Local concentration fluctuations, in turn, are intimately tied to the problem of the separation of pairs of fluid elements. We have measured this separation rate in an intensely turbulent laboratory flow and have found, in quantitative agreement with the seminal predictions of Batchelor, that the initial separation of the pair plays an important role in the subsequent spreading of the fluid elements. These results have surprising consequences for the decay of concentration fluctuations and have applications to biological and chemical systems.

Turbulent mixing of liquids and gasses is ubiquitous in nature (*1*); it is the basis of all industrial fluid mixing processes, and it determines the spread of pollutants or bioagents in the atmosphere (*2*) and oceans (*3*). Biological organisms in marine ecosystems also exploit it for their survival (*4*–*6*). A crucial component of turbulent mixing is the fluctuation of local concentration. The rate of destruction of ozone in the atmosphere, for example, is largely determined by these fluctuations rather than by the mean concentration (*7*), as is the toxicity of gas leaks or air pollution. It is natural to relate these concentration fluctuations to the separation of two nearby fluid elements; i.e., pair dispersion (*8*, *9*).

In a quiescent fluid, the relative dispersion of two fluid elements (or tracer particles) is dominated by diffusion. The particles undergo Brownian motion, and the mean square separation between them grows linearly in time. In a turbulent flow, however, if the two particles are separated by distances smaller than the characteristic size of the largest eddies in the flow, they will separate faster (superdiffusively). At large separation times and distances, the local correlations responsible for the superdiffusive separation will no longer be present, and, on average, the relative dispersion will again be linear in time.

Despite almost 80 years of scientific inquiry into relative dispersion (*2*, *9*–*17*), no clear experimental verification of the theoretical predictions has emerged. One critical unresolved question is the extent to which the initial separation of the fluid particles influences their subsequent motion. Our measurements in a laboratory water flow (*18*, *19*) in very intense turbulence suggest that the initial separation remains important for all but the most violent flows on Earth. This observation has consequences for such varied problems as pollution control; combustion modeling; hazardous chemical control; and even the understanding of how animals locate food, predators, and mates (*5*, *6*).

We measured relative dispersion in a water flow at high turbulence levels by using optical particle tracking. This technique has been used for a number of years in turbulence research (*13*, *20*) but was limited to the measurement of low–turbulence level flows, because tracer-particle motions must be resolved over times comparable to the smallest time scale of the turbulence [i.e., the Kolmogorov time scale $\tau_\eta = (\nu/\varepsilon)^{1/2}$, where ν is the kinematic viscosity and ε is the energy dissipation rate per unit mass]. In intense turbulence, these times are often very small. The turbulence level is generally quantified by the Reynolds number, which measures the ratio of the nonlinear inertial forces to the linear viscous forces. Here we report the Reynolds number based on the Taylor microscale, $R_\lambda = \sqrt{(15u'L/\nu)}$,

[1]Laboratoire des Écoulements Géophysiques et Industriels–CNRS (Unité Mixte de Recherche 5519), Boite Postale 53-38041, Grenoble Cedex 9, France. [2]Laboratory of Atomic and Solid State Physics, Cornell University, Ithaca, NY 14853, USA. [3]Max Planck Institute for Dynamics and Self-Organization, Göttingen, Germany. [4]Risø National Laboratory, DK-4000 Roskilde, Denmark.

*To whom correspondence should be addressed. E-mail: eberhard.bodenschatz@ds.mpg.de

where u' is the root mean square (rms) velocity of the turbulent fluctuations and L is the largest length scale of the turbulence. In our water flow at $R_\lambda = 815$, which is the highest Reynolds number reported in this work, $\tau_\eta = 0.54$ ms; therefore, very fast detectors must be used to resolve the fine structure of the flow. Previously, by using silicon strip detectors from high-energy physics experiments (*18*, *19*), we extended the particle tracking technique to flows with high turbulence levels. Such detectors, however, are unsuitable for measuring the statistics of many tracer particles at once. We therefore used three Phantom v7.1 digital cameras from Vision Research, Inc. (Wayne, NJ), which record 27,000 pictures per second at a resolution of 256 × 256 pixels (Fig. 1A). This camera system can be used to track several hundred particles at once (*21*). An example of two such simultaneously measured particle tracks is shown in Fig. 1B.

We generated turbulence between coaxial counter-rotating baffled disks in a closed chamber with a volume of approximately 0.1 m^3 (Fig. 1A). We made measurements in a subvolume of roughly 5 × 5 × 5 cm^3 in the center of the tank, where the mean flow is statistically zero. Polystyrene tracer particles 25 μm in diameter, comparable to the Kolmogorov length scale $\eta = (\nu^3/\varepsilon)^{1/4}$, which is the smallest scale of the turbulence, were illuminated by two frequency-doubled, pulsed Nd–yttrium-aluminum-garnet (Nd:YAG) lasers, with a combined power of roughly 150 W. The particle positions were measured with a precision of roughly 0.1 pixels (*21*), corresponding to about 20 μm in the flow. Further description of this flow has been reported previously (*18*, *19*).

By analyzing our measured particle tracks, we investigated the time evolution of the mean square separation between two fluid elements. Predictions for the superdiffusivity of this pair dispersion in turbulence date back to 1926, when Richardson (*10*) suggested that it should grow in time as t^3. By applying Kolmogorov's scaling theory (*22*), Obukhov (*23*) specified that in the inertial range of turbulence, where the only relevant flow parameter is the energy dissipation rate per unit mass ε, the pair dispersion should grow as $g\varepsilon t^3$, where g is a universal constant. Batchelor (*11*) refined this work, predicting that the mean square separation should grow as t^2 for times shorter than a characteristic timescale t_0, which depends on the initial separation of the pair.

By defining $\Delta(t)$ as the separation of two fluid elements at time t and defining Δ_0 as the initial separation between the fluid elements, Batchelor predicted that for Δ_0 in the inertial range

$$\left\langle \left[\vec{\Delta}(t) - \vec{\Delta}_0\right]^2 \right\rangle = \frac{11}{3} C_2 (\varepsilon \Delta_0)^{2/3} t^2 \quad \text{for } t < t_0 = \left(\frac{\Delta_0^2}{\varepsilon}\right)^{1/3} \tag{1}$$

where C_2 is the universal constant in the inertial range scaling law for the Eulerian second-order velocity structure function with a well-known value of approximately 2.13 (*24*). In the classical cascade model of turbulence, t_0 may be identified as the time for which the two fluid elements "remember" their initial relative velocity as they move in the same eddy of size Δ_0. At times on the order of t_0, this eddy breaks up, and the growth of the pair separation is expected to undergo a transition to Richardson-Obukhov scaling.

To distinguish between Batchelor and Richardson-Obukhov scaling, the inertial range must be large, so that there will be a large separation between the eddy turnover time T_L and the Kolmogorov time τ_η. To achieve such a wide range of scales, the turbulence level must be high because $R_\lambda \sim (T_L/\tau_\eta)$. Based on evidence from direct numerical simulation (*25*), a turbulence level of at least $R_\lambda = 600$ to 700 is required to see true inertial range scaling of a Lagrangian quantity such as relative dispersion. Previous experimental and computational studies of dispersion have been limited by their low turbulence levels ($R_\lambda < 300$) (*12*–*15*, *17*) and have not been conclusive. High turbulence levels are obtained in kinematic simulation models (*16*), but such models may not be suited to the pair dispersion problem (*26*).

Figure 2 shows measurements of relative dispersion for turbulence levels up to $R_\lambda = 815$. We found that for experimentally accessible initial separations, our data scales as t^2 for more than two decades in time, with no hint of classical Richardson-Obukhov t^3 scaling. This behavior holds throughout the entire

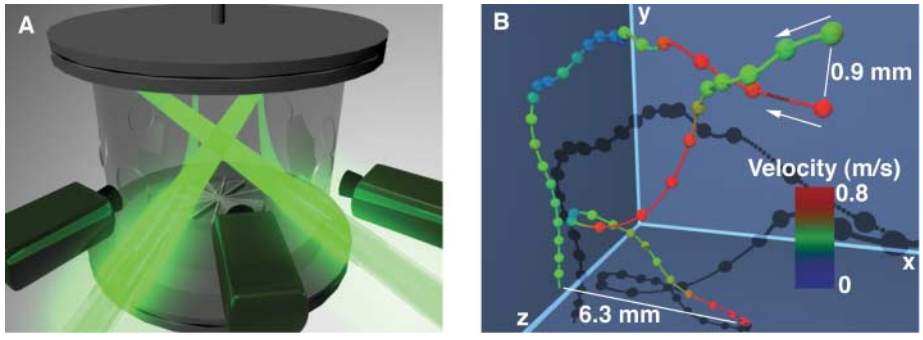

Fig. 1. (**A**) Sketch of the experimental setup. Three high-speed cameras were used to record the three-dimensional tracks of tracer particles in intense turbulence. The particles were illuminated by two high-power lasers. (**B**) A pair of measured particle trajectories at $R_\lambda = 690$. The small spheres mark every other measured position of the particles and are separated by 0.074 ms ($\approx\tau_\eta/13$) in time; the large spheres mark every 30th position. The color of the spheres indicates the magnitude of each particle's absolute velocity in units of m/s. The particles enter the measurement volume as indicated by the arrows and separate under the influence of the turbulence.

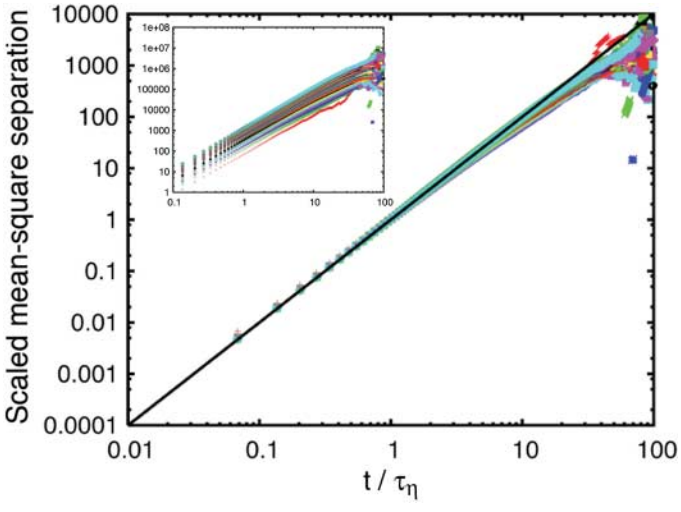

Fig. 2. Evolution of the mean square particle separation. The mean square separation between particle pairs is plotted against time for 50 different initial separations at a turbulence level of $R_\lambda = 815$, with the time axis normalized by the Kolmogorov scales. Each curve represents a bin of initial separations 1 mm wide ($\approx 43\eta$), ranging from 0 to 1 mm to 49 to 50 mm. The curves are scaled by the constant $(\frac{11}{3})C_2(\varepsilon\Delta_0)^{2/3}$ (Eq. 1). The data collapse onto a single universal power law. The bold black line is the power law predicted by Batchelor (*11*). Because the smallest Δ_0 measured is not in the inertial range, we do not expect it to scale perfectly as t^2, and indeed it does not scale as well as the larger Δ_0. The inset shows the same curves scaled simply by the Kolmogorov length, for which we see no scale collapse. For both plots, we see no Richardson-Obukhov t^3 scaling.

inertial range, even for large initial separations (up to 70% of the largest length scale of the turbulence). When we scaled our relative dispersion data by the constant predicted by Batchelor, given in Eq. 1, the curves collapsed onto a single t^2 power law. The line drawn in Fig. 2 is $(\frac{11}{3})C_2(\varepsilon\Delta_0)^{2/3}t^2$.

In Fig. 2, where time is plotted in units of τ_η, the data for different initial separations deviate from the t^2 law at times that vary with Δ_0. If, however, we scale time by Batchelor's $t_0 = (\Delta_0^2/\varepsilon)^{1/3}$ (Fig. 3), the data for each initial separation deviate from Batchelor's prediction at the same universal value of roughly 0.1 t_0, irrespective of turbulence level.

For the quantities plotted in Figs. 2 and 3, we see no Richardson-Obukhov t^3 scaling. We also, however, measured other statistics that, dimensionally, should obey the same scaling laws. One such quantity is exit time statistics (*14*). Our measurements of such statistics showed no clear t^3 behavior. Another measure of relative dispersion is shown in Fig. 4, in which we plot $(\langle\Delta^{2/3}\rangle - \Delta_0^{2/3})$ scaled by $\Delta_0^{2/3}$ as a function of t/t_0. For small initial separations for which (T_L/t_0) is of order 10, we see a transition to a scaling law consistent with the Richardson-Obukhov prediction for times greater than roughly t_0, irrespective of turbulence level. For larger initial separations for which (T_L/t_0) is smaller, however, no such scaling is seen, as shown in the inset to Fig. 4. The existence of a transition at times on the order of t_0 shows that the initial separation is an important parameter for relative dispersion and cannot be neglected.

In any practical application of relative dispersion, the initial source will have finite size and therefore have a nonzero Δ_0. Our data show that t_0 accurately quantifies the transition between the Batchelor scaling regime and the Richardson-Obukhov regime. Consequently, a clear t^3 scaling law requires not only a large separation between T_L and τ_η but also a large separation between T_L and t_0. For the initial separations accessible in our experiments, the maximum value of the ratio of (T_L/t_0) was of order 10, with no fully developed t^3 scaling. In order to apply the Richardson-Obukhov scaling law to a practical situation, then, (T_L/t_0) must be much larger than 10, which implies the necessity of a high turbulence level.

For most flows on Earth, both natural and industrial, the turbulence levels are quite small: typically, $R_\lambda < 1000$. Very turbulent atmospheric flows, such as warm clouds or the atmospheric boundary layer (*27*), have turbulence levels of about $R_\lambda \sim 10^4$. Even the most violent flows on Earth, such as plinian volcanic eruptions, have similar turbulence levels. If we consider a pair of particles with an initial separation of roughly 1 m, such as might be found in the smokestack of an industrial plant, for a turbulence level of $R_\lambda \sim 10^4$, (T_L/t_0) is only about 30, assuming typical atmospheric flow parameters (*28*).

An important consequence of these results is that in almost all flows with industrial or biological significance, the initial separation Δ_0 will influence the subsequent spreading of the two fluid elements throughout the entire period of their turbulent superdiffusive separation. This can explain, for example, measurements of the decay of the fluctuations of a passive scalar injected into the flow (*29*). This decay became slower as the separation between two sources was increased. These results may, in turn, explain why the spatial arrangement of odor sources plays such an important role in the way crayfish and other crustaceans, as well as organisms both larger and smaller (*6*), navigate their marine environments (*5*).

We observed that Batchelor's prediction is fulfilled for more than two decades in time at high turbulence levels. Although our data may be somewhat contaminated by the inhomogeneity and anisotropy present in our specific flow, the observed scale collapse onto the Batchelor law appears very robust. In addition, we showed that the initial separation of the particle pair remains important in most flows in nature up to times of order t_0, which itself depends on the initial separation. We observed a transition near t_0 only when (T_L/t_0) was of order 10 or larger. Therefore, a large separation between T_L and t_0 is required to see a fully developed Richardson-Obukhov scaling regime, requiring a turbulence level beyond the reach of current experiments and higher than will occur in most practical situations.

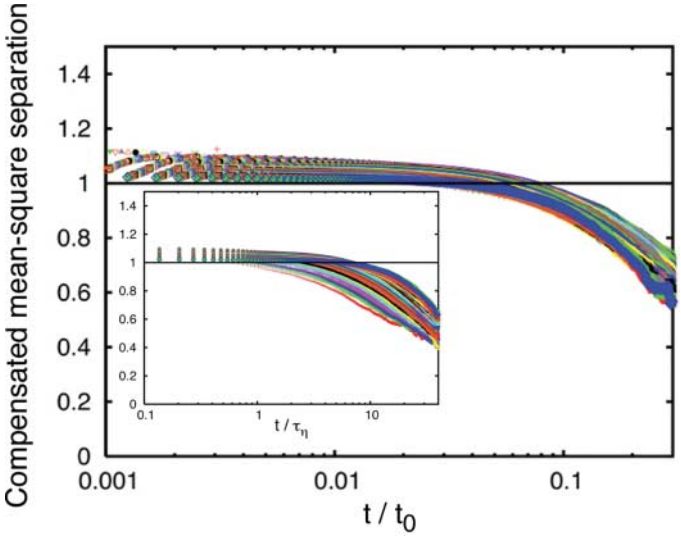

Fig. 3. Mean square separation with time scaled by t_0. The mean square separation at $R_\lambda = 815$ compensated by Batchelor's scaling law (Eq. 1) is plotted against time in units of $t_0 = (\Delta_0^2/\varepsilon)^{1/3}$. Plotted in this way, a plateau corresponds to Batchelor scaling. The inset shows the same compensated data plotted against time and scaled by the Kolmogorov time. The data clearly collapse significantly better with time scaled by t_0. The data begin to deviate from a t^2 power law at a universal time of about 0.1 t_0.

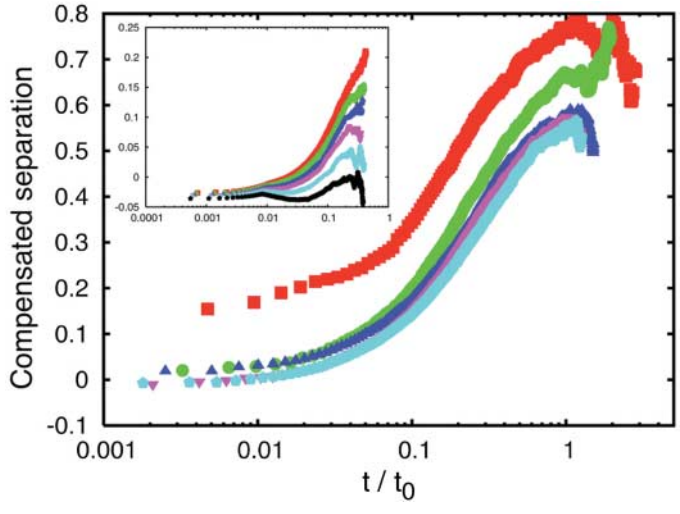

Fig. 4. $[\langle\Delta(t)^{2/3}\rangle - \Delta_0^{2/3}]$ scaled by $\Delta_0^{2/3}$ and compensated by t/t_0. The data are plotted against t/t_0; a plateau denotes Richardson-Obukhov–like scaling. The initial separation increases from 1 mm (≈43η) for the top curve to 5 mm (≈215η) for the bottom curve, and (T_L/t_0) is of order 10. The inset shows the same quantity plotted against t/t_0 for larger initial separations, ranging from 20 mm (≈860η) for the top curve to 30 mm (≈1290η) for the bottom curve.

References and Notes

1. B. I. Shraiman, E. D. Siggia, *Nature* **405**, 639 (2000).
2. M. Huber, J. C. McWilliams, M. Ghil, *J. Atmos. Sci.* **58**, 2377 (2001).

3. P. S. Berloff, J. C. McWilliams, A. Bracco, *J. Phys. Oceanogr.* **32**, 764 (2002).
4. J. B. Joergensen, J. Mann, S. Ott, H. L. Pécseli, J. Trulsen, *Phys. Fluids* **17**, 035111 (2005).
5. M. C. Wolf, R. Voigt, P. A. Moore, *J. Chem. Ecol.* **30**, 501 (2004).
6. P. Moore, J. Crimaldi, *J. Mar. Syst.* **49**, 55 (2004).
7. S. Edouard, B. Legras, F. Lefèvre, R. Eymard, *Nature* **384**, 444 (1996).
8. M. Nelkin, R. M. Kerr, *Phys. Fluids* **24**, 1754 (1981).
9. B. Sawford, *Annu. Rev. Fluid Mech.* **33**, 289 (2001).
10. L. F. Richardson, *Proc. R. Soc. London Ser. A* **110**, 709 (1926).
11. G. K. Batchelor, *Q. J. R. Meterol. Soc.* **76**, 133 (1950).
12. P. K. Yeung, *Phys. Fluids* **6**, 3416 (1994).
13. S. Ott, J. Mann, *J. Fluid Mech.* **422**, 207 (2000).
14. G. Boffetta, I. M. Sokolov, *Phys. Rev. Lett.* **88**, 094501 (2002).
15. P. K. Yeung, M. S. Borgas, *J. Fluid Mech.* **503**, 93 (2004).
16. F. Nicolleau, G. Yu, *Phys. Fluids* **16**, 2309 (2004).
17. L. Biferale *et al.*, *Phys. Fluids* **17**, 115101 (2005).
18. A. La Porta, G. A. Voth, A. M. Crawford, J. Alexander, E. Bodenschatz, *Nature* **409**, 1017 (2001).
19. G. A. Voth, A. La Porta, A. M. Crawford, J. Alexander, E. Bodenschatz, *J. Fluid Mech.* **469**, 121 (2002).
20. M. Virant, T. Dracos, *Meas. Sci. Technol.* **8**, 1539 (1997).
21. N. T. Ouellette, H. Xu, E. Bodenschatz, *Exp. Fluids* **40**, 301 (2006).
22. A. N. Kolmogorov, *Dokl. Akad. Nauk SSSR* **30**, 301 (1941).
23. A. M. Obukhov, *Izv. Akad. Nauk SSSR* **5**, 453 (1941).
24. K. R. Sreenivasan, *Phys. Fluids* **7**, 2778 (1995).
25. P. K. Yeung, *Annu. Rev. Fluid Mech.* **34**, 115 (2002).
26. D. J. Thomson, B. J. Devenish, *J. Fluid Mech.* **526**, 277 (2005).
27. S. Kurien, K. R. Sreenivasan, *Phys. Rev. E* **64**, 056302 (2001).
28. R. A. Shaw, *Annu. Rev. Fluid Mech.* **35**, 183 (2003).
29. Z. Warhaft, J. L. Lumley, *J. Fluid Mech.* **88**, 659 (1978).
30. This research was supported by the Physics Division of NSF and by the Max Planck Society. We thank L. Collins, G. Falkovich, J. Hunt, J. Schumacher, D. Vincenzi, and Z. Warhaft for helpful discussions and suggestions over the course of this work.

24 October 2005; accepted 5 January 2006
10.1126/science.1121726

Late Quaternary Atmospheric CH_4 Isotope Record Suggests Marine Clathrates Are Stable

Todd Sowers

One explanation for the abrupt increases in atmospheric CH_4, that occurred repeatedly during the last glacial cycle involves clathrate destabalization events. Because marine clathrates have a distinct deuterium/hydrogen (D/H) isotope ratio, any such destabilization event should cause the D/H ratio of atmospheric CH_4 (δD_{CH_4}) to increase. Analyses of air trapped in the ice from the second Greenland ice sheet project show stable and/or decreasing δD_{CH_4} values during the end of the Younger and Older Dryas periods and one stadial period, suggesting that marine clathrates were stable during these abrupt warming episodes. Elevated glacial δD_{CH_4} values may be the result of a lower ratio of net to gross wetland CH_4 emissions and an increase in petroleum-based emissions.

The ice core record of atmospheric CH_4 changes covering the past 650,000 years exhibits two primary frequencies. Over long time scales (greater than 10,000 years) atmospheric CH_4 changes have a substantial amount of variance concentrated in the precessional bandwidth (19,000 and 23,000 years) (*1*, *2*) that is considered to be an integral part of tropical climate throughout the late Pleistocene. One hypothesis that accounts for this observation involves an energized hydrologic cycle during periods of elevated low-latitude insolation. The invigorated hydrologic cycle promotes an increase in wetland extent driving a concomitant increase in CH_4 emissions that raise atmospheric CH_4 levels during warm periods. Embedded within the precession signal are millennial- and century-scale variations that are tightly coupled to Greenland temperature (*3*, *4*). In general, increasing atmospheric CH_4 levels are synchronous with, or slightly lag (by a few decades), the surface temperature increase over Greenland (*5*). Assessing the nature of these abrupt CH_4 events is important for understanding how ecosystems and climate are connected and in estimating the degree to which future CH_4 levels may contribute to changes in Earth's radiation budget.

There are two competing explanations for the abrupt CH_4 increases. One hypothesis holds that the terrestrial biosphere is capable of rapidly increasing CH_4 emissions in response to abrupt changes in the hydrologic cycle that are teleconnected to surface temperatures over Greenland (*3*, *4*). The other explanation involves the sudden release of marine clathrates situated along the continental margin where episodic destabilization events may have been triggered by enhanced ventilation (warming) of upper thermocline waters (*6*). The majority of the released CH_4 ultimately travels across the air-sea interface leading to atmospheric CH_4 increases.

Model estimates of changes in the primary CH_4 sink (tropospheric hydroxyl radical) during the last glacial termination suggest that the observed CH_4 variations must be due in large part to changes in the sources as opposed to changes in the rate of removal (*7*). The isotopic composition of atmospheric CH_4 therefore provides additional information on the relative contribution of the various sources. Variations in the D/H ratio of atmospheric CH_4 (δD_{CH_4}) can be used to infer variable clathrate contributions on the basis of their elevated δD values compared with all terrestrial CH_4 sources (Fig. 1). Methane clathrates within the continental margin sediments are formed almost exclusively by CO_2 reduction or thermal cracking of longer chain hydrocarbons, whereas terrestrial CH_4 emissions are primarily aceticlastic in nature (*8*, *9*). During CO_2 reduction, all the methyl hydrogen atoms come directly from porewater H_2 that is in isotopic equilibrium with the porewater (*10*). The resulting δD_{CH_4} values are lower than the porewater δD_{H_2O} due to a ~180 per mil (‰) biologically induced isotope effect associated with CO_2 reduction (*9*, *11*). Marine clathrate δD_{CH_4} values from 13 nearshore sites scattered throughout the Northern Hemisphere are surprisingly constant (–189 ± 27‰; error is SD) given the diverse nature of the geologic and sedimentologic settings and the varying proportions of microbial and thermogenic CH_4 at each site (*12*, *13*). In contrast, CH_4 production in terrestrial ecosystems is dominated by acetogenesis (acetate fermentation) where three-fourths of the hydrogen atoms in the emitted methane originate from the methyl group associated with the acetate substrate. The remaining hydrogen comes from the local water with the resulting terrestrial δD_{CH_4} values generally ranging from –250 to –380‰, with the local δD_{CH_4} value strongly influenced by the δD of precipitation (*8*, *9*).

An atmospheric δD_{CH_4} record (Fig. 2) was generated from the second Greenland ice sheet project (GISP II) ice core using a previously described technique with an external precision of ±4.2‰ (*14*). The general picture of δD_{CH_4} variations associated with the deglaciation shows a progressive decrease in δD_{CH_4} as the concentration of CH_4 increases, opposite to that predicted by increasing clathrate contributions due to warming associated with the termination. During the last glacial maximum (LGM), δD_{CH_4} values were generally ~5‰ higher than the Bolling/Allerod values [15 to 13 thousand years ago (ka)] and ~20‰ higher than early Holocene values. There are three factors that can be reasonably constrained as contributing to the elevated δD_{CH_4} values during the LGM. All three factors are temperature dependent, so

Department of Geosciences and the Earth and Environmental Systems Institute, Pennsylvania State University, University Park, PA 16802, USA. E-mail: sowers@geosc.psu.edu

III

Backwards and forwards relative dispersion in turbulent flow: An experimental investigation

Jacob Berg,* Beat Lüthi, Jakob Mann, and Søren Ott
Risø National Laboratory, 4000 Roskilde, Denmark
(Received 3 January 2006; revised manuscript received 23 May 2006; published 27 July 2006)

From particle tracking velocimetry we present an experimental measure of the ratio between backwards and forwards relative dispersion in an intermediate Reynolds number turbulent flow. Lack of time-reversal symmetry implies that their ratio may be different from 1. From a stochastic model, this has recently been studied by Sawford *et al.* [Phys. Fluids **17**, 095109 (2005)] giving ratios between 5 and 20. We find a value of approximately 2 and discuss it in the context of the characteristics of the rate of strain tensor s_{ij}. An analysis of a direct numerical simulation by Biferale *et al.* [Phys. Rev. Lett. **93**, 064502 (2004) and Phys. Fluids **17**, 021701 (2004)] gives the same result.

DOI: 10.1103/PhysRevE.74.016304 PACS number(s): 47.27.tb, 47.27.Gs

I. INTRODUCTION

Turbulence is the state of fluid flow far from its equilibrium laminar state. It is governed by the Navier-Stokes equation and is highly nonlinear. Although there have been many attempts, Kolmogorov's four-fifths law [1] is still the only result derived rigorously from the Navier-Stokes equation. An important aspect of turbulence is its ability to efficiently transport and mix matter, heat, and momentum. Relative dispersion describes the separation in time of nearby fluid particles. Transport and mixing properties in turbulent flow are therefore associated with this phenomenon.

Richardson [2] was the first to analyze relative dispersion. He linked the problem to a diffusion equation and empirically derived a scale-dependent eddy diffusivity of a cloud of fluid elements. Obukhov [3] later refined the theory relating the mean-square separation of an initially close pair of fluid elements to the kinetic energy dissipation ε of the flow,

$$\langle r^2 \rangle = g \varepsilon t^3. \tag{1}$$

The Richardson law expressed in Eq. (1) is supposed to be valid in the inertial range where influences from the large-scale forcing and small-scale viscous effects can be neglected. The Richardson-Obukhov constant g seems to be a function of Reynolds number Re_λ presumably with an asymptotic limit at high Reynolds number [4].

The Lagrangian nature of turbulent pair separation makes computational and experimental tests very difficult since a large separation of temporal scales is needed. Yeung [5] concluded based on extrapolations from low Re_λ direct numerical simulation (DNS) data that at least $\mathrm{Re}_\lambda \sim 600-700$ is needed. Previous studies at moderate Re_λ [6–9] have, however, succeeded in providing insight into the Richardson law, although a definitive scaling has hardly been observed.

A striking feature of hydrodynamical turbulence compared to a Gaussian flow is the existence of nonzero odd moments of the distributions of velocity differences: the structure functions. The four-fifths law is the most well known example of this. It implies that time reversibility breaks down in the inertial range.

A consequence is that if you follow the separation of two fluid elements forward in time, then follow the same two particles backward in time, the latter separation will occur at a different speed. In mixing applications this could play a significant role.

Calculating the future width of a puff released at time $t=0$ is a classical forwards dispersion problem. If, on the other hand, one wants to calculate the fluctuations in some scalar concentration at some time t, one will have to follow the particles backwards in time: the different trajectories carry different scalar concentrations from the past.

This forward/backward asymmetry was, however, only recently emphasized by Sawford *et al.* [10]. They noticed that both processes can be described with the Richardson law with different values of the constant g. They investigated two different Lagrangian stochastic models for relative dispersion in the inertial range and concluded that the process of backwards dispersion was much faster than the corresponding forward case. This has implications for practical calculations of turbulent mixing, such as, for example, combustion and pollution.

On an experimental level, no evidence of the asymmetry has been reported. In this paper, we will present an analysis of an intermediate Reynolds number flow. Sawford *et al.* [10] noticed the high computational costs for studying DNS data. We have, however, come up with an *easy to do* scheme that avoid this computational problem. DNS data will therefore be analyzed and compared with our experimental findings.

Determining the ratio between the backwards and forwards dispersion defined as g_b/g_f, where g_b and g_f refer to the Richardson-Obukhov constants for the backward and forward case, respectively, is the objective of the present paper.

Sections II and III will go through the technique of particle tracking velocimetry and characterize the experimental flow. In Sec. IV, we will present the results after a short discussion of how to obtain dispersion results in a finite Reynolds number flow. The section will end with a short presentation of DNS data analyzed in the same way as the experimental data. In the Discussion section, we will present some heuristic arguments relating the difference between forwards and backwards relative dispersion to the mechanism of infinitesimal material line stretching taking place in the viscous range. Section VI will conclude with our findings.

*Electronic address: jacob.berg.joergensen@risoe.dk

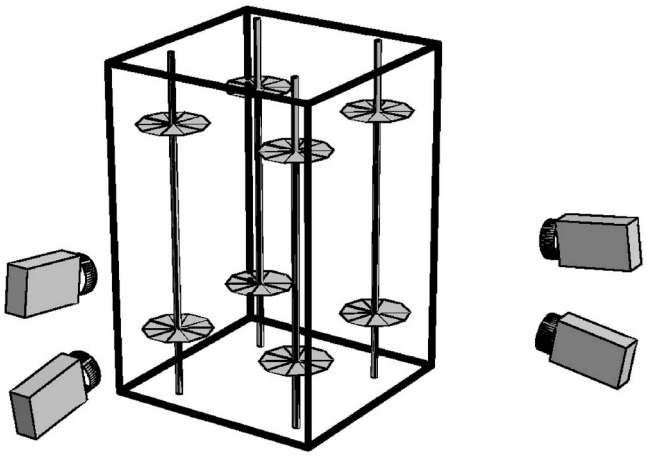

FIG. 1. Experimental setup.

II. EXPERIMENTAL METHOD

We have performed a particle tracking velocimetry (PTV) experiment in an intermediate Reynolds number turbulent flow. Lagrangian trajectories of fluid elements in water are obtained by tracking neutrally buoyant particles in space and time. The flow is generated by eight rotating propellers (which change their rotational direction in fixed intervals) placed in the corners of a tank with dimensions $32\times32\times50$ cm^3 (see Fig. 1).

The data acquisition system consists of four commercial CCD cameras with a maximum frame rate of 50 Hz at 1000×1000 pixels. Two different setups are used. The first covers a measuring volume of roughly $(12\ \text{cm})^3$. Here we use polystyrene particles with size $\sim400\ \mu$m and density very close to 1. We follow $O(1000)$ particles at each time step with a position accuracy of 0.05 pixels corresponding to less than 10 μm. Due to the large particle size and separation, we cannot study viscous effects in this setup. We therefore also use micro tracking where the volume is only $(1\ \text{cm})^3$ in order for the viscous scales to be resolved. In this setup, we use cenosphere particles with size $\sim100\ \mu$m.

In both setups, the Stokes number, τ_I/τ_η (τ_I denotes the inertial relaxation time for the particle to the flow while τ_η is the Kolmogorov time), is much less than 1 and the particles can therefore be treated as passive tracers in the flow. The particles are illuminated by a 250 W stroboscope.

The large volume (macro tracking settings) is used for the main results presented in Sec. IV while the small volume (micro tracking settings) is used only for the heuristic arguments presented in the Discussion section.

The mathematical algorithms for translating two-dimensional (2D) image coordinates from the four camera chips into a full set of three-dimensional (3D) trajectories in time involve several crucial steps: fitting Gaussian profiles to the 2*D* images, stereo matching (line of sight crossings) with a two-media (water-air) optical model, and construction of 3D trajectories in time by using the kinematic principle of minimum change in acceleration [11,12].

III. FLOW PROPERTIES

We study a particular flow at intermediate Reynolds number in the large volume (macro tracking settings). Figure 2 shows the standard deviations of the three velocity components: the two horizontal (radial) $\sigma_{u_x},\sigma_{u_y}$ and the vertical (axisymmetric) σ_{u_z}. The figure shows the standard deviations averaged over three different planes: *yz* plane, *xz* plane [both in panel (a)], and *xy* plane [in panel (b)]. In both panels the two horizontal components are observed to collapse on values around 22 mm/s with almost no dependence on the vertical or the horizontal positions. The vertical component has a dependence on the vertical coordinate z with a minimum $\sigma_{u_z}=15.1$ mm/s at $z=18$ mm indicating the symmetry plane of the flow.

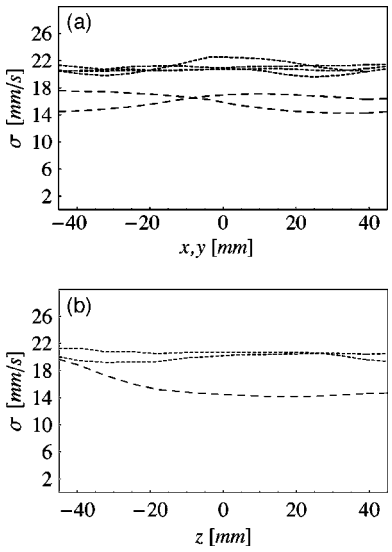

FIG. 2. (a) Standard deviations of the velocity components averaged over the *yz* plane and the *xz* plane. The dotted lines correspond to the radial components while the dashed lines correspond to the axisymmetric vertical component. (b) Same as in (a) but averaged over the *xy* plane.

The turbulence characteristics are given in Table I. The values have been obtained by fitting a von Kármán model to the experimental obtained longitudinal second-order structure function $f(r)\equiv\langle\delta v_\parallel^2(r)\rangle$ [6]. The model fit is shown in Fig. 3(a). The method determines ε with a 10% error. In computing $f(r)$ from data, the averages were taken over all separations $\mathbf{r}$ with $|\mathbf{r}|=r$ within a ball fully inside the measuring volume.

We have measured the normal component of the longitudinal mean acceleration

TABLE I. Macro tracking turbulence characteristics obtained from fits to the von Kármán model. ε is the mean kinetic energy dissipation; $\eta\equiv(\nu^3/\varepsilon)^{1/4}$ is the Kolmogorov length scale with the kinematic viscosity ν of water. $\tau_\eta\equiv(\nu/\varepsilon)^{1/2}$ is the Kolmogorov time scale. The integral length scale is L_{int} while T_L is the integral time scale. $\sigma_u^2=\frac{1}{3}(\sigma_{u_x}^2+\sigma_{u_y}^2+\sigma_{u_z}^2)$ is the standard deviation of velocity. The Reynolds number is defined as $\text{Re}_\lambda=\frac{\lambda\sigma_u}{\nu}$ with the Taylor micro scale $\lambda=\sqrt{\left(\frac{15\nu\sigma^2}{\varepsilon}\right)}$.

η	L_{int}	τ_η	T_L	ε	σ_u	Re_λ
0.25 mm	48 mm	0.07 s	2.45 s	168 mm^2/s^3	23.33 mm/s	172

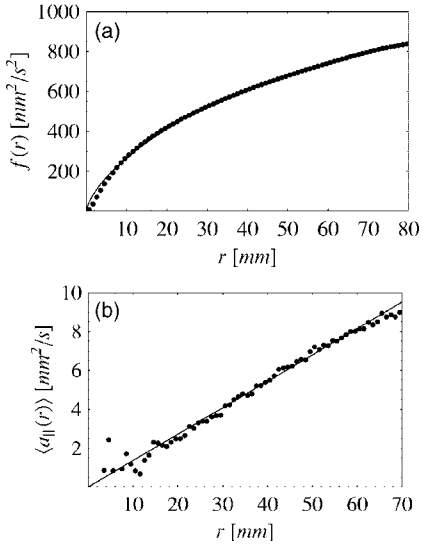

FIG. 3. (a) $f(r)$ with the fitted von Kármán model on top (full line). (b) $\langle \delta a_{\|}(r)\rangle$ with a linear fit.

$$\langle \delta a_{\|}(r)\rangle \equiv \left\langle \delta \mathbf{a}(r) \cdot \frac{\mathbf{r}}{r} \right\rangle \tag{2}$$

between two points separated a distance r. In a globally homogeneous flow, this quantity is zero for all values of r and the second-order structure of the turbulence can be solely described by a single function, namely $f(r)$ [6]. Most real flows are, however, not globally homogeneous and therefore a net mean acceleration may exist. $\langle \delta a_{\|}(r)\rangle$ is plotted in Fig. 3(b). The acceleration is observed to increase linearly. The solid straight line is a linear fit of the form $y(r)=\alpha r+\beta$. Here $\alpha=0.13$ mm/s and β is very close to zero. From the axisymmetric properties of the flow we expect the mean acceleration to be of the form $\delta u^2/r$ so that

$$\alpha r = \langle \delta a_{\|}(r)\rangle = u^2 \quad \Rightarrow \tag{3}$$

$$\phi = \frac{\sqrt{\alpha}}{2\pi} = 0.057 \text{ s}^{-1}, \tag{4}$$

where ϕ is the frequency. Because $\alpha>0$, the flow is straining (in contrast to a full body rotation with $\delta a<0$). Taking the reciprocal of ϕ gives us a characteristic time scale for the straining motion of the order 18 s. This number is much larger than the integral time scale T_L, therefore we do not expect any significant influence of the mean flow on the results presented later.

IV. RESULTS

Recently, Bourgoin *et al.* [13] performed a PTV experiment at $\mathrm{Re}_\lambda \sim 800$. Besides being the PTV experiment with the largest Re_λ so far, it is the first study to shed light on the small time expansion and acknowledge its great importance on relative separation of particles in turbulent flow.

They find a very robust ballistic regime (the mean-square separation is proportional to t^2) for times smaller than the Batchelor time $t_0=(r_0^2/\varepsilon)^{1/3}$. This is the time for which particle pairs are strongly influenced by their initial separation r_0 and can fully be described by the second-order Eulerian structure function. The Richardson law is only valid for times much larger than t_0 and should therefore be independent of initial separations, as long as they are small but still larger than the Kolmogorov scale. It is therefore an asymptotic relation that is approached at infinite Re_λ.

At finite Re_λ we have a relation of the general form

$$\langle r^2\rangle/r_0^2 = \mathcal{F}(t/t_0, \eta/r_0, \mathrm{Re}_\lambda), \tag{5}$$

where we have chosen r_0 and t_0 as scales to make the relation dimensionless. For a given Re_λ the inertial range is found where $t/t_0 \ll T_L/t_0 \propto (\eta/r_0)^{2/3}\mathrm{Re}_\lambda$ and $\eta/r_0 \approx 0$. In the inertial range, therefore, we have

$$\langle r^2\rangle/r_0^2 = \mathcal{F}(t/t_0, 0, \mathrm{Re}_\lambda). \tag{6}$$

We can now, without loss of generality, express $\mathcal{F}$ in terms of the two functions Φ and Θ,

$$\mathcal{F}(t/t_0, 0, \mathrm{Re}_\lambda) \equiv \Phi(t/t_0, \mathrm{Re}_\lambda)[t/t_0 - \Theta(\mathrm{Re}_\lambda)]^3. \tag{7}$$

If there is an asymptotic law for $\mathrm{Re}_\lambda \to \infty$, then $\Theta(\mathrm{Re}_\lambda)$ must approach a constant value and $\Phi(t/t_0, R_\lambda)$ must approach a function $\Phi(t/t_0, \infty)$ in that limit. Substituting $t_0=r_0^{2/3}\varepsilon^{-1/3}$ and letting $\mathrm{Re}_\lambda \to \infty$, we can rewrite the relation as

$$\langle r^2\rangle = \Phi(t\varepsilon^{1/3}r_0^{-2/3}, \infty)\varepsilon[t - r_0^{2/3}\varepsilon^{-1/3}\Theta(\infty)]^3. \tag{8}$$

If we let $r_0 \to 0$, then we arrive at the Richardson law *provided* that $\Phi(x, \infty)$ approaches a constant value $\Phi(\infty, \infty) \equiv g$ as $x \to \infty$, where g is the Richardson-Obukhov constant. This means, on the other hand, that keeping r_0 finite but letting $t \to \infty$ leads to the relation

$$\langle r^2\rangle = \Phi(\infty, \infty)\varepsilon[t - r_0^{2/3}\varepsilon^{-1/3}\Theta(\infty)]^3. \tag{9}$$

Denoting $\Theta(\mathrm{Re}_\lambda)$ T_0, we finally arrive at the finite Reynolds number expression as introduced by Ott and Mann [6],

$$\langle r^2(t)\rangle/r_0^2 = g(t/t_0 - T_0/t_0)^3. \tag{10}$$

When r_0 is in the inertial range, the only available time scale is t_0 so that $T_0=st_0$, where s is independent of r_0. The time shift T_0 is thus a result of processes taking place in the initial phase. When these processes have ceased, and the dispersion has lost its memory of them, the time shift is the only thing that remains—it cannot be removed by any mechanism.

The mixing of viscous and long-range effects in finite Reynolds number turbulence motivated Biferale *et al.* [9] to study exit times. The method is very promising, although it is not possible to determine the Richardson-Obukhov constant without a model for relative separation.

A. PTV

We do not expect to find any significant Richardson-Obukhov scaling. The finiteness of the Reynolds number and of the observational domain are to be held responsible for this. For the latter part: the main effect would be a bias toward lower exponents of t: rapidly separating particles may

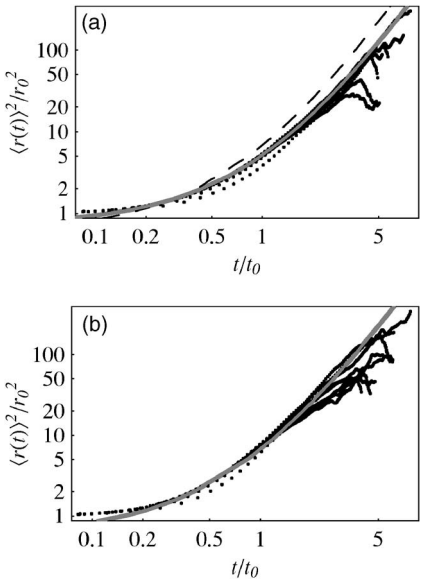

FIG. 4. (a) $\langle r^2(t)\rangle/r_0^2$ as a function of t/t_0 in the forward case. The different dotted lines correspond to different initial separations r_0 from $4-8\,\eta$ to $24-28\,\eta$. A fit to data by Eq. (10) is plotted as the gray solid line. The dashed line is the backward case fit. (b) Backward case.

leave the volume making $\langle r^2(t)\rangle$ smaller than it would have been in an infinite volume. We have tried to reduce this effect by using an observational volume several times the size of the integral length scale as well as only used pairs that start within a small subvolume ($r=30$ mm) of the full observational domain.

We look at particles that start within bins of size $4\,\eta$ corresponding to one millimeter. The largest bin is $24-28\,\eta$ while the smallest is $4-8\,\eta$. In order to make the selection of pairs independent from the previous time step, we define a new pair each time two arbitrarily chosen particles come within the bin size of the initial separation r_0. In this way, the same two particles can contribute to the ensemble many times.

Figure 4 shows $\langle r^2(t)\rangle/r_0^2$ as a function of t/t_0 in the backward and forward case. All bins are included in the two plots. A fit to the data by Eq. (10) is also shown. From around $t\sim 0.2t_0$ the fits agree with data. One curve is, however, observed to fall below the other curves. This is the smallest bin that is not expected to be in the inertial range. For times smaller than $t\sim 0.2t_0$, the separation is not in the inertial range and Eq. (10) is therefore not valid. For large times, all the curves are observed to *drop down*. It happens earlier for curves corresponding to larger bins. This is due to the narrow inertial range as well as finite volume effects, as discussed earlier.

From fits to Eq. (10) we obtain g values of $g_f=0.55\pm0.05$ and $g_b=1.15\pm0.05$ for the forward and backward case, respectively. The error is the rms value for the different r_0. No systematic dependence was found.

The forward value g_f is similar to values obtained from both DNS and experiments [6–9] at different Reynolds numbers. Franzese and Cassiani [4] derive g_f as a function of Reynolds number which saturates slightly above 0.6 for

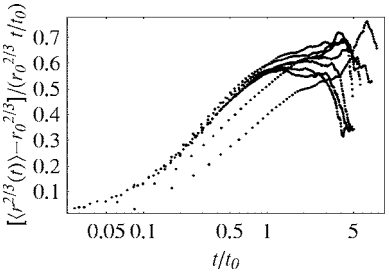

FIG. 5. $(\langle r^{2/3}\rangle - r_0^{2/3})/(r_0^{2/3}t/t_0)$ vs t/t_0. The different curves correspond to the different bins.

$\mathrm{Re}_\lambda\sim 350$. Between $\mathrm{Re}_\lambda\sim 150$ and higher, the function is only very weakly dependent on Re_λ.

The ratio g_b/g_f is 2.09, making it significantly smaller than the ratios found by Sawford *et al.* [10]. Depending on parameter choices in their stochastic models, they predict $g_b/g_f\sim 5-20$. The fact that our inertial range is narrow and that the stochastic models are based on K41 inertial range, scaling arguments might explain some of the discrepancy.

The time shift T_0 in Eq. (10) is $T_0^f=(1.12\pm0.02)t_0$ and $T_0^b=(0.80\pm0.02)t_0$. As expected, it is the same order of magnitude as t_0. Another way of arriving at the result just presented would be to follow the original lines by Ott and Mann [6], where T_0 is obtained as the zero crossing of $\langle r^2(t)\rangle^{1/3}$ with the time axis.

The excellent fit for both backwards and forwards dispersion presented in Fig. 4 supports the existence of the inertial range universal function $\mathcal{F}$ defined in Eq. (6). In our experiment, $\mathcal{F}$ is valid over a decade of t/t_0. We do not claim that we have observed true Richardson scaling. This would mean that all curves representing different bins would collapse on a single straight line in a log-log coordinate system of r versus t with slope 3 (not shown). A very large Reynolds number together with a large observational volume many times the integral scale would be necessary to observe such a regime. The clear difference between the forward and backward case that we observe is, on the other hand, a clear indication that the dynamics is much more complex than purely ballistic motion where forward and backward dispersion are the same.

Bourgoin *et al.* [13] suggested that the inequality $T_L/t_0>10$ should be fulfilled in order to observe any Richardson-like behavior. They arrive at this inequality by plotting the quantity $(\langle r^{2/3}\rangle - r_0^{2/3})/(r_0^{2/3}t/t_0)$ versus t/t_0 and looking for plateaus. Only for the smallest initial separation for which T_L/t_0 is of order 10 do they observe a transition to a plateau. For comparison (Fig. 4 in their paper) we have plotted the same quantity for the forward dispersion case in our experiment. Figure 5 show the curves for the different bins. Except for the two smallest bins, plateaus are observed at $t\sim t_0$ for all bins. Important in this context is that $T_L/t_0<10$ for all bins in our experiment.

A few differences in the two experiments might explain the difference in T_L/t_0 and the transition to a Richardson-like behavior observed in Fig. 5: r_0/η and $L_{\mathrm{vol}}/L_{\mathrm{int}}$, where L_{vol} is the diameter of the observation volume. In the experiment by Bourgoin *et al.*, $L_{\mathrm{vol}}/L_{\mathrm{int}}\sim 1$ and $r_0/\eta\in\{43;2150\}$. In our experiment, $L_{\mathrm{vol}}/L_{\mathrm{int}}\sim 2.5$ and $r_0/\eta\in\{4;28\}$. $L_{\mathrm{vol}}/L_{\mathrm{int}}$ is a

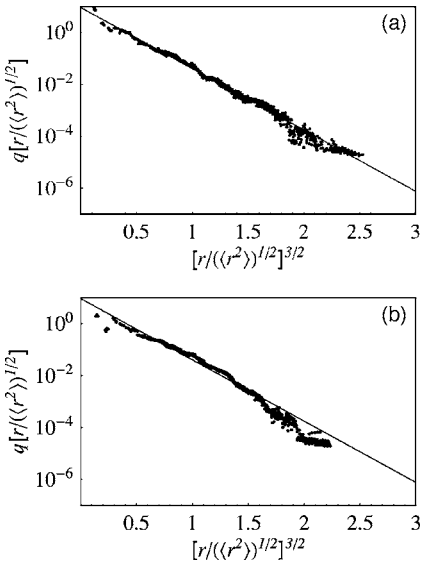

FIG. 6. (a) Distance-neighbor function for forward dispersion for pairs starting at $8-12\eta$, (b) backward case. In both plots, the straight line is the prediction by Richardson.

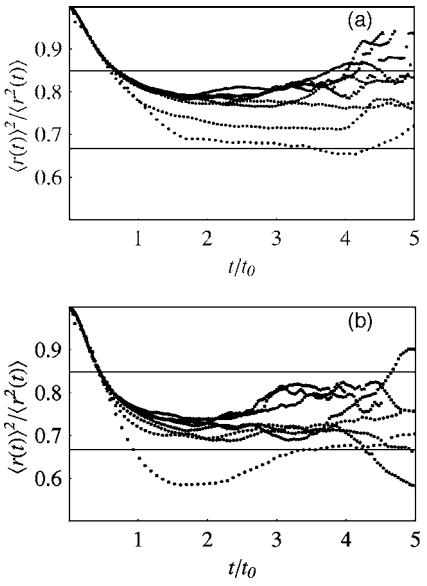

FIG. 7. (a) $\langle r(t)\rangle^2/\langle r^2(t)\rangle$ as a function of t/t_0 for the forward case. The different lines correspond to different initial separations: r_0 increasing upward from $r_0=4\eta$ to $r_0=28\eta$ in bins of 4η. The horizontal lines are the Richardson prediction at 0.67 and the Gaussian prediction at 0.85. (b) Backward case.

measure of possible finite volume bias whereas the implications of r_0/η are more subtle. Bourgoin *et al.* explore a wide range of initial separations where at least the smallest ones lie fully and unambiguously in the inertial range. Our Reynolds number is significantly lower and it is therefore not possible for us to explore the same range of initial separations in the inertial range. Because our ratios of r_0/η are smaller, we can follow particle pairs for longer times—both physical time as well as in time rescaled with t_0. An objection toward our relative low ratio of r_0/η would be that none of the separations lie fully in the inertial range. However, we defined the inertial range universal function $\mathcal{F}$ based on the argument that $\eta/r_0 \sim 0$. So for the validity of $\mathcal{F}$, the ratio r_0/η is not too low.

To quantify how far away we are from a fully developed Richardson regime, we will now look at the probability density function (pdf) of separation: the Richardson distance-neighbor function $q(r)$ is the solution to a diffusion equation with scale-dependent diffusivity $K(r) \sim r^{4/3}$ [6].

The data are plotted in Fig. 6 for initial separations between 12η and 16η. The Richardson prediction is shown as a straight line. In both case, excellent agreement is observed.

If, however, we look at the moments of the pdf, we observe that the Richardson prediction may not be the best description for the experimental data: the ratio between the first two moments of the pdf's is displayed in Fig. 7. Besides the smallest initial separations ($r_0=4\eta$ and 8η, which are probably not even in the inertial range), the curves almost collapse. The scatter observed for long times is due to poor statistics and should not be subject to any physical interpretation. Although the backward case seems to be closer to the Richardson value (the bottom most horizontal line), both cases are certainly not Gaussian (topmost horizontal line).

B. DNS

In addition to the experimental findings, we have performed a similar analysis on direct numerical simulation data (DNS). Details about the simulation can be found in Biferale *et al.* [14,15].

We have again sorted r_0 in bins of size 4η. This approach is somewhat different from the usual DNS approach, where r_0 is a finite number and not, as here, an interval. Doing it our way we can, however, get information on the backwards dispersion from databases of only tracks, without having to store the full Eulerian velocity field in time [10]. The DNS simulates the three-dimensional Navier-Stokes equations at a resolution of 1024^3 corresponding to $\mathrm{Re}_\lambda \sim 280$. In nondimensional units, $\varepsilon=0.81$, $\nu=8.8\times10^{-4}$, $\eta=5\times10^{-3}$, and $L=3.14$ with Lagrangian velocity autocorrelation time and Kolmogorov time, $T_L=1.2$ and $\tau=3.3\times10^{-2}$, respectively.

We plot $\langle r^2(t)\rangle/r_0^2$ as a function of t/t_0 in Fig. 8 for both forwards and backwards dispersion for the case $r_0=20\eta$. The dashed lines are fits to Eq. (10). After a time $t \sim t_0$, the fits are in excellent agreement with the data. Figure 9 reveals a small dependence of g_f, g_b, and g_b/g_f on r_0/η. g_b/g_f decreases from 2.4 to 2.2 with increasing r_0/η. The fact that the smallest initial separations are not in the inertial range may explain this behavior.

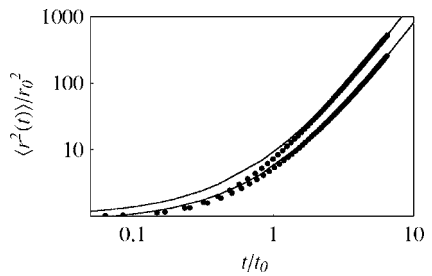

FIG. 8. $\langle r^2(t)\rangle/r_0^2$ as a function of t/t_0 for the two cases with $r_0=20\eta$. Fits by Eq. (10) are displayed on top by thin lines. The upper curve is the backward case.

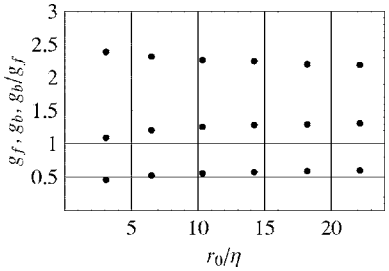

FIG. 9. g_f, g_b, and g_b/g_f (from bottom to top) as a function of r_0/η.

It is noteworthy that $g_b/g_f \sim 2$ as in the experiment, although the general flow properties of the DNS and experimental flow are different: whereas the experimental flow is axisymmetric and slightly strained, the DNS is isotropic. In DNS, the forcing on the smallest wave numbers in Fourier space gives rise to a vanishing $\langle \delta a_{\|}(r) \rangle$.

Along with these differences between the experiment and the DNS, there are other physical differences of importance. The first and probably most striking is the Lagrangian nonstationarity [16]. In the experiment, a fluid particle will experience a decrease in kinetic energy with time as it moves away from the forcing propellers. From time to time it will, however, due to the finite volume, come back to the propellers once again and gain kinetic energy. In agreement with decaying turbulence, $\frac{d}{dt}\langle u^2 \rangle = -\varepsilon$. In DNS, in contrast, we have that $\frac{d}{dt}\langle u^2 \rangle = 0$.

Another difference is the number of integral time scales observed. Whereas the DNS only has $\sim 3.7 T_L$, the experiment has $\sim 154 T_L$. The volume size in terms of integral scale is similar to our experiment ($L_{\mathrm{vol}}/L_{\mathrm{int}}=2$).

The close agreement between g_b/g_b in the experiment and in the DNS data indicates that the result is robust and, perhaps more importantly, that DNS can in a satisfactory way be used to simulate turbulence in the absence of real physical experiments.

V. DISCUSSION

The difference between forwards and backwards dispersion can be explained in part in terms of stretching of infinitesimal material line elements l. These obey the kinematic relation

$$\frac{1}{2}\frac{Dl^2}{Dt} = l_i l_j s_{ij} \tag{11}$$

with the rate of strain tensor, $s_{ij} = \frac{1}{2}\left(\frac{\partial u_i}{\partial x_j} + \frac{\partial u_j}{\partial x_i}\right)$. The eigenvalues of s_{ij}, Λ_i are defined such that $\Lambda_1 > \Lambda_2 > \Lambda_3$, and $\Sigma_i \Lambda_i = 0$ due to incompressibility. Batchelor [17] proposed that any infinitesimal material line element will, after a short time, align itself with the largest eigenvalue and therefore $\frac{1}{2}Dl^2/Dt = \Lambda_1 l^2$.

From our experimental micro tracking, we can calculate the distributions of Λ_i in a flow with $\mathrm{Re}_\lambda \sim 100$. An ansatz for the linearity of the velocity field in the proximity of the particle positions is used to obtain the eigenvalues, Λ_i. Details of the method can be found in Lüthi *et al.* [18].

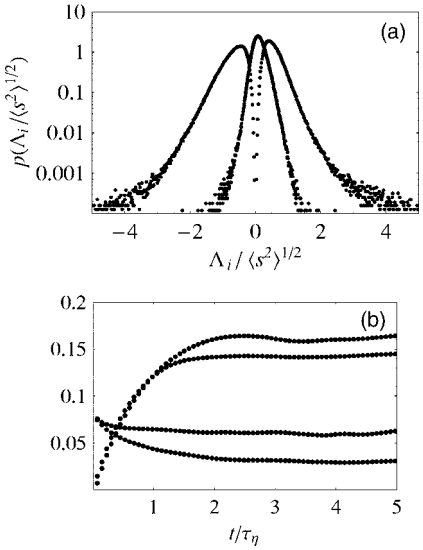

FIG. 10. (a) PDF of Λ_i. The PDFs are normalized with the rms of total strain $\langle s^2 \rangle^{1/2}$. (b) Stretching rates as a function of time. From bottom to top: var($L_f(t)$), var($L_b(t)$), $\langle L_f(t) \rangle$, and $\langle L_b(t) \rangle$.

Figure 10(a) shows the distributions of Λ_i. We find the ratio

$$\langle \Lambda_1^f \rangle : \langle \Lambda_2^f \rangle : \langle \Lambda_3^f \rangle = 1.00 : 0.20 : -1.20.$$

Other experiments found similar values: Kholmyansky *et al.* [19] in an atmospheric flow at $\mathrm{Re}_\lambda = 10^4$ and Lüthi *et al.* [18] in a magnetically forced flow at $\mathrm{Re}_\lambda = 50$. Betchov [20] calls it the jet collision situation: compression of material lines in one direction and stretching in the other two directions. We can associate this situation with forward infinitesimal separation of fluid particles. In the backward case, we simply change the sign of all three eigenvalues resulting in

$$\langle \Lambda_1^b \rangle : \langle \Lambda_2^b \rangle : \langle \Lambda_3^b \rangle = -1.00 : -0.20 : 1.20.$$

Recent studies [21–23] indicate that coarse-grained strain dynamics are similar to their viscous counterpart. More importantly, it seems that even the eigenvalues are very similar to the ones found in coarse-grained fields by Borue and Orszag [23]. The above picture may thus be extended to scales, $l > \eta$, and hence into the inertial range. In order to connect the theory for infinitesimal material line stretching to inertial range dispersion, we therefore assume self-similarity of material line stretching.

Based on the above assumptions, we can estimate the ratio, g_b/g_f. The characteristic time of separation is determined by the largest mean eigenvalue: $\langle \Lambda_1 \rangle$ and $-\langle \Lambda_3 \rangle$ for the forward and backward case, respectively. In the forward case where $t > 0$, we recall $\langle r^2(t) \rangle_f = g_f \varepsilon t^3$. Looking now at $t < 0$ with normalized time, we have

$$\langle r^2(t) \rangle_b = \left\langle r^2\left(t\frac{-\langle \Lambda_3 \rangle}{\langle \Lambda_1 \rangle}\right)\right\rangle_f = g_f \varepsilon \left(t\frac{-\langle \Lambda_3 \rangle}{\langle \Lambda_1 \rangle}\right)^3 = g_b \varepsilon t^3,$$

which means that

$$g_b/g_f = \left(\frac{\langle -\Lambda_3\rangle}{\langle \Lambda_1\rangle}\right)^3 = 1.75. \quad (12)$$

This value is within the errors of the value found earlier, even though the $\langle\Lambda_i\rangle$ was obtained from the viscous range and the relative dispersion experiment was performed in the inertial range.

The picture is, however, more complicated. To illustrate this, we compute the stretching rate $L(t)$ defined as $L(t)/\tau_\eta \equiv \frac{1}{2}l^{-2}Dl^2/Dt$ from Eq. (11). For large times, we expect $L(t)$ to reach a steady state that can be associated with the Lyapunov exponent defined as $\lambda = \lim_{t\to\infty}\langle L(t)\rangle$ [7,9]. The computation of the two cases only differs by a sign change in the time integration. $\langle L(t)\rangle$ and the variance var$(L(t))$ for both cases are shown in Fig. 10(b). Both the asymptotic λ and its variance are highest in the backward case. $\lambda_f = 0.145$ is similar to values found by others: 0.115 ± 0.005 [9] and 0.129–1.400 [24].

Comparing λ_f and λ_b with the actual largest mean eigenvalue, $\langle\Lambda_1\rangle$ in the forward case and $-\langle\Lambda_3\rangle$ in the backward case, we see that the values obtained are around 40% of the eigenvalues. This is of course reflecting the known fact that the material line elements are far from being perfectly aligned with the largest eigenvalue as proposed by Batchelor [24–26]. This is a first indication that the picture of calculating the ratio g_b/g_f from $\langle\Lambda_1\rangle$ and $\langle\Lambda_3\rangle$ alone is far too simplistic. More severe, though, is the assumption of self-similarity of material line stretching, which implies that particle separation vectors align with the coarse-grained principal strain field. Future experimental investigations will focus on this last issue.

VI. CONCLUSION

A PTV experiment in a turbulent flow has been performed. Because our Reynolds number is only of intermediate size, we do not observe a fully developed Richardson regime. We therefore propose a function $\mathcal{F}$ of particle pair separation that take into account the effect of initial separation. We show experimental evidence of the existence of this function. It is hereafter utilized to quantify dispersion rates.

The experiment showed a difference between forwards and backwards dispersion. The mean square separation following particle pairs backwards in time is twice as large as forwards. DNS data support this finding, indicating that the result is robust to forcing and Lagrangian stationarity.

Whereas Sawford *et al.* [10] focused on the role of the odd moments to explain the difference between forwards and backwards dispersion, we suggest alternatively that the positiveness of $\langle\Lambda_2\rangle$ might explain the faster backwards dispersion as compared to the corresponding forwards dispersion.

ACKNOWLEDGMENTS

We thank the supercomputing center Cineca (Bologna, Italy) for the hosting of the DNS data. This work was supported by the Danish Technical Research Council under Contract No. 26-01-0087.

[1] U. Frisch, *Turbulence* (Cambridge University Press, Cambridge, 1995).
[2] L. F. Richardson, Proc. R. Soc. London, Ser. A **110**, 709 (1926).
[3] A. M. Obukhov, Izv. Akad. Nauk SSSR, Ser. Fiz. **5**, 453 (1941).
[4] P. Franzese and M. Cassiani (unpublished).
[5] P. K. Yeung, Annu. Rev. Fluid Mech. **34**, 115 (2002).
[6] S. Ott and J. Mann, J. Fluid Mech. **422**, 207 (2000).
[7] G. Boffetta and I. M. Sokolov, Phys. Fluids **6**, 094501 (2002).
[8] T. Ishihara and Y. Kaneda, Phys. Fluids **14**, L69 (2002).
[9] L. Biferale, G. Boffetta, A. Celani, B. J. Devenish, A. Lanotte, and F. Toschi, Phys. Fluids **17**, 115101 (2005).
[10] B. L. Sawford, P. K. Yeung, and M. S. Borgas, Phys. Fluids **17**, 095109 (2005).
[11] J. Willneff, Ph.D. thesis, ETH, Zürich (2003).
[12] N. T. Ouellette, H. Xu, and E. Bodenschatz, Exp. Fluids **40**, 301 (2006).
[13] M. Bourgoin, N. T. Ouellette, H. Xu, J. Berg, and E. Bodenschatz, Science **311**, 835 (2006).
[14] L. Biferale, G. Boffetta, A. Celani, B. J. Devenish, A. Lanotte, and F. Toschi, Phys. Rev. Lett. **93**, 064502 (2004).
[15] L. Biferale, G. Boffetta, A. Celani, B. J. Devenish, A. Lanotte, and F. Toschi, Phys. Fluids **17**, 021701 (2005).
[16] S. Ott and J. Mann, New J. Phys. **7**, 142 (2005).
[17] G. K. Batchelor, Proc. R. Soc. London, Ser. A **213**, 349 (1952).
[18] B. Lüthi, A. Tsinober, and W. Kinzelbach, J. Fluid Mech. **528**, 87 (2005).
[19] M. Kholmyansky, A. Tsinober, and S. Yorish, Phys. Fluids **13**, 311 (2001).
[20] R. Betchov, J. Fluid Mech. **1**, 497 (1956).
[21] B. Tao, J. Katz, and C. Meneveau, J. Fluid Mech. **457**, 35 (2002).
[22] F. van der Bos, B. Tao, and J. K. C. Meneveau, Phys. Fluids **14**, 2456 (2002).
[23] V. Borue and S. A. Orszag, J. Fluid Mech. **366**, 1 (2002).
[24] S. S. Girimaji and S. B. Pope, J. Fluid Mech. **220**, 427 (1990).
[25] A. Tsinober, *An Informal Introduction to Turbulence* (Kluwer, Dordrecht, 2001).
[26] M. Guala, B. Lüthi, A. Liberzon, A. Tsinober, and W. Kinzelbach, J. Fluid Mech. **533**, 339 (2005).

IV

beat.luthi@risoe.dk

Self similar two particle separation model

Beat Lüthi, Jacob Berg, Søren Ott and Jakob Mann*

(Dated: June 19, 2006)

We present a new model for relative two particle separation in turbulence. The core of our approach is that the process of material line stretching also occurs beyond the viscous range, with time scaling according to K41, i.e. in the inertial range as $\varepsilon^{-1/3}r^{2/3}$. The model predictions agree with numerical and experimental results for various initial particle separations. We present model results for fixed time and fixed scale statistics. We find that for the Richardson-Obukhov law, $\left\langle r\left(t\right)^2\right\rangle = g\varepsilon t^3$, to hold and to also be observed in experiments, high Reynolds numbers are necessary, $Re_\lambda > \mathcal{O}\left(1000\right)$, the integral scale needs to be large compared to initial separation, $\mathcal{L}/r_0 > 30$, and $d/\mathcal{L} > 3$ need to be fulfilled, where d is the size of the field of view. Removing the constraint of finite inertial range the model is used to explore separation dynamics in the asymptotic regime. As $Re_\lambda \to \infty$ the distance neighbour function takes on a constant shape, as predicted by the Richardson diffusion equation. For the Richardson constant we obtain that $g \to 0.95$ as $Re_\lambda \to \infty$. This asymptotic limit is reached at $Re_\lambda > 1000$. For the Richardson constant g the model predicts a ratio of $g_b/g_f \approx 1.9$ between backwards and forwards dispersion.

PACS numbers: Valid PACS appear here

*Risø Nat. Lab., DK-4000 Roskilde; URL: `http://www.risoe.dk`

I. INTRODUCTION

Relative particle dispersion [1] is of practical importance to many applied problems in mixing and reactions in industrial as well as environmental flows and has recently been reviewed by Sawford [2]. In e.g. [3–5] its relevance also for biological systems has been emphasized. To date, relative particle dispersion serves as a bench-mark problem for our current understanding of turbulence. By comparing predicted dispersion properties against properties that are actually observed in experiments, current views and theories of the turbulence phenomena are put to a direct test. The work of Batchelor [6], Richardson [1] and Obukhov [7] that led to today's understanding of the ballistic regime, $\left\langle r^2 - r_0^2 \right\rangle \propto t^2$, and to the $\left\langle r^2 \right\rangle = g\varepsilon t^3$ law, have been explored by a number of experiments, e.g. [8–13]. A clear understanding of the transition between the two regimes is still subject to research. In addition, to date the precise value(s) of the Richardson constant, g, is still not known. In [14] it is argued that g is a function of Re_λ and that it reaches an asymptotic value of $g \approx 0.65$ at high Reynolds numbers. Particle tracking velocimetry (PTV) experiments at $Re_\lambda \approx 90$ and $Re_\lambda \approx 170$ yielded $g \approx 0.5$ and $g \approx 0.6$ [8, 13] and for DNS simulations at $Re_\lambda = 200 - 283$, values of $g \approx 0.5 - 0.7$ are reported [9–11, 13]. The influence on dispersion dynamics of finite Re_λ flows is still subject of discussions. In [12] it is inferred, that, in order to observe the Richardson-Obukhov law, a ratio of integral time to Batchelor time $\mathcal{T}/\tau_B > 10$ is required, with $\mathcal{T}/\tau_\eta = (\mathcal{L}/\eta)^{2/3}$, where $\mathcal{L}$ is the integral scale and $\tau_B = \left(r_0^2/\varepsilon\right)^{1/3}$ is the Batchelor time. They base this inequality on missing plateaus of the curves $(\left\langle r^{2/3} \right\rangle - r_0^{2/3})/(r_0^{2/3} t/t_0)$ vs. t/τ_B. In the experiment reported by [13] plateaus of the same curves were observed for $t > \tau_B$, despite the fact that $\mathcal{T}/\tau_B < 10$. In [13] the function

$$\left\langle r^2\left(t\right)\right\rangle / r_0^2 = g\left(t/\tau_B - T_0/\tau_B\right)^3 \tag{1}$$

as it was introduced by [8] is re-derived. Provided that $\eta/r_0 \sim 0$ this function describes well the particle separation and it allows to extract a Richardson constant g already from intermediate Reynolds number data. The function fits nicely to experimental and DNS data [13]. Finally, the influence of finite sized experimental observation domains has not yet been conclusively addressed. Part of the motivation for this work has thus been to investigate this influence.

The idea of this contribution is to reproduce known experimental dispersion data with a model as simple and physical as possible. Then the model is to be used to explore the influence of initial particle separation r_0, the influence of various observation domain scales, and the influence of various ratios of $\mathcal{L}/\eta$, e.g. to mimic the dispersion process at various Reynolds numbers.

It has already been shown by Borgas and Yeung [15] that *"stochastic models can be an effective and efficient*

representation of the dispersion process". The basis of such models go back to [16]. In [15] the model is based on a Langevin-type equation for the relative velocity between two particles. The drift term is derived from the Eulerian transport equation: relative acceleration is parametrized as a quadratic closure of relative velocity and a correction term which guarantees smooth transitions between the different regimes. The diffusion term is a scale dependent Wiener process.

In principle the model of [15] could be used for our purpose. However, we present and employ here a slightly different and simpler stochastic model, one that exploits a K41-type scaling argument [17] for the field of coarse grained velocity derivatives. In [18] evidence is given, based on DNS simulations at $Re_\lambda = 130$, that coarse grained strain, $\widetilde{s}^2$, actually does scale according to K41 and that $\left\langle \widetilde{s}^2 \right\rangle \sim r^{-4/3}$. Not just the magnitude but also the geometrical properties of velocity derivatives are reported to behave similarly in the inertial range as in the viscous range [19, 20]. From DNS results and holographic PIV results it is shown that a number of characteristic features of the velocity derivative tensor, $A_{ij} = \partial u_i / \partial x_j$, are also present in its coarse grained counterpart, $\widetilde{A}_{ij}$. A detailed overview on these properties is given in [21].

Given these similarities it is natural to ask if also the process of material line stretching has its counterpart in the inertial range. The main idea is that particle separation is governed by a time scale, t^*, that increases with increasing particle distance. In the viscous range we have $t^* = \tau_\eta$ and in the inertial regime the separation dynamics become slower according to K41 scaling: $t^* \propto r^{2/3}$. As will be shown below, the precise value for $t^*(r)$ is obtained from a parametrized form of the second order structure function [15]. Linking the particle separation process to material line stretching, which is governed by a single time scale $t^*(r)$, results in a relatively simple formulation of a quasi 1D stochastical model with only one 'free' model parameter for each of the viscous, inertial and diffusive separation regimes. This will be explained in detail in the following sections.

The paper is organized as follows: in the next section a very brief overview on material line stretching is given. In the modelling section expressions are derived to mimic the process of particle dispersion. We outline how the model simulates finite observation domains. In the results section we show how the model compares with data from existing experiments. Finally, the model is used to explore the influences of finite field of view and of the scale separation $\mathcal{L}/\eta$. In a last section we make a summary and draw some conclusions.

II. MATERIAL LINE STRETCHING

The process of infinitesimal material line stretching has been studied extensively [21–26] and is described by the kinematic relation

$$\frac{1}{2}\frac{dr^2}{dt} = r_i r_j s_{ij}, \tag{2}$$

with $\mathbf{r} = \mathbf{x}^{(2)} - \mathbf{x}^{(1)}$ denoting the particle separation and $s_{ij} = \frac{1}{2}\left(\frac{\partial u_i}{\partial x_j} + \frac{\partial u_j}{\partial x_i}\right)$ the rate of strain tensor. The stretching rate has been measured, both in direct numerical simulations and with particle tracking velocimetry [11, 13, 22, 24–26]. It has been found that the non-dimensionalized stretching rate

$$L(t) = r_i(t)\, r_j(t)\, s_{ij}(t) \cdot \frac{t^*}{r^2}, \tag{3}$$

with $t^* = \tau_\eta$, the Kolmogorov time scale, $\tau_\eta = (\nu/\varepsilon)^{1/2}$, is seemingly independent of Re_λ, at least for $Re_\lambda < 300$. After a time of $t/\tau_\eta \approx \mathcal{O}(1)$ the stretching rate takes on a mean value in the range of $\langle L(t)\rangle \approx 0.11 - 0.14$, which is equal to about $0.4\,\langle\Lambda_1\rangle\,\tau_\eta$. Λ_1 is the largest principal eigenvector of s_{ij}. It is not clear how the slight discrepancy between the different measurements can be explained. For both, experimental [13, 25, 26] and DNS [11, 22] investigations the same range of stretching rates has been found, with no systematic dependence e.g. on Reynolds number.

$\langle L(t)\rangle$ can be understood better if interpreted geometrically by decomposing eqn. 3 into its terms that are associated with each eigenvalue, Λ_i, and eigenvector, $\lambda_\mathbf{i}$, of the rate of strain tensor, s_{ij}, [21] as

$$L(t) = \tau_\eta \sum\nolimits_i \Lambda_i \cos^2(\lambda_i, \mathbf{r}). \tag{4}$$

From eqn. 4 it becomes clear that $L(t)$ depends on the alignment to the principal strain axis of s_{ij} as well as on the magnitude of the associated eigenvalues. Batchelors assumption [27] of full alignment of $\mathbf{r}$ with $\lambda_\mathbf{1}$ was corrected by [22] who showed that mainly due to rotation of the strain eigenframe only about 40% of the maximal theoretical stretching actually occurs, see also [23, 26]. For the mean of eqn. 4 an upper value of $\langle L(t)\rangle \leq 0.5$ can be derived as follows: If we use the convention $\Lambda_1 > \Lambda_2 > \Lambda_3$, $\Lambda_1 + \Lambda_2 + \Lambda_3 = 0$ due to incompressibility and the fact $\langle\Lambda_2\rangle > 0$, we can express $\langle\Lambda_1\rangle$ in terms of $s^2 = s_{ij}s_{ij}$ as

$$\langle\Lambda_1\rangle < \frac{\left\langle\sqrt{s^2}\right\rangle}{\sqrt{2}}. \tag{5}$$

For the Kolmogorov time we have an upper bound as

$$\tau_\eta = \frac{1}{\sqrt{2\,\langle s^2\rangle}} < \frac{1}{\sqrt{2}\left\langle\sqrt{s^2}\right\rangle}. \tag{6}$$

Assuming full alignment of $\mathbf{r}$ with $\lambda_\mathbf{1}$ and using eqn. 5 and eqn. 6 an upper bound for the average of eqn. 4 can be written as

$$\langle L(t)\rangle < \frac{1}{\sqrt{2}\left\langle\sqrt{s^2}\right\rangle}\cdot\frac{\left\langle\sqrt{s^2}\right\rangle}{\sqrt{2}} = \frac{1}{2}. \tag{7}$$

A non perfect alignment of $\mathbf{r}$ with $\lambda_\mathbf{1}$, a positive intermediate eigenvalue $\langle\Lambda_2\rangle > 0$, and a flat distribution of s^2 will all contribute to reduce the actual mean value. From e.g. the PTV data of $Re_\lambda \approx 70$ turbulence [13] we measure $\left\langle\cos^2(r,\lambda_1)\right\rangle \approx 0.35$, $\langle\Lambda_1\rangle = 0.9\left\langle\sqrt{s^2}\right\rangle/\sqrt{2}$, and $\tau_\eta = 0.9/\left(\sqrt{2}\left\langle\sqrt{s^2}\right\rangle\right)$, which is consistent with a mean stretching rate of $\langle L(t)\rangle \approx 0.14$ that is also reported in [13]. The PDFs of $L(t)$ for different times and initially randomly oriented r is shown in figure 1.

III. MODELLING

The stochastical model that we present here is quasi 1D with Langevin-type equations for the evolution of relative particle separation. From figure 1(a) we observe that the complex underlying processes lead to a relatively simple overall behaviour of the non-dimensional stretching rate $L(t)/\sigma$. The strain tensor evolves in time with changing intensity, shape and orientation of its principal strain frame. Infinitesimal material elements experience non-persistent straining because of these dynamics [22, 23, 26]. The overall stretching rate we find however to a good first approximation normally distributed around an asymptotic mean value, that we call L_m. The asymptotic state is reached after a few τ_η. This allows us to simulate $L(t)$ using a 1D Ornstein-Uhlenbeck process, with a time scale that in the viscous range is $t^* = \alpha\tau_\eta$, as

$$dL = -\frac{1}{\alpha\tau_\eta}(L - L_m)\,dt + \sigma\sqrt{\frac{2}{\alpha\tau_\eta}}dW(t). \tag{8}$$

$dW(t)$ is a Wiener process with the properties $\langle dW(t)\rangle = 0$ and $\langle dW(t)\,dW(t')\rangle = \delta(t-t')\,dt$ for $(t \neq t')$. The normally distributed $L(t)$ has an autocorrelation time $\alpha\tau_\eta$ and a variance σ^2. With eqns. 2 and 3 we can write

$$dr = \frac{r}{\tau_\eta}L(t)\,dt. \tag{9}$$

Expressions 8 and 9 depend on the 'free' parameters α, L_m and σ and they describe the separation process of two particles in the viscous range. We will now show how the range of validity for expression 9 can be extended also to larger separations, and, with the help of the second order structure function and the well-mixed condition, how the number of free parameters is reduced to one for each of the viscous, inertial and diffusion regimes.

Substituting $1/\tau_\eta$ by $f'(r)$ the longitudinal second order structure function $S_2(r)$ can be expressed in terms of expression 8 and 9 as

$$S_2(r) = \left\langle \left(\frac{dr}{dt}\right)^2 \right\rangle = r^2 f'^2 \sigma^2. \tag{10}$$

With the parametrized form of $S_2(r)$ employed by [15]

$$\widetilde{S}_2(r) = 2\left(1 - \exp\left(-\frac{r}{(15C_k)^{3/4}\left(\frac{\nu^3}{\varepsilon}\right)^{1/4}}\right)\right)^{4/3} \cdot (\varepsilon\mathcal{L})^{2/3}\left(\frac{r^4}{\frac{64\mathcal{L}^4}{C_k^6} + r^4}\right)^{1/6}, \tag{11}$$

the second order structure function is expressed as a function of separation r, the viscosity ν, the flow properties $\mathcal{L}$ and ε and the Kolmogorov constant C_k. For C_k we use the approximation

$$\begin{aligned} C_0 &= \frac{7.0}{1 + 7.5 \cdot 7.0^2 \cdot Re_\lambda^{-1.64}} \\ C_k &= \frac{2.1}{\left(1 + 7.5 \cdot C_0^2 \cdot Re_\lambda^{-1.64}\right)^{2/3}}, \end{aligned} \tag{12}$$

as proposed by [28]. For Re_λ we use

$$Re_\lambda = \sqrt{15}\left(\frac{\mathcal{L}}{\eta}\right)^{2/3}. \tag{13}$$

Substituting $f'(r)\sigma$ with $f(r)$, L_m/σ with $l_m(r)$, $L(t)/\sigma$ with $\xi(t)$ and $\alpha\sigma$ with $\tau_i(r)$ and dividing expression 8 by σ we get the final form of the model as

$$d\xi = -\frac{f(r)}{\tau_i(r)}(\xi - l_m(r))\,dt + \sqrt{\frac{2f(r)}{\tau_i(r)}}dW(t) \tag{14}$$

and

$$dr = r f(r)\,\xi(t)\,dt, \tag{15}$$

with the governing frequency

$$f(r) = \sqrt{\widetilde{S}_2(r)/r^2}. \tag{16}$$

The number of 'free functions' is thus reduced to two: $l_m(r)$ and $\tau_i(r)$. Through expression 16 with $1/f(r)$ a time scale is now defined for all ranges and for $\eta \ll r \ll \mathcal{L}$ we have $t^* \propto r^{2/3}$, consistent with K41 arguments. The physical interpretation of this is that coarse grained material lines, in our case the separation vectors $\mathbf{r}$, are stretched by a coarse grained strain field.

For these stochastic differential equations we can write the corresponding Fokker-Planck equation [29] as

$$\frac{\partial P}{\partial t} + \frac{\partial}{\partial r} f(r)\, r\xi P - \frac{f(r)}{\tau_i}\frac{\partial}{\partial \xi}(\xi - l_m)\,P - \frac{f(r)}{\tau_i}\frac{\partial^2}{\partial \xi^2}P = 0. \tag{17}$$

To ensure that the well-mixed condition [16] is fulfilled the probability distribution, $P(r,t)$, needs to be stationary in time, i.e. an initially uniformly distributed set of particle separations has to remain uniformly distributed for all times. A solution of the form $P = r^2 e^{-\xi^2/2}$ exists provided that

$$\frac{l_m}{\tau_i} = \frac{\partial}{\partial r}\left(f(r)\, r^3\right) \frac{1}{f(r)\, r^2}. \tag{18}$$

With expression 18 the number of free functions is thus reduced to one, i.e. it is enough to define $l_m(r)$. As can be seen from figure 2 there are three distinct regimes: A viscous regime, the inertial regime itself and a diffusive regime. We expect the separation processes to be similar but not identical in the three different regimes. In the viscous regime separation is driven by only the viscous scale. In the inertial range however, the scale associated with r is governing but it is not alone. In the diffusive regime the dominant time scale is essentially frozen to the value associated with $\mathcal{L}^{2/3}$ and therefore we can expect $l_m(r) = L_m(r)/\sigma(r)$ to again change. We thus create a function $l_m(r)$ with three discrete levels, l_ν, l_i and l_d and let the transitions between them be governed by the properties of expression 18 as

$$l_m(r) = l_d + 64\mathcal{L}^4 \cdot \frac{l_d - e^{-\frac{r}{(15C_k)^{3/4}\eta}}\left(l_\nu + l_i\left(e^{\frac{r}{(15C_k)^{3/4}\eta}} - 1\right)\right)}{-64\mathcal{L}^4 - C_k^6 r^4}. \tag{19}$$

The behaviour of expression 20 is plotted in figure 3 for $l_\nu = 0.39$, $l_i = 0.71$ and $l_d = 0.34$. These three values are obtained from fitting the model to all the available experimental and numerical data. They are used unchanged for all simulations that are presented in the following.

Two randomly selected particles are initially not predominately aligned with the principal strain axis. The asymptotic state of mean alignment of $\mathbf{r}$ with $\lambda_\mathbf{1}$ is reached only after a characteristic time $\tau_i\tau_\eta$. This alignment effect is modelled with the initial condition $\langle \xi(0,r)\rangle = 0$. The such modelled $\xi(t)$ behaves similar to the measurements and is shown in figure 1(b). The initial separations used for this figure are very small and thus during the course of their evolution do not exceed the viscous range, i.e. $r \ll \eta$.

Recently, the role of backwards dispersion has been emphasized by [30, 31] and experimental evidence of the phenomenon has been reported in [13]. As it is already mentioned in [13] a characteristic feature of particle separation with time going backwards is that material line elements tend to align with the most compressing eigenvector of the rate of strain tensor. Despite the fact that this was observed and reported only for the viscous range there are good reasons to assume and also preliminary experimental evidence to believe that the same is true also in the inertial range. Due to $\langle\Lambda_2\rangle > 0$ in turbulent flows and due to incompressibility, $\Lambda_i = 0$, we have that $\langle|\Lambda_3|\rangle > \Lambda_1$. Consequently, the mean stretching rate backwards in time is higher than the mean stretching rate forwards in time.

From PTV experiments described in [13] a ratio of $\langle L(t)\rangle_{back.} \approx 1.25\,\langle L(t)\rangle_{forw.}$ was measured in the viscous range. The parameters l_ν and l_i are thus multiplied with this factor of 1.25 to model the case of backwards dispersion. Beyond the inertial range odd moments vanish and $\langle \Lambda_2 \rangle = 0$, if coarse grained at $r > \mathcal{L}$, and thus l_d can be left unchanged. Expression 20 is computed for the values $l_\nu = 0.49$, $l_i = 0.89$ and $l_d = 0.34$ and the resulting l_m is plotted in figure 3 denoted as a dash-dotted line. From eqn. 18 it follows that with an increased value for l_m also τ_i should increase. This is fully consistent with [31] who interprets the Lagrangian time scale as the memory effect of the flow and finds that the case of backwards dispersion is associated with a longer memory, i.e. a larger time scale.

With the model introduced and its parameters defined it can be run for any scale separation $\mathcal{L}/\eta$ for any initial separation r_0. However, in order to also compare the model with experimental results one important feature is still missing: Real experiments always have an only finite field of view, resulting in a finite observation scale, d. A finite field of view causes particles with a separation much larger than their corresponding mean to leave the field of view 'too early', which will lead to a truncation of the separation distribution. Sweeping velocities which translate separating particle pairs across the field of view make the situation even worse. In the following, we explain how this effect is captured in the presented model.

The principal idea is to use Sawfords stochastic one particle model [28] for the evolution of the centre of mass of evolving particle pairs. Each moving centre of mass is started at a random position inside a virtual observation domain. Together with the modelled evolving relative separation the particle positions of the pairs are defined. The orientation of the pair is chosen randomly for each realization and is fixed in time. As soon as the first of the particles leaves the virtual domain, the separating pair is considered 'lost' for the statistics.

The stochastic model is a Langevin equation describing a particles Lagrangian acceleration $A(t)$ in an asymptotically stationary process as

$$dA(t) + \alpha_1 A(t)\,dt + \alpha_2 \int_0^t A(t')\,dt'dt = \sqrt{2\alpha_1\alpha_2\sigma_m^2}\,dW(t)\,, \tag{20}$$

with

$$
\begin{aligned}
\alpha_1 &= -\left(\beta_1+\beta_2\right) \\
\alpha_2 &= \beta_1\beta_2 \\
\beta_1 &= C_0\cdot\varepsilon/\left(2\sigma_m^2\right) \\
\beta_2 &= -2a_0/C_0\cdot\sqrt{\varepsilon/\nu} \\
a_0 &= 5/\left(1+110/Re_\lambda\right)) \\
\sigma_m^2 &= 1/2\left[\sigma_p^2+R_u\left(r\right)\sigma_p^2\right] \\
\sigma_p &= \sqrt{Re_\lambda}\cdot\left(\varepsilon\nu/15\right)^{1/4} \\
R_u\left(r\right) &= -\left(\widetilde{S}_2-2\sigma_p^2\right)/\left(2\sigma_p^2\right).
\end{aligned}
\tag{21}
$$

The only difference to [28] is that the velocity variance of the centre of mass drops to half the value of a single particle, i.e. $\sigma_m^2=1/2\sigma_p^2$, when the velocities of the two particles decorrelate.

IV. RESULTS

A. $Re_\lambda=170$, particle tracking and model

All results that are presented in the following are obtained from Monte Carlo Simulations of the above described model with 10000 realizations for each of the different conditions. As a first result we show in figure 4 how the model predictions compare to measured data obtained from a particle tracking velocimetry (PTV) experiment at $Re_\lambda\approx 170$ [13]. For the PTV experiment an integral scale of $\mathcal{L}=48$mm and a Kolmogorov length of $\eta=0.25$mm are measured so that $\mathcal{L}/\eta=190$. The observation domain d is 150mm. In figure 4, where $\left\langle r^2\right\rangle$ is plotted over time for the different initial separations, we see that their is good agreement between measured and modelled data.

We do not observe the Richardson-Obukhov law and only the runs for the two smallest initial separation assume something like a t^3 slope.

To see to what degree the finite field of view, $d=150$mm and $d/\mathcal{L}\approx 3$, is influencing these results we show in figure 5 the evolution of the mean square separation with and without a finite field of view. After about $t/\tau_\eta=40\approx\mathcal{T}$ the separations for the two cases become different. At this late time the separations are already $\mathcal{O}\left(\mathcal{L}\right)$ and the finite observation scale effect is thus negligible, i.e. the reason that no Richardson-Obukhov law is observed clearly is the too low Reynolds number.

B. $Re_\lambda = 280$, DNS and model

At slightly higher Reynolds number, $Re_\lambda = 280$, we simulate with $\mathcal{L}/\eta = 628$ and $d = \infty$ the conditions of the DNS experiment reported by Biferale et al. [11]. In figure 6 mean square separation is plotted over time for different initial separations, $r_0/\eta = 1.2, 2.5, 10, 20$, as in the DNS case. In the inset the Richardson constant as obtained from $g = \left\langle r^2 \right\rangle / (\varepsilon t^3)$ is plotted as a function of time. From both figures we observe that at around $t/\tau_\eta \approx 80$ the particle separation dynamics become less intense. This is reflected in a slight departure from the t^3 slope for $\left\langle r^2 \right\rangle$ and in the maximum of the values for g for the two small initial separations, shown in the inset. The separations start to feel the influence of the finite inertial range. In this sense, there is again good agreement between modelled and measured data.

The effect of the finite inertial range is shown more clearly in figure 7 where distant neighbour functions for $r_0/\eta = 1.2$ for various times are plotted. For times $9 \leq t/\tau_\eta \leq 77$ they all collapse around the distribution as predicted by the Richardson diffusion equation. For very early times and for times $t/\tau_\eta \geq 80$, the distributions are closer to Gaussian.

We also measure the correlation of the relative separation velocity along the particle pair trajectories. In the inset of figure 8 we plot $D(t,\tau) = \left\langle \delta u_{||}(t)\, \delta u_{||}(t+\tau) \right\rangle$ versus t/τ_η for pairs with initial separation $r_0 = 1.2\eta$. As also observed by [11] $D(t,\tau)$ broadens with increasing travel time, confirming that the separation velocities decorrelate more slowly at larger travel times. In the body of the same figure we plot the same data rescaled with the time t_0 at which $D(t,\tau) = 0$. The good agreement with fig. 12 of [11] validates that the characteristic time τ_i, as obtained from eqn. 18, is consistent not only with the well-mixed condition, but also with actual turbulent flows as obtained from DNS results.

Model results for forwards and backwards dispersion mimicking the case of $Re_\lambda = 280$ DNS conditions, $\mathcal{L}/\eta = 628$ and $d = \infty$, are presented in figure 9. Particle separations $\left\langle r^2 \right\rangle$ are plotted over time $t - T_0$, as proposed and employed by [8] and recently by[13]. Basically T_0 accounts for the processes occurring in the initial phase of separation, in our frame of reference this would be the alignment of $\mathbf{r}$ with the principal strain axis of the corresponding scale. Not surprisingly T_0 is always found to be close to τ_B [13]. The two dashed lines are $y = 0.6\varepsilon t^3$ and $y = 1.2\varepsilon t^3$, the ratio of the Richardson constants for backwards and forwards dispersion is thus found to be $g_b/g_f \approx 2$. This result is in good agreement with [13] where also $g_b/g_f \approx 2$ is reported. The ratio is clearly lower than the values $g_b/g_f \approx 5 - 20$ proposed by [30].

The modelled dispersion is consistent also with exit time statistics introduced by [32]. We show in figure 10 and

figure 11 results for exit times, for Lyapunov exponents and for Richardson constants as employed in [11]. $T(r)$ is defined as the average time it takes for a separation r to reach the sphere r_{n+1} from the sphere r_n, with $r_n = \rho^n r_0$, $n = 1, 2, 3...$, and $\rho = 1.25$. The choice of $\rho = 1.25$ is common but arbitrary, however, the sensitivity of the results to ρ is very low. Following [11] the Lyapunov exponent and the Richardson constant can be obtained from $T(r)$ as

$$\lambda = \lim_{r\to\infty} \frac{1}{\langle T(r)\rangle} \log(\rho) \tag{22}$$

$$g^* = \frac{143}{81} \frac{\left(\rho^{2/3}-1\right)^3}{\rho^2} \frac{r^2}{\langle T(r)\rangle^3}. \tag{23}$$

Results are given for the cases of forwards and backwards dispersion. Results for the case of forwards dispersion agree well with [11]. From figure 11 we observe that the ratio for the Richardson constant for backwards and forwards dispersion as derived from exit times is $g_b^*/g_f^* \approx 1.8$, i.e. almost equal to g_b/g_f, but now with $g_b^* \approx 0.8$ and $g_f^* \approx 0.45$. In [31] an explanation for this discrepancy is given. Sawford argues that the way the Richardson constant is obtained from exit times, the memory of the flow is essentially neglected. From his quasi 1D model for particle dispersion he estimates that g_f can be underestimated by 30% and that the estimate for g_b can easily be 50% too small. This is reflecting that (i) the flow does have a memory and (ii) that the flows memory is longer in the backwards dispersion case. From results in [31], which are derived from first order exit time moments, it follows that $g_b/g_f \geq g_b^*/g_f^*$.

C. $Re_\lambda = 815$, particle tracking and model

Recently, the currently highest Reynolds number particle tracking experiment performed has been reported by Bourgoin et al. [12]. Here, particle separation has been successfully measured in an $Re_\lambda = 815$ flow. Initial particle separations are in the range $40 \leq r_0/\eta \leq 1300$. The scale separation is $\mathcal{L}/\eta = 3000$, with an integral scale $\mathcal{L} = 70$mm, $\mathcal{T}/\tau_\eta = 208$ and an observation domain of $d = 50$mm. With these parameters we attempt to mimic the $Re_\lambda = 815$ case with the presented model. In [12] it is found that the ballistic regime, where particles separate as $\langle r^2\rangle \propto t^2$, is valid for times smaller than τ_B, as it was predicted by Batchelor [6]. No transition to the Richardson-Obukhov regime was observed.

For clarity, the plotted initial separations are kept to $r_0/\eta = 40, 80, 150, 200$. The behaviour of separations with $r_0/\eta > 200$ does not change. In figure 12 we find the modelled results to agree well with the experimental findings of [12] as all the separations follow the $\propto t^2$ line that was predicted by Batchelor [6] He proposed that for $t < \tau_B$

$$\left\langle (r-r_0)^2 \right\rangle = \frac{11}{3} C_k (\varepsilon r_0)^{2/3} t^2. \tag{24}$$

To see the influence of the rather small field of view, i.e. $d/\mathcal{L} \approx 1$, we show with dashed lines the evolution of separations for the same Re_λ but without the finite domain effect. After their corresponding Batchelor times, $11 < \tau_B/\tau_\eta < 35$ for the given r_0, we observe how the separations become faster than $\propto t^2$ until $r \approx \mathcal{O}(\mathcal{L})$. This is especially true for separations with $\mathcal{L}/r_0 > 30$ as can be seen from figure 12. Note that $\mathcal{L}/r_0 > 30$ is equivalent to $\mathcal{T}/\tau_B > 10$ and that via a different way we arrive at the same result as [12]. It thus seems that here the finite field of view is not negligible. Precisely at the time where the beginning of a Richardson-Obukhov regime may occur particles leave the observation domain. Future experiments will tell if this prediction can actually be observed in real flows.

D. $Re_\lambda \to \infty$, only model

In figure 13 we show results for the same initial separations r_0 but now for the ideal case of $Re_\lambda \to \infty$ and $d = \infty$. The transition between a ballistic regime with $\left\langle r(t)^2 \right\rangle \propto t^2$ and a $\left\langle r(t)^2 \right\rangle \propto t^3$ regime is clearly visible. In figure 13(a) we see that this transition occurs at around $t = \tau_B$. In figure 13(b) we observe how at late times indeed the influence of initial conditions starts to vanish and together with the t^3 slope we can thus speak of a true Richardson-Obukhov regime.

We can now ask, to what value and how fast the Richardson constant, $g = \left\langle r^2 \right\rangle / \left(\varepsilon t^3\right)$, converges for $Re_\lambda = \infty$. From figure 14 we see that after a time long enough for a set of r to evolve and reach its asymptotic state, the Richardson constant g approaches a constant value for both the forwards and backwards dispersion cases. These values are approximatively $g_f \approx 0.95$ and $g_b \approx 1.8$, i.e. $g_b/g_f \approx 1.9$.

To see more clearly how the distribution of r reaches this asymptotic state, we show in figure 15 the evolution in time of the skewness, $S(t) = \left\langle \left(r(t) - \overline{r(t)}\right)^3 \right\rangle / \left(\sigma_r^2(t)\right)^{3/2}$, and kurtosis, $S(t) = \left\langle \left(r(t) - \overline{r(t)}\right)^4 \right\rangle / \left(\sigma_r^2(t)\right)^2$, coefficients for the same initial separations as in figure 14. After a transition time both distribution parameters assume constant values, which are close to those that one obtains from the Richardson diffusion equation. During the transition however, especially for small r_0, we observe high values for skewness and kurtosis. This observation is in perfect agreement with [11, 15]. As can be seen in figure 7 and as it was observed in [8] viscous separation dynamics lead to distributions where quite a few particles stay close together for a long time, while others have already started their fast separation. We attribute the observed peaking of distribution parameters to the exponential stretching nature in the viscous regime: Here $dr^2/dt \propto r^2$ amplify separation rate differences much more than in the inertial range. In the inertial range however, separation is less intense, i.e. $dr^2/dt \propto r^{4/3}$, and slower separations persist for a shorter time than fast separation rates. In other words a slowly separating pair has 'more chances' to change to a faster regime,

than an already fast separating pair has to change to a slower regime. This leads to less extreme distributions of r in the inertial regime as compared to the viscous regime.

Finally, in figure 16 we observe in what way the Richardson constant is a function of Reynolds number. For runs with $r_0 = 50$ and $d = \infty$ for various Re_λ the Richardson constant is extracted by fitting function 1 to modelled separations, up to times before the mean separation starts to be influenced by the end of the inertial regime, as it is done in [13]. This procedure may be questionable for low Reynolds numbers, $Re_\lambda < \mathcal{O}(100)$, but yields clear results as Re_λ increases. From figure 16 it appears that g increases with Re_λ and that at $Re_\lambda \geq \mathcal{O}(1000)$ an asymptotic value of $g \approx 0.95$ is approached. This result is similar to [33] who, based on extrapolated DNS data, inferred that Re_λ should be as high as $600 - 700$ for a fully developed Lagrangian inertial range. Contrarily, [14] report an analytical result, that already after $Re_\lambda \geq 300$ the Richardson constant should assumes a value of $g \approx 0.65$.

V. SUMMARY AND CONCLUSION

In this paper we have introduced a new stochastic model to mimic the process of two particle separation. A comparison with DNS and experimental results yields good agreement. The model assumes that material line stretching in a modified form occurs also in the inertial range. A coarse grained material line is stretched by a coarse grained straining field. From K41-type arguments it follows that the involved time scale becomes larger with increasing r and that for $\eta \ll r \ll \mathcal{L}$ time should be $\propto \varepsilon^{-1/3} r^{2/3}$. We show that with a parametrized form of the second order structure function, which defines the time scale for the stretching process, and the well-mixed condition the model is governed by one function $l_m(r)$. This function can be described with one 'free' parameter for each of the viscous, inertial and diffusive regimes. The model results fit well with experimental and DNS data reported by several authors. We present results for separation distributions measured at fixed times as well as exit time statistics.

We show results for the case of backwards dispersion. In agreement with [13], we find that the ratio of the Richardson constant for forwards and backwards dispersion is $g_b/g_f \approx 2$ for intermediate Reynolds numbers. As $Re_\lambda \to \infty$ our model predicts that $g_b/g_f \to 1.9$. If derived from exit times we obtain $g_b^*/g_f^* \approx 1.8$ which is consistent with [31] who suggests that $(g_b^*/g_f^*) < g_b/g_f$.

The model is used to explore the influence of finite observation domains. Our conclusion is that in order to observe a transition from the Batchelor regime, $\langle r^2 \rangle \propto t^2$, to the true Richardson-Obukhov regime, $\langle r^2 \rangle = g\varepsilon t^3$, both, physical and experimental conditions need to be fulfilled. The physical condition is that, besides that the flow should be turbulent enough, i.e. $Re_\lambda > \mathcal{O}(1000)$, the flows integral scale should be large in comparison with the initial

separation, $\mathcal{L}/r_0 > 30$. In addition to these 'physical' conditions we find the experimental condition that the flows integral time needs to be at least matched by the available observation time, which is mainly defined through the size of the experimental field of view. Otherwise, a transition to $\propto t^3$ may well occur, but can not be observed. As a rule of thumb we suggest that $d/\mathcal{L} > 3$.

We found support for these arguments from our model when we mimicked a $Re_\lambda = 815$ flow case, once for experimental conditions as in [12] and once with the finite field of view constraint removed. With an unlimited field of view, allowing for long enough observation times, the model predicts that for $r_0/\eta \leq 200$ the separation occurs according to $\left\langle r^2 \right\rangle \propto t^3$ during the time interval $\tau_B < t < \mathcal{T}$.

Finally, we use the model to investigate the dispersion process as $Re_\lambda \to \infty$. For the smallest separations, $r_0/\eta < \mathcal{O}(10)$, we find extreme skewness and flatness coefficients at intermediate times, like it is known from e.g. [11, 15]. We attribute this to a viscous process governed by exponential stretching. At later times the separation distribution is in fair agreement with the Richardson diffusion equation. Further, we find that for high Reynolds numbers, $Re_\lambda > \mathcal{O}(1000)$, times $t/\tau_\eta \approx \mathcal{O}(1000)$ are necessary for the Richardson constant to converge to an asymptotic value of $g_f \approx 0.95$ and $g_b \approx 1.8$, for forwards and backwards dispersion, respectively. The transition of $0.5 \leq g \leq 0.95$ occurs over a range of Reynolds number from $\mathcal{O}(100) \leq Re_\lambda \leq \mathcal{O}(1000)$.

The presented model seems to work satisfactory and is consistent with a variety of experimental and DNS investigations. The model is simple in the sense that it is reducing the complex separation dynamics to one single time scale, which is defined by the separation r itself. Despite this simplification the model seems to be capturing well the essential processes of the relative particle dispersion problem. To what degree the good results are also obtained for the right reasons, future experiments will have to show, e.g. the alignment of the separation vector $\mathbf{r}$ to the corresponding coarse grained strain field will have be measured. Similarly, our findings on the influence of finite observation domain and on the precise value for the Richardson constant need to be checked by experiments.

ACKNOWLEDGEMENTS

Part of this work was financed by the EU project 'Fluid Mechanical Stirring and Mixing: the Lagrangian Approach', coordinated by A. Pumir. We greatfully acknowledge helpful comments and discussion with A. Liberzon and M. Guala.

---

[1] L. F. Richardson, Proc. Roy. Soc. London A **110**, 709 (1926).

[2] B. Sawford, Ann. Rev. Fluid Mech. **33**, 289 (2001).

[3] J. Mann, S. Ott, H. L. Pecseli, and J. Trulsen, Phys. Rev. E **65**, 026304 (2002).

[4] J. Mann, S. Ott, H. L. Pecseli, and J. Trulsen, J. Fluid Mech. **534**, 1 (2005).

[5] J. B. Jørgensen, J. Mann, S. Ott, H. L. Pecseli, and J. Trulsen, Physics of Fluids **17**, 035111 (2005).

[6] G. K. Batchelor, Proc. Cambridge Phil. Soc. **48**, 345 (1952).

[7] A. M. Obukhov, Izv. Aka. Nauk SSSR **5**, 453 (1941).

[8] S. Ott and J. Mann, J. Fluid Mech. **422**, 207 (2000).

[9] T. Ishihara and Y. Kaneda, Physics of Fluids **14**, L69 (2002).

[10] G. Boffetta and I. M. Sokolov, Phys. Rev. Lett. **88**, 094501 (2002).

[11] L. Biferale, G. Boffetta, A. Celani, B. J. Devenish, A. Lanotte, and F. Toschi, Physics of Fluids **17**, 111701 (2005).

[12] M. Bourgoin, N. T. Ouellette, H. Xu, J. Berg, and E. Bodenschatz, Science **311**, 835 (2006).

[13] J. Berg, B. Lüthi, J. Mann, and S. Ott, accepted for publication in Phys. Rev. E (2006).

[14] P. Franzese and M. Cassiani, submitted to JFM (2006).

[15] M. S. Borgas and P. Yeung, J. Fluid Mech. **503**, 125 (2004).

[16] D. J. Thomson, J. Fluid Mech. **210**, 113 (1990).

[17] U. Frisch, *Turbulence: The Legacy of A. N. Kolmogorov* (Cambridge University Press, 1995).

[18] A. Naso and A. Pumir, Phys. Rev. E **72**, 056318 (2005).

[19] V. Borue and S. A. Orzag, J. Fluid Mech. **366**, 1 (1998).

[20] B. Tao, J. Katz, and C. Meneveau, J. Fluid Mech. **457**, 35 (2002).

[21] A. Tsinober, *An Informal Introduction to Turbulence* (Kluwer Academic Publishers, 2001).

[22] S. S. Girimaji and S. B. Pope, JFM **220**, 427 (1990).

[23] E. Dresselhaus and M. Tabor, J. Fluid Mech. **236**, 415 (1994).

[24] M.-J. Huang, Physics of Fluids **8**, 2203 (1996).

[25] B. Lüthi, A. Tsinober, and W. Kinzelbach, J. Fluid Mech. **528**, 87 (2005).

[26] M. Guala, B. Lüthi, A. Liberzon, A. Tsinober, and W. Kinzelbach, J. Fluid Mech. **533**, 339 (2005).

[27] G. K. Batchelor, Proc. R. Soc. Lond. **213**, 349 (1952).

[28] B. L. Sawford, Physics of Fluids **3**, 1577 (1991).

[29] C. W. Gardiner, *Handbook of Stochastic Methods* (Springer Verlag, 1985).

[30] B. Sawford, P. K. Yeung, and M. S. Borgas, Physics of Fluids **17**, 095109 (2005).

[31] B. Sawford, J. of Turbulence **7**, 1 (2006).

[32] V. Artale, G. Boffetta, A. Celani, M. Cencini, and A. Vulpiani, Physics of Fluids (1997).

[33] P. K. Yeung, Ann. Rev. Fluid Dyn. **34**, 115 (2002).

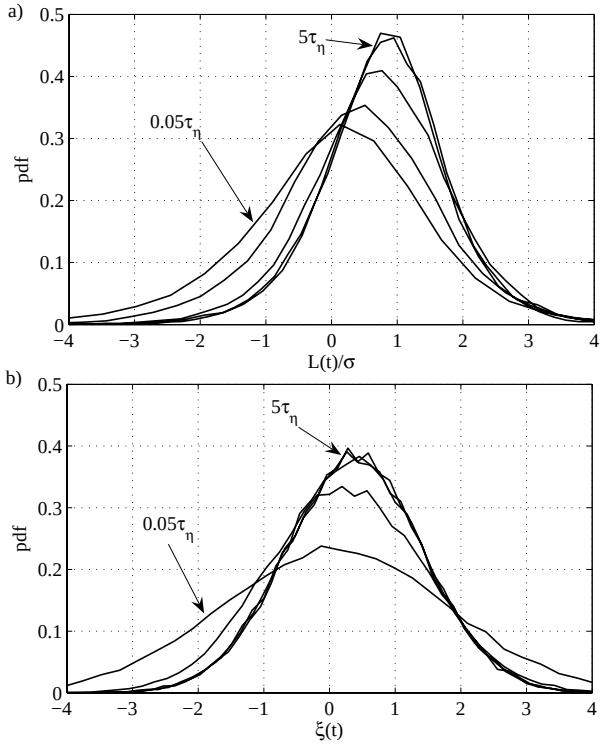

FIG. 1: (a) PDFs of the measured stretching rate, $L(t)$, for different times, $t/\tau_\eta = 0.05$, 0.5, 1.5, 3, 5, from bottom to top. The measurements are from the particle tracking experiment (PTV), described in [13]. (b) PDFs of the modelled $\xi(t)$, for different times, $t/\tau_\eta = 0.05$, 0.5, 1.5, 3, 5, from bottom to top.

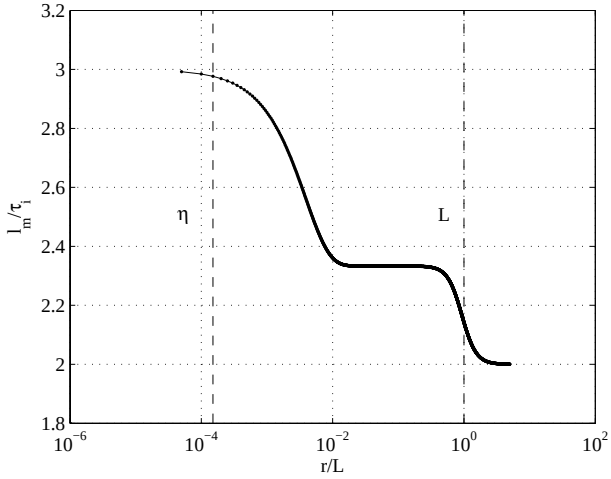

FIG. 2: The ratio of l_m/τ_i that is required in order for the the well-mixed condition to be full-filled is plotted versus $r/\mathcal{L}$.

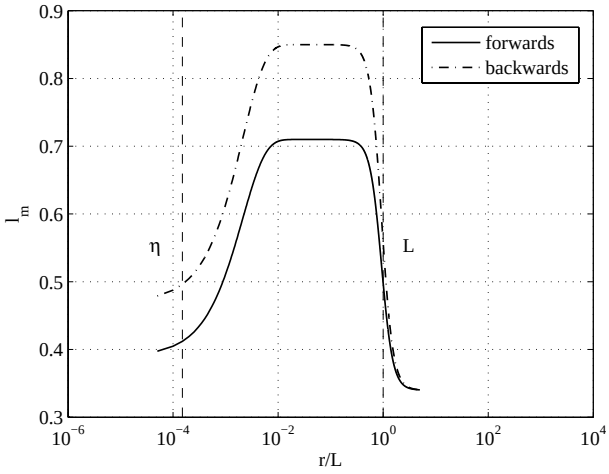

FIG. 3: $l_m\,(r)$ as obtained from expression 20 is plotted versus $r/\mathcal{L}$ for forwards (solid line) and backwards (dash-dot line) case.

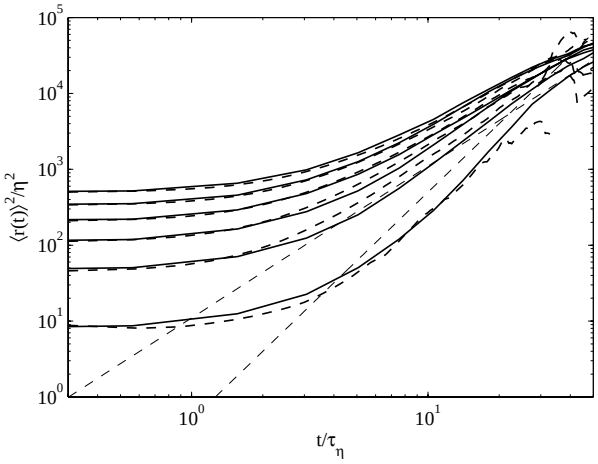

FIG. 4: Comparison of particle separations as obtained from particle tracking (dashed lines) versus model prediction (solid lines). The straight dashed lines are $y \propto t^2$ and $y = 0.5\varepsilon t^3$.

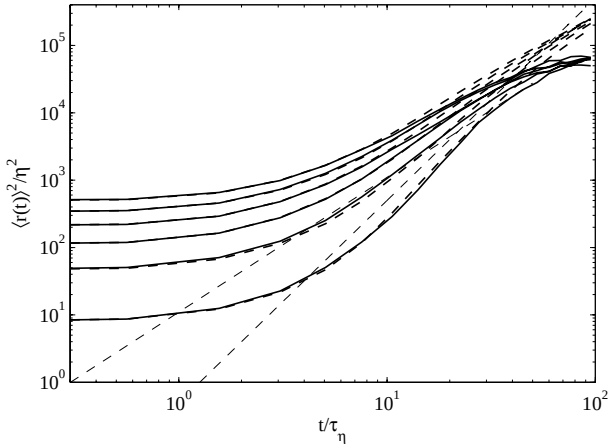

FIG. 5: Comparison of mean square separations as obtained with $d = 150$mm (solid lines) and $d = \infty$ (dashed lines). The straight dashed lines are $y \propto t^2$ and $y = 0.5\varepsilon t^3$.

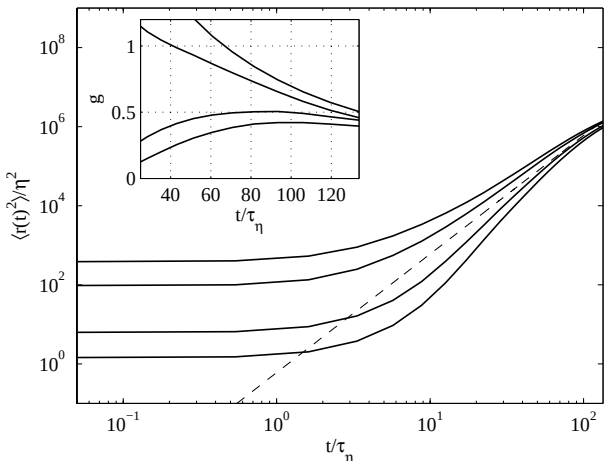

FIG. 6: Model predictions for particle separations over time and $g = \left\langle r\left(t\right)^2\right\rangle / \left(\varepsilon t^3\right)$ (inset), for conditions as in [11]. The dashed line is $y = 0.6\varepsilon t^3$.

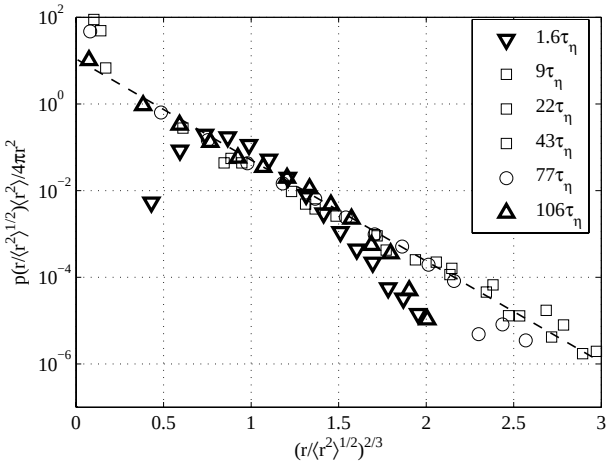

FIG. 7: Model predictions for the distance neighbour functions at different times, for $r_0/\eta = 1.2$, and for conditions as [11]. Straight dashed line denotes the solution as obtained from the Richardson diffusion equation.

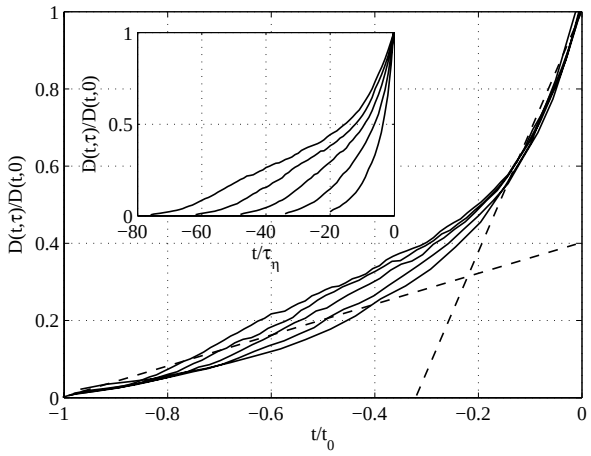

FIG. 8: Model predictions for the normalised correlation function $D(t,\tau)/D(t,0)$ versus t/t_0, with t_0 as the time where the correlation crosses zero, as shown in the inset. Conditions are as in [11]. Straight dashed lines denote results reported by [11].

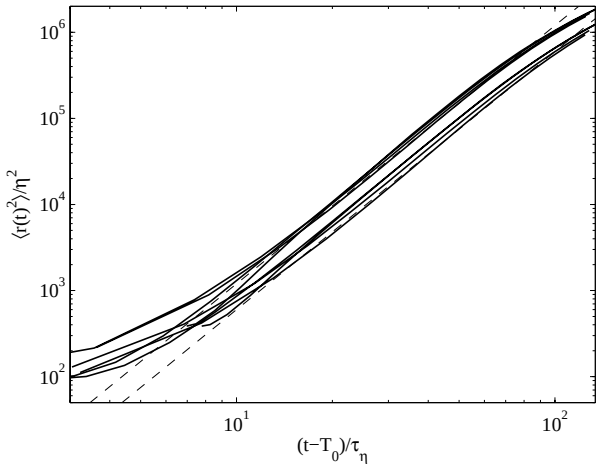

FIG. 9: Model predictions for the forwards and backwards dispersion. The dashed lines are $y = 0.6\varepsilon t^3$ and $y = 1.2\varepsilon t^3$.

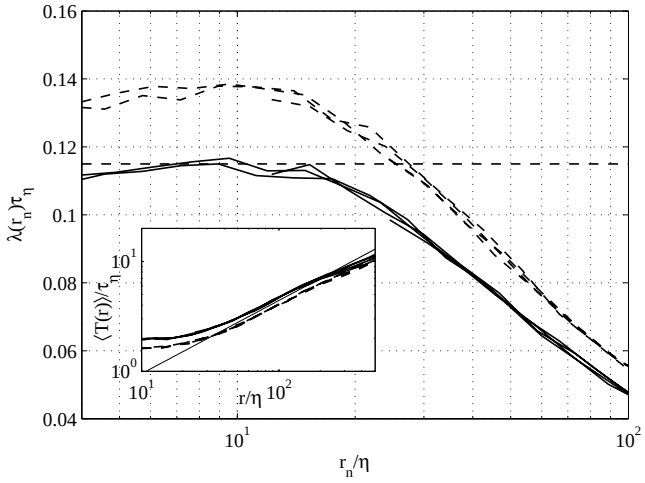

FIG. 10: Model predictions for the finite sized Lyapunov exponents for forwards and backwards dispersion with $\rho = 1.25$, dashed lines are for the backwards case, $Re_\lambda = 280$. The straight dashed line denotes the result obtained by Biferale et al. [11], $\lambda(r_n)\tau_\eta = 0.115$. Inset: Model predictions for mean exit times, dashed lines are for the backwards case, $Re_\lambda = 280$. The straight line is proportional to $r^{2/3}$.

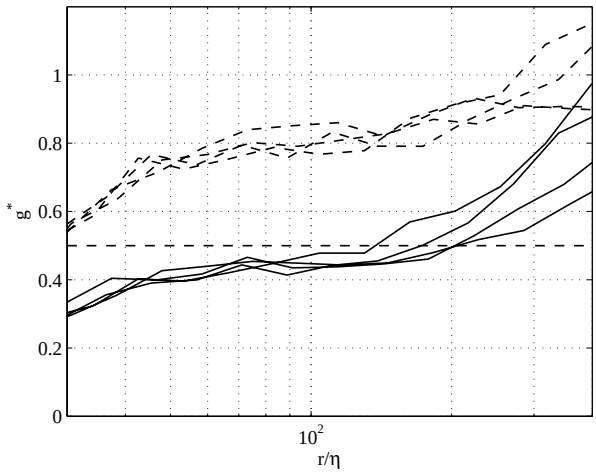

FIG. 11: Model predictions for the Richardson constant as obtained from eqn. 23, for forwards and backwards dispersion with $\rho = 1.25$, dashed lines are for the backwards case, $Re_\lambda = 280$. The straight dashed line denotes the result obtained by Biferale et al. [11], $g^* \approx 0.5$.

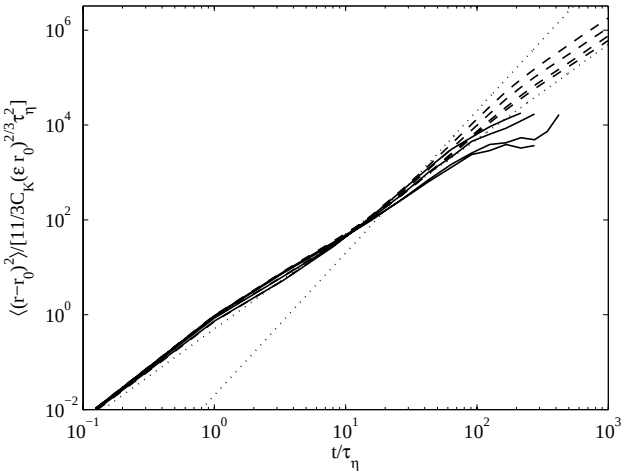

FIG. 12: Model predictions for $\left\langle (r - r_0)^2 \right\rangle$ normalized with $11/3 C_k (\varepsilon r_0)^{2/3} \tau_\eta^2$ versus time for initial separations: $r_0/\eta = 40, 80, 150, 200$, top to bottom. Experimental conditions of [12] are mimicked with $\mathcal{L}/\eta = 3000 \Rightarrow Re_\lambda = 815$, $d = 50mm$ (solid lines). Results for the same Reynolds number but with $d = \infty$ are plotted with dashed lines. Straight lines are proportional to t^2 and t^3.

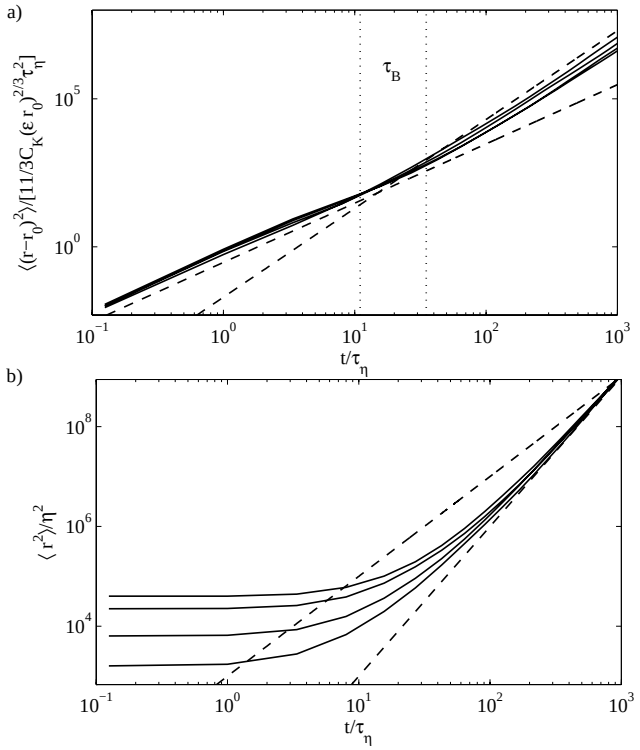

FIG. 13: Results for the ideal case with $Re_\lambda \to \infty$ and $d = \infty$ for initial separations $r_0/\eta = 40, 80, 150, 200$. Straight lines are proportional to t^2 and t^3. (a) Separation is plotted as in [12], dotted lines denote the range of τ_B. (b) Identical data as in (a) but plotted as in [11].

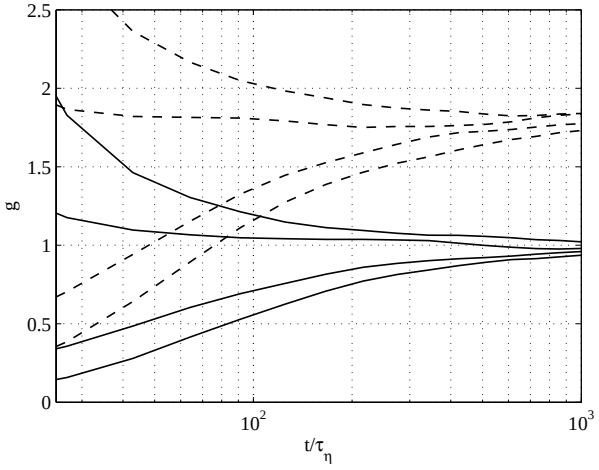

FIG. 14: Model predictions for $g = \left\langle r\,(t)^2 \right\rangle / \left(\varepsilon t^3\right)$ without inertial range constraint, $Re_\lambda \to \infty$, and with infinitely large observation domain, $r_0/\eta = 1.2$, 2.5, 10, 20. Results are given for forwards and backwards dispersion, dashed lines are for the backwards case.

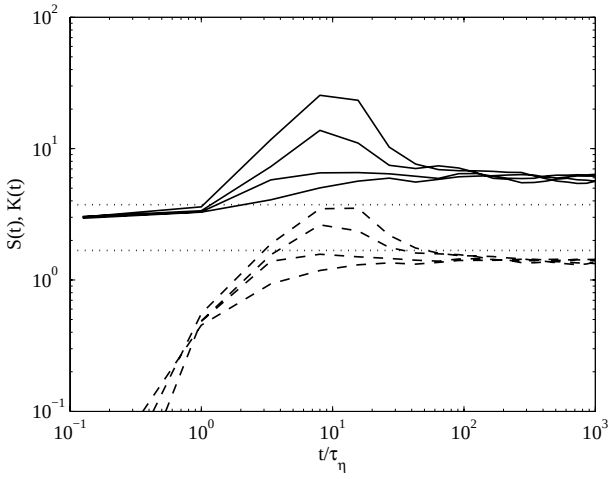

FIG. 15: Model predictions for skewness (dashed lines) and kurtosis (solid lines) coefficient of r without inertial range constraint. Initial separations from top to bottom are $r_0/\eta = 1.2$, 2.5, 10, 20. Dotted lines denote $S_R = 1.68$ and $K_R = 3.74$ as obtained from the Richardson diffusion equation.

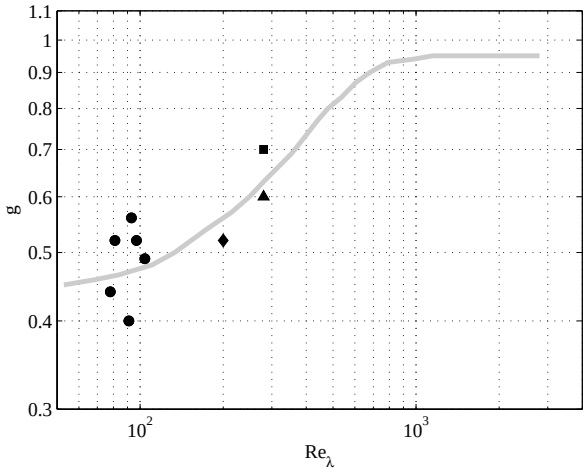

FIG. 16: Richardson constant g versus Re_λ as obtained from the presented model, $r_0/\eta = 50$ and $d = \infty$. Circles: Ott and Mann (2000) [8], diamond: Boffetta and Sokolov (2002) [10], square: Ishihara and Kaneda (2002) [9], triangle: Berg et al. (2006) [13] as obtained from data by [11].

V

Lagrangian multi-particle statistics

Beat Lüthi, Jacob Berg, Søren Ott and Jakob Mann

Risø National Laboratory beat.luthi@risoe.dk

Summary. Combined measurements of the Lagrangian evolution of particle constellations and the coarse grained velocity derivative tensor $\partial\widetilde{u}_i/\partial x_j$ are presented. The data is obtained from three dimensional particle tracking measurements in a quasi isotropic turbulent flow at intermediate Reynolds number. Particle constellations are followed for as long as integral time and for several Batchelor times. We suggest a method to obtain quantitatively accurate $\partial\widetilde{u}_i/\partial x_j$ from velocity measurements at discrete points. We obtain good scaling with $t_* = \sqrt{2r^2/15S_r\left(r\right)}$ for filtered strain and vorticity and present filtered R-Q invariant maps with the typical 'tear drop' shape that is known from velocity gradients at viscous scales. Lagrangian result are given for the growth of particle pairs, triangles and tetrahedra. We find that their principal axes are preferentially oriented with the eigenframe of coarse grained strain, just like constellations with infinitesimal separations are known to do. The compensated separation rate is found to be close to its viscous counterpart as $1/2\left(dr^2/dt\right)/r^2 \cdot t_*/\sqrt{2} \approx 0.11 - 0.14$. It appears that the contribution from the coarse grained strain field, $r_i r_j \widetilde{s}_{ij}$ filtered at scale $\Delta = r$, is responsible only for roughly 50% of the separation rate. The rest stems from contributions with scales $\Delta < r$.

1 Introduction

An important consequence of turbulence is effective mixing and dispersion of advected Lagrangian particles [1]. Recent work on two particle dispersion [2, 3] raised the question to what degree two particle separation in the inertial range is governed by the coarse grained velocity derivative field $\widetilde{A}_{ij} = \partial\widetilde{u}_i/\partial x_j$. Moreover, it has been recognized for a few years now that constellations with more than two particles have a rich structure at scales smaller than the integral scale $\mathcal{L}$ [4, 5, 6, 7, 8]. Work that started with [5] and currently is being further developed by [9] is relating the dynamics of $\widetilde{A}_{ij}$ to the evolution of tetrahedra and a stochastical model has been developed for its simulation. Experimental and numerical studies have investigated some of the properties of $\widetilde{A}_{ij}$ [10, 11]. The most important finding is that coarse grained velocity derivatives exhibit

roughly the same properties like their small scale counterparts. Probably the most important property is that $\left\langle \widetilde{\Lambda}_2 \right\rangle > 0$, where $\widetilde{\Lambda}_i$ are the eigenvalues of the rate of strain tensor $\widetilde{s}_{ij} = 1/2\,(\partial\widetilde{u}_i/\partial x_j + \partial\widetilde{u}_j/\partial x_i)$. It means that also for inertial range scales the field of velocity derivatives experiences self-amplification.

In this contribution, we present first time experimental results that attempt to combine measurements of $\widetilde{A}_{ij}$ with measurements of the evolution of particle pairs, triangles, and tetrahedra. The filter scale covers a good part of the inertial range and the particle constellations are followed as long as the integral time, $\mathcal{T}$, and for several Batchelor times, $\tau_B = R_0^{2/3}/\varepsilon^{1/3}$, where R_0 is the scale of the constellation at $t = 0$. Since Batchelor [12] it is known that for the case of two particle separation at τ_B the relative separation regime changes from $\left\langle r^2 - r_0^2 \right\rangle \propto t^2$, known as the ballistic regime, to $\left\langle r^2\,(t) \right\rangle = g\varepsilon t^3$, which is known as the Richardson law. The importance of having observation times $t > \tau_B$ can also be expressed in terms of kinetic energy of relative motion in a particle swarm of size R with N points, $E = 1/2\left\langle \left(\mathbf{u}^N - \mathbf{U}\right)^2 \right\rangle_R$: Only if tracking times are long enough a transition from the regime where $dE/dt < 0$ to a regime whith $dE/dt > 0$ can be observed [13]. The former regime is essentially governed by Eulerian dynamics while the latter is governed by the Lagrangian evolution of particle constellations.

One can define the tensor $\widetilde{A}_{ij}$ coarse grained at scale Δ as

$$\widetilde{A}_{ij} = \frac{1}{V_\Delta}\int_V \frac{\partial u_i}{\partial x_j} d^3x, \tag{1}$$

where $V_\Delta \approx \Delta^3$. If we provide an at least one time differentiable approximation to the velocity field as

$$\widetilde{\mathbf{u}}\,(\mathbf{x}) \approx \frac{1}{V_\Delta}\int_V \mathbf{u}\,(\mathbf{x})\, d^3x \tag{2}$$

we overcome the difficulty of having to measure $\frac{\partial u_i}{\partial x_j}$ directly but can instead differentiate the filtered velocity field to obtain

$$\widetilde{A}_{ij} = \partial\widetilde{u}_i/\partial x_j. \tag{3}$$

The left hand side of eqn. 2 can be approximated by least square fitting linear polynomials to discrete velocities of at least $n = 4$ points. Different to [14] here spherical polynomials that by definition are incompressible and orthogonal are used. Since for $\Delta > \eta$ the velocity field is not smooth $n > 4$ is necessary to obtain convergence for $\widetilde{\mathbf{u}}\,(\mathbf{x})$ to $1/V_\Delta \int_V \mathbf{u}\,(\mathbf{x})\, d^3x$. As we will demonstrate below in the result section we have found that $n > 12$ is sufficiently high.

2 3D-PTV Experiment

In our attempt to simultaneously measure $\widetilde{A}_{ij}$ and the evolution of particle constellations we have performed a Particle Tracking Velocimetry (PTV) experiment in an intermediate Reynolds number turbulent flow. PTV is by now a well established non-intrusive flow measuring technique [15, 16, 17, 18, 19, 14, 20, 2] which naturally allows to probe a flows Lagrangian properties. To meet the competing goals of high tracer seeding density to allow for coarse graining, and high trackability of particle constellations to reach $t > \tau_B$ some trade off's in the experimental design had to be made: Typically 900 particles are tracked in an observation volume of $15 \times 15 \times 15\text{cm}^3$. This results in an average particle distance of $d_p \approx 50\eta$ and tracking lengths longer than integral scales $t_T > \mathcal{T}$ and $t_T > 10\tau_B$. For the sake of 'good' statistics the total recording time is $t_R \approx 500\mathcal{T}$.

The flow is forced with eight rotating propellers placed in the corner of a water tank of $32 \times 32 \times 50\text{cm}^3$ and neutrally buoyant tracer particles are recorded with four synchronized, 50Hz CCD cameras. To suppress the development of a mean flow the propellers change their rotational direction after 0.5s of stirring and after an additional 0.5s of pausing. A typical propeller tip velocity is 50cm/s. Further details of the experiment are described in [2]. The characteristic flow properties are summarized in table 1. A recent modification of tracking 3d particle positions through consecutive time frames allows to connect tracked particle trajectories that are only interrupted by one 'missing' point. The main impact of this feature is a drastic increase of the number of long trajectories. The number of tracks with length $t_T > \mathcal{T}$ has more than doubled while the number of tracks with $t_T > 2\mathcal{T}$ is one order of magnitude larger.

Table 1. Flow properties of the turbulent flow as already reported in [2].

η	$\mathcal{L}$	τ_η	$\mathcal{T}$	ε	σ_u	$\mathcal{L}/\eta$	Re_λ
0.25mm	48mm	0.07s	2.45s	$168\text{mm}^2/\text{s}^3$	23mm/s	190	172

3 Properties of $\partial\widetilde{u}_i/\partial x_j$

In this section we present Eulerian results for $\widetilde{A}_{ij}$ for $100 < \Delta/\eta < 300$, where $\eta = \left(\nu^3/\varepsilon\right)^{1/4}$ is the Kolmogorov constant. The lower bound of Δ is defined by our experimental tracer seeding density. Only for volumes larger than $100\eta^3$ the number of particles is $n > 12$. In fig. 1(a) we plot the averages of $\widetilde{s}^2$ and $\widetilde{\omega}^2$ as a function of filtering scale Δ/η. The comparison with the straight dashed line that is proportional to $r^{-4/3}$ shows that there is no clear K41 scaling,

which is not surprising at the relatively low scale separation of $\mathcal{L}/\eta = 190$. Based on the longitudinal second order structure function $S_2(r)$ we construct a time, $t_*(r)$ with which a better compensation of $\widetilde{A}_{ij}$ can be obtained. We define

$$t_* = \sqrt{\frac{2r^2}{15S_2(r)}}, \tag{4}$$

which for $r \ll \eta$ gives $t_*(r) = \sqrt{2}\tau_\eta$ in order that $\left\langle s^2 \right\rangle \cdot t_*^2 = 1$. For $\eta \ll r \ll \mathcal{L}$ eqn. 4 is proportional to $r^{2/3}$. With the parametrized form of $S_2(r)$ employed by [21]

$$\widetilde{S}_2(r) = 2\left(1 - \exp\left(-\frac{r}{(15C_k)^{3/4}\,\eta}\right)\right)^{4/3} \cdot (\varepsilon\mathcal{L})^{2/3}\left(\frac{r^4}{\frac{64\mathcal{L}^4}{C_k^6} + r^4}\right)^{1/6} \tag{5}$$

the second order structure function is expressed as a function of separation r, the viscosity ν, the flow properties $\mathcal{L}$ and ε and the Kolmogorov constant C_k. Again in fig. 1(a) we show $\left\langle \widetilde{s}^2 \right\rangle \cdot t_*^2$ and $\left\langle \widetilde{\omega}^2 \right\rangle \cdot t_*^2$ as a function of Δ/η. Clearly the more general scaling with eqn. 4 holds over our entire range of $100 < \Delta/\eta < 300$ as $\widetilde{s}^2 \cdot t_*^2 \approx 1$. To see how far off the approximation of $\widetilde{A}_{ij}$ is with a too low number of points we show in fig. 1(b) the same quantities for $n = 4$ points. Up to $\Delta/\eta \approx 160$ there is a seemingly nice K41 scaling. However, at $\Delta/\eta = 100$ we have $\left\langle \widetilde{s}^2 \right\rangle \approx 50$, which is much too high if we keep in mind that for $\varepsilon = 168\mathrm{mm}^2/\mathrm{s}^3$ at the smallest scale $\left\langle s^2 \right\rangle \approx 80$. Furthermore, the compensated strain is much too high with $s^2 \cdot t_*^2 \approx 8$.

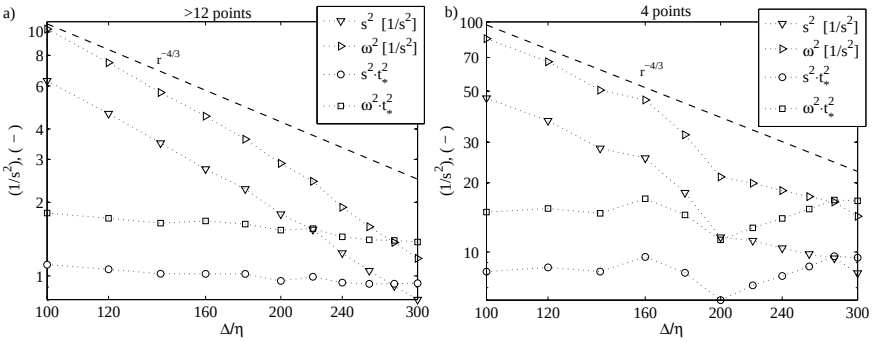

Fig. 1. Coarse grained mean strain $\left\langle \widetilde{s}^2 \right\rangle$ and enstrophy $\left\langle \widetilde{\omega}^2 \right\rangle$ are plotted versus filtering scale Δ/η along with the compensated values $\left\langle \widetilde{s}^2 \right\rangle \cdot t_*^2$ and $\left\langle \widetilde{\omega}^2 \right\rangle \cdot t_*^2$. In (a) results are obtained from $n > 12$ points per least square fit to linear polynomials and in (b) only $n = 4$ points are used.

The qualitative difference between $\widetilde{A}_{ij}$ as obtained from $n = 4$ or $n > 12$ becomes even clearer if we look at the PDFs of the strain 'shape' Λ_2/Λ_1.

It is known that in the viscous range $\langle \Lambda_2 \rangle / \langle \Lambda_1 \rangle \approx 0.15$ over a wide range of Reynolds numbers [22, 23, 14] and also for inertial scales it is reported that $\left\langle \widetilde{\Lambda}_2 / \widetilde{\Lambda}_1 \right\rangle > 0$ [10, 11]. This means that also larger scale $\widetilde{A}_{ij}$ have a self-amplifying nature. In fig. 2(a) we see that the PDFs for the shapes obtained for $100 < \Delta/\eta < 300$ almost collapse and yield a mean value of $\left\langle \widetilde{\Lambda}_2 / \widetilde{\Lambda}_1 \right\rangle \approx 0.15$. Contrary, in fig. 2(b) the same PDFs but obtained from only $n = 4$ points peak at zero and $\left\langle \widetilde{\Lambda}_2 / \widetilde{\Lambda}_1 \right\rangle \approx 0$, i.e. one of the most important turbulent property is lost completely.

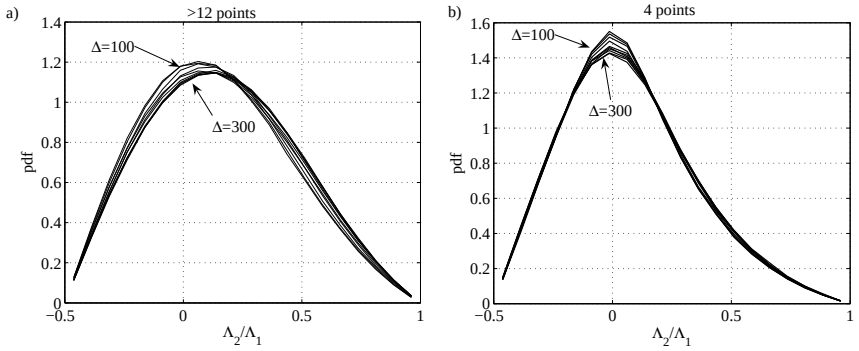

Fig. 2. PDFs for the coarse grained strain shape $\widetilde{\Lambda}_2/\widetilde{\Lambda}_1$ for filter scales $100 < \Delta/\eta < 300$. In (a) results are obtained from $n > 12$ points per least square fit to linear polynomials and in (b) only $n = 4$ points are used.

In fig. 3(a,b) we show how the large scale axis-symmetry that for this experiment was already reported in [2] is reflected in $\widetilde{A}_{ij}$, especially for large Δ/η. In fig. 3(a) we see the preferential orientation with $\mathbf{x}_3$ of the most stretching principal strain axis $\widetilde{\lambda}_1$ of $\widetilde{s}_{ij}$. $\mathbf{x}_3$ is the vertical tank axis, which with $32 \times 32 \times 50\text{cm}^3$ is higher than wide. Towards lower scales a slow relaxation of this anisotropy can be observed, similar to reports of [9]. For $\widetilde{\omega}$ the situation is slightly different as is shown in fig. 3(b). It seems that consistent with the tank dimensions large scale vorticity is preferentially aligned with the longer vertical tank axis but equally distributed over both directions of rotation. Towards larger scales the symmetry is broken slightly as the horizontal component of vorticity starts to align with $+\mathbf{x}_1$ and $-\mathbf{x}_2$.

Finally we show in fig. 4 the topological property of measured $\widetilde{A}_{ij}$ by means of the two invariants R and Q [24]. The normalized invariants are defined as

$$Q = -\frac{1}{2} Tr\left(\widetilde{A}_{ij}^2\right) / \left\langle \widetilde{s}^2 \right\rangle, \; R = -\frac{1}{3} Tr\left(\widetilde{A}_{ij}^3\right) / \left\langle \widetilde{s}^2 \right\rangle^{3/2}. \tag{6}$$

For plots obtained from only $n = 4$ points we see that essentially for all scales $100 < \Delta/\eta < 300$ the RQ-shapes look like such obtained from Gaussian

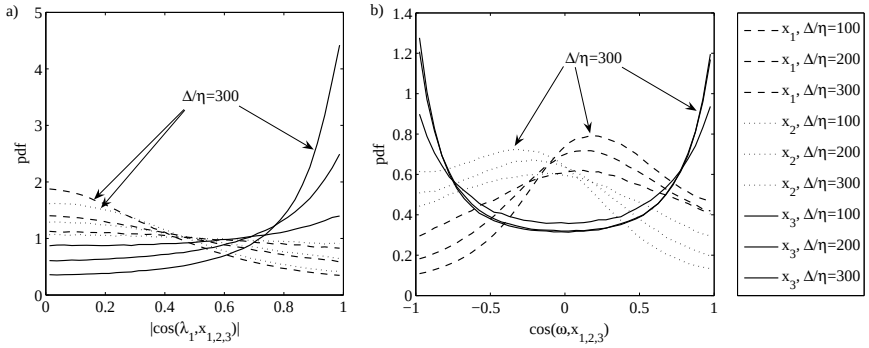

Fig. 3. (a) PDFs of the cosines between the most stretching principal coarse grained eigenvector $\widetilde{\lambda}_1$ and the coordinate directions $\mathbf{x}_{1,2,3}$ for three different scales Δ/η. $\mathbf{x}_{1,2}$ are the horizontal directions and $\mathbf{x}_3$ is the vertical direction. (b) PDFs of the cosines between coarse grained vorticity $\widetilde{\omega}$ and the coordinate directions $\mathbf{x}_{1,2,3}$ for three different scales Δ/η.

velocity fields [22]. Very differently for $n > 12$ the well known 'tear drop' shapes are recovered for all scales. This is at first surprising since we would expect Gaussian RQ-shapes for $\Delta > \mathcal{L}$. Indeed, for $\Delta/\eta = 200$ we observe the most symmetric RQ-shape for the $n > 12$ figures. The only explanation we have is that the observed 'tear drop' shapes at larger than integral scales are caused by large scale mean strain. This effect has already been observed in stochastical model results [9].

4 Multi point statistics

In the previous section we established that the measured $\widetilde{A}_{ij}$ is approximating well the actual coarse grained velocity derivative tensor. In this section we show how particle pairs, triangles and tetrahedra grow in time and how their principal axes are oriented with respect to $\widetilde{A}_{ij}$. In addition, we check to what degree the kinematic relation for the growth of pairs r

$$\frac{1}{2}\frac{dr^2}{dt} = r_i r_j s_{ij}, \tag{7}$$

which in the viscous range is exactly true, also holds in the inertial range.

We start with the growth of particle constellations. In fig. 5(a,b) we show how normalized separations, areas and volumes grow in time. Times are normalized with τ_B that correspond to initial scales R_0, which for pairs are r_0. For evolving triangles or tetrahedra we use $R_0 = \sqrt{g_1}$, where g_1 is the largest eigenvalue of the moment of inertia tensor

$$g^{ab} = \sum \rho_i^a \rho_i^b \tag{8}$$

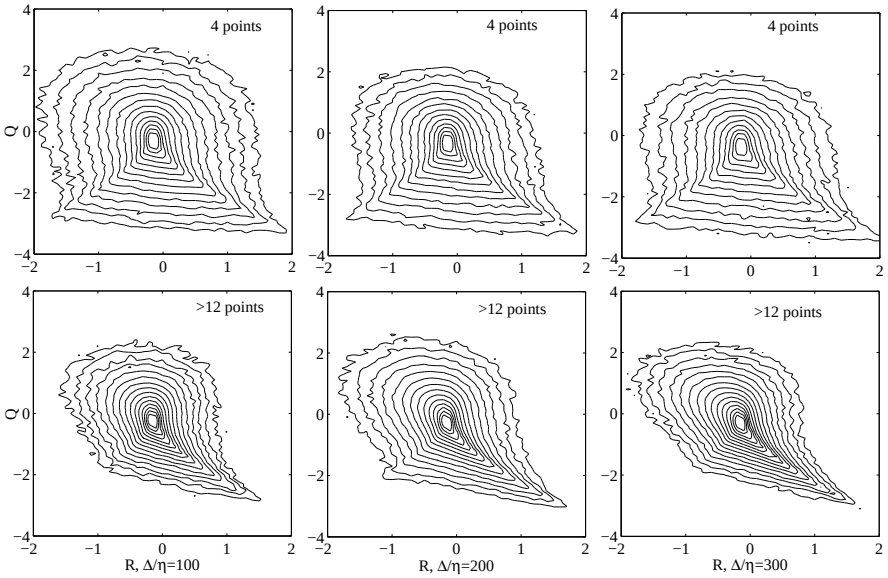

Fig. 4. Joint PDFs of the invariants R and Q as defined in eqn. 6. Shown are results from $n > 12$ points per least square fit to linear polynomials (bottom row) and $n = 4$ points (top row) for three different filtering scales $\Delta/\eta = 100, 200, 300$. The isoprobability contours are logarithmically spaced.

$$\rho_1 = (\mathbf{x}_1 - \mathbf{x}_2)/\sqrt{2}$$
$$\rho_2 = (2\mathbf{x}_3 - \mathbf{x}_1 - \mathbf{x}_2)/\sqrt{6}$$
$$\rho_3 = (3\mathbf{x}_4 - \mathbf{x}_1 - \mathbf{x}_2 - \mathbf{x}_3)/\sqrt{12}$$

that was introduced in [5]. Growth is scaling nicely with the Batchelor time τ_B. However, neither pairs, nor triangles nor volumes reach a convincing Richardson scaling of $\propto \varepsilon^{1/2}t^{3/2}$, εt^3, or $\varepsilon^{3/2}t^{9/2}$, denoted by the straight dotted lines. We attribute this to the too low scale separation of our experiment. In fig. 5(a) it can be seen how shortly before $r_0 = \mathcal{L}$ (denoted by circles) the growth rate starts weakening. For triangles and volumes reaching of integral scale coincides with data becoming too sparse.

Fig. 6 shows the temporal evolution of the eigenvalues of the tensor g^{ab} defined in eqn. 9 and the evolution of the mean shape factors $\langle w \rangle$ and $\langle I_2 \rangle$ for triangles and tetrahedra respectively. These shape factors are a measure for the elongation and $w = 0$ and $I_2 = 0$ would be obtained for needle-like objects. Following [6] they are defined as

$$I_2 = g_2/R^2 \tag{9}$$
$$w = 2\sqrt{I_2\,(1 - I_2)} \tag{10}$$

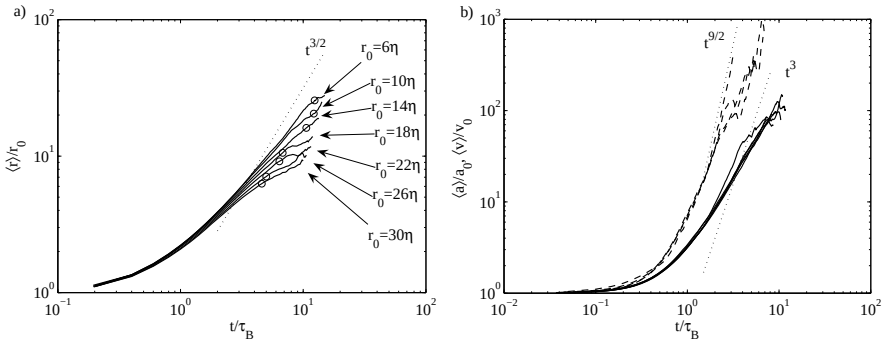

Fig. 5. Normalized mean separation $\langle r\rangle/r_0$ (a), triangle areas $\langle a\rangle/a_0$ and tetrad volumes $\langle v\rangle/v_0$ versus t/τ_B (b). Initial scales are $6 < r_0/\eta < 30$ (a) and $14 < r_0/\eta < 30$ and $22 < r_0/\eta < 30$ for triangles and volumes(b). The straight dotted lines are proportional to $t^{3/2}$, t^3, $t^{9/2}$. Circles in (a) denote when $\langle r\rangle = \mathcal{L}$.

where $R^2 = \rho_1^2 + \rho_2^2 + \rho_3^2$ is the radius of gyration. Again, the eigenvalues do not reach Richardson scaling that is denoted by straight dotted t^3 lines in fig. 6(a,b). For the tetrahedra it can be observed how at early times, where due to small scales the velocity field is still quite smooth, the volumes are almost conserved. This is reflected in initially decreasing mean values of g_3, which are the most compressed directions of the tetrahedra. Both shape factors reach a stable plateau after a short transient time in which the initially regular shapes assume their intermediate state. It is difficult to answer if these intermediate states are self-similar or just Gaussian. The noise level is relatively high and our inertial range is very small. In addition, as can be seen by the straight dotted lines of fig. 6(c), the values for self-similar and Gaussian shapes are fairly close together. From slightly higher Reynolds number DNS simulations [8] deduced $I_2 \approx 0.16$ for the inertial range while the Gaussian value is $I_2 \approx 0.22$ [6]. Our data lies inbetween for tetrahedra and, since three points are 'easier' to follow, probably also for triangles for which we don't know the corresponding values.

We now look at how evolving particle constellations are oriented with respect to the strain eigenframe spanned by the coarse grained eigenvectors $\widetilde{\lambda}_i$. For the following Lagrangian results we use as an evolving filtering scale $R_0(t) = r(t)$ or $R_0(t) = \sqrt{g_1(t)}$. For infinitesimal separations and also for infinitesimal areas is is well known that after a transient time of $t/\tau_\eta > 1$ separation vectors are predominately aligned with the most stretching axis $\widetilde{\lambda}_1$ and that surface normals are predominately aligned with the most compressing axis $\widetilde{\lambda}_3$ [25, 22, 14, 26]. It is natural to expect the larger scale counterparts r_0, g_1, and g_3 of pairs, areas and volumes to behave similarly. In fig. 7 and 8 we present experimental evidence for this. PDFs for all cases are shown for $t > \tau_B$, i.e. τ_B is replacing τ_η as the relevant time scale. Initial scales range from $6 < \eta < 30$, $14 < \eta < 30$, and $22 < \eta < 30$, for pairs, triangles and

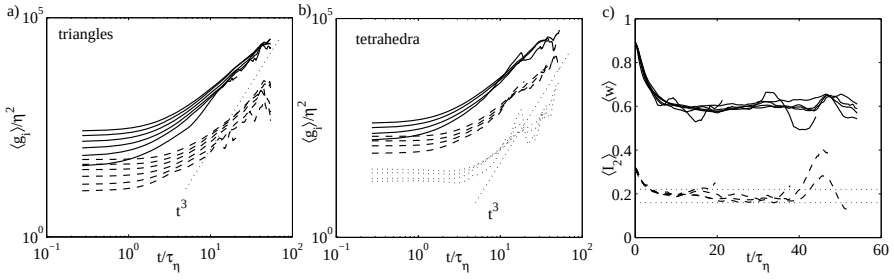

Fig. 6. Temporal evolution of mean eigenvalues of the tensor g^{ab}, solid lines for g_1, dashed lines for g_2 and dotted lines for g_3(a,b). Initial separations range from $14 < \eta < 30$ for triangles and from $22 < \eta < 30$ for tetrahedra with 4η spacing. (c) Mean shape factors $\langle w \rangle$ and $\langle I_2 \rangle$ for triangles and tetrahedra. The straight dotted lines denote inertial range value $I_2 \approx 0.16$ and the Gaussian value $I_2 \approx 0.22$.

tetrahedra respectively. This is reflecting that it is more difficult to find e.g. four points close by and to be able to track them for a long time than it is to find and track 'just' a pair. In all cases we observe a clear alignment of r and g_1 with $\widetilde{\lambda}_1$ (fig.7), and moreover, the PDFs for pairs, triangles and tetrahedra are almost identical also on a quantitative level. For the surface normals of triangles and the smallest eigen-direction of tetrahedra, g_3, we see a clear preferential alignment with the compressing principal axis $\widetilde{\lambda}_3$ (fig. 8). These alignments are one way to explain why in the inertial range flat and elongated structures can be observed as it is reported in [6, 8].

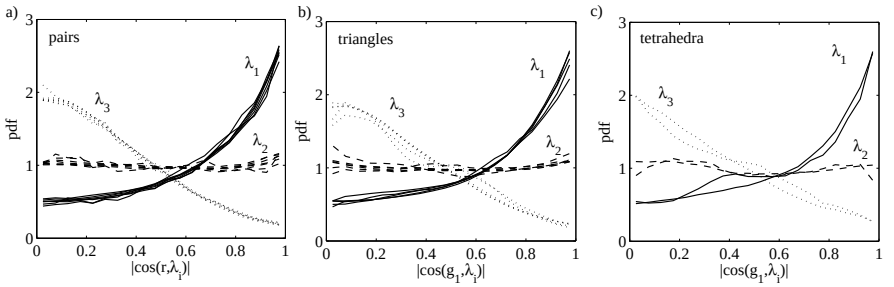

Fig. 7. PDFs of the cosines between the most elongated axis of particle constellations and the eigenframe of the filtered strain tensor $\widetilde{s}_{ij}$ at $t > \tau_B$. (a) Particle pairs with initial separations r_0 of $6 < r_0/\eta < 30$. (b) Particle triangles with initial $R_0 = \sqrt{g_1}$ of $14 < R_0/\eta < 30$. (c) Particle tetrahedra with initial $R_0 = \sqrt{g_1}$ of $22 < R_0/\eta < 30$.

Such alignments to principal axes only affect separations if the corresponding strain field $\widetilde{s}_{ij}$ is strong enough. As we have seen above in fig. 1 this seems to be the case. For particle pairs we now directly check how much the inertial

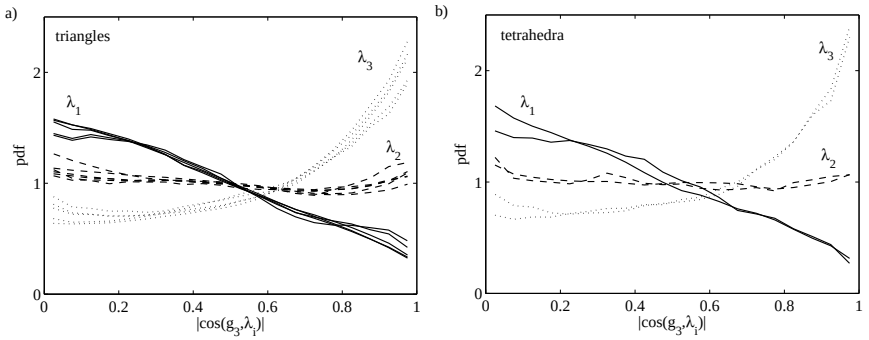

Fig. 8. PDFs of the cosines between the shortest axis of particle constellations and the eigenframe of the filtered strain tensor $\widetilde{s}_{ij}$ at $t > \tau_B$. (a) Triangles with initial $R_0 = \sqrt{g_1}$ of $14 < R_0/\eta < 30$. (c) Tetrahedra with initial $R_0 = \sqrt{g_1}$ of $22 < R_0/\eta < 30$.

counterpart of eqn. 7

$$\frac{\frac{1}{2}\frac{dr^2}{dt}}{r^2} \cdot \tau_\eta \cong \frac{r_i r_j \widetilde{s}_{ij}}{r^2} \cdot \tau_\eta \tag{11}$$

is balanced. In other words, we check to what degree particle separation

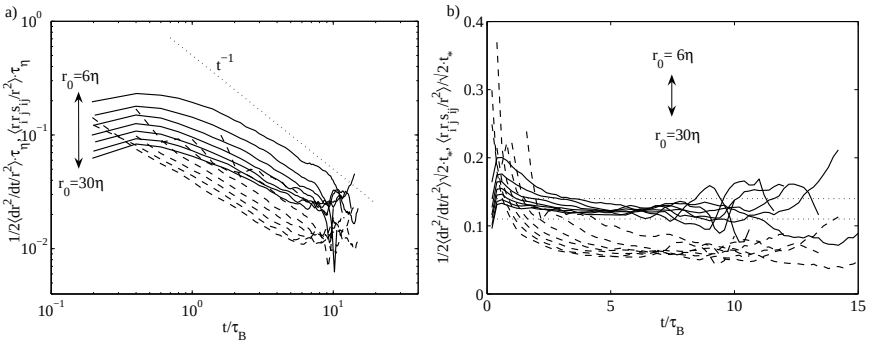

Fig. 9. (a) Temporal evolution of the means of l.h.s (solid lines) and r.h.s. (dashed lines) of eqn. 11. Initial separations are $6 < r_0/\eta < 30$ with 4η spacing. (b) Same data as in (a) but all quantities are compensated with $t_*/\sqrt{2}$ of eqn. 4. The two straight dotted lines denote the interval between 0.11 and 0.14.

$dr\,(t)\,/dt$ is governed by the strain field filtered at the local scale $\Delta = r\,(t)$ as it is assumed in [3]. Fig. 9(a) shows the temporal evolution of averages of the l.h.s. and r.h.s. of eqn. 11 for initial separations $6 < r_0/\eta < 30$. For the r.h.s. values are only given if separations are large enough to find $n > 12$ particles inside volumes of $v = r^3\,(t)$. We see how at early times the terms

are roughly balanced but at later times it is clear that $1/2dr^2/dt > r_i r_j \widetilde{s}_{ij}$. This means that a significant part of separation must be caused by scales $\Delta < r\,(t)$. In fig. 9(b) we show the same quantities but compensated with $t_*/\sqrt{2}$ that was introduced above with eqn. 4. We observe a good scaling for $1/2\left(dr^2/dt\right)/r^2$ while the compensated $r_i r_j \widetilde{s}_{ij}/r^2$ continues to decrease. The two straight dotted lines at 0.11 and 0.14 denote the interval of the seemingly universal stretching rate for the viscous scales [25, 22, 14, 26, 2]. Our data for the compensated large scale separation rates fall into this range. It thus appears, that the total separation rate indeed does behave like its viscous counterpart, also on a quantitative level, as it was assumed in [3]. However, we infer that the total separation must be the sum of contributions that stem also from smaller scales $\Delta < r$. The contribution from $r_i r_j \widetilde{s}_{ij}$, filtered at scale $\Delta = r$, is in our case roughly 50%.

References

1. Brian Sawford. Turbulent relative dispersion. *Ann. Rev. Fluid Mech.*, 33:289–317, 2001.
2. Jacob Berg, Beat Lüthi, Jakob Mann, and Søren Ott. An experimental investigation: backwards and forwards relative dispersion in turbulent flow. *accepted for publication in Phys. Rev. E*, 2006.
3. Beat Lüthi, Jacob Berg, Søren Ott, and Jakob Mann. Self similar two particle separation model. *submitted to Phys. Fluids*, 2006.
4. Laurent Mydlarski, Alain Pumir, Boris I. Shraiman, Eric D. Siggia, and Zellman Warhaft. Structures and multipoint correlators for turbulent advection: Predictions and experiments. *Phys. Rev. Lett.*, 81(20):4373–4376, 1998.
5. Misha Chertkov, Alain Pumir, and Boris I. Shraiman. Lagrangian tetrad dynamics and the phenomenology of turbulence. *Physics of Fluids*, 11(8):2394–2410, August 1999.
6. Alain Pumir, Boris I. Shraiman, and Misha Chertkov. Geometry of Lagrangian dispersion in turbulence. *Phys. Rev. Lett.*, 85(25):5324–5327, December 2000.
7. A. Naso and A. Pumir. Scale dependence of the coarse-grained velocity derivative tensor structure in turbulence. *Phys. Rev. E*, 72:056318, 2005.
8. L. Biferale, G. Boffetta, A. Celani, B. J. Devenish, A. Lanotte, and F. Toschi. Multiparticle dispersion in fully developed turbulence. *Physics of Fluids*, 17(11):111701, 2005.
9. A. Naso and A. Pumir. Scale dependence of the coarse-grained velocity derivative tensor: Influence of large-scale shear on small-scale turbulence. *J. of Turbulence*, 7(41), 2006.
10. Vadim Borue and Steven A. Orzag. Local energy flux and subgrid-scale statistics in three-dimensional turbulence. *J. Fluid Mech.*, 366:1–31, 1998.
11. Fedderik van der Bos, Bo Tao, Charles Meneveau, and Joseph Katz. Effects of small-scale turbulent motions on the filtered velocity gradient tensor as deduced from holographic particle image velocimetry measurements. *Physics of Fluids*, 14(7):2456–2474, 2002.
12. G. K. Batchelor. Diffusion in a field of homogeneous turbulence. II The relative motion of particles. *Proc. Cambridge Phil. Soc.*, 48:345–363, 1952.

13. Alain Pumir, Boris I. Shraiman, and Misha Chertkov. The Lagrangian view of energy transfer in turbulent flow. *EuroPhys. Lett.*, 56(3):379–385, 2001.
14. Beat Lüthi, Arkady Tsinober, and Wolfgang Kinzelbach. Lagrangian measurement of vorticity dynamics in turbulent flow. *J. Fluid Mech.*, 528:87–118, 2005.
15. T. Chang and G. Taterson. Application of image processing to the analysis of three-dimensional flow fields. *Opt. Engng*, 23:283–287, 1983.
16. R. Racca and J. Dewey. A method for automatic particle tracking in a three-dimensional flow field. *Experiments in Fluids*, 6:25–32, 1988.
17. Marko Virant and Themistocles Dracos. 3D PTV and its application on Lagrangian motion. *Meas. Sci. Technol.*, 8:1529–1552, 1997.
18. Søren Ott and Jakob Mann. An experimental investigation of the relative diffusion of particle pairs in three dimensional turbulent flow. *J. Fluid Mech.*, 422:207–223, 2000.
19. A. La Porta, Greg A. Voth, Alice M. Crawford, Jim Alexander, and Eberhard Bodenschatz. Fluid particle accelerations in fully developed turbulence. *Nature*, 409:1016–1017, Feb. 2001.
20. Mickaël Bourgoin, Nicholas T. Ouellette, Haitao Xu, Jacob Berg, and Eberhard Bodenschatz. Pair Dispersion in Turbulence. *Science*, 311:835–838", 2006.
21. Michael S. Borgas and P.K. Yeung. Relative dispersion in isotropic turbulence. part 2. A new stochastic model with Reynolds-number dependence. *J. Fluid Mech.*, 503:125–160, 2004.
22. A. Tsinober. *An Informal Introduction to Turbulence*. Kluwer Academic Publishers, 2001.
23. M. Kholmyansky, A. Tsinober, and S. Yorish. Velocity derivatives in the atmospheric surface layer at Re-lambda=10^4. *Physics of Fluids*, 13(1):311–314, 2001.
24. B.J. Cantwell. Exact solution of a restricted euler equation for the velocity-gradient tensor. *Physics of Fluids*, 4(4):782–793, 1992.
25. S. S. Girimaji and S. B. Pope. Material-element deformation in isotropic turbulence. *J. Fluid Mech.*, 220:427–458, 1990.
26. Michele Guala, Beat Lüthi, Alex Liberzon, Arkady Tsinober, and Wolfgang Kinzelbach. On the evolution of material lines and vorticity in homogeneous turbulence. *J. Fluid Mech.*, 533:339–359, 2005.

VI

Coarse-grained strain dynamics and backwards/forwards dispersion

Jacob Berg,* Beat Lüthi, Søren Ott, and Jakob Mann

Risø National Laboratory, 4000 Roskilde, Denmark

(Dated: August 30, 2006)

Abstract

A Particle Tracking Velocimetry experiment has been performed in a turbulent flow at intermediate Reynolds number. We present experimentally obtained stretching rates for particle pairs in the inertial range. Only when compensated by a characteristic time scale for coarse-grained strain do we observe constant stretching. This indicate that the process of material line stretching taking place in the viscous subrange has its counterpart in the inertial subrange. We investigate both forwards and backwards dispersion. We find a faster backwards stretching and relate it to the problem of relative dispersion and its time asymmetry.

*Electronic address: jacob.berg.joergensen@risoe.dk

I. INTRODUCTION

Fluid turbulence is still not fully understood. Although the governing equation, the deterministic Navier-Stokes equation is well known, its solutions are not. Phenomenological models are therefore central to turbulence theory [8]. These models, inspired by Richardson and Kolmogorov, describe the statistical structures of small scale turbulence under *ideal* homogeneous and isotropic conditions. For flow with more realistic boundary conditions such as flow over a complex terrain [1, 6] or the flow around an wind turbine rotor [21] prognostic turbulence models are utilized. With different degree of success they manage to capture the most important turbulence characteristics central to some specific task [17]. A promising class of models are the Large Eddy simulations (LES). In LES the Navier-Stokes equation is explicitly solved for scales larger than a filtering scale Δ. Below this scale the dynamics are parameterized. One of the big challenges in LES is thus to choose the right parametrization: in non-linear systems infinitesimal errors introduced on the smallest scales can in a finite time grow so that even the largest scales in the system are affected.

The parameterization can be thought of as a coarse-graining of Lagrangian fluid particles [19]. We therefore expect Kolmogorov similarity scaling to hold for the coarse-grained quantities as long as the filtering scale is less than the integral scale in the flow where the turbulence is solely represented by the kinetic energy dissipation of the flow, ε [4, 7, 11, 14, 19, 22, 23].

We define the coarse-grained velocity gradient tensor to be

$$\widetilde{A}_{ij}^{\Delta} = \frac{\partial \widetilde{u}_j^{\Delta}}{\partial x_i}, \tag{1}$$

where $\tilde{\mathbf{u}}^{\Delta}(\mathbf{x}, t)$ is the coarse-grained velocity over scale Δ:

$$\widetilde{u}_i^{\Delta}(\mathbf{x}) = \frac{1}{V} \int_{B_{\Delta/2}} d\mathbf{r}\, u_i(\mathbf{x} + \mathbf{r}). \tag{2}$$

Here $B_{\Delta/2}$ denotes a Ball with radius $\Delta/2$ and V its volume.

Berg et al. [2] speculated that the kinematic governing infinitesimal material line stretching has its counter-part in the inertial range and that different stretching rates could then explain the difference in forwards and backwards dispersion observed in their Particle Tracking Velocimetry (PTV) experiment. Through a finite Reynolds number formulation of the much celebrated Richardson law $\langle r^2 \rangle = g\varepsilon t^3$ describing inertial range separation r of nearby

particle pairs, it was found that following two particles backwards in time the dispersion was faster by a factor of approximately two compared with following the particles forwards in time. The work was motivated by a stochastic model study by Sawford et al. [20] where it was also found that backwards dispersion is the faster.

Yet another stochastic model was developed by Lüthi et al. [11]. By assuming that stretching rates in the inertial range are self-similar the results by [2] was verified. By self-similar stretching rates we think of stretching rates which are similar on the different scales. The self-similarity of stretching rates has, however, not been shown.

In this paper we will follow the lines of the above mentioned work and present experimental evidence of self-similar stretching rates in a turbulent flow of intermediate Reynolds number. The result is linked to particle pair separation and is able to account for the difference in forwards and backwards dispersion observed in [2].

II. EXPERIMENTAL METHOD

We have performed a Particle Tracking Velocimetry (PTV) experiment in an intermediate Reynolds number turbulent flow. The flow has earlier been reported in [2]. PTV is an experimental method suitable for obtaining Lagrangian statistics in turbulent flows [5, 12, 13, 15, 18, 25]: Lagrangian trajectories of fluid particles in water are obtained by tracking neutrally buoyant particles in space and time. The flow is generated by eight rotating propellers, which change their rotational direction in fixed intervals in order to suppress a mean flow, placed in the corners of a tank with dimensions $32 \times 32 \times 50\text{cm}^3$ (see Fig 1). The data acquisition system consists of four commercial CCD cameras with a maximum frame rate of 50Hz at 1000×1000 pixels. The measuring volume covers roughly $(12\text{cm})^3$. We use polystyrene particles with size $\sim 400\mu$m and density very close to one. We follow $\mathcal{O}(1000)$ particles at each time step with a position accuracy of 0.05 pixels corresponding to less than 10μm.

The Stokes number, τ_I/τ_η (τ_I denotes the inertial relaxation time for the particle to the flow while τ_η is the Kolmogorov time) is much less than one and the particles can therefore be treated as passive tracers in the flow. The particles are illuminated by a 250W flash lamp.

The mathematical algorithms for translating two dimensional image coordinates from the

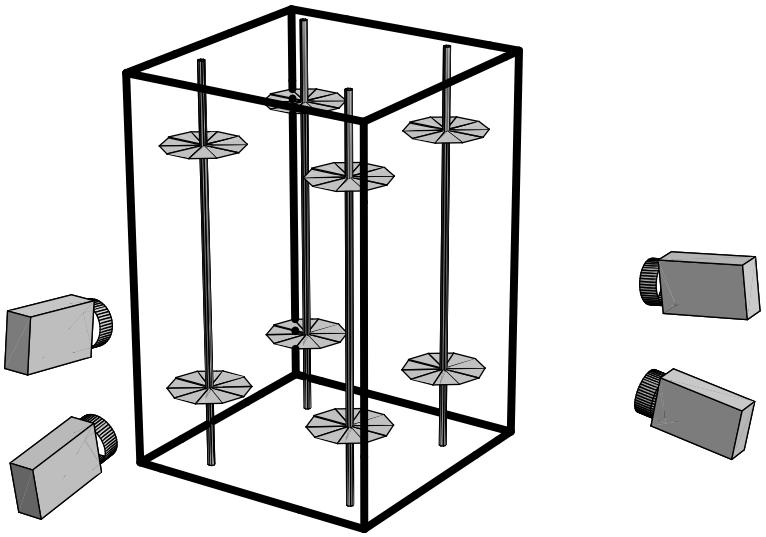

FIG. 1: Experimental setup

η	L_{int}	τ_η	T_L	ε	σ_u	Re_λ
0.25mm	48mm	0.07s	2.45s	168mm^2/s^3	23.33mm/s	172

TABLE I: Turbulence characteristics obtained from the von Kármán model [15]: Mean kinetic energy dissipation ε, Kolmogorov length $\eta \equiv (\nu^3/\varepsilon)^{1/4}$, Kolmogorov time $\tau_\eta \equiv (\nu/\varepsilon)^{1/2}$, integral length L_{int}, integral time T_L, velocity fluctuations $\sigma_u^2 = \frac{1}{3}(\sigma_{u_x}^2 + \sigma_{u_y}^2 + \sigma_{u_z}^2)$. The Reynolds number is defined as $Re_\lambda = \frac{\lambda \sigma_u}{\nu}$ with the Taylor micro scale $\lambda = \sqrt{(\frac{15\nu\sigma^2}{\varepsilon})}$.

four camera chips into a full set of three dimensional trajectories in time involve several crucial steps: fitting gaussian profiles to the 2d images, stereo matching (line of sight crossings) with a two media (water-air) optical model and construction of 3d trajectories in time by using the kinematic principle of minimum change in acceleration [16, 24].

From eqn. 1 we can define the coarse grained strain $\langle \widetilde{s}^2 \rangle$ and $\langle \widetilde{\Omega}^2 \rangle$ where $\langle \widetilde{s}_{ij} \rangle$ and $\langle \widetilde{\Omega}_{ij} \rangle$ are the symmetric and anti-symmetric part of the coarse-grained velocity gradient tensor $\langle \widetilde{A}_{ij} \rangle$. The eigenvalues and eigenvector of $\langle \widetilde{s}_{ij} \rangle$ is denoted $\langle \widetilde{\Lambda}_i \rangle$ and $\langle \widetilde{\lambda}_i \rangle$ respectively. Due to incompressibility $\sum_i \langle \widetilde{\Lambda}_i \rangle = 0$. In addition we define $\langle \widetilde{\Lambda}_1 \rangle > \langle \widetilde{\Lambda}_2 \rangle > \langle \widetilde{\Lambda}_3 \rangle$ so that the most positive principal direction of strain is $\langle \widetilde{\Lambda}_1 \rangle$.

The filtered velocity field (eqn. 2) is approximated by least square fits of spherical in-

compressible and orthogonal linear polynomials to discrete velocities of fluid particles inside spherical balls with diameter Δ. At least four particles are necessary to describe a three-dimensional shape and hence to estimate $\langle \widetilde{A}_{ij} \rangle$. Four particles form a tetrahedron and is the backbone of the analysis by Chertkov et al. [7]. In [11] we show that $\widetilde{A}_{ij}$ obtained from only four particles is quite far from the definition in eqn. 2 and therefore that using only four particles are not sufficient.

We find that at least twelve particles are needed in order to obtain a reasonable approximation of eqn. 2 of the coarse-grained quantities. Using this many particles has the drawback that we can not study the dynamics at the smallest scales. In Figure 2 (a) the radial distribution of particles is shown. The probability $Np(r)$ of finding a given number N of particles on the surface of a ball centered in our measuring volume with radius r is observed to increase with r^2 up to $\sim 200\eta$. This means that the particle density can be considered uniform up to this scale. For lager radius the density drops down because of non-perfect illumination at the boundary of the measuring volume. The cumulative distribution is show in (b) and is interesting because it gives us an estimate of the number of particles we can expect to find in a ball with radius r. The number is, however, only an upper bound since the ball is centered in the measuring volume and not around all individual particles in the flow.

The smallest scale for which $\langle \widetilde{u} \rangle$ and hence $\langle \widetilde{s}^2 \rangle$ and $\langle \widetilde{\Omega}^2 \rangle$ can be resolved is 80η. A higher particle seeding density which again makes particle tracking more difficult can decrease this number. All results reported use a minimum of twelve particles.

As already reported in [2, 11] the mean flow is slightly straining though with a characteristic time scale many times larger than the integral time scale of the flow. An alternative way of emphasizing the large scale mean strain is shown in Figure 3. $\cos^2(x_i, \widetilde{\lambda}_1)$, where x_i is the three coordinate axes, is observed to peak for large r in the vertical direction while the horizontal axes decrease in agreement with an axis-symmetric flow. A slow convergence towards isotropy is observed as $r = \Delta$ is reduced.

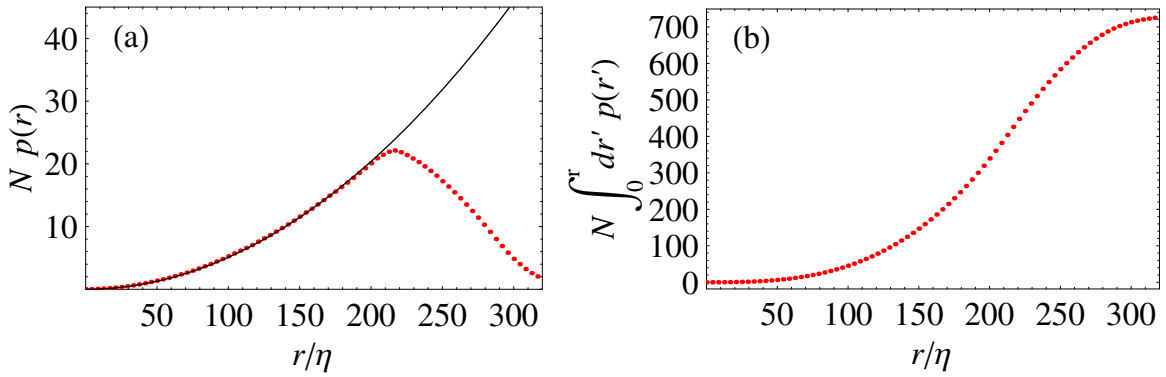

FIG. 2: Radial distribution of particles where N is the total number of particles in the volume. a) The probability of finding a particle in a spherical shell with thickness dr and with distance r from the center of the measuring volume. b) Cumulative distribution of (a).

III. COARSE-GRAINED STATISTICS

In the viscous subrange the stretching rate of infinitesimal material lines governs particle pair separation. The stretching rate is defined as

$$L(t) = \left\langle \frac{1}{2r^2}\frac{dr^2}{dt} \right\rangle . \tag{3}$$

where d/dt denotes Lagrangian differentiation (following the particles). In the viscous subrange $L(t)$ when rescaled with the Kolmogorov time scale τ_η becomes constant after a short time [2, 3, 9, 10, 12]. In the viscous sub range the second order Eulerian longitudinal structure function $f(r) = \langle\{[u_i(\mathbf{x}+\mathbf{r}) - u_i(\mathbf{x})]r_i/r\}^2\rangle$ is given by

$$f(r) = \frac{\langle s^2\rangle}{15}r^2 \qquad r \ll \eta \tag{4}$$

Through the definitions $\varepsilon = 2\nu\langle s^2\rangle$ and $\tau_\eta^2 = \nu/\varepsilon$ we can form $\tau_\eta^2 = r^2/(30f(r))$. Thus motivated by viscous subrange scaling we move to the inertial range and define a time scale

$$t_\star(r) = \sqrt{\frac{2r^2}{15f(r)}} \qquad r \ll L_{int}. \tag{5}$$

In the limit $r \ll \eta$ we have $t_\star = \sqrt{2}\tau_\eta$.

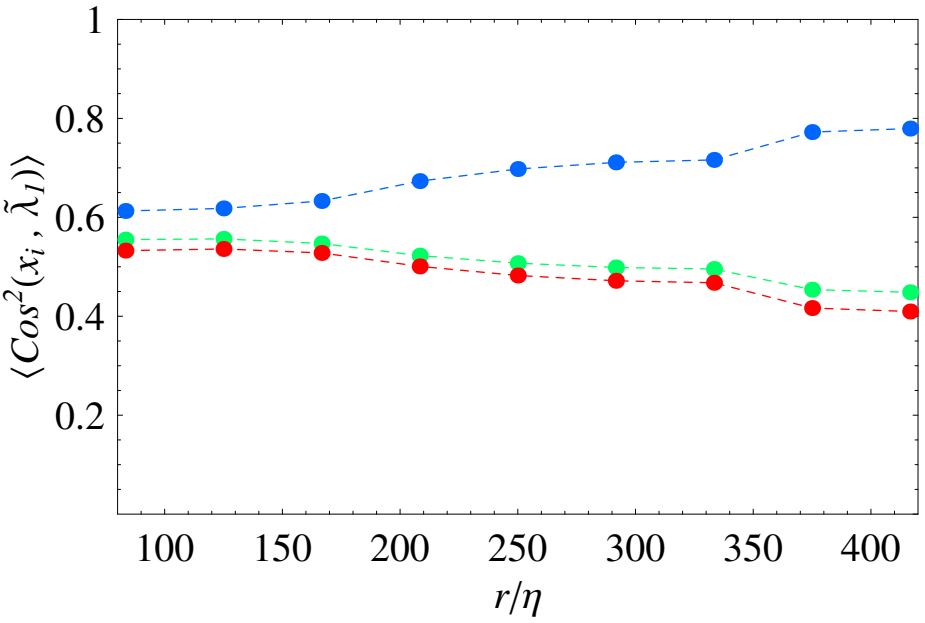

FIG. 3: Squared cosine between the most stretching principle coarse grained eigenvector, $\widetilde{\lambda}_1$, and the three coordinate directions. Blue is the vertical axis-symmetric direction while the green and red is the horizontal directions.

As a function of scale $r = \Delta$ we plot $\langle \widetilde{s}^2 \rangle$ and $\langle \tilde{\Omega}^2 \rangle$ in Figure 4. Both quantities are in the inertial range observed to be in agreement with the Kolmogorov similarity prediction $r^{-4/3}$. For $r \to 0$ the ratio $\langle \widetilde{s}^2 \rangle / \langle \tilde{\Omega}^2 \rangle \to 2$.

Also in Figure 4 we have plotted $\langle \widetilde{s}^2 \rangle$ and $\langle \widetilde{\Omega}^2 \rangle$ multiplied with $t_\star^2$. In the inertial range we find that $\langle \widetilde{s}^2 \rangle t_\star^2 \sim 1$ and $\langle \widetilde{\Omega}^2 \rangle t_\star^2 = 1.85$. It thus seems that $t_\star$ as defined in eqn. 5 serves as a characteristic time scale for $\langle \widetilde{s}^2 \rangle$ and therefore $t_\star \sim 1/\sqrt{\langle \widetilde{s}^2 \rangle}$.

In [11] $f(r)$ in eqn. 5 was defined through a model valid for homogeneous and isotropic turbulence. In this paper $f(r)$ are obtained directly from data. The behavior therefore is therefore slightly different.

IV. PARTICLE PAIR SEPARATION

The rescaled eigenvalues $\langle \widetilde{\Lambda}_i \rangle t_\star$ are shown in Figure 5. The trademark of turbulence, namely $langle\widetilde{\Lambda}_2\rangle > 0$ which is necessary for both positive mean enstrophy and strain production is observed for all values of r. A slight decrease in $\widetilde{\Lambda}_2$ is observed which could be taken as a sign of the coarse-graining field becoming more Gaussian and hence $\langle \widetilde{\Lambda}_2 \rangle = 0$. Both

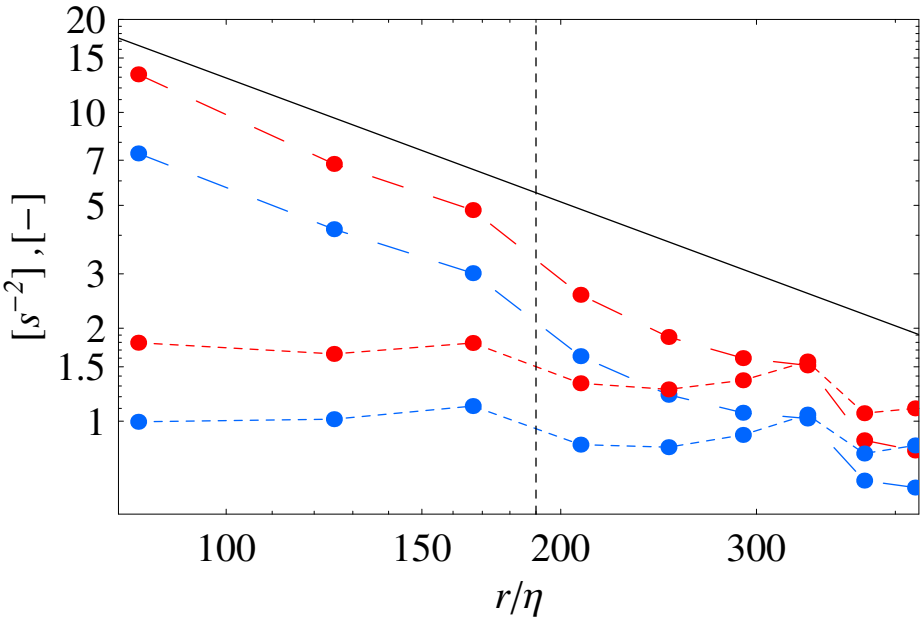

FIG. 4: Coarse grained strain $\langle \widetilde{s}^2 \rangle$ (long dashed red) and $\langle \widetilde{\Omega}^2 \rangle$ (long dashed blue) as a function of coarse graining scale r. The solid black line is $r^{-4/3}$. The dotted lines are $\langle \widetilde{s}^2 \rangle$ and $\langle \widetilde{\Omega}^2 \rangle$ multiplied by $t_\star^2$. The vertical black dotted line indicates the integral length scale.

$\langle \widetilde{\Lambda}_1 \rangle t_\star$ and $\langle \widetilde{\Lambda}_3 \rangle t_\star$ are constant and so are their ratio $|\langle \widetilde{\Lambda}_3 \rangle|/|\langle \widetilde{\Lambda}_1 \rangle|$. For a direct comparison with viscous result we have divided the results with $\sqrt{2}$.

When time is running forward two particles in a mean strain field will on average separate from each other along the direction of $\langle \widetilde{\lambda}_1 \rangle$. In the backward case they will separate along the direction of $\langle \widetilde{\lambda}_3 \rangle$. Since $\langle \widetilde{\Lambda}_2 \rangle > 0$ and therefore $|\langle \widetilde{\Lambda}_3 \rangle| > |\langle \widetilde{\Lambda}_1 \rangle|$ backwards separation is the faster one. This is shown in Figure 6 for times $t_B < t < 5t_B$ where $t_B = (r_0^2/\varepsilon)^{1/3}$ is the Batchelor time, characterizing the time for which the initial separation should be regarded an important parameter in the separation process [5]. By closer inspection of Figure 6 we can see that in the backward case r is slightly more aligned with $\langle \widetilde{\lambda}_3 \rangle$ than it is aligned with $\langle \widetilde{\lambda}_1 \rangle$ in the forward case. This is due to the positiveness of $\langle \widetilde{\Lambda}_2 \rangle$ and a corresponding increase in the alignment of r with $\langle \widetilde{\lambda}_2 \rangle$ in the forward case compared to in the backward case is therefore also observed. The values of $\cos^2(r, \widetilde{\lambda}_i)$ are in the forward case 0.50, 0.32 and 0.19 for $i = 1, 2, 3$ respectively. In the backward case the same values are 0.19, 0.28 and 0.53.

Stretching rates rescaled by $t_\star$ are presented in Figure 7 as a function of t/t_B for different

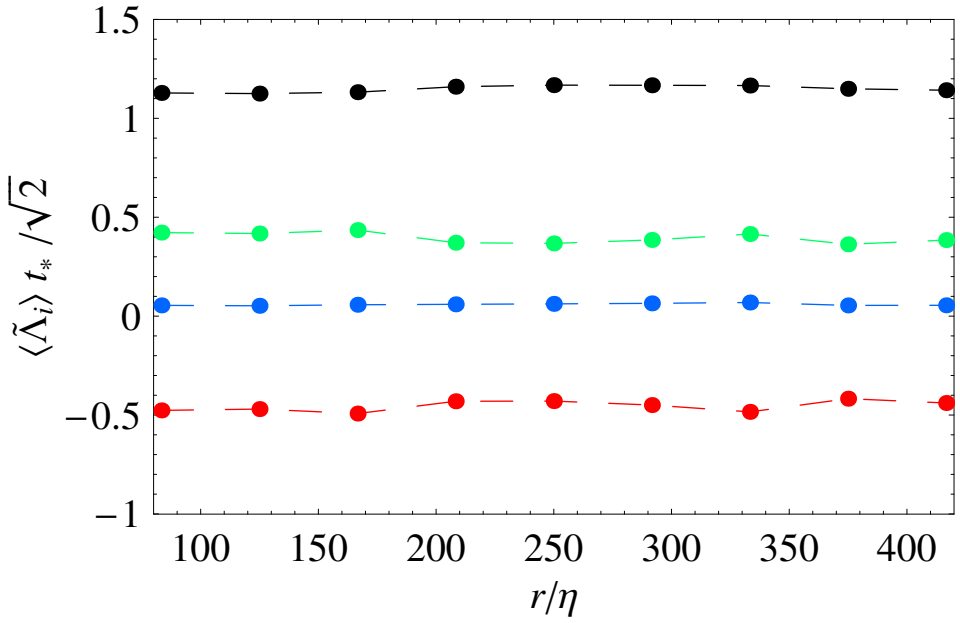

FIG. 5: Eigenvalues $\langle\widetilde{\Lambda}_i\rangle t_\star$ of $\langle\widetilde{s}_{ij}\rangle$. $i = 1$: green, $i = 2$: blue and $i = 3$: red. The black curve is the ratio $|\langle\widetilde{\Lambda}_3\rangle|/|\langle\widetilde{\Lambda}_1\rangle|$.

initial separation of pairs.

For times $t \sim 0.5t_B$ the forward stretching and backward stretching occurs with the same speed. The separation vector is still randomly oriented and has therefore not yet aligned itself with the principal directions of the strain field. For longer times the backwards stretching rates saturates at 0.235 ± 0.005 while the forwards saturate at 0.18 ± 0.005. Whereas all curves in the forward case collapse for times up to $3 - 4t_B$ the curves in the backward case do not collapse so nicely. Because backward separation is faster the particles leave the measurement volume earlier: the larger r_0, the earlier. The particle pairs we thus observe for large times are likely to be slow pairs with low stretching rate. To reduce the effect of finite volume we only choose pairs which start within a small sub volume (30mm) of the full measuring volume. There is, however, no systematic way in which we can totally neglect the effect of a finite volume.

The maximum stretching rates would occur if the particle separation vector $\mathbf{r}$ is fully aligned with the principal strain axes. In this case the rescaled stretching rates would be $\langle\widetilde{\Lambda}_1\rangle t_\star$ and $-\langle\widetilde{\Lambda}_3\rangle t_\star$ in Figure 5 for the forward and backward case respectively. The forward value $L_f(t)/\sqrt{2}/t_\star = 0.18 \pm 0.005$ is close to the values obtained in the viscous sub

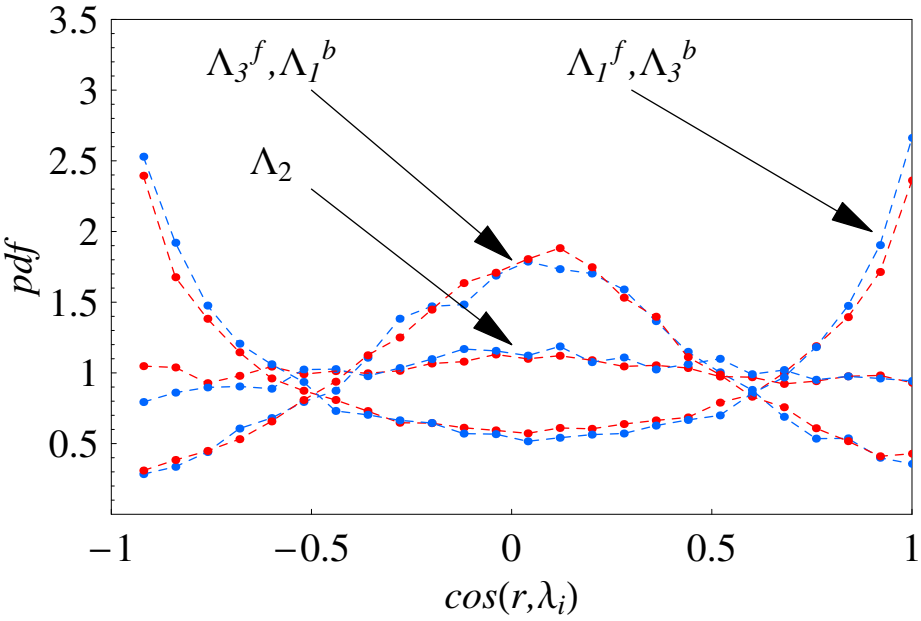

FIG. 6: Angular dependence between $\langle\widetilde{\lambda}_i\rangle$ and the separation vector r for times $t_B \gg t \gg 5t_B$. Red curves are forwards dispersion while blue are backwards dispersion.

range [2, 3, 9, 10].

Berg et al. [2] hypothesized that, if the particle separation was perfectly aligned with the principal strain axes, the ratio between forwards and backwards dispersion rates characterized by the Richardson-Obukhov constant ratio g_b/g_f could be determined as $(-\langle\widetilde{\Lambda}_3\rangle/\langle\widetilde{\Lambda}_1\rangle)^3$. From Figure 5 this number equals $1.13^3 = 1.44$. From the calculated stretching rates we find that this is certainly not the case since $0.235/0.18 = 1.31$. With the same argumentation this would give a ratio $g_b/g_f = 2.23 \pm 0.33$ within errors of what was measured directly in [2]. Although $L(t)_f \leq |\langle\widetilde{\Lambda}_1\rangle|$ and $L(t)_b \leq |\langle\widetilde{\Lambda}_3\rangle|$ we thus have $L(t)_b/L(t)_f \leq |\langle\widetilde{\Lambda}_3\rangle/\langle\widetilde{\Lambda}_1\rangle|$ and hence a larger ratio than in the fully aligned case.

V. CONCLUSIONS

We have given evidence of the existence of, what we call self-similar stretching rates: when scaled by a relevant time $t_\star$ scale which is a function of the second order structure function stretching rates of infinitesimal material lines has its counterpart in the inertial range. Furthermore it turns out that this relevant time scale $t_\star$ is related to the coarse-grained strain field. The stretching is like in the viscous range far from being perfectly

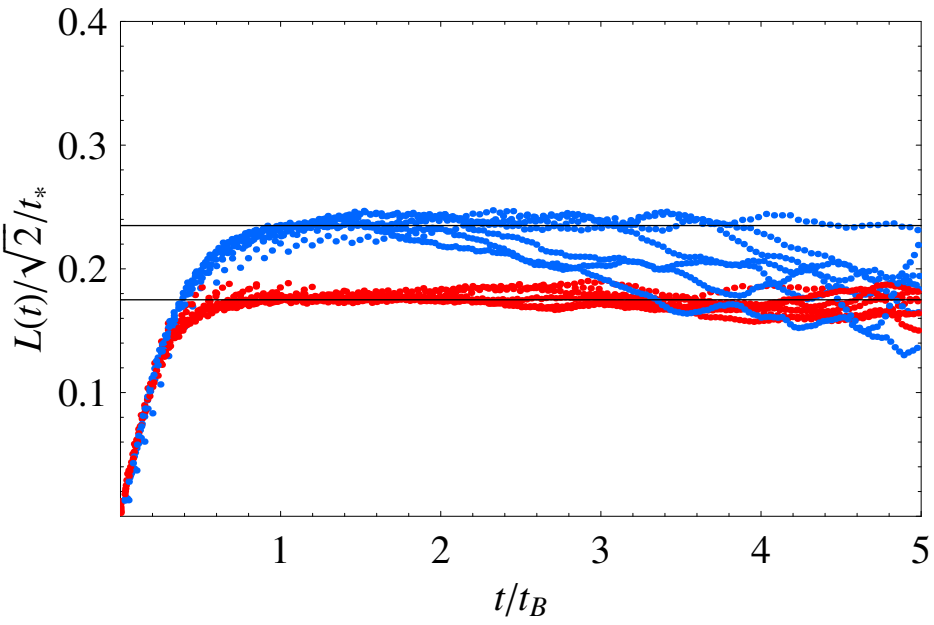

FIG. 7: Stretching rates $L(t)$ rescaled by $t_\star$. The blue curves correspond to forwards separation while the red curves corresponds to backwards separation (time running backwards) for different initial separations r_0. Particle pairs with r_0 from $3-4$mm to $9-10$mm in steps of $1mm$ are shown. We have divided the y-axis with $\sqrt{2}$ in order to match the viscous limit.

aligned with the most positive direction of strain which we have shown would lower the ratio between forwards and backwards dispersion.

Whether or not the Lagrangian stretching rates found in this paper are universal or specific for this particular turbulent flow other experiments and/or DNS will have to decide.

[1] T. Allen and R. Brown. Large-eddy simulation of turbulent separated flow over rough hills. *Boundary Layer Met.*, 102:177, 2002.

[2] J. Berg, B. Lüthi, J. Mann, and S. Ott. Backwards and forwards relative dispersion in turbulent flow: An experimental investigation. *Phys. Rev. E*, 34:115, 2006.

[3] L. Biferale, G. Boffetta, A. Celani, B. J. Devenish, A. Lanotte, and F. Toschi. Lagrangian statistics of particle pairs in homogeneous isotropic turbulence. *Phys. Fluids*, 17:115101, 2005.

[4] V. Borue and S. A. Orszag. Local energy flux and subgrid scale statistics in three-dimensional turbulence. *J. Fluid Mech.*, 366:1, 2002.

[5] M. Bourgoin, N. T. Ouellette, H. Xu, J. Berg, and E. Bodenschatz. The role of pair dispersion in turbulent flow. *Science*, 311:835, 2006.

[6] F. A. Castro, J. M. L. M. Palma, and A. Silva Lopez. Simulation of the askervein flow. part i: Reynolds averaged navier-stokes equation. *Boundary Layer Met.*, 107:501, 2003.

[7] M. Chertkov, A. Pumir, and B. I. Shraiman. Lagrangian tetrad dynamics and the phenomenology of turbulence. *Phys. Fluids*, 11:2394, 1999.

[8] U. Frisch. *Turbulence – the legacy of A. N. Kolmogorov*. Cambridge, 1995.

[9] S. S. Girimaji and S. B. Pope. Material-element deformation in isotropic turbulence. *J. Fluid Mech.*, 220:427, 1990.

[10] M. Guala, B. Lüthi, A. Liberzon, A. Tsinober, and W. Kinzelbach. On the evolution of material lines and vorticity in homogeneous turbulence. *J. Fluid Mech.*, 533:339, 2005.

[11] B. Lüthi, J. Berg, S. Ott, and Mann J. Lagrangian multi-particle statistics. *submitted*, 2006.

[12] B. Lüthi, A. Tsinober, and W. Kinzelbach. Lagrangian measurements of vorticity dynamics in tubulent flow. *J. Fluid Mech.*, 528:87, 2005.

[13] N. Mordant, P. Metz, O. Michel, and J.-F. Pinton. Mearesurement of lagrangian velocity in fully developed turbulence. *Phys. Rev. Lett.*, 87:214501, 2001.

[14] A. Naso, M. Chertkov, and A. Pumir. Scale dependence of the coarse-grained velocity derivative tensor: influence of large-scale shear on small-scale turbulence. *J. turbulence*, 7:41, 2006.

[15] S. Ott and J. Mann. An experimental investigation of the relative diffusion of particle pairs in three-dimensional flow. *J. Fluid Mech.*, 422:207, 2000.

[16] N. T. Ouellette, H. Xu, and E. Bodenschatz. A quantitative study of three-dimensional lagrangian particle tracking algorithms. *Exp. in Fluids.*, 40:301, 2006.

[17] S. B. Pope. *Turbulent flows*. Cambridge University press, 2000.

[18] A. La Porta, G. A. Voth, J. Alexander A. M. Crawford, and E. Bodenschatz. Fluid particle accelerations in fully developed turbulence. *Nature*, 409:1017, 2001.

[19] A. Pumir and B. I. Shraiman. Lagrangian particle approach to large eddy simulations of hydrodynamic turbulence. *J. Stat. Phys.*, 113:693, 2003.

[20] B. L. Sawford, P. K. Yeung, and M. S. Borgas. Comparison of backwards and forwards relative dispersion in turbulence. *Phys. Fluids*, 17:095109, 2005.

[21] N. N. Sørensen, J. A. Michelsen, and S Schreck. Navier-Stokes predictions of the NREL Phase VI rotor in the NASA Ames 80ft $\times$ 120 ft wind tunnel. *Wind Energy*, 5:151–169, 2002.

[22] B. Tao, J. Katz, and C. Meneveau. Statistical geometry of subgrid-scale stresses determined from holographic particle image velocimetry measurements. *J. Fluid Mech.*, 457:35, 2002.

[23] F. van der Bos, B. Tao, and J. Katz C. Meneveau and. Effects of small-scale turbulent motions on the altered velocity gradient tensor as deduced from holographic particle image velocimetry measurements. *Phys. Fluids*, 14:2456, 2002.

[24] J. Willneff. *A spatio-temporal mathing algorithm for 3D-particle tracking velocimetry.* PhD thesis, ETH Zürich, 2003.

[25] H. Xu, M. Bourgoin, N. T. Ouellette, and E. Bodenschatz. High order lagrangian velocity statistics in turbulence. *Phys. Rev. Lett.*, 96:024503, 2006.

VII

Lagrangian one-particle velocity statistics from the Risø PTV experiment

Jacob Berg*

Risø National Laboratory, 4000 Roskilde, Denmark

(Dated: August 31, 2006)

Abstract

We present Lagrangian one-particle statistics from the Risø PTV experiment. We estimate the Lagrangian Kolmogorov constant C_0 and find that it is affected by the large scale inhomogeneities of the flow. The pdf of temporal velocity increments are highly non-Gaussian for small time which we interpret as a consequence of intermittency. Using Extended Self-Similarity we manage to quantify the intermittency and find that the deviations from Kolmogorov 1941 similarity scaling is larger in the Lagrangian framework than in the Eulerian. Through the multifractal model we calculate the multifractal dimension spectrum.

*Electronic address: jacob.berg.joergensen@risoe.dk

η	L	τ_η	T_E	ε	σ_u	Re_λ
0.30mm	53.80mm	0.09s	2.83s	$128\text{mm}^2/\text{s}^3$	19.02mm/s	124

TABLE I: Turbulence characteristics: ε is the mean kinetic energy dissipation, $\eta \equiv (\nu^3/\varepsilon)^{1/4}$ is the Kolmogorov length scale with the kinematic viscosity $\nu = 1$ of water. $\tau_\eta \equiv (\nu/\varepsilon)^{1/2}$ is the Kolmogorov time scale and $\sigma_u^2 = \frac{1}{3}(\sigma_{u_x}^2 + \sigma_{u_y}^2 + \sigma_{u_z}^2)$ is the standard deviation of velocity. The integral length scale is defined as $L = \sigma^3/\varepsilon$ while T_E is the eddy turnover time $T_E = L/\sigma_u$. The Reynolds number is defined as $Re_\lambda = \sqrt{15}(L/\eta)^{2/3}$.

I. INTRODUCTION

In the present contribution we focus on Lagrangian one-particle statistics from an experiment with the Risø Particle Tracking Velocimetry (PTV) setup. We focus on small-scale statistics. The small-scale statistic is analyzed with Extended Self-Similarity [2] and the results are presented in the spirit of the multifractal model of turbulence [10].

We use a Lagrangian database from a recording with a lower Reynolds number than presented in [3, 4, 12]. The flow characteristics are presented in Table I. The mean flow is axisymmetric with a significant vertical straining on the largest scales and we did not find any significant differences from the flow reported in [3, 12], where properties of the mean flow can be found together with a description of the experimental setup.

Here we look at a sub-volume of the full measuring volume. Only particles which we can observe within a ball of radius 50mm is considered and the turbulence characteristics given in Table I are thus only determined from particles inside this ball. The ball is centered approximately in the center of the tank where the velocity standard deviation σ_u has a global minimum. Inside the ball the particles are uniformly distributed. With $\tau_\eta = 0.09s$ and a recording frequency at $50Hz$ the temporal resolution is $\sim 4\text{frames}/\tau_\eta$.

The database is the largest we have compiled and it consists of $\sim 10^6$ individual trajectories with an average length of $\sim 8\tau_\eta$, a standard deviation of $\sim 13\tau_\eta$ and the longest tracks we find are $\sim 150\tau_\eta$. The number of tracks was an important requirement since the calculation of high order moments is considered important.

Throughout the paper we will denote the *Lagrangian* velocity along a particle trajectory for $\mathbf{v}(t)$ and the *Eulerian* velocity in a fixed frame of reference for $\mathbf{u}(\mathbf{x}, t)$.

II. FINITE VOLUME MEASUREMENTS

A nice property of Eulerian statistic is that it is stationary in time in the present experiment. This is not the case for the Lagrangian statistics. The non-stationarity is showed

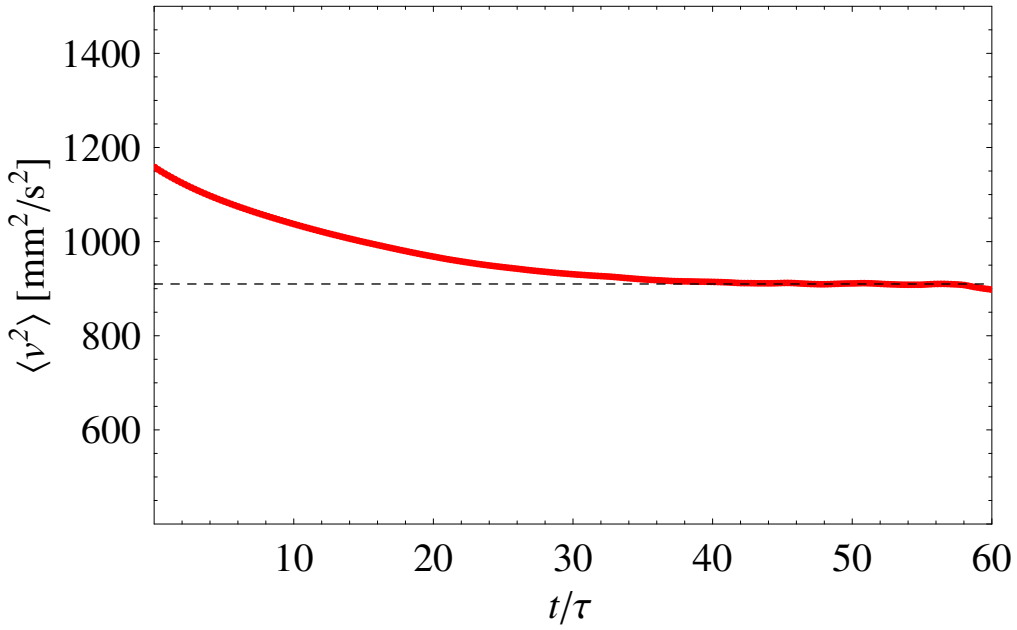

FIG. 1: $\langle v^2(t+t_0)\rangle$. The average is taken over all particles which were observed inside B at both time t_0 and t_0+t.

in Figure 1 where $\langle v^2 \rangle$ is observed to decrease over time. This reflects the finite measuring volume and the non-uniform forcing in space in our experiment: the particles only gain kinetic energy close to the propellers. During their subsequent motion the particles loose kinetic energy until they again come close to the propellers which are constantly spinning. Looking at a finite measuring volume away from the propellers, there will therefore be a flux of kinetic energy into the volume. Inside the volume the kinetic energy is dissipated and hence we have at the entry of the volume

$$\frac{1}{2}\frac{d}{dt}\langle v^2 \rangle = -\varepsilon, \tag{1}$$

where we recognize the mean kinetic energy dissipation ε. From Figure 1 we find $\varepsilon = 124\text{mm}^2/\text{s}^2$. This number is close to the number obtained from the second order Eulerian Structure Function $\varepsilon = 132\text{mm}^2/\text{s}^2$. We take the difference as the uncertainty in estimating

ε. Eqn. 1 can also be derived directly from the Navier-Stokes equation by assuming global homogeneity.

The Lagrangian second-order structure function is defined as

$$S_L^2(\tau) = \langle [v(t+\tau) - v(t)]^2 \rangle, \tag{2}$$

where $v(t)$ is here the velocity component along a fluid trajectory. Similar the Lagrangian co-variance function is defined as

$$R_L(\tau) = \langle v(t)v(t+\tau) \rangle. \tag{3}$$

The non-stationarity of $\langle v^2 \rangle$ means that

$$S_L^2(t) = \langle v^2(t) \rangle + \langle u^2 \rangle - 2R_L(t) < 2(\langle u^2 \rangle - R_L(t)), \tag{4}$$

where we have used that the Lagrangian velocity on the boundary of the measuring volume B equals the Eulerian velocity and therefore $\langle v^2(t=0) \rangle = \langle u^2 \rangle$. $S_L^2(t)$ is plotted in Figure 2 for all three velocity components. It is clear that for long times S_L^2 does not approach $2\langle u^2 \rangle$

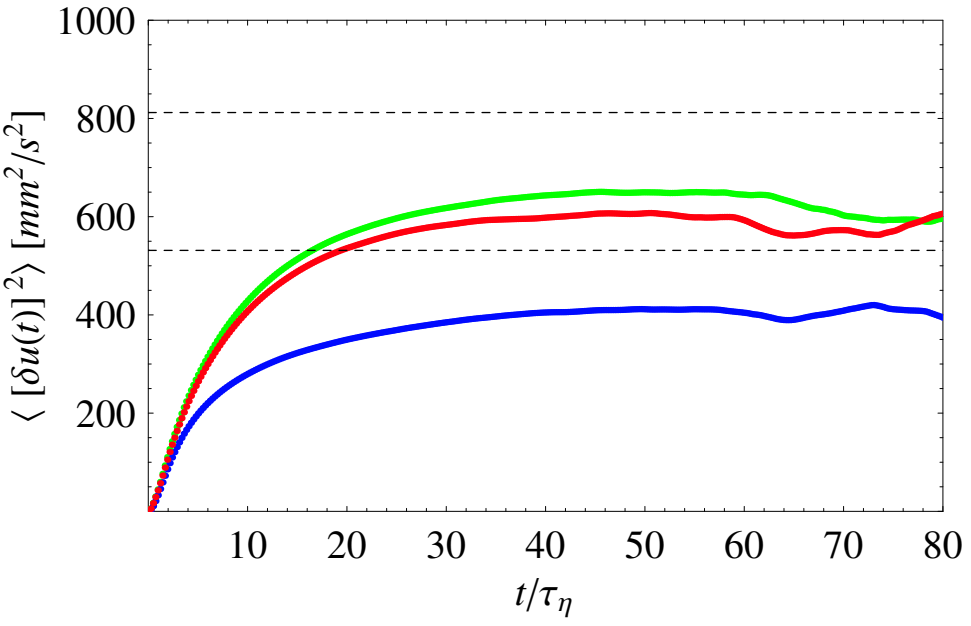

FIG. 2: Second order Lagrangian structure function for the three coordinates of $\mathbf{v}(t)$. x : green (radial component), y : red (radial component) and z : blue (vertical component). The horizontal lines is the Eulerian velocity variance $\langle u^2 \rangle$.

in agreement with eqn. 4.

A common interpretation of the finite volume influence on Lagrangian statistics is that the particles we can observe for long times are relatively slow ones or particles which are trapped in high intensity vortices (see later). Here we emphasize the equivalence with the energy argument of decaying turbulence described above. Particles which can be observed for long times are slow because it is long time ago they gained kinetic energy at the forcing site.

In Direct numerical simulations (DNS) forcing occurs in wave-number space on the lowest wave-numbers. We therefore have $d\langle v^2\rangle/dt = 0$ and consequently Lagrangian stationarity. Most physical flows encountered in nature will, however, be Lagrangian non-stationary.

III. ANISOTROPY AND INERTIAL RANGE SCALING

The linear dependence of Re_λ on T_L/τ_η implies that a very high Reynolds number is needed in order to obtain a clear Lagrangian inertial range. Yeung [30] concluded, based on extrapolations from Eulerian fields in DNS, that at least $Re_\lambda \sim 600 - 700$ was needed. Experimental flows at $Re_\lambda = 1000$ [16] and $Re_\lambda = 815$ [18] do, however, not show a very pronounced inertial range defined as a linear regime in the second-order structure function S_L^2.

In the inertial range $\tau_\eta < \tau < T_L$, K41 similarity theory predicts

$$S_{L,ij}^2(\tau) = C_0 \varepsilon \tau \delta_{ij}, \tag{5}$$

where the Lagrangian Kolmogorov constant C_0 is supposed to be universal for infinite Reynolds numbers [21]. C_0 plays a crucial role in stochastic models [22] and has lately been shown to reflect anisotropy in the large-scale forcing [18]. In Figure 3 we present results of C_0 for the three coordinates of $\mathbf{v}$. According to eqn. 5, C_0 should be determined from a plateau in the inertial range. The parabolic form therefore reflects the almost vanishing inertial range in our experiments. The difference between radial and the axisymmetric component stems from the large scale anisotropy. Since C_0 is maximum for times around $2 - 4\tau$ and therefore mainly associated with small scales the difference is a clear signature of small-scale anisotropy. The values of C_0 are 5.34 ± 0.16, 5.08 ± 0.15 and 4.09 ± 0.12 for the three components x, y and z respectively.

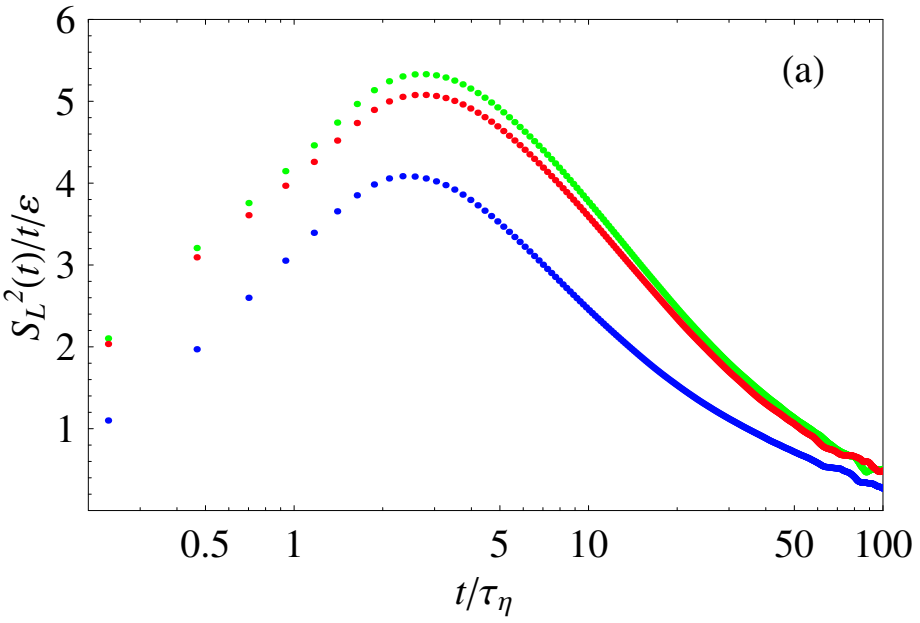

FIG. 3: C_0 for the radial components (green and red) and the axisymmetric component (blue).

It is interesting to see that the slight difference in the radial forcing is surviving all the way down. The propellers forcing the flow are attached to four rods placed in the corners of the tank. The reason for the radial components being different is probably small differences in the manual vertical placement of the propellers on the rods. The lack of small-scale isotropy in the current experiment should not be taken as a failure of Kolmogorov's hypothesis of local isotropy. For that the Reynolds number is not high enough. Other experiments at much higher Reynolds number do, however, all indicate that the large scale inhomogeneities are also present at smaller scales although with smaller amplitude [18, 24, 25].

Alternatively one can calculate the lagrangian velocity spectrum $\Phi(\omega)$ and calculate C_0 from this. $\Phi(\omega)$ is defined as the fourier transform of the velocity co-variance function $R_L(\tau)$ [27]:

$$\Phi(\omega) = \frac{1}{2\pi}\int_{-\infty}^{\infty} d\tau \exp\left(-\imath\omega\tau\right) R_L(\tau). \tag{6}$$

In the inertial range K41 predicts

$$\Phi_{ij}(\omega) = \beta\varepsilon\omega^{-2}, \tag{7}$$

with $C_0 = \pi\beta$. In Figure 4 (a) we have plotted $R_L(t)$ in the three directions. The radial components fall off exponential with e-folding times $T^x_{exp} \sim 10.7\tau_\eta$ and $T^y_{exp} \sim 9.4\tau_\eta$ while

the vertical axisymmetric component has more undulations and $T^z_{exp} \sim 14\tau_\eta$. Since $R_L(\tau)$ is composed of eddies of all size in the flow, the energy containing scales and hence the large scale inhomogeneities strongly effects its form. The integration of $R_L(t)/\sigma^2$ gives the Lagrangian integral time scale T_L. We find values of $T_L \sim T_{exp}$. The velocity spectrum

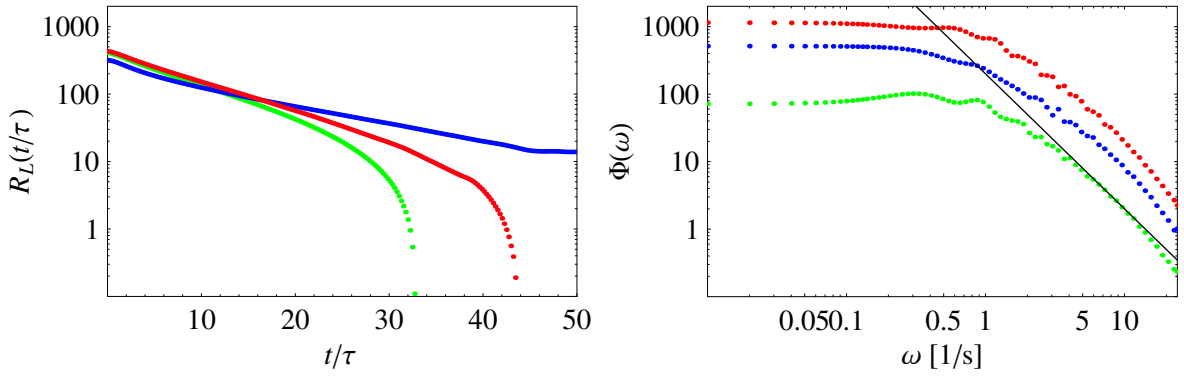

FIG. 4: (a) $R_L(\tau)$. (b) $\Phi(\omega)$. The straight line is the K41 prediction $\sim \omega^{-2}$. Color codes as in Figure 3. The curves have been shifted vertically for clarity.

$\Phi(\omega)$ is shown in (b). For small frequencies ω the spectrum for all three components are white. This corresponds to uncorrelated velocities for long time lags on a track. For higher frequencies all three spectra turn red with slope of ~ -2 in agreement with the Kolmogorov prediction. Due to a relative low sampling rate ($dt = 0.021$s) the Nyquist frequency prevent us from studying frequencies higher than $\omega = 23.8\text{s}^{-1}$.

Lien and D'Asaro [11] studied the scaling properties in a simple Lorentzian model spectrum and found that with a finite Reynolds number it is easier to obtain inertial range scaling from the spectrum than from the structure function $S^2_L(\tau)$. We have plotted the spectrum compensated with ω^2 in Figure 5 in order to have a better look at the existence of an inertial range. For all three components a narrow inertial range is observed as a plateau. The horizontal lines are used for estimating C_0. We find values equal to 4.91 ± 0.15, 4.79 ± 0.14 and 4.07 ± 0.12 for the three components respectively. These values are smaller and a bit more isotropic than those calculated from the structure functions. This is in contrast to the arguments by Lien and D'Asaro [11] C_0 who state that they should be larger.

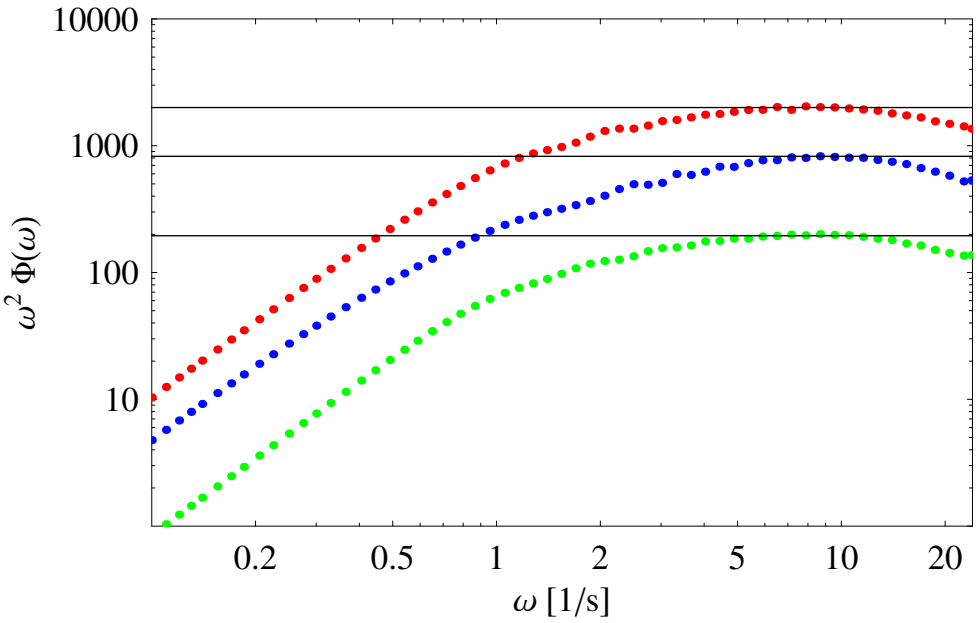

FIG. 5: Compensated velocity spectrum $\omega^2\Phi(\omega)$. Color code as in Figure 3. The curves have been shifted vertically for clarity. One can therefore not determine the magnitude of $\omega^2\Phi(\omega)$ from the different curves. The horizontal lines are the levels from which C_0 is calculated.

IV. SMALL-SCALE INTERMITTENCY

From the study of the lower moments we proceed to higher order moments describing the most extreme events.

The pdf of temporal velocity increments $\delta v(\tau) = v(t+\tau) - v(t)$ are shown in Figure 6 for different time lags τ. All three components are shown. The three components show the same over all behavior: for large time lags the distributions are Gaussian while they for small time lags have fat tails. The curves corresponding to the smallest time lags have a flat plateau at $\delta v \sim 0$. This is a binning artifact and does therefore not represent any physical trend in the data. The non-Gaussianity for small times is more clear by looking at the flatness. The flatness of the distributions is defined as

$$F(\tau) \equiv \frac{\langle \delta v^4(\tau) \rangle}{\langle \delta v^2(\tau) \rangle^2} \tag{8}$$

and is shown in Figure 7. F is monotonically decreasing for all three components and reaches a Gaussian level at time lags: $\tau \sim 40\tau_\eta$, which is substantial larger than T_L. We do not at present have any explanation for this.

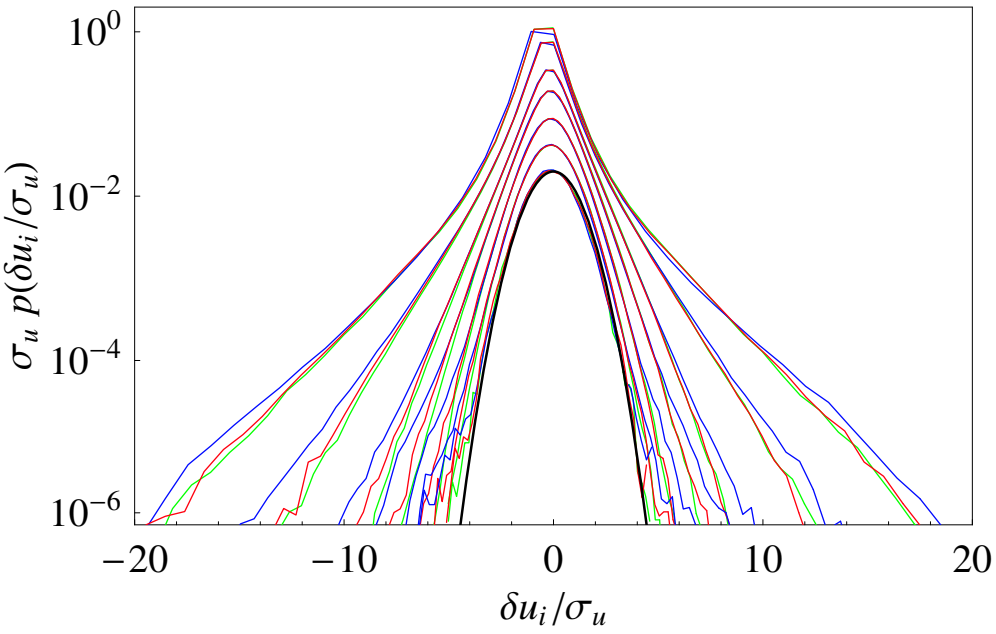

FIG. 6: pdf of velocity increments $\delta v(\tau)$ for times (decreasing downwards) $\tau = 1.0\tau_\eta, 1.7\tau_\eta, 3.6\tau_\eta, 6\tau_\eta, 12\tau_\eta, 24\tau_\eta$ and $48\tau_\eta$. The curves have been shifted vertically for clarity. Color coding as in Figure 3. The black curve is a Gaussian.

The results presented in Figure 6 and 7 are strong evidence of Lagrangian intermittency, i.e. non-Gaussian behavior of the smallest temporal scales in the flow. These results agree with observations by Mordant et al. [17] and Direct Numerical Simulations (DNS) by Biferale et al. [6].

Our findings suggest that intermittency can be studied in flows with a moderate Reynolds number of order $\mathcal{O}(100)$. The only necessary condition seems to be the size of the ensemble: a large number of particles is needed to observe rare events.

A. Higher order structure functions and ESS

Before we look at the higher order moments we check for convergence of these. In Figure 8 we show $\delta v^n p(\delta v)$ for $n = 4, 6, 8, 10$. The time lag in all four plot is $\tau = 2.1\tau_\eta$. For $n < 8$ we observe convergence. For $n = 8$ we start to get into trouble, but it seems like we have captured most of the signal – at least for the radial components (red and green curves). In an incompressible flow $\langle \delta u(\tau) \rangle = 0$: the non-zero skewness observed in all the curves is

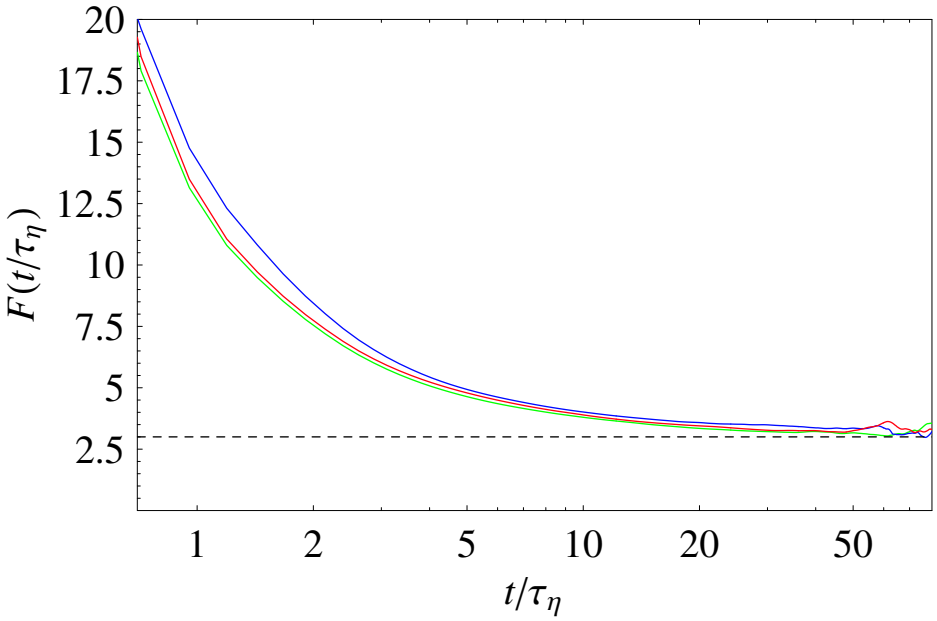

FIG. 7: The flatness of $\delta v(\tau)$. The color coding as in Figure 3. The horizontal line $F = 3$ is the Gaussian prediction.

therefore an artifact of sampling errors and or tracking of particles. This is an issue which has to be resolved before more dramatic conclusions can be made.

K41 similarity theory predicts in the inertial range for the p order structure function:

$$S_L^p(\tau) \equiv \langle \delta v^p(\tau) \rangle \sim \varepsilon^{p/2} \tau^{p/2}. \tag{9}$$

Intermittency can be defined as the departure from K41 similarity scaling. This means that eqn. 9can be replaced by a more general form taking intermittency into account:

$$\langle \delta v^p(\tau) \rangle \sim \tau^{\zeta_p}, \tag{10}$$

where $\zeta(p)$ is commonly named the Lagrangian anomalous scaling exponent. Only recently it has been possible to measure $\zeta(p)$ and hence quantitatively describe the extreme dynamics present in the fat tails of the distribution of $\delta v(\tau)$ for $\tau \to 0$ [5, 16, 17, 28, 29]. The data presented here is therefore merely a verification of already obtained results.

In Figure 9 (a) structure functions $S_L^p(t)$ of order $p = 2, 4, 5, 6, 8$ are shown as a function of τ. Power laws have been fitted to each function in the region $2\tau_\eta \leq t \leq 4\tau_\eta$ corresponding to the maxima of $S_L^p(t)/t/\varepsilon$. The fits are not convincing. First of all, the inertial range

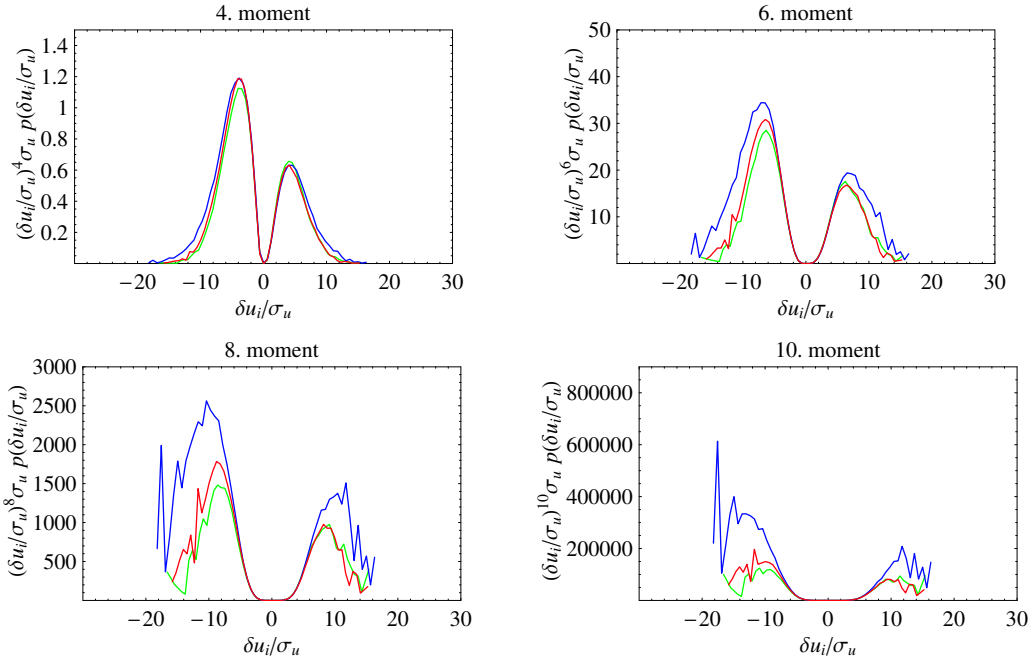

FIG. 8: $\delta v^n p(\delta v)$ for $n = 4, 6, 8, 10$. The time in all four plot is $\tau = 2.1\tau_\eta$.

is too narrow and we therefore can not expect any universal scaling. Secondly, and less importantly, we know that the small scales are affected by the large-scale inhomogeneities.

A popular way of looking at scaling exponent is instead to measure ratios of scaling exponents. This method is called Extended self-similarity (ESS) and was introduced by Benzi et al. [2]. The method was introduced in the Eulerian frame but can be transferred to the Lagrangian frame if we assume that $\zeta_2 = 1$ following K41 similarity theory. The crucial step is to treat all velocity increments as positive. This affects the odd-numbered structure functions. We therefore define

$$S^p_{L,ESS}(\tau) \equiv \langle |\delta v(\tau)|^p \rangle \sim \tau^{\zeta^\star_p}. \tag{11}$$

In Figure 9 (b) $S^p_{L,ESS}(t)$ is shown as a function of $S^2_L(t)$. The scaling is now much better, which explains the wide popularity of the method. The different scaling exponents are printed in Table II and plotted in Figure 10 for the radial components. The error bars represent small deviations between the two radial components as well as an error estimated from fitting the straight lines in Figure 9. The errors increase with p and are significantly larger for ζ^L_p compared to the ESS approach $\zeta^\star_p/\zeta_2$.

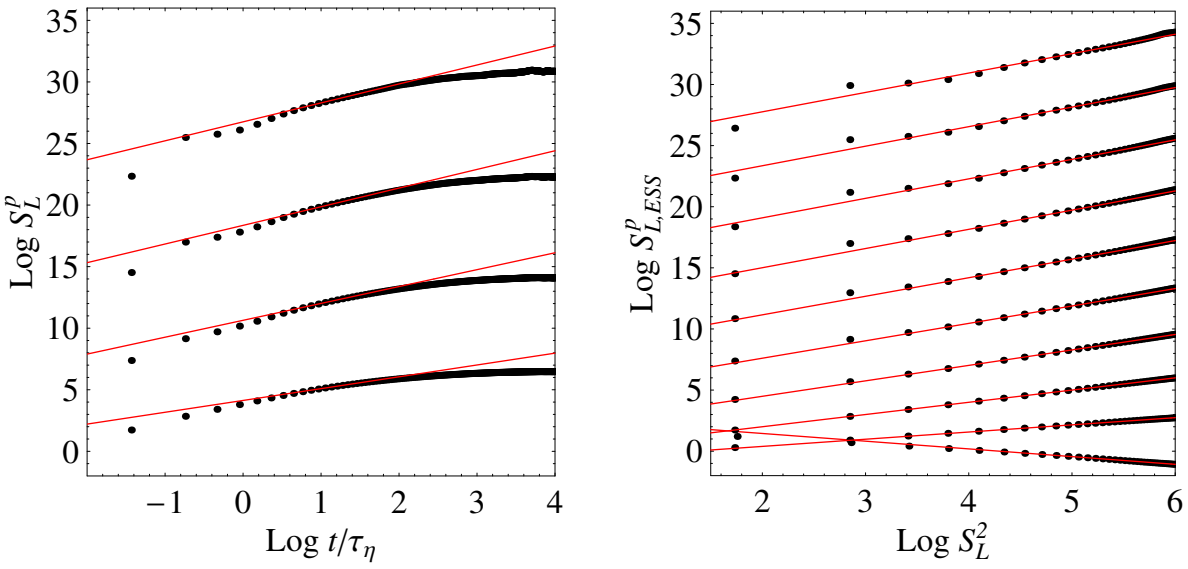

FIG. 9: (a) $S_L^p(t)$ as a function of t/τ_η for $p = 2, 4, 6, 8$ increasing upwards. (b) Extended self-similarity: $S_{L,ESS}^p(t)$ as a function of $S_L^2(t)$ for $p = -1, 1, 2, ..., 9$. In both panels data from the radial x-component are used.

p	-1	1	2	3	4
ζ_p^L	–	–	0.98 ± 0.07	–	1.40 ± 0.08
$\zeta_p^\star/\zeta_2$	-0.62 ± 0.07	0.59 ± 0.02	1	1.27 ± 0.03	1.43 ± 0.06

p	5	6	7	8	9
ζ_p^L	–	1.56 ± 0.10	–	1.66 ± 0.17	–
$\zeta_p^\star/\zeta_2$	1.53 ± 0.05	1.60 ± 0.06	1.65 ± 0.09	1.70 ± 0.13	1.75 ± 0.19

TABLE II: Lagrangian anomalous scaling exponents

Some remarks about ESS should be made at this point. In the original paper Benzi et al. [2] argued, based on experimental evidence of $|\langle \delta_r u^3(r) \rangle| \sim \langle |\delta_r u(r)|^3 \rangle$, that $\langle |\delta_r u(r)|^p \rangle = B_p \langle |\delta_r u(r)|^3 \rangle^{\zeta_p^L}$. As also emphasized in the paper this is not a rigorous result which can be deduced from the Navier-Stokes equation. By plotting absolute (defined by positive velocity increments) structure functions vs. the third order structure function (Eulerian frame) or the second order structure function (Lagrangian frame), an extended scaling range can be observed because undulations in the structure functions are correlated and hence disappear

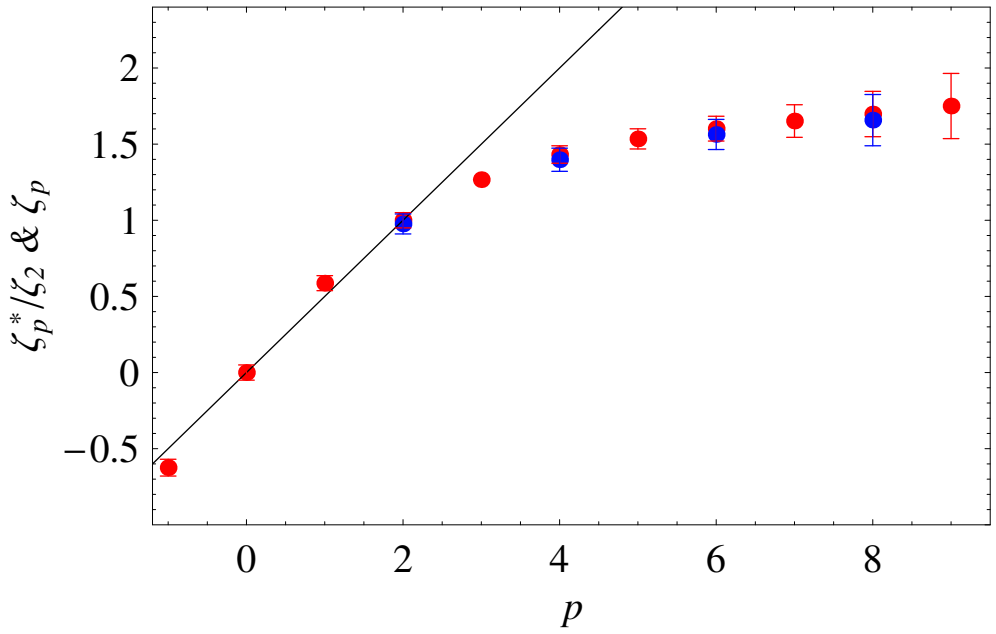

FIG. 10: Anomalous scaling exponents ζ_p^L (blue curve) and the Extended self-similarity $\zeta_p^\star/\zeta_2$ (red curve). The straight line is the K41 prediction.

when plotted against each other. ESS is widely used and gives seemingly universal scaling exponents for flows in a wide range of Reynolds numbers. As pointed out by Arneodo et al. [1] no consensus besides the observed facts exists about the interpretation or even significance of ESS. Whether the observed scaling in ESS is the signature of hidden physical laws is speculated. In the Lagrangian frame an additional problem arise. As already mentioned K41 predicts linear dependence of time scale for the Lagrangian second order structure function and hence $\zeta_2 = 1$. This is motivated by the scaling in the Eulerian frame and specifically from the *four-fifth* law. A similar *exact* result does not exist for the Lagrangian structure functions. So all in all, one could state that *it is a wonder that it works!*

The values in Table II are in excellent agreement with results obtained by Xu et al. [29] and Mordant et al. [16]. The values by Biferale et al. [5] are somehow higher and was by Xu et al. [28] explained as a different choice of inertial range.

B. The multifractal framework

The multifractal model of turbulence was introduced by Parisi and Frisch [19] in the Eulerian frame after an early attempt by Mandelbrot [13] who used multifractal measures

to characterize the spatial structure of dissipation in turbulence.

The multifractal model is phenomenological and has been able to successfully predict the corrections to K41 similarity scaling for high order moments of spatial velocity increments [10, 14, 26].

Borgas [8] discusses multifractals in the Lagrangian frame and introduces a bridge to the Eulerian framework. The litterature is, however, not very rich on work on Lagrangian multifractals, which could have to do with the difficulties in obtaining reliable Lagrangian data set more than a animosity against the multifractal model. Work by Biferale et al. [5, 7], Chevillard et al. [9], Mordant et al. [15, 16], Xu et al. [29] have, however, shed light on the issue of multifractals in the Lagrangian frame.

In the Lagrangian multifractal model the flow is assumed to possess a range of scaling exponents $h_{min}, ..., h_{max}$ with a certain probability so that

$$\delta v(\tau) \sim \tau^h. \tag{12}$$

For each scaling exponent h there is a fractal set with a h-dependent dimension $D^L(h)$. The embedding dimension is one ($\tau \in \mathcal{R}$) and hence $D^L(h) \leq 1$ for all h. The probability $P_h^L(\tau)$ of having an exponent h at time τ is therefore proportional to $1 - D^L(h)$. From a steepest descent argument one can calculate a relation between the anomalous scaling exponents ζ_p^L and the fractal dimension $D^L(h)$ given by [10]:

$$\zeta_p^L = \inf_h [ph + 1 - D^L(h)]. \tag{13}$$

If $D^L(h)$ is *concave* a Legendre transformation gives

$$D^L(h) = \inf_p [ph + 1 - \zeta_p^L]. \tag{14}$$

In Figure 11 we have plotted $D^L(h)$ obtained through eqn. 14. First we calculated ζ_p^L for both integer and non-integer values of p between $p = -1$ and $p = 9$. The result is the red curve in the Figure 11.

The black dots are the result by Xu et al. [28] who in a PTV experiment of Reynolds number $Re_\lambda = 200, 690$ and 815 measured $D^L(h)$ both trough $P_h^L(\tau)$ which they manage to measure directly and through eqn. 14 as we have done here. They arrived at the same $D^L(h)$ from both calculations putting confidence in the multifractal model for Lagrangian velocity increments. The agreement between their data and ours is very good. Only for $h > 0.6$ in the linear portion of $D^L(h)$ we observe a discrepancy.

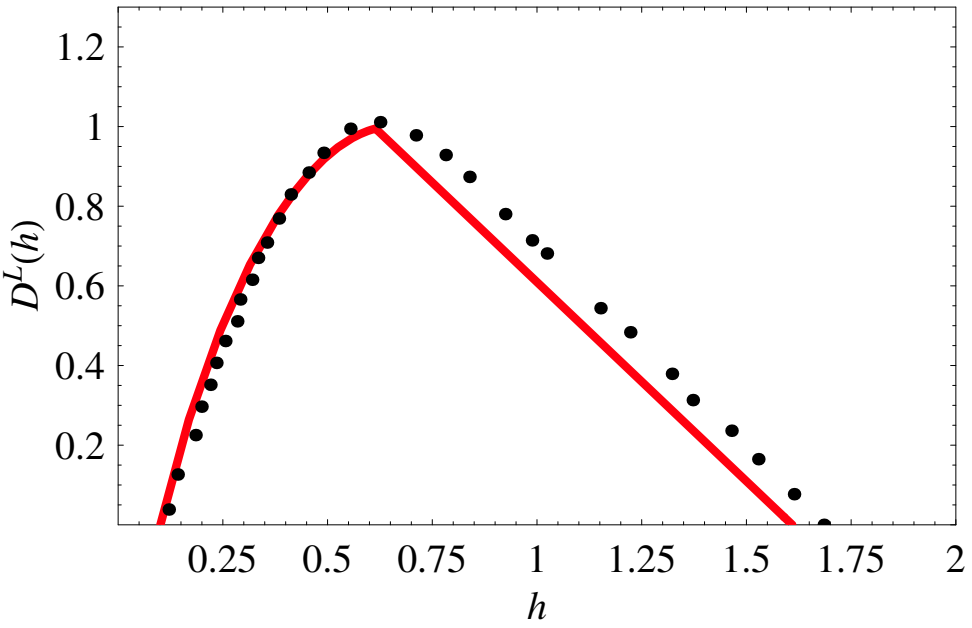

FIG. 11: The Lagrangian multifractal dimension spectrum $D^L(h)$. The black dots are the result by Xu et al. [28].

This linear portion of $D^L(h)$ was by Xu et al. [28] explained in the following way. Because the domain of h is finite eqn. 13 will become a linear function after some p'. This linear behavior is also observed in Figure 10 for large ps. The transition point h' happens where p' minimizes the right hand side of eqn. 13. For $p > p'$ we therefore have that $\zeta_p^L = h_{min}p + 1$. Since only moments of the structure functions of order larger than -1 converge we have $p' = -1$ and the linear part of the curve is $D^L(h) = -h + 1 - \zeta_{-1}$. Xu et al. [28] successfully corrected the models by Biferale et al. [5] (from a theoretical prediction by She and Leveque [23]) and Chevillard et al. [9] and found a remarkable match. The discrepancy in Figure 11 therefore stems from different estimates of ζ_{-1}^L and the uncertainty in measuring it.

Chevillard et al. [9] came up with a formula for the connection between $D^L(h)$ and its Eulerian counterpart $D^E(h)$. The formula is

$$D^L(h) = -h + (1+h)\left(D^E\left(\frac{h}{1+h}\right) - 2\right). \tag{15}$$

From our database we have calculated the Eulerian anomalous scaling exponents from ESS structure functions

$$S^p_{E,ESS}(r) \equiv \langle |\delta_r u(r)|^p \rangle \sim r^{\zeta_p^{\star E}}. \tag{16}$$

Results are shown in Figure 12. In (a) $S^p_{E,ESS}(r)$ are plotted from $p = 1, ...9$. For all orders ESS seems to work fine. In (b) the anomalous scaling exponents $\zeta^{\star E}_p$ are shown.

The values are in perfect agreement with the theoretical model by She and Leveque [23]. More interesting is the departure from the K41 prediction which is smaller than in the Lagrangian frame. This is interpret as Lagrangian statistics being more intermittent.

Just like in the Lagrangian frame there is a Legendre transformation between ζ^E_p and $D^E(h)$:

$$D^E(h) = \inf_p [ph + 3 - \zeta^E_p] \tag{17}$$

The only difference from eqn. 14 is the embedding dimension which in the Eulerian frame is three ($\mathbf{r} \in \mathcal{R}^3$).

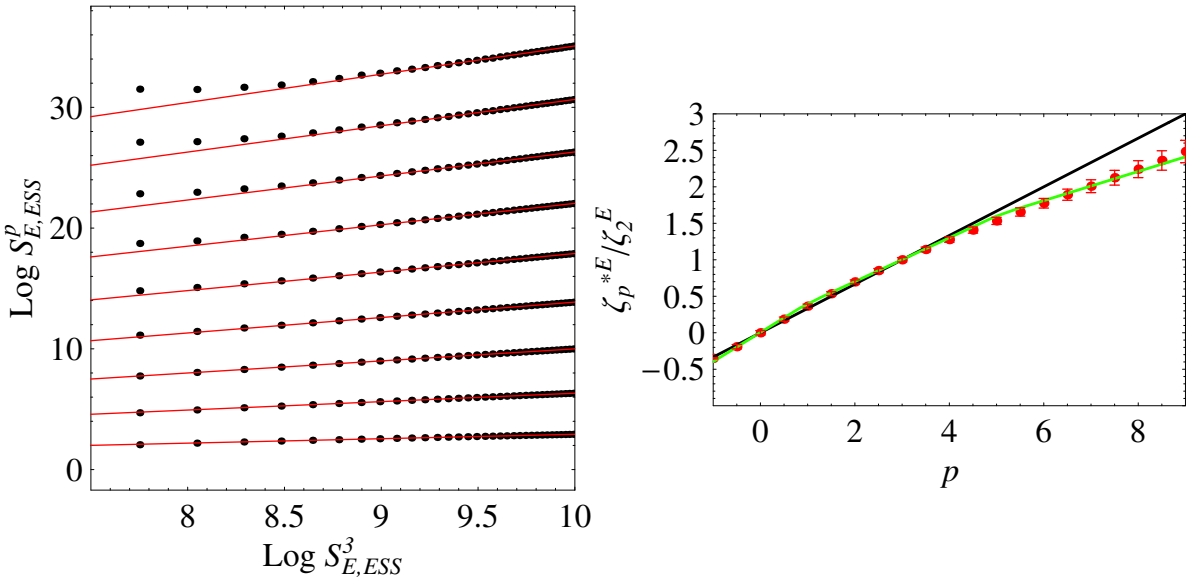

FIG. 12: (a) ESS Eulerian structure functions $S^p_{E,ESS}(r)$ of order p as a function of $S^3_E(r)$. $p = 1, .., 9$ increasing upwards. (b) Anomalous scaling exponent determined from (a) (red dots). The straight line is the K41 prediction and the green curve is the theoretical model by She and Leveque [23].

From eqn. 17 and 15 we can find $D^L(h)$ from the Eulerian anomalous scaling exponent presented in Figure 12 (b). The comparison is plotted in Figure 13. Again we observe a discrepancy in the linear part of D^L_h. Whether it comes from the determination of the anomalous scaling exponents from ESS or that there is a flaw in eqn. 15 we can not say at the

moment. A direct measurement of the probability P_h in both the Eulerian and Lagrangian frame might give more insight into the connection between the two frames.

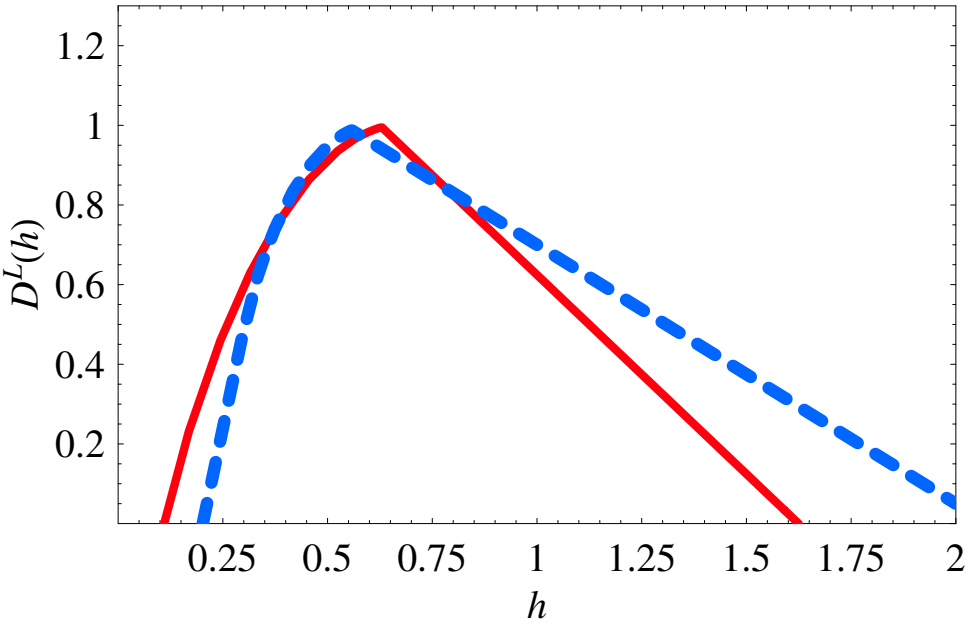

FIG. 13: The Lagrangian multifractal dimension spectrum $D(h)$. The red curve is calculated from Lagrangian ESS structure functions while the blue is obtained though Eulerian structure functions and 15.

The physical interpretation of the multifractal model is not that easy. In K41 similarity scaling only one scaling exponent is possible, namely $h = 1/3$ and thus $\zeta_p^E = p/3$. This is motivated from the fact the Navier-Stokes (N-S) equation is only invariant under one scaling group. This group is characterized by an exponent $\bar{h}$ obtained by scaling the N-S with the following transformation (time,position,velocity): $t, \mathbf{r}, \mathbf{u} \mapsto \lambda^{1-\bar{h}} t, \lambda \mathbf{r}, \lambda^{\bar{h}} \mathbf{u}$ for $\lambda \in \mathcal{R}_+$. The solution is $\bar{h} = -1$. In the limit of infinite Reynolds number the viscosity term in the N-S equation becomes negligible and we find that the N-S equation. is now invariant to infinitely many exponents $\bar{h}$. This is one of the motivations for the multifractal model. It is, however, not a justification. Another important aspect of the model is the fact that when an eddy breaks up into smaller eddies in the Richardson picture the smaller eddies do not cover the same amount of space. Instead they cover only a fraction equal to $3 - D^E(h)$. We thus have regions in the flow with large activity and regions with almost calm waters. In the Lagrangian frame this would mean that the individual fluid particles are *not free* to move around in all directions. For example as reported by [20] and [7] are particles often trapped

by intense vortices. The large accelerations and velocity increments of these events are therefore of dimension lower than 3 in the Eulerian frame and lower than 1 in the temporal. This spiral motion of fluid particle around a fluid filament is also the fluid mechanical picture of intermittent events in the model by She and Leveque [23]: by entraining surrounding fluid kinetic energy fluctuations are effectively dissipated along the axis of the filament.

As emphasized by Borgas [8] the multifractal model does, however, not imply that the trajectories of fluid particles are fractal trajectories themselves.

V. CONCLUSIONS

We have measured Lagrangian one-particle statistics and looked at small-scale behavior. The finiteness of the measuring volume can be used to calculate the mean kinetic energy dissipation ε in the flow without any further assumptions. The small scales do seem to be affected by the large-scale inhomogeneities present in our flow. We do not observe a significant inertial range but by Extended Self-Similarity we are able to extract a quantitative measure of the structure functions of high order. From these we calculate the Lagrangian anomalous scaling exponents and find excellent agreement with already published results.

Via the multifractal model we have calculated the Lagrangian multifractal dimension spectrum. The spectrum is similar to the one published by Xu et al. [29] even though our Reynolds number is significantly lower and our mean flow is different.

Most importantly we have shown that a high Reynolds number is not necessary to obtain results in the Lagrangian frame. All experiments and DNS do show the same qualitative features and no clear Lagrangian inertial range has been observed. Whether it is because current experiments are performed with too low Reynolds number or it simply do not exist future experiments will tell.

---

[1] A. Arneodo, C. Baudet, F. Belin, R. Benzi, B. Castaing, B. Chabaud, R. Chavarria, S. Ciliberto, R. Camussi, F. Chilla, B. Dubrulle, Y. Gagne, B. Hebral, J. Herweijer, M. Marchand, J. Maurer, J. F. Muzy, A. Naert, A. Noullez, J. Peinke, F. Roux, P. Tabeling, W. Van de Water, and H. Willaime. Structure functions in turbulence, in various flow configurations, at

reynolds number between 30 and 5000 using extended self-similarity. *Europhys. Lett.*, 34:411, 1996.

[2] R. Benzi, S. Ciliberto, R. Tripiccione, C. Baudet, and S. Succi. Extended self-similarity in turbulent flow. *Phys. Rev. E.*, 48:29, 1993.

[3] J. Berg, B. Lüthi, J. Mann, and S. Ott. Backwards and forwards relative dispersion in turbulent flow: An experimental investigation. *Phys. Rev. E*, 34:115, 2006.

[4] J. Berg, B. Lüthi, S. Ott, and J. Mann. Coarse-grained strain dynamics and backwards/forwards dispersion. *manuscript in preparation*, 2006.

[5] L. Biferale, G. Boffetta, A. Celani, B. J. Devenish, A. Lanotte, and F. Toschi. Multifractal statistics of lagrangian velocity and acceleration in turbulence. *Phys. Rev. Lett.*, 93:064502, 2004.

[6] L. Biferale, G. Boffetta, A. Celani, B. J. Devenish, A. Lanotte, and F. Toschi. Multiparticle dispersion in fully developed turbulence. *Phys. Fluids.*, 17:111701, 2005.

[7] L. Biferale, G. Boffetta, A. Celani, B. J. Devenish, A. Lanotte, and F. Toschi. Particle trapping in three-dimensional fully developed turbulence. *Phys. Fluids*, 17:021701, 2005.

[8] M. A. Borgas. The multifractal lagrangian nature of turbulence. *Phil. Trans. R. Soc. Lond. A.*, 342:379, 1993.

[9] L. Chevillard, S. G. Roux, E. Lévêque, N. Mordant, J.-F. Pinton, and A. Arneodo. Lagrangian velocity statistics in turbulent flow: effects of dissipation. *Phys. Rev. Lett.*, 91:214502, 2003.

[10] U. Frisch. *Turbulence – the legacy of A. N. Kolmogorov*. Cambridge, 1995.

[11] R.-C. Lien and E. A. D'Asaro. The kolmogorov constant for the lagrangian velocity spectrum and structure function. *Phys. Fluids.*, 14:4456, 2002.

[12] B. Lüthi, J. Berg, S. Ott, and Mann J. Lagrangian multi-particle statistics. *submitted*, 2006.

[13] B. B. Mandelbrot. Intermittent turbulence in self-similar cascades: divergence of high moments and dimension of the carrier. *J. Fluid Mech.*, 62:331, 1975.

[14] C. Meneveau, K. R. Sreenivasan, P. Kailanath, and M. S. Fan. Joint multifractal measures: Theory and applications to turbulence. *Phys. Rev. A*, 41:894, 1990.

[15] N. Mordant, J. Delour, E. Lévêque, A. Arnéodo, and J.-F. Pinton. Long time correlatios in lagrangian dynamics: a key to intermittency in turbulence. *Phys. Rev. Lett.*, 89:254502, 2002.

[16] N. Mordant, E. Lévêque, and J.-F. Pinton. Experimental and numerical study of the lagrangian dynamics of high Reynolds turbulence. *New. J. Phys.*, 6:116, 2004.

[17] N. Mordant, P. Metz, O. Michel, and J.-F. Pinton. Mearesurement of lagrangian velocity in fully developed turbulence. *Phys. Rev. Lett.*, 87:214501, 2001.

[18] N. T. Ouellette, H. Xu, M. Bourgoin, and E. Bodenschatz. Small-scale anisotropy in lagrangian turbulence. *New. J. Phys.*, 8:102, 2006.

[19] G. Parisi and U. Frisch. On the singularity structure of fully developed turbulence. *Turbulence and predictability in geophysical fluid dynamics, Proceed. Intern. School of Physics 'E. Fermi', 1983, Varenna, Italy 84-87, eds. M. Ghil, R. Benzi and G. Parisi. North Holland, Amsterdam.*

[20] A. La Porta, G. A. Voth, J. Alexander A. M. Crawford, and E. Bodenschatz. Fluid particle accelerations in fully developed turbulence. *Nature*, 409:1017, 2001.

[21] B. Sawford. Reynolds number effects in lagrangian stochastic models of turbulent dispersion. *Phys. Fluids A*, 3:1577, 1991.

[22] B. Sawford. Turbulent relative dispersion. *Annu. Rev. Fluid Mech.*, 422:207, 2001.

[23] Z.-S. She and E. Leveque. Universal scaling laws in fully developed turbulence. *Phys. Rev. Lett.*, 72:336, 1994.

[24] X. Shen and Z. Warhaft. The anisotropy of the small scale structure in high Reynolds number ($Re_\lambda \sim 1000$) turbulent shear flow. *Phys. Fluids*, 12:2976, 2000.

[25] X. Shen and Z. Warhaft. Longitudinal and transverse structure functions in sheared and unsheared wind-tunnel turbulence. *Phys. Fluids*, 14:370, 2002.

[26] K. R. Sreenivasan and R. A. Antonia. The phenomenological of small-scale turbulence. *Annu. Rev. Fluid Mech.*, 29:435, 1997.

[27] H. Tennekes and J. L. Lumley. *A first course in turbulence.* MIT Press, 1972.

[28] H. Xu, M. Bourgoin, N. T. Ouellette, and E. Bodenschatz. High order lagrangian velocity statistics in turbulence. *Phys. Rev. Lett.*, 96:024503, 2006.

[29] H. Xu, N. T. Ouellette, and E. Bodenschatz. Multifractal dimension of lagrangian turbulence. *Phys. Rev. Lett.*, 96:114503, 2006.

[30] P. K. Yeung. Lagrangian investigations of turbulence. *Annu. Rev. Fluid Mech.*, 34:115, 2002.